PARAMETRIC AMPLIFICATION OF MID-INFRARED PICOSECOND RADIATION

Maria Grigore

A thesis submitted in partial fulfilment of
the requirements of the University of
Abertay Dundee for the degree of
Doctor of Philosophy
February 2006

PARAMETRIC AMPLIFICATION OF MID-INFRARED PICOSECOND RADIATION

Maria Grigore

A thesis submitted in partial fulfilment of the requirements of
the University of Abertay Dundee for the degree of
Doctor of Philosophy

This research programme was carried out in collaboration with
the FOM Instituut voor Plasmafysica "Rijnhuizen",
3430 BE Nieuwegein, The Netherlands.

February 2006

I certify that this thesis is a true and accurate version of the thesis approved by the external examiners.

Signed .. [redacted] Date....12-6-06.....

Declaration

I hereby declare that while registered as a candidate for the degree for which this thesis is presented I have not been a candidate for any other award. I further declare that, except where stated, the work in this thesis is original and was performed by myself.

Signed:  (Maria Grigore), Date: 12 May, 2006.

Acknowledgements

I thank everyone who contributed to this thesis, especially to my supervisors, Dr. Allan MacLeod and Prof. Dr. Allan Gillespie. They offered great support to me.

Although I was a student at a UK university, I have been working at a laboratory in The Netherlands – the FOM Instituut voor Plasmafysica, "Rijnhuizen" at Nieuwegein. I want to thank the scientists at the FELIX facility, who helped me in organizing my experimental work, namely to Dr. Lex van der Meer, Dr. Giel Berden and Dr. Britta Riedlich. Dr. Giel Berden was cooperating with me on a daily basis, and he dedicated a lot of time and energy for helping and guiding me in various aspects of my work. I thank the technicians at FELIX group and the technicians and workers at the workshop.

Special thanks to Arlee V. Smith from Sandia National Laboratories. He wrote for me a custom version of his SNLO code. This contributed a lot to the simulations performed for this thesis.

I want to thank Dr. Ian Bradley for helping me performing experiments in the beginning of my doctoral studies.

I am grateful also to Alexey Merkulov who gave assistance in programming work.

I want finally to thank my family and my spiritual father, Pr. Prof. Dr. Constantin Coman, for their love and support.

Abstract

High power, tunable, mid-infrared sources are important in many fields, like spectroscopy and medical applications. This thesis presents a technique for realising a high power tuneable mid-infrared picosecond source, by combining the radiation from a free electron laser with a powerful Nd:YAG pump laser. The method allows obtaining an amplified energy of the order of one millijoule, for pulse durations of few picoseconds and a repetition rate of 10 Hz. The radiation is tuneable in the wavelength range of 4-11 μm. The amplified energy depends on the wavelength and varies between few hundreds of microjoules to one millijoule, while the input pulse duration is preserved.

Table of contents

Chapter 1 Introduction

The purpose of the work described in this *Thesis* is developing a powerful, tuneable, mid-infrared source, in the range of 4-11 μm. This source uses the mid-infrared radiation emitted by the free-electron laser existing at the FELIX facility in Nieuwegein, the Netherlands. The energy of typically a few microjoules in picosecond pulses delivered by the free-electron laser is amplified to values of the order of one millijoule, while maintaining the short pulse duration. This unprecedented power opens up new possibilities in nonlinear spectroscopy studies, studies of biological samples, alignment of molecules or Coulomb explosion, but also in the investigation of nonlinear optical properties of organic or inorganic materials.

In this *Introduction* the general characteristics of the currently available powerful mid-infrared sources, and several important applications of such sources, are presented. A description of different types of currently available sources follows. These fall into two main categories: the parametric sources and the free electron lasers. The *Introduction* ends with a concise description of the work presented in this *Thesis* and its contribution to realizing a new powerful picosecond mid-infrared source, as a combination (hybrid) of the two classes of sources firstly presented.

1.1 Powerful tuneable ultrafast mid-infrared sources

There are many definitions of the 'mid-infrared region of the spectrum'. For example, the wordiq Encyclopedia defines it as the 2.5-10 μm wavelength range, Encyclopedia Britannica as 2.5-25 μm and others refer to 2-30 μm [1]. In this thesis, the mid-infrared range under consideration is 4-11 μm.

The mid-infrared spectral region is interesting especially for vibrational spectroscopy, because the fingerprints (the characteristic set of infrared absorption lines) of molecules lie in this region of the spectrum. A wide variety of spectroscopy applications like atmospheric remote sensing, environment monitoring, and analysis of impurities in production of highly purified materials for pharmaceutical, microbiology, and electronic industries make use of this important region of the spectrum. The same wavelength range is also important for medical applications [2]

like dentistry, keratectomy, microsurgery, diagnosis using breath analysis, cardiology, and dermatology. Most of the medical applications are based, on the strong absorption of the mid-infrared radiation in the human tissue, caused by the presence of the chromophores. Thus, the most important target material for surgical applications use the strong absorption in water in the range 2.5-7 μm, and of dentin and enamel (3-20 μm), and apatite and cholesterol in the range 5.5-12 μm. [2] The water absorption is used in the surgery of tissues with high water content like cornea, brain cartilage, disk material, enamel and dentin are typical for dental surgery, while the apatit and cholesterol absorption in mid-infrared are used in surgery of arteroschlerotic plaques of various compositions. The applications in diagnosis, like human breath analysis, use spectroscopy methods to identify chemical components.
For spectroscopy applications, the ideal mid-infrared source characteristics are [3]: enough optical power to enable high signal to noise ratios; (rapid) tuneability in a wide range with high wavelength selectivity, narrow bandwidth, good pointing stability and low wavelength jitter in both the short and the long term; and low sensitivity to environment conditions like humidity, temperature and pressure. However, the temporal structure, the bandwidth, the tunability range and power are parameters that are required by the envisaged application. Thus, linear spectroscopy studies can be performed using thermal or other continuous low power sources (diodes-lead-salt diode lasers, quantum cascade lasers and antimonide lasers, narrow-linewidth optical parametric oscillators (OPOs), etc.), but high energies in short pulses (picosecond and subpicosecond pulse duration) are desired features of infrared sources for nonlinear spectroscopy and study of the dynamics of various samples. Ultrafast sources with femtosecond or picosecond pulse duration are useful tools for studying the dynamics of processes with relaxation time on a picosecond scale. The broadband spectrum of femtosecond pulses naturally limits the wavelength selectivity and resolution. Nonlinear spectroscopy with picosecond pulse duration is a good trade-off between the requirement of short pulse duration, and the requirement of relatively narrow bandwidth [4].

It is much more difficult to define an ideal source for medical applications, because of the large diversity of effects involved in the laser-tissue interaction. The effects depend on laser fluence, wavelength and operation regime (pulsed or CW), and on the tissue itself. The three main requirements are wavelength selectivity,

safety and efficacy [2]. The ideal medical source should be less invasive, and the damages of thermal and mechanical nature should be minimized.

1.2 Classes of ultrafast tuneable mid infrared sources

There are several major ways of generating ultra-short pulses light in the mid-infrared range, but generally they can be divided in two major classes: frequency conversion devices, and Free Electron Lasers (FELs).

1.2.1 The frequency conversion devices

Although the first prototype device was realised in 1965 [5], it took about twenty years of research oriented into the development of suitable pump laser sources and high quality nonlinear crystals to reach the stage when frequency conversion devices became reliable sources for spectroscopy applications. This delay was caused by difficulties related to the stability, coherence, high intensity in the desired wavelength range, and spectral characteristics of the pump sources and to nonlinear crystals (high nonlinear constant, high transparency, high damage threshold). The crystals that revolutionized the optical parametric oscilators (OPOs) field for mid-infrared generation were β-BaB_2O_4 (BBO), LiB_3O_5, $KTiPO_4$ (KTP) with its arsenate analogues $KTiOAsO_4$ (KTA), $RbTiOAsO_4$ (RTA). The properties of the "classical" crystals like $ZnGeP_2$ (ZGP), $AgGaS_2$ (AGS), $AgGaSe_2$, etc. were greatly improved by a better understanding of the material properties (especially of the origin of the defects) and developing of growth techniques which made available longer crystals with improved transparency and higher damage threshold. For the wavelength range of interest in this thesis, the most commonly used crystals for mid-infrared frequency conversion are AGS, ZGP, $AgGaSe_2$, GaSe, CdS [6]

An important turning-point was the development of crystals with periodic structure (the periodical poled crystals), providing the possibility of non-critical phase matching which greatly improved the nonlinear constant and the efficiency of the parametric devices [7-11]. These are usually ferroelectric crystals ($LiNbO_3$, KTP, KTA, RTA), which present the possibility of changing the sign of nonlinearity by applying a local electric field at high temperatures.

The frequency conversion devices use second order nonlinear effects to convert radiation from an initial wavelength to other wavelengths. For obtaining high output power, the pump radiation is provided by mode-locked lasers (Nd:YAG,

Nd:YLF, Nd:YVO_4, Er:YAG, etc.) or self-mode locked lasers (Ti:Sapphire lasers) with pulse durations ranging from tens of femtoseconds to tens of picoseconds.

Further, these devices can be classified as optical parametric oscillators (OPOs), difference frequency generation (DFG), (travelling wave) optical parametric generation (OPG) and/or optical parametric amplification (OPA) devices. The choice of the laser sources and nonlinear crystal depends on the envisaged wavelength range and on the nonlinear crystal used for generating the mid-infrared radiation.

The tuneable-wavelength range and output characteristics of the parametric sources depend on both the laser sources and nonlinear crystals. Typically, the covered wavelength range in the mid-infrared region is limited by the crystal properties. Tuneable devices operating up to 20 μm have been developed [6,12,13]. The output energy and conversion efficiency of any parametric device vary with wavelength. Typically, the output energies are about several microjoules per pulse and maximum values of few tens of microjoules can be obtained [14].

1.2.2 Free-electron lasers

The second major class of powerful mid-infrared laser is formed by the FELs. An FEL is based on a free relativistic electron beam that traverses a periodic magnetic field, thus generating laser light. The light beam is captured between two mirrors, forming the laser resonator. FELs can generate light in virtually any wavelength range [15,16] by choosing a suitable electron energy and magnetic field strength. Furthermore the temporal structure of the generated light resembles the electron beam structure, so that, in the case of Linac-based FELs, the radiation emerges in macropulses of few microseconds length. Each macropulse consists of trains of micropulses with duration comparable with the one of the electron beam. This is adjustable for the mid-infrared wavelength range between few hundreds femtoseconds to several picoseconds.

In comparison with the parametric devices, which are commonly table-top systems, the FELs are often major facilities. At present, there are several large FEL facilities in the world providing mid-infrared light [17].

Table 1-1 shows an overview of the most important parameters of some of the FELs emitting in the mid infrared.

The output characteristics of the FELs differ considerably and consequently, the applications targeted by their users [18-21]. The widest tuneability ranges are

available at FELIX (Nieuwegein, The Netherlands) between 4.5-250 μm (from 3 μm on the third harmonic [18]) and at CLIO (LURE – Orsay, France) 3-90 μm, recent developments expanding the wavelength range to 120 μm [22]. The other facilities cover more or less only the mid-infrared range, or the far-infrared. The temporal structure of the emitted radiation is also very different. A common feature is the micropulses train, which for the normal conductive linac-driven FELs is emitted in macropulses with duration of several microseconds and repetition rate up to tens of Hz and high micropulse peak power. For nonlinear spectroscopy the micropulse peak-power is a very important feature. The highest energy/per micropulse values available from FELs are obtained at CLIO (~100 μJ) and Jefferson Laboratory (~100-300 μJ) while, for the same wavelength range, the micropulse energy at FELIX is ~ 5-50 μJ, in the wavelength range of 4-11 μm. The energy per pulse depends on the pulse duration. For longer pulses (and narrower spectral bandwidth), generally the energy decreases.

The pulse structure of an FEL follows the electron beam structure. For FELIX, this structure is presented in Chapter 4, Figure 4-7.

	CLIO [22,23]	Jlab [24]	FELIX [18]	Vanderbilt [20,25]	Duke [19,20]	Tokyo [26]	Darmstadt [27, 28]	Stanford [21]	BFEL [29]
Wavelength range (μm)	3-90	1.5-14	4.5-250	2.1-9.8	2-10	5-16	3-10	3-15	7-19
Micro-pulse duration (ps)	0.5-6 ps	0.5-1.7	6-100 optical cycles	>1	0.5-3	1-2	~2	0.7-3	4
Spectral bandwidth	0.2-10%	0.3-2%	0.4-7%		0.3-2%	0.2%		1.9-2.2%	0.5-2%
Micro-pulse repetition rate (MHz)	62.5	4.7- 75	25 or 1000	2856	2856	2856	10	11.82	
Micro-pulse energy (μJ)	<100	100-300	1-50	20	1-6	8-25	0.3	2	0.4-2
Micro-pulse peak power (MW)	100		0.5 ÷ 100	6.6		2-5	0.150	-	
Macro-pulse duration (μs)	~10	CW	< 10	3-6	0.5-6	1-3	4000-8000	5000	2
Macro-pulse repetition rate (Hz)	6.25-25	-	<10	1-30	1-30	10	-	20 Hz	
Average power (W)		10000		0-15		~ 1	3	1.2	

Table 1-1 Parameters of FELs emitting mid-infrared light

1.3 Enhancing the pulse energy in mid-infrared

In spite of the large range of possible applications that can be covered with parametric devices and FELs, there exist applications needing higher peak power of the mid-infrared light, like Coulomb explosion, alignment of molecules, or spectroscopy studies of biological samples.

Increasing the pulse power is desirable also for nonlinear spectroscopy applications. A high peak power can greatly enhance the envisaged nonlinear effect, giving more accurate experimental results, and in the mean time creating the possibility of observing new nonlinear. Maintaining a short pulse duration is desirable for dynamics studies, or time-resolved spectroscopy.

The long relaxation times of the various systems investigated, for example, in pump-probe experiments impose a limit to the repetition rate of the mid infrared pulses. Irradiation of the samples with long relaxation times, can result in un-wanted heating, with long cooling times (of the order of milliseconds or even tens of milliseconds [20]), due to the pulse repetition rate is higher than 1 kHz, as is the case of the most FELs. That is why, the repetition rate usually provided by an FEL is too high for such studies and it leads to the heating of the samples, and thus to modifications of real signals [20]. The cooling times of the samples set the repetition rates for which the sample heating can be neglected. The high power per pulse is needed to overcome the water absorption in mid-infrared and to accomplish a nonlinear response in the biological sample [20]).

The work described in this thesis aimed at increasing the peak-power at FELIX, in the wavelength range of 4-11 μm, from energies of several microjoules to values close to 1 mJ, in few picoseconds long pulses. For this purpose, a powerful 10 Hz Nd:YAG regenerative amplifier is used as a pump source for parametric amplification in a $AgGaS_2$ crystal, leading to either optical parametric amplification (OPA) or optical parametric chirped-pulse amplification (OPCPA) of the free electron laser at FELIX. In both cases, the temporal structure of the amplified pulses is determined by the pump laser repetition rate of 10 Hz. The OPA and OPCPA processes are described in detail in Chapter 7 and Chapter 8, respectively. In the OPA case, the pump laser interacts with the picosecond mid-infrared FELIX pulses, while in the OPCPA case, the FELIX pulses are stretched and comparable in length

with the pump, leading to better efficiency and higher amplified energy. The pulse duration is shortened back by the use of a compressor. The amplified energy reaches values close to 1 mJ, which is the highest obtained energy in mid-infrared picosecond pulses. Because of the un-precedented mid-infrared peak-power level obtained by OPCPA method, new fields of interesting applications in nonlinear spectroscopy are opened up. It is possible to investigate biological samples with long relaxation times by minimizing the input energy of the FEL macropulse, while the amplified pulse reaches several hundreds microjoules, at a frequency of 10 Hz, and in this way avoiding the sample heating. The source is also appropriate for studying nonlinear absorption in atmosphere. The OPCPA with the $AgGaS_2$ crystal can be applied for any tuneable picosecond radiation source, emitting in the same mid-infrared range, which can be synchronized with the pump source.

The advantages of using an FEL as the signal source are the fast tuneability, the possibility of adjusting the pulse length and spectral properties, and the quite high initial pulse energy. In principle, the FEL can be replaced with an OPO pumped by a Ti: sapphire-pumped OPG/OPA system. For the wavelength range of 4-11 μm the main advantage of the FEL is the higher pulse energy.

1.4 Outline of the remainder of the thesis

The work in this thesis is structured as follows:

Chapter 1 is an introduction presenting the available powerful mid-infrared sources with their general characteristics.

Chapter 2 and 3 present a fundamental description of the nonlinear second order interaction. The concepts introduced in these chapters are necessary for understanding the experimental results presented (Chapters 5, 6 and 7), as well as the results of the simulations presented in Chapter 8.

In Chapter 4 a description of the laser sources involved in experiments is given, with highlighting the features of the laser sources that make them suitable for the parametric amplification experiments. Chapter 5 describes in detail the nonlinear crystal used for parametric amplification. The advantages that make the nonlinear crystal $AgGaS_2$ an efficient crystal for parametric amplification and the drawbacks limiting the power of the amplified are presented and explained.

In Chapter 6, various simulations are described. The first part describes the calculations leading to the choice of the nonlinear crystal used in experiments, while inthe second part a comparison between the simulations and the experimental results is presented.

Chapters 7 and 8 are the core of the thesis. They present the experimental results with the two methods used for enhancing FELIX micropulse energy. The OPA method, together with its results and limitations, is discussed in Chapter 7. The OPCPA method, which can substantially improve the amplified pulse energy is presented in Chapter 8. The results of the amplified energy, spectral modifications and autocorrelation traces are also presented and compared to the parameters of the un-amplified pulses. High energies of more than 1 mJ in picosecond pulse durations are obtained using the OPCPA method.

Chapter 9 presents an overview and outlook of the work.

1.5 Bibliography

1. T. Sorokina and K.L. Vodopyanov, *Solid Stated Mid-Infrared Laser Sources*, Topics in Applied Physics, vol. 89, Springer Verlag, Berlin, 2003, "Preface"

2. B. Jean and T. Bende, "*Mid-IR applications in medicine*", in T. Sorokina and K.L. Vodopyanov, *Solid Stated Mid-Infrared Laser Sources*, Topics in Applied Physics, vol. 89, Springer Verlag, Berlin, 2003, pp. 511-544

3. F.K. Tittel, D. Richter, and A, Fried, "*Mid-infrared laser applications in spectrocscopy*", in T. Sorokina and K.L. Vodopyanov, *Solid Stated Mid-Infrared Laser Sources*, Topics in Applied Physics, vol. 89, Springer Verlag, Berlin, 2003, pp.445-510

4. C. W. Hoyt, M. Sheik-Bahae, and M. Ebrahimzadeh, "*High-power picosecond optical parametric oscillator based on periodically poled lithium niobate*", Opt. Lett., Vol. 27, pp1543-1545, 2002.

5. J. A. Giordmaine and Robert C. Miller, "*Tunable coherent parametric oscillation in $LiNbO_3$ at optical frequencies*", Phys. Rev. Lett. Vol. 14, pp. 973–976, 1965

6. K. L. Vodopyanov, "*Parametric generation of tunable infrared radiation in $ZnGeP_2$ and GaSe pumped at 3 μm*", J. Opt. Soc. Am. B, Vol. 10, pp. 1723-1729, 1993

7. G.A. Magel, M.M. Fejer, and R.L. Byer, "*Quasi-phase-matched second harmonic generation of blue light in periodically-poled $LiNbO_3$*", Appl. Phys. Lett. Vol. 56, pp.108-110, 1990

8. L.E. Myers, R.C. Eckardt, M.M. Fejer, R.L. Byer, and W.R. Bosenberg, Multigrating "*Quasi-phase-matched optical parametric oscillator in periodically poled $LiNbO_3$*", Opt. Lett. Vol. 21, pp.591-593, 1996

9. W.R. Bosenberg, A. Drobshoff, J. Alexander, L.E. Myers, and R.L. Byer, "*Continuous-wave singly resonant optical parametric oscillator based on periodically poled $LiNbO_3$*," Opt. Lett. Vol. 21, pp. 713-715, 1996

10. D. Butterworth, V. Pruneri, and D.C. Hanna, "*Optical parametric oscillation in periodically poled lithium niobate based on continuous-wave synchronous pumping at 1.047 μm*", Opt. Lett., Vol. 21, pp.1345-1347, 1996

11. G.D. Miller, R.G. Batchko, W.M. Tulloch, D.R. Weise, M.M. Fejer, and R.L. Byer, "*42%-efficient single-pass CW second-harmonic generation in periodically poled lithium niobate*", Opt. Lett., Vol. 22, pp. 1834-1836, 1997

12. K. L. Vodopyanov and P. G. Schunemann, "*Efficient difference-frequency generation of 7–20-μm radiation in $CdGeAs_2$*", Opt.Lett., Vol. 23, pp. 1096-1098, 1998

13. K.L. Vodopyanov and V Chazapis "*Extra-wide tuning range optical parametric generator*", Opt. Commun., Vol. 135, pp.98–102, 1997

14. V. Petrov, F. Rotermund and F Noack, "*Generation of high-power femtosecond light pulses at 1 kHz in the mid-infrared spectral range between 3 and 12 μm by second order nonlinear processes in optical crystals*", J. Opt. A: Pure Appl. Opt., Vol. 3, pp. 1-19, 2001

15. W.B. Colson, E. D. Johnson, Michael J. Kelley, and H. A. Schwettman, "*Putting free-electron lasers to work*", Phys. Today, Vol. 55, pp. 35-41, 2002

16. P. O. Shea and H. P. Freund, "*Free-electron lasers: status and applications*", Sci., Vol. 292, pp. 1853-1858, 2001

17. W. B. Colson and and B. W. Williams, "*Free electron lasers in 2004",* Proceedings of the 2004 FEL Conference, pp.706-710

18. A.F.G. van der Meer, "*FELs, nice toys or eficient tools?*", Nucl. Instr. and Meth.A, Vol. 528, pp 8–14, 2004

19. http://www.fel.duke.edu/lightsources/mk3.html

20. S. Edwards, R. H. Austin, F E. Carroll, M. L. Copeland, M. E. Couprie, W. E. Gabella, R. F. Haglund, B. A. Hooper, M. S. Hutson, E. D. Jansen, K. M. Joos, D. P. Kiehart, I. Lindau J. Miao, H. S. Pratisto, J. H. Shen, Y. Tokutake, A. F. G. van der Meer, A. Xie, "*Free-electron-laser-based biophysical and biomedical instrumentation*", Rev. of Sci. Instr., Vol. 74, pp.3207-3245, 2003

21. T.I. Smith , H.A. Schwettman, "*Issues at a university based FEL center*", Nucl. Instr. and Meth. B, Vol. 144, pp.18-24, 1998

22. R. Prazeres F. Glotin and J. M. Ortega, "*New results of the 'CLIO' infrared FEL*" Nucl. Instr. and Meth. A, Vol.528, pp. 83-87, 2004
23. R. Prazeres, F. Glotin, J.M. Ortega, C. Rippon, R. Andouart, J.M. Berset, E. Arnaud, R. Chaput "*Study of the "CLIO" FEL properties at long wavelengths*", Nucl. Instr. and Meth. A, Vol. 445, pp.204-207, 2000

24. http://www.jlab.org/FEL/felspecs.html

25. C.A. Brau, "*The Vanderbilt University free-electron laser center*", Nucl. Instr. and Meth. A, Vol. 318, pp 38-44, 1992

26. A.V. Chernyshev, K. Nomaru, A.K. Petrov, M. Kawai, K. Toyoda, K. Nakai H. Kuroda, "*Status of FEL-SUT project, and the experimental setup for multiphoton dissociation and isotope separation in the gaseous phase*", Nucl. Instr. and Meth.A, Vol.470, pp. 76–79, 2001

27. M. Brunken, S. Dobert, R. Eichhorn, H. Genz, H.-D. Graf, H. Loos, A. Richter, B. Schweizer, A. Stascheck and T. Wesp "*First lasing of the Darmstadt CW free electron laser*", Nucl. Instr. and Meth. A Vol. 429, pp. 21-26, 1999

28. http://linac.ikp.physik.tu-darmstadt.de/fel/introduction.html

29. M. Sobajima, Y. Li, J. Xie, K. Yoshikawa, M. Ohnishi, Y.Yamamoto, H. Toku, K. Masuda, J. Kitagaki and T. Nakamura, "*Numerical study on improvements of Beijing FEL lasing performances through modifications of the beam-duct geometry*", Nucl. Instr. and Meth. A, Vol. 407, pp. 121–125,1998

Chapter 2 Three-wave nonlinear processes

In this chapter a schematic description of the three-wave (or second-order) nonlinear interaction is given.

This aims to introduce the reader to one particular case of these processes, the optical parametric amplification, which is actually extensively used in experiments described in this *Thesis*. The optical parametric amplification is characterized in Chapter 3, while in this chapter the basic elements necessary for understanding the second-order processes are introduced and the physical parameters which are fundamental to these processes are defined.

The description begins with a short overview of the propagation properties of light in uniaxial crystals. The discussion is restricted to uniaxial crystals (crystals presenting an axis of symmetry for the refractive index, called optical axis), and not extended to biaxial crystals (crystals with two symmetry axes), because the crystal used in amplification experiments described in this thesis is uniaxial. For an exhaustive treatment of light propagation in anisotropic media, see [1]. After a schematic mathematical overview of the second-order nonlinear processes, the phase matching condition, types of phase matching, effective nonlinear constant are defined and discussed.

2.1 Light propagation in nonlinear uniaxial crystals

Understanding light propagation in birefringent nonlinear crystals is crucial for the characterization of nonlinear processes. Birefringent crystals are very commonly used in parametric devices, and birefringence is a key element for the efficiency of nonlinear processes. This is due to several factors which will be elaborated upon in the course of the presentation of this chapter: the phase matching condition, effective nonlinear constant, parametric gain, group velocity mismatch, group velocity dispersion.

The optical properties of uniaxial birefringent crystals depend on the direction of propagation and polarization of light, via the refractive index. The expressions of the refractive index are derived from Maxwell's equations in a linear anisotropic medium:

$$\nabla \times \vec{E} = -\frac{\partial \vec{B}}{\partial t}$$

$$\nabla \times \vec{B} = \mu_0 \vec{J} + \mu_0 \varepsilon_0 \frac{\partial \vec{E}}{\partial t} + \mu_0 \frac{\partial \vec{P}}{\partial t}$$

$$\nabla \cdot \vec{D} = 0$$

$$\nabla \cdot \vec{B} = 0 \qquad (2\text{-}1)$$

where $\vec{E}$ is the electrical field, $\vec{B}$ the magnetic induction, $\vec{J}$ the current density, $\vec{P}$ the polarization, $\vec{D}$ the displacement vector ε_0 is the vacuum electrical permittivity, μ_0 the magnetic permeability.

and $\vec{J}$ are given by the constitutive relations:

$$\vec{D} = \varepsilon_0 \vec{E} + \vec{P}$$

$$\vec{J} = \sigma \vec{E} \qquad (2\text{-}2)$$

$$\vec{P} = \varepsilon_0 \hat{\chi} \vec{E}$$

where $\hat{\chi}$ is the linear electrical susceptibility tensor and σ the electric conductivity.

The anisotropy of the medium is expressed by the tensorial nature of the electrical susceptibility, while σ accounts for the losses in the medium. For harmonic waves, the temporal dependence of electric and magnetic fields can be expressed by:

$$\vec{E}(\vec{r},t) = \frac{\vec{E}_0}{2}[\exp j(\omega t - \vec{k} \cdot \vec{r}) + CC],\ \vec{B}(\vec{r},t) = \frac{\vec{B}_0}{2}[\exp j(\omega t - \vec{k} \cdot \vec{r}) + CC] \qquad (2\text{-}3)$$

with $\vec{k}$ being the propagation constant and ω the optical frequency, $\vec{E}_0$ and $\vec{B}_0$ are the amplitudes of the electric and magnetic fields and CC means the complex conjugate. Maxwell's equations reduce to:

$$\vec{k} \times \vec{E}_0 = \omega \vec{B}_0$$

$$\vec{k} \times \vec{B}_0 = \omega \mu_0 \varepsilon \vec{E}_0 \qquad (2\text{-}4)$$

Combining the two equations (2-4) yields:

$$\vec{k}(\vec{k} \cdot \vec{E}_0) - k^2 \vec{E}_0 + \omega^2 \mu \varepsilon \vec{E}_0 = 0 \qquad (2\text{-}5)$$

In Eq.(2-5) ε is the dielectric permittivity, which in the anisotropic case is a tensor.

$$\varepsilon_{ij} = \varepsilon_0(1+\chi_{ij}) \tag{2-6}$$

Eq.(2-5) is in fact a system of three equations in E_{0x}, E_{0y}, and E_{0z}. It has non-trivial solutions if the determinant formed with the coefficients of these variables is 0. With $\vec{k} = \frac{n(\omega)\cdot\omega}{c}\cdot\vec{s}$, $c = \frac{1}{n\sqrt{\varepsilon_0\mu}}$, one gets an equation expressing the refractive index n as function of direction of propagation of the light in the crystal:

$$\frac{s_x^2}{n^2-n_x^2}+\frac{s_y^2}{n^2-n_y^2}+\frac{s_z^2}{n^2-n_z^2}=\frac{1}{n^2}, n \neq n_{x,y,z} \tag{2-7}$$

with $\vec{s}$ being the unit vector of the propagation vector $\vec{k}$ and s_i its projections on the coordinate axes. In the form written above, Eq.(2-7) makes sense for $n \neq n_{x,y,z}$, although $n_{x,y,z}$ are possible solutions for n. For $n = n_{x,y,z}$, the direction of propagation coincides with the axis ox,y,z, respectively.

When obtaining Eq.(2-7) the permittivity tensor was considered in a coordinate system in which it has a diagonal form, coordinate system called principal dielectric frame. In this case, the expressions of the refractive indices are given by:

$$n_i = \sqrt{\frac{\varepsilon_{ii}}{\varepsilon_0}}, \text{ i=x,y,z} \tag{2-8}$$

The reference frame is shown in Figure 2-1. The direction of the optical axis coincides with the direction of OZ. The projection of the $\vec{k}$ vector on the XY plane forms the angle φ with the OX axis, while θ denotes the angle between the $\vec{k}$ vector and the optical axis (OZ). In the figure the unit vector $\vec{s}$ replaces the $\vec{k}$ vector.

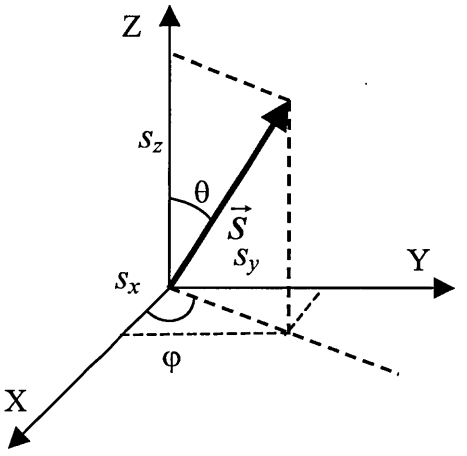

Figure 2-1 The dielectric reference frame for uniaxial crystals. The optical axis is in direction of OZ axis. The $\vec{s}$ vector (the unit vector in direction of $\vec{k}$) forms the angle θ with OZ. θ, φ and z are polar coordinates

In the dielectric coordinate system in Figure 2-1, the projections of the unit vector $\vec{s}$ are:

$$\begin{aligned} s_x &= \sin\theta\cos\varphi \\ s_y &= \sin\theta\sin\varphi \\ s_z &= \cos\theta \end{aligned} \tag{2-9}$$

For uniaxial crystals, $n_x=n_y=n_o$, called also the ordinary index, and $n_z=n_e$, extraordinary refractive index. The permittivity tensor has a diagonal form:

$$\varepsilon = \varepsilon_0 \begin{pmatrix} n_o^2 & 0 & 0 \\ 0 & n_o^2 & 0 \\ 0 & 0 & n_e^2 \end{pmatrix} \tag{2-10}$$

Replacing (2-9) and (2-10) in Eq.(2-7) leads to:

$$\left(n_o^2 - n^2\right)\left(\frac{1}{n^2} - \frac{\sin^2\theta}{n_e^2} - \frac{\cos^2\theta}{n_o^2}\right) = 0 \tag{2-11}$$

Eq.(2-11) is quadratic in n^2 and provides two solutions (eigenmodes) for the propagation in the anisotropic medium.

The solutions are:

(a) $n=n_o$ and $\vec{E} \perp \vec{k}$

(b) $$n(\theta) = \frac{1}{\sqrt{\dfrac{\sin^2(\theta)}{n_e^2} + \dfrac{\cos^2(\theta)}{n_o^2}}}, \quad \vec{E}\cdot\vec{k} \neq 0 \tag{2-12}$$

For $\vec{k}$ || OZ ($s_x=s_y=0$), the solution for n is degenerate $n=n_o$ and $\vec{E} \perp \vec{k}$.

For $\vec{k}$ ⊥OZ, there are two solutions, $n=n_o$ ($\vec{E} \perp \vec{k}$) and $n=n_e$ ($\vec{E}$ || OZ).

Eq.(2-12a) describes the ordinary ray while Eq.(2-12b) describes the extraordinary ray.

The principal plane is defined by the optical axis, OZ, and the propagation vector $\vec{k}$. The polarization of the ordinary ray is perpendicular to the principal plane, and the polarization of the extraordinary ray is contained in it.

The anisotropy (birefringence) of the crystal is characterized by the two different refractive indices, n_o and n_e. If $n_o<n_e$ the crystal is said to be positive, while if $n_o>n_e$, the crystal is negative.

In practical situations, one wants to determine the propagation characteristics of the incident beams through the crystal, when the incidence angles and the cut-angle of the crystal angle θ_c are known. After refraction at the surface of the crystal, a light wave with arbitrary polarization is virtually decomposed in two polarizations, one contained in the principal plane (extraordinary ray) and one perpendicular to it (ordinary ray). The ordinary ray propagates with the phase velocity c/n_o and does not depend on the orientation of the $\vec{k}$ vector with respect to the optical axis OZ. The refraction angle for this ray is determined only by the incidence angle and the ordinary refractive index. The extraordinary ray propagates with the phase velocity $c/n_e(\theta)$, were $n_e(\theta)$ is given by Eq.(2-12b). This is because the solutions for the wave equation (2-5) are defined as in (2-3) with the two solution for the refractive index given by Eqs.(2-12) For the extraordinary ray, the refraction angle depends on the cut-angle of the crystal and on the incidence angle, because the refractive index depends on the orientation of the optical axis with respect to $\vec{k}$. The angles used in calculations for the extraordinary ray are illustrated in Figure 2-1.

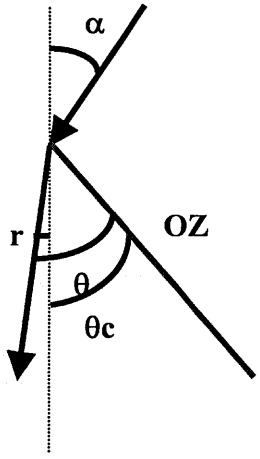

Figure 2-2 The definitions of incidence angle α, cut-angle θ_c, and refraction angle r in an anisotropic crystal. θ is the angle between the optical axis (OZ) and the refracted ray. The incident and refracted rays and the optical axis are in the same plane

The incidence and refraction angles are related by Snell's law:

$$sin(\alpha) = n(\theta)sin(r)$$

$$r = \theta - \theta_c \tag{2-13}$$

The angle α is considered positive when the incident ray is at the same side of the normal as the optical axis Z. Combining Eq.(2-12b) and Eqs. (2-13) and using some simple algebra, one obtains the expression for θ, (the angle between the optical axis and direction of propagation in the crystal) and r (the refraction angle) as a function of the incidence angle, cut angle and refractive indices:

$$\tan(\theta) = \frac{\sin(\theta_c)\cos(\theta_c) + \sin(\alpha)\sqrt{\frac{\cos^2(\theta_c)}{n_o^2} + \frac{\sin^2(\theta_c)}{n_e^2} - \frac{\sin^2(\alpha)}{n_o^2 n_e^2}}}{\cos^2(\theta_c) - \frac{\sin^2(\alpha)}{n_e^2}}$$

$$r = \theta - \theta_c \tag{2-14}$$

The angles θ and r can take two different values depending on the sign of α. At normal incidence α=0, $\theta = \theta_c$ and propagation through the crystal is described by the phase velocity $c/n(\theta_c)$.

2.2 The walk-off angle

In anisotropic crystals, the direction of the energy flow of non-ordinary beams does not coincide with the direction of the $\vec{k}$ vector. The direction of the energy flow is given by the Poynting vector:

$$\vec{S} = \vec{E} \times \vec{B} / \mu_0 \tag{2-15}$$

An electric field with arbitrary (linear) polarization can be decomposed in two components, propagating with two different phase velocities. For the extraordinary ray, due to the anisotropy of the medium, the direction of the Poynting vector forms an angle with the propagation vector, called the walk-off angle [2]. The walk-off angle ρ, defined as the angle between the direction of $\vec{S}$ with respect to $\vec{k}$ can be expressed as:

$$\rho(\theta) = \pm \arctan\left[\left(\frac{n_o}{n_e}\right)^2 \tan(\theta)\right] \mp \theta \tag{2-16}$$

as described in [2]. In Eq.(2-16), the upper sign refers to negative crystals and the lower signs to positive ones. Figure 2-3 shows an incident ray of arbitrary linear polarization, at normal incidence on a nonlinear crystal, cut at angle θ_c. The light decomposes into ordinary and extraordinary components, propagating with different phase velocities, as shown by Eq.(2-12). The propagation vectors are not shown in the figure, but they are oriented along the normal, as it easily deduced from Snell's law. The Poynting vector of the ordinary ray also follows the normal direction, while a different energy flow direction, defined by the angle ρ, appears for the extraordinary ray.

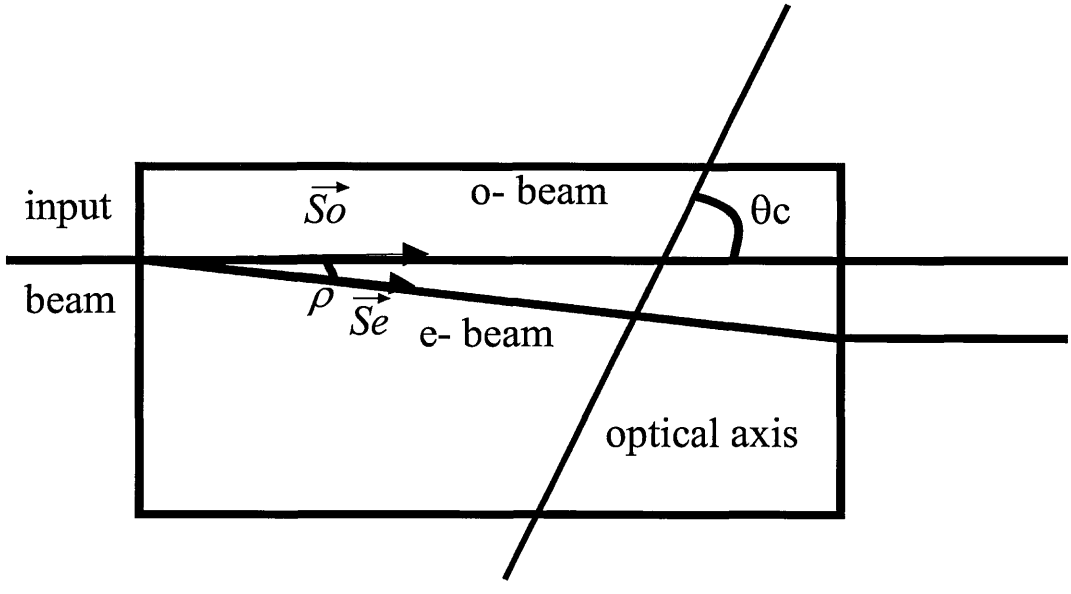

Figure 2-3 The walk-off angle at normal incidence. The ordinary and extraordinary rays are separated by the walk-off effect. Only the $\vec{S}_e$ vector of the extraordinary beam deviates from normal propagation with the angle ρ. The effect exists only when the direction of propagation is not collinear with the optical axis, and the deviation takes place in the principal plane.

The walk-off effect is a direct consequence of the medium anisotropy, and it exists only if the direction of propagation is not along the optical axis. (In Eq. (2-16), θ=0 implies ρ=0). The separation of the ordinary and extraordinary rays allows the evaluation of θ_c, when the crystal length is known.

If several beams interact in a crystal, even if the $\vec{k}$ -vectors are collinear, the walk-off angles might affect the spatial overlap of the interacting beams, and thus the efficiency of the nonlinear process. The overall effect depends on the crystal length. The value of the effective nonlinear constant is also affected, as will be shown later in this chapter.

2.3 The theory of nonlinear processes

The theory of nonlinear processes is presented in many textbooks [3-6] or articles [7]. The nonlinear processes take place when the response of the media to the strong electric field is not linear. The response of a medium to the action of an electrical field is characterized in terms of polarization of the medium. In the quadratic case, it is written as:

$$\vec{P}(\vec{r},t) = \vec{P}^{L}(\vec{r},t) + \vec{P}^{NL}(\vec{r},t) \tag{2-17}$$

$\vec{P}(\vec{r},t)$ is the total polarization of the medium, while, $\vec{P}^{L}(\vec{r},t)$ is the linear polarization and $\vec{P}^{NL}(\vec{r},t)$ is the second order nonlinear polarization.

$$\vec{P}^{L}(\vec{r},t) = \varepsilon_0 \hat{\chi}\vec{E}(\vec{r},t)$$

$$P_{NL}^{i}(\vec{r},t) = \varepsilon_0 \chi_{ijk}^{(2)} E_j(\vec{r},t) E_k(\vec{r},t) \tag{2-18}$$

with $\chi^{(2)}$ being the second order nonlinear susceptibility tensor.

The nonlinear processes are described by Maxwell's equations (2-1). By combining Maxwell Equations with the constitutive relations (2-2) with the polarization vector $\vec{P}(\vec{r},t)$ given by Eqs.(2-17) and (2-18), one obtains the wave equation:

$$\nabla^2(\vec{E}(\vec{r},t)) - \varepsilon_0\mu_0 \frac{\partial^2 \vec{E}(\vec{r},t)}{\partial t^2} - \mu_0\sigma \frac{\partial \vec{E}(\vec{r},t)}{\partial t} = \mu_0 \frac{\partial^2 \vec{P}(\vec{r},t)}{\partial t^2} \tag{2-19}$$

This equation is the basis of any calculation related to the nonlinear processes. Solving Eq.(2-19) with the initial and boundary conditions for the electric field $\vec{E}(\vec{r},t)$ in the general case, is in principle a very difficult task, but several

approximations can give a good understanding of the parameters that play an important role in the three-wave interactions, and lead to equations which can easily be solved.

The propagation of two light waves with optical frequencies $\omega_{1,2}$ in a medium with second order nonlinearity gives rise to other light waves. The frequency of the third wave is $\omega_1 \pm \omega_2$.

- sum-frequency mixing ($\omega_1+\omega_2 \rightarrow \omega_3$)
- difference frequency mixing ($\omega_1-\omega_2 \rightarrow \omega_3$)
- parametric luminescence ($\omega_1 \rightarrow \omega_2+\omega_3$)

The total electrical field is considered as a sum of three interacting waves at three different frequencies. It can be expressed as a superposition of the three interacting waves [3]:

$$\vec{E}(\vec{r},t) = \frac{1}{2}\sum_{n=1}^{3}\left(\vec{p}_n E_n(\vec{r},t)\exp\left(j(\omega_n t - \vec{k}_n \vec{r})\right) + C.C.\right) \qquad (2\text{-}20)$$

where E_n are the amplitudes and $\vec{p}_n$ the normalized vectors for polarization (not to be confused with the components of polarization vector $\vec{P}(\vec{r},t)$), ω_n are the optical frequencies $\vec{k}_n$ the propagation vectors and CC the complex conjugate. As mentioned before in this chapter, the propagation vector $\vec{k}_n$ can be expressed as:

$$\vec{k}_n = \frac{n(\omega_n)\cdot\omega_n}{c}\cdot\vec{s}_n, \qquad (2\text{-}21)$$

In Eq.(2-21) $\vec{s}_n$ is the unit propagation vector for the wave with the optical frequency ω_n and $n(\omega)$ is the refractive index for the same optical frequency, c is the speed of light in vacuum and ω the optical frequency. Using the slowly varying amplitudes approximation (SVEA) , when $\left|\frac{\partial^2 E_i}{\partial z^2}\right| << k\left|\frac{\partial E_i}{\partial z}\right|$, in Eq.(2-19), written for each component of the vector $\vec{E}$, the equations that describe the behaviour of the three interacting waves are [5]:

$$\begin{aligned}\hat{M}_1 E_1 &= j\kappa_1 E_3 E_2^* e^{j\Delta kz} \\ \hat{M}_2 E_2 &= j\kappa_2 E_3 E_1^* e^{j\Delta kz}\end{aligned} \qquad (2\text{-}22)$$

$$\hat{M}_3 E_3 = -j\kappa_3 E_1 E_2 e^{-j\Delta kz}$$

The operator M_i is given by:

$$\hat{M}_i = \frac{\partial}{\partial z} + \rho_i \frac{\partial}{\partial x} + \frac{j}{2k_i}\left(\frac{\partial}{\partial x^2} + \frac{\partial}{\partial y^2}\right) + u_i^{-1}\frac{\partial}{\partial t} + jg_i\frac{\partial}{\partial t^2} + \alpha_i + R_i(E) \qquad (2\text{-}23)$$

The walk-off of the extraordinary beam is in the XZ plane, and:

ρ_i = the walk-off angles

κ_i = the nonlinear coupling coefficients, $\kappa_{1,2,3} = \dfrac{\omega_{1,2,3} \cdot d_{eff} \cdot c}{n_{1,2,3}}$

u_i are the group velocities $u_i = c\left(\dfrac{\partial \omega}{\partial (n\omega)}\right)\Bigg|_{\omega_i}$

g_i are the dispersive coefficients $g_i = \dfrac{1}{2}\left(\dfrac{\partial^2 k}{\partial \omega^2}\right)\Bigg|_{\omega_i}$

α_i=linear absorption coefficients

R_i = nonlinear absorption terms,

and Δk the phase mismatch,

$$\Delta k = \left|\vec{k}_3 - \vec{k}_2 - \vec{k}_1\right| \qquad (2\text{-}24)$$

The terms appearing in the operator M_i give a general idea about the main physical parameters influencing the nonlinear interaction and thus the energetic transfer between the three waves. Some of these parameters are related to the crystal properties (length, aperture, transparency etc.) and others are related to the light wave properties (divergence, pulse duration, energy, beam size). Thus, one can notice that the second term of Eq. (2-23) is related to the walk-off effects, the third involves diffraction effects, the fourth expresses group velocity or bandwidth (pulse-duration) effects, the fifth –second order dispersion effects. All these effects are specific to certain interaction conditions and are discussed in section 2.4. Moreover, Eqs.(2-22) express the possibility of energy transfer between the interacting waves. Thus, the amplitude of the electric field at one of the optical frequencies ω_i can increase or decrease due to the nonlinear optical coupling through the nonlinear constant. Together with it is the nonlinear absorption term. The linear losses, expressed by the linear absorption coefficients α_i, are not related to the coupling with the other fields.

Analytically solving Eqs.(2-22) is still a very difficult or even impossible task, if all the effects are to be taken into account. In principle, the numerical codes are the only way to overcome the analytic difficulties [7, 8]. In this work, the SNLO code [9] was used for determining the main parameters of the nonlinear processes. There are three types of functions included in the SNLO menu. Firstly, the crystal properties such as phase-matching angles, effective nonlinear coefficients, group velocity, and birefringence can be calculated using the functions Ref. Ind., Qmix, Bmix, QPM, Opoangles, and GVM. The second set, functions PW-mix-LP, PW-mix-SP, PW-mix-BB, 2Dmix-LP, 2D-mix-SP, PW-OPO-LP, PW-OPO-SP, PW-OPO-BB, and 2D-OPO-LP, model the performance of nonlinear crystals in various applications, and the third set, Focus, Cavity, and Help, are helper functions for designing stable cavities, computing gaussian focus parameters, and displaying help text for each of the functions.

The first group of functions is very useful in selecting the proper crystal for a specific application. The functions in the second group can be used for specific parameters of interacting pulses. The functions with 'mix' in their title handle single-pass mixing, while the ones with OPO can model mixing in an optical cavity. The functions with the 'PW' prefix model plane-wave mixing, those with the '2D' prefix include Gaussian spatial profiles with diffraction and birefringent walk off. The plane-wave models run much faster than the '2D' models, so they can be used to arrive at an approximate set of conditions that can then be fine tuned with the diffractive models. The functions with suffix 'LP' ignore group velocity effects and are appropriate for monochromatic ns and longer pulses, or for monochromatic cw beams. Functions with suffix 'SP' incorporate group velocity effects and are useful for picosecond and femtosecond pulses. The suffix 'BB' indicates that the pulses are long but broadband so there is temporal structure on a time scale short enough to require inclusion of group velocity effects [9].

The functions PW-mix-SP and 2D-mix-SP have been extensively used in simulations performed in this Thesis. A custom version provided by the author of the code permitted fast calculations by varying one of the input parameters. The use of this code for the specific applications in this Thesis is described in more detail in Chapter 6.

2.4 Effective lengths

An easier and intuitive way to evaluate the influence of the above mentioned terms (diffraction, pulse duration, etc) in Eqs.(2-22) can be obtained by defining the effective lengths of the interaction process [10]. The effective interaction lengths are defined as hypothetical lengths of the nonlinear medium for which some specific effects, related to each interaction length and to corresponding terms in Eq. (2-23), cannot be neglected in solving Eq.(2-22).

These lengths are presented in Table 2-1.

Aperture length:	Diffraction length:	Quasi-static interaction length:	Dispersive spreading length	Nonlinear interaction length
$L_a=d_0/\rho$	$L_{dif}=\pi d_0^2/4\lambda$	$L_{qs}=\frac{\tau}{1/v_{g1}-1/v_{g2}}$	$L_{ds}=\tau^2/g$	$L_{NL}=\frac{1}{\sigma a}$

Table 2-1 The effective lengths

In the expression contained in Table 2-1, d_0 is the waist of the beam, ρ the walk-off angle, $a=\sqrt{|a_1|^2+|a_2|^2+|a_3|^2}$ and a_i the initial amplitudes of the beams.

Calculating these lengths for any specific applications and comparison with the crystal length indicates if a certain approximation can be applied and if a specific effect (term) can be neglected in the coupled wave equations.

The most common approximations are [6, 10]:

- The plane-wave approximation – diffraction effects are neglected
- The plane-wave fixed-field approximation $L<L_{NL}$ and all other are "infinite"
- The fixed-field approximation;
- The fixed-intensity approximation – only wave amplitudes are assumed constant;
- The quasistatic approximation $L<L_{qs}$ – the effect of group velocity mismatch is neglected.

In a first step, the plane-wave, fixed-field approximation is very useful. Based on it, some physical parameters can be defined, that allow a rapid comparison of the possible different nonlinear media for the desired application (with specific interacting wavelengths). This approximation is useful also for understanding the importance of the parameters contributing to the efficiency of the nonlinear process.

For parametric amplification, this approximation is used in Chapter 3, when the important parameters like parametric gain and field gain coefficient are introduced and discussed. Nevertheless, for obtaining a good agreement between theoretical description of the nonlinear process under consideration and experimental results, one has to take into account all factors involved in experimental situation. This can imply for example the finite pulse durations, group velocity effects, the pump depletion, the diffraction effects and finite beam diameters, spatial walk-off of the beams. But for a first and rapid evaluation of the feasibility of a nonlinear device, the fixed-field approximation is useful, even if not entirely correct.

2.5 The effective nonlinear constant

A fundamental feature of nonlinear crystals is their ability to give a nonlinear response to an external electric field. This response is characterized by the second order susceptibility ($\chi_{ijk}^{(2)}$), or by the second order nonlinear coefficient tensor ($d_{ijk}^{(2)}$).

$$P_i(\vec{r},t) = 2\sum_{j,k} \varepsilon_0 d_{ijk}^{(2)} E_j(\vec{r},t) E_k(\vec{r},t)$$

$$\chi_{ijk}^{(2)} = 2 d_{ijk}^{(2)} \tag{2-25}$$

Each nonlinear crystal is characterized by a nonlinear tensor. The nonlinearity is a tensor of second rank; however, due to Kleinman's symmetry [11] (which allows permutations of the three indices when the losses are neglected for the spectral range under consideration and polarization of the medium is purely electronic) and to specific symmetry in each crystal, the number of significant nonzero components is reduced, and the tensor is often represented by a matrix:

$$\begin{pmatrix} d_{11} & d_{12} & d_{13} & d_{14} & d_{15} & d_{16} \\ d_{21} & d_{22} & d_{23} & d_{24} & d_{25} & d_{26} \\ d_{31} & d_{32} & d_{33} & d_{34} & d_{35} & d_{36} \end{pmatrix} \tag{2-26}$$

where for the first index 1,2,3 mean X,Y,Z, while for the second one, 1=XX, 2=YY, 3=ZZ, 4=ZY=YZ, 5=XZ=ZX, 6=XY=YX.

Actually, this tensor accounts for all possible interactions between the three waves with given frequencies and arbitrary polarizations. From the experimental point of view, it is useful to define the effective nonlinear response of the crystal [11]:

$$d_{eff} = p_i d_{ijk}^{(2)} p_j p_k \tag{2-27}$$

with p_j being the unit vectors of the three waves polarizations and with summation convention over the i, j, k indices. Usually the values of $d_{ijk}^{(2)}$ are expressed in the dielectric frame. In this frame and for a uniaxial crystal, for ordinary and extraordinary rays, the components of the normalized polarization vector are, respectively:

$$\begin{pmatrix} -\sin\varphi \\ \cos\varphi \\ 0 \end{pmatrix} \qquad \begin{pmatrix} \cos\theta\cos\varphi \\ \cos\theta\sin\varphi \\ -\sin\theta \end{pmatrix} \tag{2-28}$$

(ordinary) (extraordinary)

where θ and φ are the polar angles in Figure 2-1.

For the ordinary polarization vector, the expression is easily obtained from the condition of normality on both the optical axis and on the propagation vector. This implies that the polarization is contained in the XY plane (0 component along OZ), and that the angle with the X axis is the complement of φ in Figure 2-4. As for the extraordinary polarization component, this is contained in the principal plane. When considering also the polarization vector normal to the propagation vector, in the principal plane, one obtains the expression for the extraordinary components in Eq.(2-28),

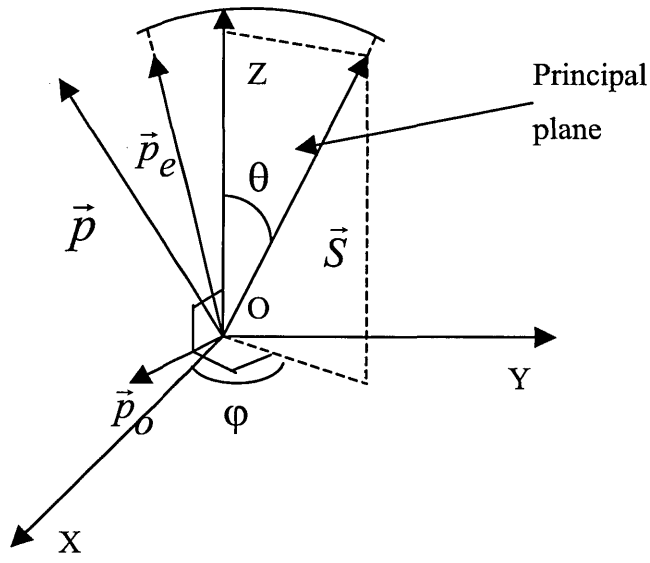

Figure 2-4 The vector diagram for $\vec{p}$, the unit polarization vector of the electric field. The $\vec{p}_e$ component is contained in the principal plane, formed by the optical axis OZ and the vector $\vec{s}$, and it is the extraordinary polarization. The ordinary component $\vec{p}_o$ is perpendicular to the principal plane, and contained in the XY plane. The angles θ and φ are defined in Figure 2-1.

In reality, it is not the electric vector that is perpendicular to $\vec{s}$, but the displacement vector $\vec{D}$. That is why, due to the influence of the walk-off angle, the expression of the angle θ must be corrected to $\theta - \rho$, where ρ is taken positive for positive uniaxial crystals and negative for the negative ones. In order to evaluate d_{eff}, one has to know, additionally to the nonlinear tensor the values of θ and φ, i.e.the orientation of the beams relatively to the optical axis. They can be adjusted to maximize d_{eff}. This is done usually by choosing optimum crystal cut angles and polarizations of the beams. The cut angles are adjusted for giving the highest d_{eff} for normal incidence.

For the crystal used in the experimental work of this thesis ($AgGaS_2$, which is a negative uniaxial crystal, with symmetry class 42m), the expression of the nonlinear constant is given by [11]:

$$d_{eff} = d_{36}\sin(\theta+\rho)\sin(2\varphi) \qquad (2\text{-}29)$$

which corresponds to two ordinary polarized vectors and one extraordinary polarized. The expression can be calculated using Eqs.(2-27 and (2-28) and using the symmetry properties of the class to which the crystal belongs. The wavelength dependence of d_{eff} is governed by Miller's rule [12], which basically shows a dependence of the nonlinear susceptibilities on the linear susceptibilities.

2.6 Phase matching condition

The concept of phase matching is introduced as a condition (or set of conditions) that must be fulfilled by the crystal and interacting waves in order to maximize the nonlinear interaction efficiency. For each second-order nonlinear process, there is a unique expression of the nonlinear efficiency, depending on the type of the process [15]. They are derived from the solution of the coupled wave equations in the plane-wave, fixed-field approximation. For all types of processes, a common feature is the efficiency dependence on the "phase mismatch" (expressed by Eq. (2-24). For all the processes, the conversion efficiency is maximized when the phase mismatch is zero, or in other words, when the phases are matched, or when the phase matching condition is fulfilled. For three interacting beams, the phase matching condition, or momentum conservation, is expressed as:

$$\vec{k}_1 + \vec{k}_2 = \vec{k}_3 \tag{2-30}$$

A supplementary condition used in calculation of phase-matched configurations is the energy conservation:

$$\omega_1 + \omega_2 = \omega_3 \tag{2-31}$$

Because the refractive indices depend on wavelength, temperature and, for anisotrpoic crystals, on the direction of propagation and polarization, their values for a set of wavelengths which propagate through the nonlinear medium can be adjusted for phase-matching by varying the temperature, by orientation of the beams relatively to the crystal, or by tuning the wavelength. This possibility of fulfilling phase matching depends on the dispersion properties of the crystal. One can derive the proper values of the refractive index using the temperature-dependence and Sellmeier equations [13]. For the nonlinear crystal used in experiments, these equations are given in Chapter 5, Eqs. (5-1)-(5-3).

2.6.1 Types of phase matching

Fulfilling the phase matching condition in a given material essentially means finding the appropriate directions of propagation and polarizations of interacting beams for maximizing the conversion efficiency. The types of phase matching are defined as very general situations of phase matching, which can occur in certain types of crystals with particular polarizations of interacting beams. These conditions define the possible configuration of interaction for positive and negative crystals.

There are two main types of phase matching [14]:

a) The two beams with lower frequencies have the same polarizations (Type I)

In negative crystals, the phase matching is possible if:

$$\vec{k}_{o1} + \vec{k}_{o2} = \vec{k}_{e3}(\theta) \qquad \text{(ooe)}$$

Indices 1 and 2 denote the beams with lower frequencies, while the index 3 denotes the beam with the highest frequency. This notation includes all three-waves nonlinear interaction processes. The angle θ has been defined in Figure 2-1. By definition, only the extraordinary beam experiences a dependence on it.

In positive crystals the phase matching condition is expressed as:

$$\vec{k}_{e1}(\theta) + \vec{k}_{e2}(\theta) = \vec{k}_{o3} \qquad \text{(eeo)}$$

b) The two beams with lower frequencies have different polarizations (Type II)

$$\vec{k}_{o1} + \vec{k}_{e2}(\theta) = \vec{k}_{e3}(\theta) \qquad \text{(oee)}$$

$$\vec{k}_{e1}(\theta) + \vec{k}_{o2} = \vec{k}_{e3}(\theta) \qquad \text{(eoe)}$$

$$\vec{k}_{o1} + \vec{k}_{e2}(\theta) = \vec{k}_{o3} \qquad \text{(oeo)}$$

$$\vec{k}_{e1}(\theta) + \vec{k}_{o2} = \vec{k}_{o3} \qquad \text{(eoo)}$$

2.7 The phase mismatch

The goal of phase-matched beams is difficult to achieve in practice. The factors contributing to the phase mismatch are the angular dispersion (diffraction of the beams), the finite bandwidth (the non-monochromaticity of the beams) and the temperature effects. A general expression unifying these contributions to the phase mismatch is given by [15]:

$$\Delta k(T, \delta\theta, \omega) \cong \Delta k(0) + \frac{\partial \Delta k}{\partial T}\Delta T + \frac{\partial \Delta k}{\partial(\delta\theta)}\Delta\theta + \frac{\partial \Delta k}{\partial \omega}\Delta\omega \qquad \text{(2-32)}$$

where T is the temperature. Eq.(2-32) expresses the first order terms in the development in series of the phase mismatch as a function of temperature, angle and optical frequency. As it will be shown later in this Thesis, this expression is very important in understanding the dependence of the parametric gain and of the energy gain on parameters like divergence of the interacting beams, temperature changes and bandwidth limitations.

2.8 Bibliography

1. M. Born, E. Wolf, *Principles of optics*, chapter XV, Cambridge University Press, ISBN 0 521 642221, 1999

2. V. G. Dimitriev, G.G. Gurzadyan, D.N. Nikogosyan, *Handbook of Nonlinear Optical Crystals*, Springer Series in Optical Sciences, 1999, Vol. 64, pp. 9-10

3. A. Yariv, *Introduction to Optical Electronics*, Holt, Rinhart, and Winston Series in Electrical Engineering, ISBN 0030898927, 1976, Ch. 8.6, pp.186

4. W. Koechner, *Solid –State Laser Engineering*, Springer, 1999,Vol.1, ch.10

5. V. G. Dimitriev, G.G. Gurzadyan, D.N. Nikogosyan, *Handbook of Nonlinear Optical Crystals*, Springer Series in Optical Sciences, 1999, Vol. 64, pp. 33-34

6. V. G. Dimitriev, G.G. Gurzadyan, D.N. Nikogosyan, *Handbook of Nonlinear Optical Crystals*, Springer Series in Optical Sciences, 1999, Vol. 64, pp. 48-65

7. J.A. Armstrong, N. Bloembergen, J. Ducuing, P.S. Pershan, "*Interaction between light waves in a nonlinear dielectric*", Phys. Rev., Vol.127, pp.1928-1939, 1962

8. J.-J. Zondy, "*The effects of focusing in type-I and type-II difference-frequency generations*" Opt. Commun. Vol. 149, pp.181–206, 1998

9. SNLO nonlinear optics code available from A.V. Smith, Sandia National Laboratories, Albuquerque, NM 87185-1423, USA

10. V. G. Dimitriev, G.G. Gurzadyan, D.N. Nikogosyan, *Handbook of Nonlinear Optical Crystals*, Springer Series in Optical Sciences, 1999, Vol. 64, pp. 36-39

11. V. G. Dimitriev, G.G. Gurzadyan, D.N. Nikogosyan, *Handbook of Nonlinear Optical Crystals*, Springer Series in Optical Sciences, 1999, Vol. 64, pp. 24-25

12. A. Yariv, *Quantum Electronics* (Wiley, New York,), pp. 378–406, 1988

13. J.-J. Zondy and D. Touahri, "*Updated thermo-optic coefficients of $AgGaS_2$ from temperature-tuned noncritical 3ω-$\omega \rightarrow 2\omega$ infrared parametric amplification*", JOSA B, Vol. 14, pp. 1331-1338, 1997

14. V. G. Dimitriev, G.G. Gurzadyan, D.N. Nikogosyan, *Handbook of Nonlinear Optical Crystals*, Springer Series in Optical Sciences, 1999, Vol. 64, pp. 10-11

15. V. G. Dimitriev, G.G. Gurzadyan, D.N. Nikogosyan, *Handbook of Nonlinear Optical Crystals*, Springer Series in Optical Sciences, 1999, Vol. 64, pp. 40

Chapter 3 Optical parametric amplification

While Chapter 2 described in a general manner the second order nonlinear processes, this chapter emphasizes on the Optical Parametric Amplification (OPA) process. The most important parameters characterizing OPA are introduced and described in an intuitive way, based on simplifying assumptions (plane-wave fixed field approximation). The parametric gain and the influence of the phase matching condition are discussed in relation to the particular crystal used for experiments. Moreover, factors limiting the approximations used for the intuitive description of the features of OPA are explained, emphasizing the importance of different parameters.

3.1 Introduction

The three-wave nonlinear processes include:

- sum-frequency mixing ($\omega_1+\omega_2\rightarrow\omega_3$)
- difference frequency mixing ($\omega_1-\omega_2\rightarrow\omega_3$)
- parametric luminescence ($\omega_1\rightarrow\omega_2+\omega_3$)

In the case of the difference frequency processes, the pump and the signal interact in the crystal and a third beam (called the idler) is generated due to the nonlinear process. The pump is a strong beam at the "bluest" wavelength, while the "signal" can be associated with the wavelength of interest. Other conventions relate the "idler" to the reddest beam, and the "signal" to the intermediate wavelength between the pump and the idler. We adopt the convention of "signal" designating the wavelength of interest (to be amplified), the "pump" has the bluest wavelength and the "idler" is the beam generated in the nonlinear process.

Within the class of difference frequency mixing processes one may distinguish two particular cases. The difference frequency generation (DFG) and OPA are characterized by different amplification regimes [1]. For DFG, the signal and pump pulses have comparable intensities while for OPA, the main goal is the amplification of an initially weak signal, compared to the pump. Due to the energy flow from the pump to the signal, the signal intensity can be amplified at very high rates in the OPA case, while in the DFG case the amplified signal intensity is comparable to the input signal intensity.

Figure 3-1 illustrates a schematic view of the nonlinear, non-collinear difference frequency mixing process.

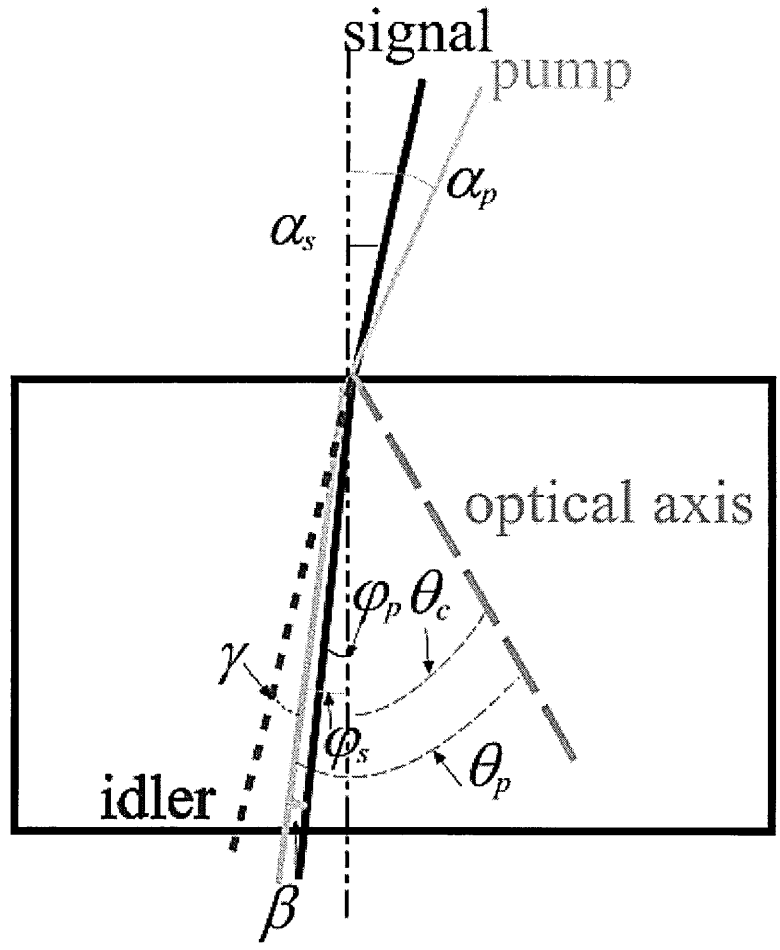

Figure 3-1Difference frequency mixing scheme: The pump and the signal beams interact in a (uniaxial) nonlinear crystal, generating the idler beam. α_p and α_s are the incidence angles for the pump and signal beams respectively, φ_p, φ_s are the refraction angles and θ_c is the crystal cut angle, and θ_p is the pump phase matching angle, β and γ are the degrees of noncollinearity for the signal and idler beams

The theory of light propagation and frequency conversion for nonlinear processes presented in Chapter 2 also applies to difference mixing processes. The specific parts for DFG and OPA are the initial conditions, related to pump and signal input intensity and wavelength. As mentioned in Chapter 2, energy transfer is possible (and desired) from the pump to the signal beam (to be amplified) and to the generated idler. The energy transfer is also possible in the opposite direction, i.e. from the idler and signal to the pump, but this process takes place in the conditions of strong saturation (the saturation effect will be discussed in section 3.3), under strong pump beam depletion. An important issue from the point of view of applications, in our specific case from the point of view of amplifying the signal

power, is the efficiency of the parametric process, the experimental conditions, which optimise it, and the possible limitations of the efficient transfer of energy from the pump to the signal beam.

3.2 The parametric gain in OPA

Evaluation of the efficiency of the parametric process under consideration is crucial for designing any parametric device. Depending on the aim of the difference-frequency mixing process, the efficiency might be characterized by the conversion efficiency – in the DFG case- or by the single-pass parametric gain in the OPA case.

The conversion efficiency is a measure of the generated power at the desired wavelength relatively to the input pump power. The parametric gain characterizes the amplified signal, and is defined as the ratio between the intensity of the amplified signal to the input signal intensity. The optimisation of the conversion efficiency or parametric gain is always desirable because the damage threshold of the crystal can limit the pump power.

A rough estimation of the efficiency of a second-order nonlinear process is based on the plane-wave, un-depleted pump approximation. In this approximation, the variation of the pump intensity during the mixing process is neglected and so are the diffraction and temporal walk-off effects. Even if sometimes far from the experimental situation, this approximation can give a good understanding of the physics of the nonlinear interaction, and all the parameters of practical importance can be calculated rather easily with some algebraic manipulation from the coupled-wave equations, phase matching conditions and dispersion relations.

In the undepleted plane wave approximation, the coupled wave equations (2-22) are written as:

$$\frac{\partial E_i(z)}{\partial z} = j\kappa_i E_p(z) E_s^*(z) e^{j\Delta kz}$$

$$\frac{\partial E_s(z)}{\partial z} = j\kappa_s E_p(z) E_i^*(z) e^{j\Delta kz}$$

$$\frac{\partial E_p(z)}{\partial z} = -j\kappa_p E_i(z) E_s(z) e^{-j\Delta kz} \qquad (3\text{-}1)$$

with $\kappa_{s,i,p} = \frac{\omega_{s,i,p} \cdot d_{eff} \cdot c}{n_{s,i,p}}$, *s, i, p* denoting the signal, pump and idler beams and Δk is defined as the phase mismatch (see also Eq. 2-32).

In the DFG case, $I_p(0) \cong I_s(0)$ and the solution for the conversion efficiency is given by [2]:

$$\frac{I_i}{I_s(0)} = \frac{8\pi d_{eff}^2 l^2 I_p(0)}{\varepsilon_0 c n_i n_s n_p} \sin c^2\left(\frac{\Delta k l}{2}\right) \tag{3-2}$$

with $I_{i,s,p} = \epsilon_0 n_{i,s,p} c |E_{i,s,p}(z)|^2 / 2$, n_p, n_i, n_s the refractive indices, c the speed of light, l the crystal length, ω_s, ω_i the angular frequency for the signal and idler pulses and Δk the phase mismatch.

Solving the coupled wave equations with initial condition of only two incident beams, but considering a weak input signal, yields the single pass gain G of an optical parametric amplifier [3]:

$$G = \frac{I_s}{I_s(0)} = 1 + \sinh^2(\Gamma_{eff} l)\left(1 + \left(\frac{\Delta k}{2\Gamma_{eff}}\right)^2\right) \tag{3-3}$$

with the effective gain coefficient Γ_{eff} given by:

$$\Gamma_{eff} = \sqrt{\Gamma^2 - \left(\frac{\Delta k}{2}\right)^2} \tag{3-4}$$

and the gain coefficient Γ expressed as:

$$\Gamma^2 = \frac{2deff^2}{n_p n_s n_i} \cdot \frac{\omega_s \omega_i I_p}{\varepsilon_0 c^3} \tag{3-5}$$

Eq. (3-3) shows the behaviour of the single pass gain as a function of pump and crystal parameters in the approximation considered. Eq.(3-5) expresses the gain coefficient in the case of collinear interaction and in the absence of the phase mismatch and linear absorption. For non-collinear interaction, one has to take into account the angles between the three waves and the phase matching angle of the pump, which slightly influences on the value of the nonlinear constant d_{eff} and refractive indices. Nevertheless, a more important effect, in the case of small beam diameters and large noncollinear angles can arise from the bad spatial overlap of the three beams. In this case the gain coefficient is expressed by [4, 5]:

$$\Gamma^2 = \frac{2 g_s d_{eff}^2(\theta) \omega_s \omega_i I_p}{\varepsilon_0 n_s n_i n_e(\theta) c^3 \cos\beta \cos\gamma} \tag{3-6}$$

with g_s being the overlap factor, and the angles γ and β the degree of noncollinearity as shown in Figure 3-1.

An alternative parameter for characterizing the gain is the field gain coefficient [6]. This coefficient is independent of the pump intensity and is defined as:

$$g = \frac{\Gamma}{\sqrt{I_p}} = \sqrt{\frac{2g_s d_{eff}^2(\theta)\omega_s\omega_i}{\varepsilon_0 n_s n_i n_e(\theta) c^3 \cos\beta\cos\gamma}} \tag{3-7}$$

This parameter is useful because Eqs.(3-6) and (3-4) reveal several important conclusions related to the experimental conditions under which the gain coefficient can be optimised. Firstly, the crystal must be phase matchable with the pump and signal, transparent at the corresponding interacting wavelengths and with a high damage threshold. In Eqs. (3-3)- (3-6), the absorption losses are neglected. High absorption losses can not only decrease the efficiency, but also lead to crystal heating and damage, or to phase mismatch due to thermal effects.

A high value of the effective nonlinear constant for efficient amplification is also required. Nevertheless, the availability of large crystals and with high damage thresholds can balance the inconvenience of a moderate nonlinear constant. The gain coefficient increases with the frequencies involved in the frequency conversion process, and with the pump intensity. But the dependence on wavelength is correlated with the dispersion of the material, through the values of refractive indices and, via Miller's rule, in the value of nonlinear constant. It depends also on the geometry of interaction (the superposition of the interacting beams and corresponding phase matching angles). These considerations help with the choice of a proper pump wavelength, for a certain range of signal wavelengths considered for amplification. Additionally, two-photon absorption wavelengths have to be avoided, in order to preserve high efficiency and eliminate possible damages of the crystal.

Both Eqs.(3-2) and (3-3) contain the phase mismatch term. In the case of single-pass amplification, the gain can decrease dramatically because of phase mismatch. The phase mismatch is determined by the laser sources properties (beam divergence, spectral bandwidth) and by the dispersive, absorptive and thermal properties of the crystal. Phase mismatch will be discussed in more detail in paragraph 3.4. Phase matching can be achieved by temperature tuning, birefringent (angular) tuning, or by wavelength tuning in devices with possibility of tuning the

wavelength of one of the incoming beams. These methods are based on the dependence of the refractive index on temperature, polarizations and angles with the optical axis, and on the wavelengths of interacting beams. Thus, adjusting one of the three parameters till the phase matching is achieved can be chosen depending on the properties of the crystal and of the laser sources.

The simple picture given by Eqs. (3-6) and (3-4) is restricted to the plane-wave, fixed-field approximation, without absorption losses in the crystal. Diffraction and beam divergence are important in the case of focused beams, with a short Rayleigh range compared to the crystal length. For picosecond and femtosecond pulses, additional effects should be taken into account when describing the parametric gain, and they are related to the temporal overlap of the interacting pulses, the group velocity mismatch and to group velocity dispersion, which, due to the larger spectrum of ultrashort pulses, becomes important for femtosecond pulses.

Nevertheless, Eqs. (3-6) and (3-4) are a good starting point in designing a nonlinear device for parametric amplification, because they allow an estimation of the gain that can be obtained using specific crystals and pump and signal beams with known parameters.

3.3 The saturation effect

In practice, when the pump intensity starts to decrease significantly due to the increase in the signal and idler intensity, the un-depleted pump approximation is not valid. In terms of interaction lengths, defined in Chapter 2, Table 2-1, the effect is noticeable at a crystal length comparable to the non-linear length (L_{NL}), or longer. In the non-saturated case, the gain does not depend on the signal intensity, as shown in Eqs. (3-3)- (3-4), and increases almost exponentially in the high gain limit and linearly in the low gain limit with the pump intensity and crystal length. This effect is described in detail in Chapter 6, section 6.3.1. There saturation is discussed as a function of several parameters, using the SNLO code. The saturation effect indicates a dependence of the gain on the signal intensity. When pump depletion starts to influence the energy transfer between the three beams significantly, the parametric gain decreases with the signal intensity, and the amplified pulse energy cannot scale any more with the input signal intensity. When the saturation becomes very strong, the photons of idler and signal beams start to recombine back to pump photons. In

principle, it is easier to reach saturation with a long crystal and high initial signal intensity and high gain.

As mentioned in the previous section (Eqs. (3-5)-(3-6)), the single pass gain increases with the wavelengths of interacting pulses, with the pump intensity and with the nonlinear constant. The saturation manifests itself by limitations in the amplified energy and by spectral/temporal modifications of the amplified signal in comparison with the input pulse. The spectral/temporal changes induced by saturation will be discussed in more detail in Chapter 6.

When spatial effects are taken into account, a description of the overall energy gain becomes very complicated. Several authors have determined an optimised configuration of the pump and signal intensity profiles in which the total energy extracted in the amplified pulse is maximised [7-10]

In order to improve the extracted energy in the amplified pulse, the pump has to have a top-hat profile both in space and in time with respect to the signal. In fact, this is not the ideal case for the overall efficiency of the process (a lot of pump energy is actually lost in the wings).

3.4 Angular acceptance, angular tolerance of the crystal, bandwidth acceptance

As shown in Eq. (3-4) the single pass gain can decrease dramatically due to the phase mismatch. Using Eq. (3-2) for the DFG case, one obtains that the efficiency drops to one half of the phase matching value if:

$$\Delta k = 0.886\frac{\pi}{l} \tag{3-8}$$

The three main factors contributing to the phase mismatch are the angular dispersion, the temperature and the finite bandwidth of the interacting wavelengths. The term of angular acceptance is used relatively to the divergence of the pump beam, while the angular tolerance indicates the tilt away of the crystal from the phase-matching position to fulfil the condition expressed by Eq. (3-8).

Usually, in literature, the angular acceptance, bandwidth acceptance and temperature bandwidth (or angular, spectral and temperature bandwidth) are defined and calculated within the fixed-field approximation [11], because in this

approximation calculations are rather easy. Commonly, they are defined as the value of the phase mismatch that halves the parametric gain. Nevertheless, the picture of the process is very simplified, because in the case of high gain the behaviour of the parametric gain with respect to the input beam properties can be very different from the fixed-field approximation. The phase mismatch depends also on the type of interaction (ooe, eeo, eoe, oeo, eoo, oee). The angular bandwidth is actually an internal angular bandwidth, measured in terms of the angular dispersion of the phase matching angle, while the angular tolerance of the crystal is determined in terms of external angles. The angular properties are very important when focused beams are used; as expressed by Eq. (3-5) the gain coefficient is a function of intensity and sometimes the beams are focused to increase the gain factor. In this case it is important to know the angular acceptance in order to optimise the focused beam diameter for the highest gain.

The bandwidth acceptance is an important issue for short and ultrashort pulses, because it is related to the temporal walk-off of the interacting beams.

The gain bandwidth in the OPA case is defined by the group velocity mismatch between the signal and idler pulses. This is because the pump wavelength is fixed and only the wavelengths of the signal and idler pulses vary. Taking into account the energy conservation law:

$$\omega_i = \omega_p - \omega_s \tag{3-9}$$

it results $\Delta\omega_s = -\Delta\omega_i$ and:

$$\Delta k = \left(\frac{\partial k_i}{\partial \omega_i} - \frac{\partial k_s}{\partial \omega_s}\right)\Delta\omega_s = \left(\frac{1}{v_i} - \frac{1}{v_s}\right)\Delta\omega_s = v\Delta\omega_s \tag{3-10}$$

where v_s and v_p are the group velocity indices for the signal and idler beams and $v = \left(\frac{1}{v_i} - \frac{1}{v_s}\right)$. $\Delta\omega_s$ is the signal spectral bandwidth for which the gain - given by Eq. (3-1) drops at half of the maximum value (obtained in the phase matching case). In the high gain approximation, Eq.(3-3) leads to an exponential dependence on crystal length of the single pass gain:

$$G \cong 0.25\exp(2\Gamma_{eff} l) \tag{3-11}$$

Using Eqs. (3-4) and(3-10), it results for the gain bandwidth [2,12]:

$$\Delta\omega = \frac{\sqrt{4\ln(2)}}{|v|}\sqrt{\frac{\Gamma^2}{l}} \qquad (3\text{-}12)$$

In terms of effective lengths, defined in Chapter 2, Table 2-1, the bandwidth acceptance is related to the quasistatic length of the crystal. Eq. (3-12) shows the impact of the crystal length on the bandwidth acceptance. When a pulse with an initial large bandwidth has to be amplified, a high gain coefficient is essential for preserving the bandwidth, while the crystal length acts as a limiting factor. These considerations are valid for the un-depleted pump approximation.

The angular acceptance, bandwidth acceptance and bandwidth gain can be increased by noncollinear interaction. The angular acceptance can be increased by matching the phase velocities, while the gain bandwidth by operation close to degeneracy, group velocity matching [13,14], by using tilted-front pulses [15, 16], multiple beam pumping [12,17], and simultaneously chirping of both pump and signal pulses.

3.5 Spectral and temporal behaviour of the amplified pulse

The spectral and temporal characteristics of the amplified pulse are crucial features to be considered when designing a parametric device, because of their influence on the output power. The amplified pulse duration can be changed by spectral losses at optical components, (as for example vignetting in the stretcher compressor system), high-order dispersion effects, bandwidth acceptance of the crystal, bad spatial and temporal overlap of the interacting beams and saturation effects. The temporal pulse shape is related to the spectral bandwidth of the amplified pulse, which is influenced by the gain bandwidth. Preserving a short pulse duration can affect the overall energy efficiency of the process, because the bandwidth of the amplified pulse is limited by the crystal length, as shown by Eq. (3-12). In the approximation of undepleted pump, the parametric gain increases with the crystal length and pump power, but the pump power does not influence the bandwidth of the amplified pulse. A correct balance of the effects leading to the highest output power is given by minimizing the crystal length and maximizing the pump power untill the limit of the safe operation, given by the damage threshold of the crystal.

In terms of effective lengths, defined in Chapter 2, Table 2-1, it is the quasi-static interaction length, which describes the bandwidth of the crystal. The temporal walk-away of the interacting pulses -which takes place because the dispersion properties of the crystal- affects the gain bandwidth. This effect is important for picosecond pulses and shorter. The higher order dispersion terms are important for femtosecond pulses, because of their larger spectral widths.

If the crystal length is longer than L_{qs}, the group velocity mismatch cannot be neglected in calculations, and usually a spectral narrowing of the pulse is the effect of the temporal walk-off of interacting pulses.

There are several ways for circumventing group velocity walk-off, which in the ultrashort pulses generation: group velocity matching, by non-collinear interaction, pulse front tilting, pumping with several beams, or operating near degeneracy.

The beam diameters, input powers, divergence, spatial walk-off must be taken into account in order to get a realistic description of the spectral changes induced by parametric amplification. The saturation can also influence the temporal and spectral features of the amplified pulse.

A basic description starts with the plane-wave, fixed field approximation. When this approximation is not valid, numerical simulations are the only way to predict the temporal and spectral behaviour of amplified pulses. In a simple representation, an initially Gaussian spectrum signal interacting with a pump pulse with narrower spectral bandwidth, will suffer spectral modifications, because the spectrum is not uniformly amplified and the gain is nonlinear. The situation is different in the saturated regime, when the central part saturates. Thus, saturation effect can help in obtaining a better spectral shape. Nevertheless, as it will be shown, the regime of deep saturation can induce severe deformation of the amplified spectral shape. A more detailed discussion of the spectral and temporal influence of various parameters is presented in Chapter 6.

3.6 Phase matching angles. Example of calculation for the AGS crystal

The phase matching angles are defined as the angles formed by the propagation vectors ($\vec{k}$) with the optical axis of the crystal, for the phase matching case (see also Chapter 2, section 2.6). In Figure 3-2, they are denoted with θ_p and θ_s

for the pump and signal beams, while β and γ are the degree of non-collinearity for the signal and idler beams with respect to the pump.

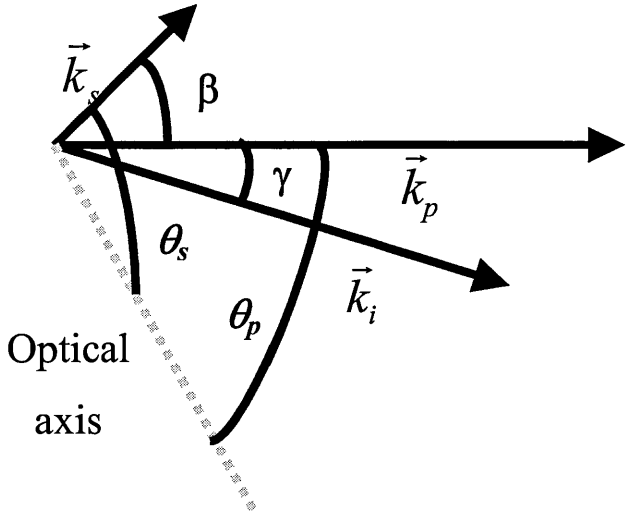

Figure 3-2 The $\vec{k}$ -vectors of the pump ($\vec{k}_p$), signal ($\vec{k}_s$) and idler ($\vec{k}_i$) beams. The angle $\theta_{p,s}$ are the phase matching angles of the pump and signal respectively, while β and γ are the degree of non-collinearity for the signal and idler beams with respect to the pump.

From a practical point of view, it is convenient to express the phase matching angles as functions of the external (incidence) angles. This is of particular interest for the experimental configuration in the case of OPA, when two beams are incident on the crystal, and the phase matching condition is dictated by both the cut-angle of the crystal and the relative positions of the two beams with respect to the crystal face. The knowledge of these angles is important for characterising the tuning properties of the device, the angular acceptance, the walk-off angles, and efficiency of the frequency-mixing process. Due to the crystal anisotropy, the propagation through the crystal (direction, phase and group velocities) and the phase matching angles are sensitive to the orientation of the incidence beams with respect to the optical axis. When the interacting pulses are ultrashort, and broadband acceptance is desired for maintaining a high power of the amplified pulse, the knowledge of the angular properties of the crystal with respect to the incoming beams is crucial. The group velocity components can be matched to adjust the bandwidth acceptance by a proper orientation of the beams with respect to the crystal face and axis.

In the collinear case, the three $\vec{k}$ -vectors have the same direction, and the equation for momentum conservation becomes scalar. In the case when the $\vec{k}$ -vectors are not collinear, the equation for momentum conservation is Victoria.

In this case, the phase matching angles are derived from the phase matching condition by decomposing the $\vec{k}$ -vectors along $\vec{k}_p$, assuming that the generated idler beam adjusts the direction for the minimum phase mismatch ($\Delta\vec{k}_\perp$)=0.

It results:

$$\Delta k_{II} = k_p - k_s \cos(\beta) - k_i \cos(\gamma) \tag{3-13}$$

and $k_s \sin(\beta) = k_i \sin(\gamma)$, with:

$$k_{p,s,i} = \frac{n_{p,s,i}(\omega_{p,s,i}) \cdot \omega_{p,s,i}}{c} \tag{3-14}$$

From the cosine theorem a value for cos(β) can be derived:

$$\cos(\beta) = \frac{k_p^2 + k_s^2 - k_i^2}{2k_p k_s} \tag{3-15}$$

The solution of Eq.(3-15) for β and γ exists if the absolute value of the right part of the equation containing the cosine function is less or equal to 1. This condition relates the crystal characteristics to the three interacting waves; if the solution exists, then the crystal is "phase matchable" with the interacting beams.

As shown in Figure 3-2, the degree of non-collinearity can be expressed also as:

$$\beta = \theta_p - \theta_s \tag{3-16}$$

An angle $\Delta\alpha$, an analogue of the degree of non-collinearity, but in the air, is defined as:

$$\Delta\alpha = \alpha_p - \alpha_s \tag{3-17}$$

with $\alpha_{s,p}$ being the incidence angles for the pump and signal beams as shown in Figure 3-1. The sign convention for the incidence angles $\alpha_{p,s}$ is that they are positive when on the same side of the normal to the surface with the optical axis.

The incidence angles are related to the refraction ones via Snell's law:

$$\sin\alpha_p = n_p \sin\varphi_p$$

$$\sin\alpha_s = n_s \sin\varphi_s, \tag{3-18}$$

with $\varphi_{p,s}$ being the refraction angles.

The values of the refractive indices $n_{s,p}$ depend on the polarization of the beams, as explained in Chapter 2, paragraph 2.1 and Eq. (2.12). In the case of extraordinary beams, the refractive indices depend on θ, which was calculated to be

a function of incidence angle (α) and crystal cut angle θ_c, and is derived in Chapter 2, Eq. 2.14 as:

$$\tan(\theta) = \frac{\sin(\theta_c)\cos(\theta_c) + \sin(\alpha)\sqrt{\frac{\cos^2(\theta_c)}{n_o^2} + \frac{\sin^2(\theta_c)}{n_e^2} - \frac{\sin^2(\alpha)}{n_o^2 n_e^2}}}{\cos^2(\theta_c) - \frac{\sin^2(\alpha)}{n_e^2}} \qquad (3\text{-}19)$$

For an $AgGaS_2$, the crystal used in parametric amplification experiments, there are two possible types of interaction for the signal wavelength in the range of 4-12 μm, and 1.064 μm for the pump wavelength:

- Type I ooe (signal and idler beams are ordinary and pump beam is extraordinary)
- Type II eoe (signal and pump are extraordinary beams, while the generated idler beam is ordinary).

Eq. (3-19) is useful in type I ooe interaction only for the pump beam (because it is the extraordinary one) and for signal and pump beams in type II eoe, (when both pump and signal are extraordinary). The existence of the solution for the angle θ is conditioned by the existence of the square root in Eq. (3-19). This depends on the dispersive properties of the nonlinear material under consideration.

In order to study the possibility of realising a tuneable source using parametric amplification with $AgGaS_2$ crystal, Eqs (3-14)-(3-15) can be written for the both cases (types I and II).

The relation between the incidence and phase matching angles for fixed input beams configuration is found by combining them with Snell's law and with Eq. (3-16).

For the type II eoe interaction the relation between the incidence angles and the phase matching angles becomes:

$$\sqrt{1-\frac{\sin^2\alpha_s}{n_s^2(\theta_s)}}\sqrt{1-\frac{\sin^2\alpha_p}{n_p^2(\theta_p)}} + \frac{\sin\alpha_p}{n_p(\theta_p)}\frac{\sin\alpha_s}{n_s(\theta_s)} = \frac{n_p^2(\theta_p)\omega_p^2 + n_s^2(\theta_s)\omega_s^2 - n_i^2\omega_i^2}{2n_p(\theta_p)n_s(\theta_s)\omega_p\omega_s} \qquad (3\text{-}20)$$

While for the type I ooe the same equation holds, with the difference that $n_s(\theta_s)$ is replaced by n_{os}, the ordinary index for the signal beam, which does not depend on the propagation angle θ_s.

$$\sqrt{1-\frac{\sin^2\alpha_s}{n_{os}^{\ 2}}}\sqrt{1-\frac{\sin^2\alpha_p}{n_p^2(\theta_p)}}+\frac{\sin\alpha_p}{n_p(\theta_p)}\frac{\sin\alpha_s}{n_{os}}=\frac{n_p^2(\theta_p)\omega_p^{\ 2}+n_{os}^{\ 2}\omega_s^2-n_i^2\omega_i^2}{2n_p(\theta_p)n_{os}^{\ 2}\omega_p\omega_s} \quad (3\text{-}21)$$

By solving Eqs. (3-20) and (3-21), the values of the external angles for phase-matched interaction can be determined, for the two types of interaction. If the angle between the two external beams is fixed to a certain value $\Delta\alpha$, then all the possible values of $\alpha_{s,p}$ for which the interaction is phase-matched in the crystal as a function of wavelength can be expressed as a function of $\Delta\alpha$, refractive indices and θ_c, with the refractive indices given by the dispersion relations, which are specific for each crystal. For the AGS crystal, they are given by Bhar and Smith [18], with coefficients updated by Zondy et al. [19].

The Eqs. (3-20)-(3-21) are used in Chapter 5 for calculating the phase matching angles for the AGS crystal used in experiments.

3.7 Conclusion

OPA is a suitable process for amplification of ultra-short pulses if proper pump and signal sources and nonlinear crystal are used. OPA can achieve high, broad-bandwidth gain and tuneability. Rotating the crystal along an axis perpendicular to its principal plane adjusts the phase-matching condition at any wavelength in the transparency range. For a crystal with high transparency at the pump, signal and idler wavelengths, the process is free of thermal effects, because the difference between the pump and signal energy is transferred entirely to the idler pulse. The limiting factors for OPA gain performance are the pump and signal stability [20], the crystal damage threshold, its size, the temporal and spatial overlap between interacting beams and the saturation effect.

3.8 Bibliography:

1. V. Petrov, F. Rotermund and F Noak, "*Generation of high-power femtosecond light pulses at 1 kHz in the mid-infrared spectral range between 3 and 12 μm by second order nonlinear processes in optical crystals*" J. Opt. A: Pure and Appl.Opt. Vol. 3, pp. R1-R19, 2001

2. V Petrov, F. Rotermund and F. Noack "*Femtosecond traveling-wave optical parametric amplification in $MgO:LiNbO_3$*", Appl. Opt., Vol. 37, pp. 8504-8511, 1998

3. D. J. Armstrong, W. J. Alford, and T. D. Raymond, and A. V. Smith, "*Absolute measurement of the effective nonlinearities of KTP and BBO crystals by optical parametric amplification*", Appl. Opt.,Vol. 35, pp. 2040- 1996

4. M. J. McCarthy and D. C. Hanna, "*All-solid-state synchronously pumped optical parametric oscillator*", J. Opt. Soc. Am. B, Vol. 10, pp. 2180-2190, 1993

5. L. A. W. Gloster, Z. X. Jiang, and T. A. King, "*Characterization of an Nd:YAG-pumped ß-BaB_2O_4 optical parametric oscillator in collinear and noncollinear phase-matched configurations*", IEEE J. Quantum Electron., vol. 30, pp. 2961-2969, 1994

6. SNLO nonlinear optics code available from A.V. Smith, Sandia National Laboratories, Albuquerque, NM 87185-1423, USA

7. I. N. Ross, P. Matousek, M. Towrie, A. J. Langley, and J. L. Collier, "The prospects for ultrashort pulse duration and ultrahigh intensity using optical parametric chirped pulse amplifiers," Opt. Commun. Vol. 144, pp. 125–133, 1997

8. I. N. Ross, J. L. Collier, P. Matousek, C. N. Danson, D. Neely, R. M. Allott, D. A. Pepler, C. Hernandez-Gomez, and K. Osvay, "Generation of terawatt pulses by use of optical parametric chirped pulse amplification," Appl. Opt. **39**, 2422–2427 (2000)

9. I. A. Begishev, A. A. Gulamov, E. A. Erofeev, E. A. Ibragimov, S. R. Kamalov, T. Usmanov, and A. D. Khadzhaev, "*Highly efficient parametric amplification of optical beams. I. Optimization of the profiles of interacting waves in parametric amplification*," Sov. J.Quantum Electron. Vol. 20, pp. 1100–1103, 1990.

10. I. A. Begishev, A. A. Gulamov, E. A. Erofeev, E. A. Ibragimov, S. R. Kamalov, T. Usmanov, and A. D. Khadzhaev, "*Highly efficient parametric amplification of optical beams. II. Parametric interaction of waves with conformal profiles*," Sov. J. Quantum Electron. Vol. 20, pp. 1104–1106, 1990

11. V. G. Dimitriev, G.G. Gurzadyan, and D.N. Nikogosyan, *Handbook of Nonlinear Optical Crystals*, Springer Series in Optical Sciences, Vol. 64, 1999.

12. E. Zeromskis, A. Dubietis, and G. Tamosauskas, and A. Piskarskas, "*Gain bandwidth broadening of the continuum-seeded optical parametric amplifier by use of two pump beams*", Opt. Commun. Vol. 203, pp. 435–440, 2002

13. F. Rotermund, V. Petrov, and F. Noack, "*Femtosecond noncollinear parametric amplification in the mid-infrared*", Opt. Commun. Vol. 169, pp. 183-188, 1999

14. P. Di Trapani, A. Andreoni, C. Solgia, P. Foggi, R. Danielius, A. Dubietis, and A. Piskarkas, "*Matching of group velocities in three wave parametric interaction with femtosecond pulses and application to travelling-wave generators*", J. Opt. Soc. Am. B, Vol. 12, pp. 2237-2244, 1995

15. A. Dubietis, G. Valiulis, G. Tamosauskas, R. Danielius, and A. Piskarskas, "*Nonlinear pulse compression in the ultraviolet*", Opt. Commun, Vol. 144 pp. 55-59, 1997

16. A. Shirakawa, I. Sakane, and T. Kobayashi, "*Pulse-front-matched optical parametric amplification for sub-10-fs pulse generation tuneable in the visible and near infrared*", Opt. Lett. Vol. 23, No. 16, pp1292-1294, 1998

17. A. Dubietis,R. Danielius,G. Tamosauskas, and A. Piskarskas, "*Combining effect in a multiple-beam-pumped optical parametric amplifier*", J. Opt. Soc. Am. B, Vol. 15, pp. 1135-1139, 1998

18. G. C. Bhar and R. C. Smith, "*Optical properties of II-IV-V2 and I-II-VI2 crystals with particular reference to transmission limits*," Phys. Status Solidi A Vol. 13, pp. 157–168, 1972.

19. J.-J. Zondy and D. Touahri, "*Updated thermo-optic coefficients of AgGaS2 from temperature-tuned noncritical 3ω-ω→2ω infrared parametric amplification*", JOSA B, Vol. 14, pp 1331-1338,1997

20. S.K. Zhang, M. Fujita, M. Yamanaka, M. Nakatsuka, Y. Izawa, and C. Yamanaka "*Study of the stability of optical parametric amplification*", Opt. Commun. Vol.184, pp. 451-455, 2000

Chapter 4 The lasers

This chapter describes the laser systems used in the amplification experiments. First, the most important requirements for the two laser sources (pump and signal) for optical parametric amplification are presented. The characteristics of the pump laser and of the free electron laser (FEL) at FELIX facility (Free Electron Laser for Infrared eXperiments), in Nieuwegein, the Netherlands) are briefly described, emphasizing the parameters of the laser systems which are significant in obtaining high-amplified energy in short pulse duration of the amplified FELIX pulses with good stability.

4.1 Laser sources for optical parametric amplification

Besides the choice of a nonlinear material for OPA which is described in detail in Chapter 5, the pump and signal lasers are equally important in designing a powerful source for spectroscopic applications. The parameters of the lasers influence the parametric gain and on the stability of the amplified signal.

The parameters of the pump laser source are extremely important: the pump wavelength should be in the transparency range of the crystal and phase-matchable with the signal. The power delivered by the pump source should be high enough to obtain a large gain. The stability is another important parameter: fluctuations of pump energy imprint large fluctuations on the amplified pulse energy and temporal instability can create drastic problems if the temporal overlap with the signal pulse is affected [1].

The pump beam profile has to be uniform, because the presence of hot spots can cause damage on the crystal surface or even in the bulk. The pump beam profile is also important in optimizing the gain; ideally is a top hat compared to the signal beam profile, but due to the effects of saturation and to nonlinear amplification of different parts of the signal beam, it is possible to determine an ideal shape which in given experimental conditions would produce an amplified signal beam with a perfect Gaussian profile [2].

Due to the critical dependence of the gain on the phase mismatch, the finite divergence and bandwidth of the pulse are also to be considered for maximization of the gain. Other important requirements are the short and long term stability of the

laser sources. Several considerations contribute to establishing the optimum pump pulse duration. Ideally, in analogy with the beam profiles, the pump should be temporally a top hat compared to the signal pulse. A large pump pulse duration (compared to the signal duration) enables the use of the Optical Parametric Chirped Pulse Amplification (OPCPA) method. Nevertheless, the damage threshold of the crystal decreases with the pulse length and it is much lower at nanosecond pulse durations than to tens of picoseconds pulse duration (see also Chapter 5, section 5.2.3). Thus, an increase of the pump pulse length would be an advantage in OPCPA experiments, allowing for larger stretching of the signal pulse without spectral narrowing or instabilities, but would lead to a decrease of the damage threshold of the crystal. High pump intensities, of the same order with the picosecond pulse intensity – which are necessary for obtaining a high gain – cannot be used because they would damage the crystal.

Regarding the signal source, the wavelength is required to be phase matchable with the pump in the crystal. For a good stability of the parametric process it is important that the wavelength is stable (the central wavelength does not fluctuate) and the bandwidth does not change on a long or short time scale. If the signal pulse is tunable, it is then desirable that the tuneability and selectivity of the wavelength is easy and fast and does not involve misalignments of the signal and pump beams.

The jitter between the two interacting pulses is another important condition for obtaining a stable amplified-pulse energy. It is clear that, for a nonlinear interaction, a high instability of the two interacting pulses results in high fluctuations of the amplified pulse. The jitter effects are even more important for OPCPA. As it will be shown in Chapter 6 and 8, it can lead to the instability of the central wavelength of the amplified pulse. Generally, if the pump pulse is much longer than the stretched signal, the influence of the jitter is less important. But the intensity or central wavelength flucutuations can be caused by the relative movement of the pump peak intensity with respect to the stretched-signal pulse.

4.2 The pump laser

The pump laser is a commercial flashlamp pumped Nd:YAG regenerative amplifier (RGA 60, Continuum, CA USA) seeded by a continuous mode:locked oscillator (Model 131, Lightwave, CA USA). The amplifier consists of two stages,

the regenerative amplifier and a single-pass laser-amplification stage. A schematic view of the laser system is shown in Figure 4-1. The train of mode-locked pulses generated by the seed laser at 111 MHz passes through a Faraday isolator (FI) and enters the regenerative amplifier. The Faraday isolator prevents back reflections from the amplifier to the seed laser. The assembly of Pockels cell 1 (PC1), the quarter wave plate (W3) and polarizer P1 selects one pulse from the train of pulses at 111 MHz (at a frequency of 10 Hz) to enter the resonator. The polarizers do not reflect the light with horizontal polarization. The vertically polarized light incident on the polarizer P1 is transmitted to the resonator and is trapped by applying an appropriate voltage to PC1, which rotates the polarization through 90 degrees. After being trapped in the cavity formed by the mirrors M1 and M2, the pulse traverses several times the laser resonator of the regenerative amplifier. By switching on and off the voltage on PC2, P2 either transmits or reflects the light passing through the resonator. The delay between the voltages applied to PC1 and PC2 can be optimised to allow the pulse to circulate in the cavity till it acquires a high gain. By switching the voltage of the PC2, the polarization is restored to vertical and is reflected by the polarizer P2. Thus, the amplified pulse is dumped out of the cavity, and then further amplified in a final amplification stage. For that, the beam diameter is increased with the aid of the telescope T and the profile is smoothed with the apodiser A3.

Both laser rods are flashlamp-pumped at the same repetition rate with FELIX macropulse (for more details on the temporal structure of FELIX, see the next paragraph).

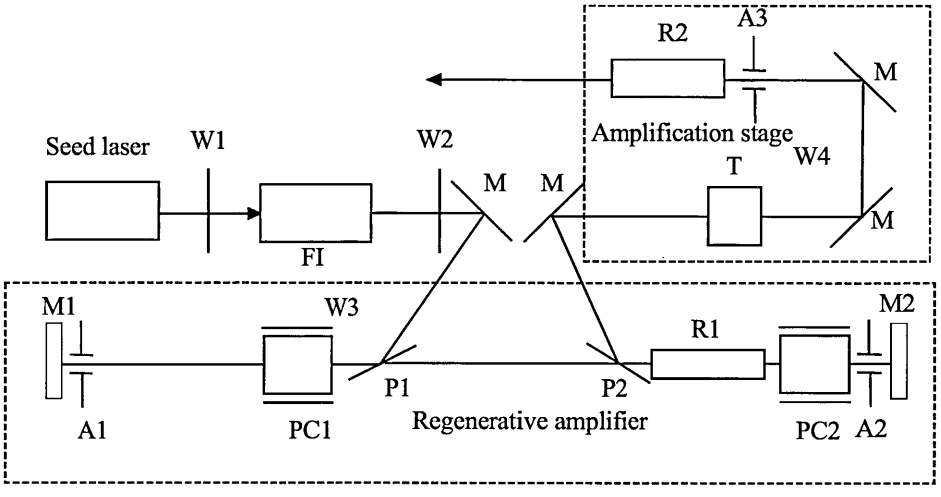

Figure 4-1 Schematic of the pump laser. FI is the Faraday isolator, M= mirrors, M1 and M2 the laser cavity mirrors, R1 and R2 are the laser rods, W1, W2, W4 are half waveplates, W3 is a quarter wave plate, P1, P2 polarizers, T=telescope, A1, A2, A3 = apodizers, PC1, PC2= Pockels cells

This laser system is able to deliver pulses at different repetition rates, the one used in experiments being 10 Hz. The amplified energy at the output of the regenerative amplification is typically 25-26 mJ, and can easily increase to 70-100 mJ and more after the second amplification stage, which consists in a single-pass laser amplifier. However, the damage threshold of the crystal used for parametric amplification (AGS in our experiments) limits the energy. The beam diameter at the exit of the laser is very small compared with the size of the crystal (~ 1mm). The beam is transported via a 16 m beam path to the laboratory where the experiments take place and the diameter of the beam is increased on the table via a telescope to a size of 11 mm FWHM (full width at half maximum). The beam profile was determined with a linear SPIRICON beam profiler. This device is a linear pyroellectric array, with 256 elements, and a length of one inch. An example of the profile is given in Figure 4-2.

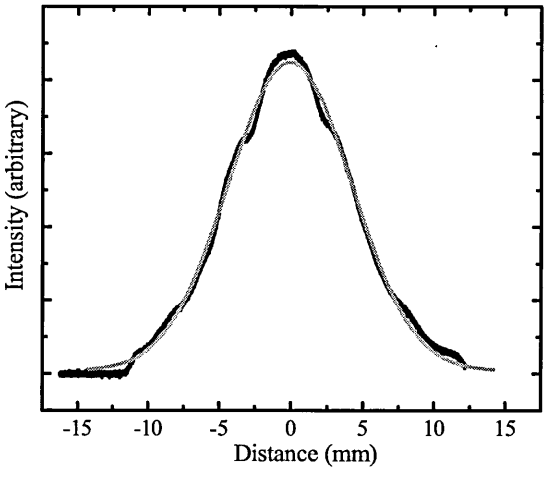

Figure 4-2 Pump beam profile, measured in the horizontal plane. The black line represents the measurements, while the grey curve is a Gaussian fit with the FWHM diameter approximately 11 mm

Autocorrelation measurements have been performed with a crossed-beams autocorrelator, which used a BBO crystal, shown in Figure 4-3.

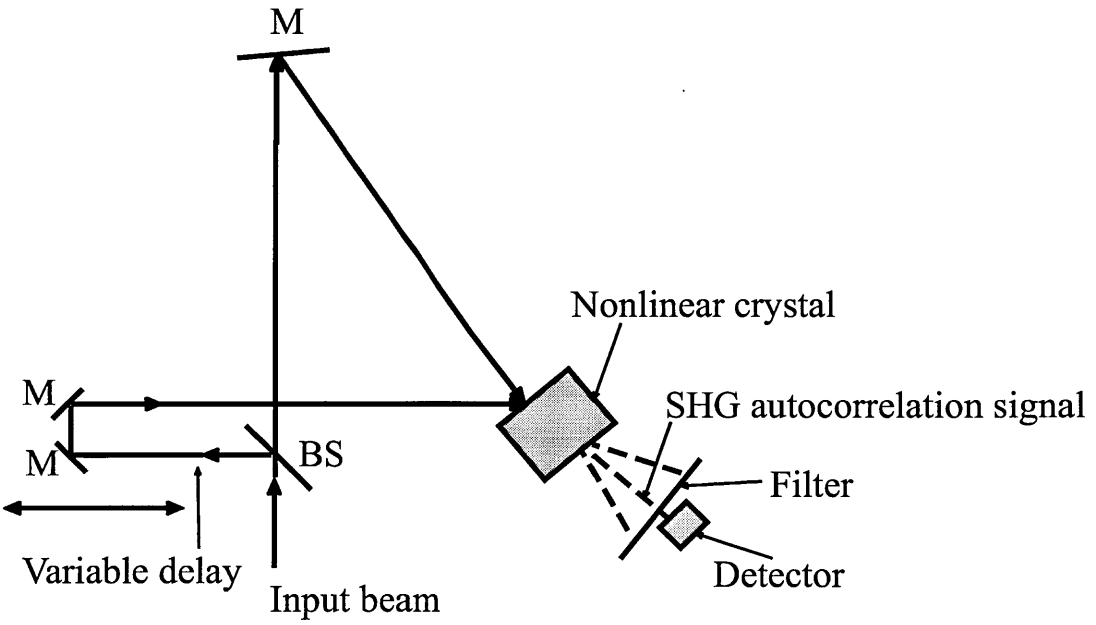

Figure 4-3 Autocorrelation setup. The input beam is split by the beam-splitter BS in two beams: the refracted beam is directed to the crystal by a mirror (M), while the reflected beam is passing through to a variable delay stage and then reaches the crystal. The second harmonic autocorrelation signal is produced when the beams are spatially and temporally overlapped, and the crystal is phase-matched for second harmonic generation. The fundamental beam is eliminated by a filter and signal is detected by a photodiode.

A beam splitter (BS) separates the incoming beam in two paths: the transmitted beam has a fixed length, while the reflected one has a variable length, which can be adjusted by moving the holder of the two mirrors M. The crystal is phase-matched for second harmonic generation at 1.064 μm (fundamental wavelength). The autocorrelation signal is detected if the pulses coming from the different paths are spatially and temporally overlapped. A filter is used to eliminate the fundamental beam at the detector. The autocorrelation signal is recorded by scanning the delay. The pulse shape is assumed Gaussian. In this case, the FWHM pulse duration can be calculated by multiplying the FWHM of the autocorrelation trace with 0.707.

The pulse duration, as determined from the autocorrelation trace, was 85 ps. However, the measurements revealed a second peak in the autocorrelation trace, suggesting that a second peak accompanies the main pulse. The second peak, noticeable in both autocorrelation traces and amplification experiments is situated at about 200 ps from the main one. Because the delay stage used in autocorrelation measurements was shorter than necessary, the trace is not complete.

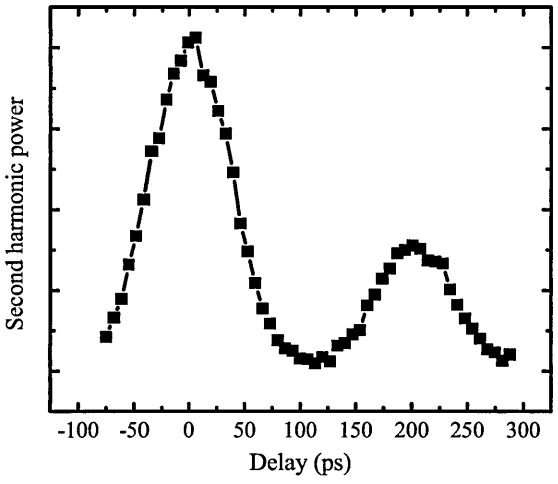

Figure 4-4 Detail of the autocorrelation trace of the pump pulse A second peak appears at a distance of approximately 200 ps from the main peak. The full width at half maximum for the main peak is 85 ps

The stability of the pulse is 2% for operation at 80 mJ output energy. However, the stability can be drastically affected by the possible instabilities in the mode-locked oscillator, and are caused mainly by thermal effects.

4.3 FELIX

FELIX (the Free Electron Laser for Infrared eXperiments) is well known as the first Free Electron Laser (FEL)-user facility in Europe. The wavelength range covered at FELIX is rather large, spanning the mid-infrared (3 μm) to far infrared (250 μm). The wide wavelength range is covered by two FELs, FEL 1 (25-250 μm) and FEL 2 (3-30 μm). The properties of radiation emitted by the two FELs at FELIX (wavelength range, rapid tuneability, temporal structure and possibility of adjustment of the laser pulse and bandwidth) make them suitable for applications in physics, chemistry or biology.

For our experiment, the signal pulse for parametric amplification is provided by one of its FELs, (FEL 2).

The principle of an FEL in shown in Figure 4-5.

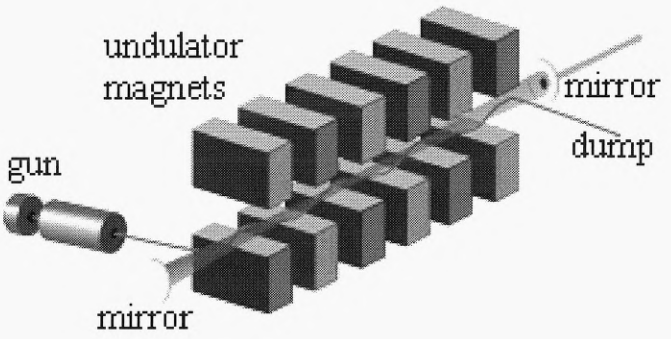

Figure 4-5 The FEL lasing scheme: The electrons produced by the gun enter the undulator, which is situated in the laser cavity formed by two mirrors. Due to the magnetic force of the alternate magnets, the electrons emit synchrotron radiation. The wavelength of the emitted light depends on the energy of the electrons, on the magnetic field and on the period of the undulator. The radiation emitted is resonated in the laser cavity and the electrons are dumped

The main parts consist of the source of electrons, the undulator and the laser cavity. The undulator consists of a row of alternatively poled permanent magnets, which creates a periodically varying magnetic field structure. When passing through the undulator, the electrons are forced to wiggle due to Lorentz force, and they emit light. The undulator is a gain medium transparent for any wavelength. The emitted light is resonated in the laser cavity and reinforced by fresh electrons, while the electrons are dumped at the exit after passing the cavity and emitting light.

The general layout of the two FELs is shown in Figure 4-6.

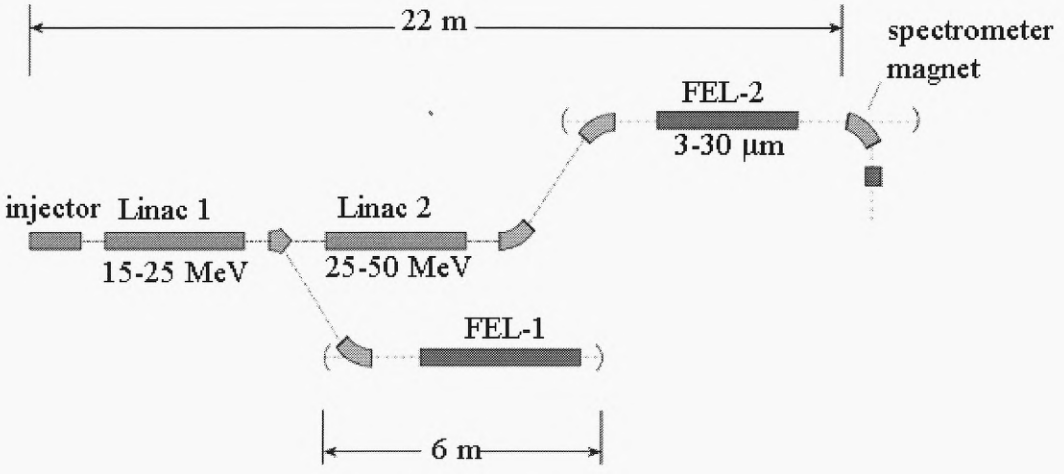

Figure 4-6 A schematic of FELIX. The injector and the linear accelerators produce relativistic electrons. After acceleration, the electrons are directed to the resonators, where the electrons emit radiation under the influence of the periodic magnetic field of the undulator. FEL1 is designed to produce radiation in the wavelength range 25-250 μm, while FEL2 produces laser radiation in the range 3-30 μm.

Both FELs have the same electron source. The electron beam injector consists of the thermionic triode gun, which produces bunches of electrons. The

bunches are shortened in the pre-buncher and buncher, in order to have the proper duration for injection in the linear accelerators (Linacs).

At the entrance of the first linear accelerator, Linac 1, the electron bunches have already relativistic energy (3.8 MeV) and electrons are accelerated to 15-25 MeV energy. After passing Linac 1, there are two possible options. The first possibility is directing the beam to the second accelerator, Linac 2, where the electrons are further accelerated to ~50 MeV, and injected into FEL 2. The second option is the beam injection in FEL-1. After acceleration, the beam is directed into the resonators. The FEL cavities consist of two copper mirrors, which can be finely adjusted with motorized stages. The resonator length is 6 m, and the geometry of the resonator creates the beam waist almost in the middle of the undulator. The radiation is coupled out from the laser cavity through a hole in the output mirror and transported to user stations via an evacuated beam transport system. The undulators of both FELs consist of two series of samarium-cobalt permanent magnets forming 38 field periods with a length of 65 mm. The wavelength can be scanned by changing the distance between the two poles according to [3]:

$$n\lambda_0 = \frac{\lambda_u(1+K^2)}{2\gamma^2} \tag{4-1}$$

where λ_0 is the wavelength of the radiation, n is the harmonic number, λ_u is the period of the undulator and K is a dimensionless constant, depending on the magnetic field, and γ the relativistic constant, $\gamma^2>>1$. The parameters that influence the wavelength are λ_u, the intensity of the magnetic field, and the energy of the electrons. The rapid wavelength change is accomplished by the variation of undulator field strength.

The temporal structure of FELIX radiation, shown in Figure 4-7, follows the electron beam structure.

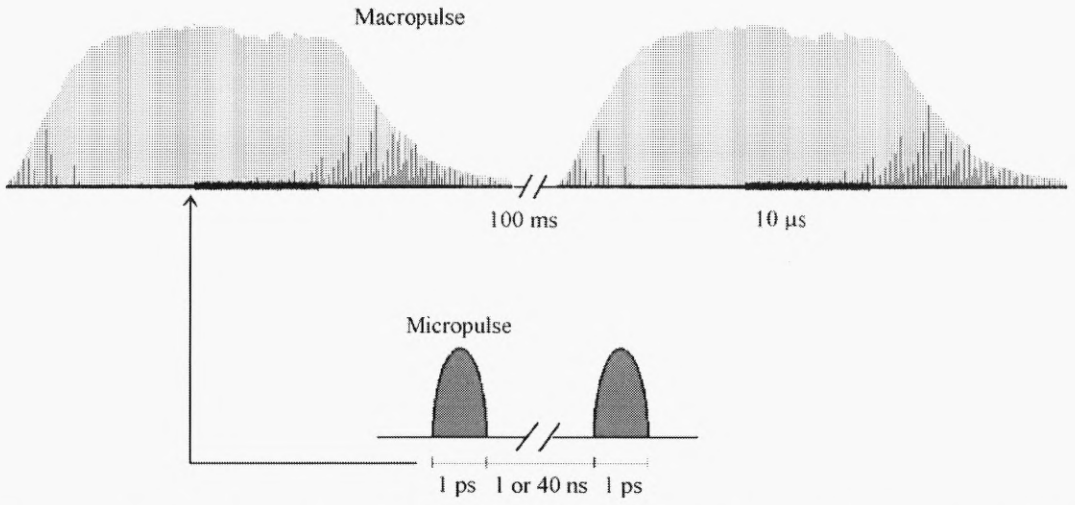

Figure 4-7 Temporal structure of FELIX. The macropulse has a repetition rate up to 10 Hz. The macropulses consists of trains of micropulses, delivered at 1GHz or 25 MHz (time separtion fo 1 or 40 ns between micropulses). The macropulse duration can be adjusted typically to 10 μs, and the micropulse between 6-100 optical cycles (hundreds of femtoseconds to few picoseconds for the wavelength range 4-10 μm).

The FEL delivers (macro) pulses at repetition rate up to 10 Hz, with a macropulse duration that can vary in a range of few microseconds to 10 μs. A macropulse consists of a train of much shorter micropulses, with an adjustable duration of few picoseconds. The separation between the micropulses in the train is either 1 or 4 ns, corresponding to repetition rates of 1 GHz and 25 MHz respectively. The micropulse duration can be adjusted between 6-100 optical cycles, which, translated in time units, leads to hundreds of femtoseconds to few picoseconds for the wavelength range 4-10 μm. In amplification experiments only one micropulse in the macropulse train is used. In order to avoid the unnecessary heating of the crystal, a 25 MHz micropulses repetition rate was chosen.

The temporal shape and spectrum of the micropulses are in principle flexible and they depend mainly on the cavity detuning [4]. It has been shown that, with a proper choice of FELIX parameters, the optical pulses are transform-limited [4].

The maximum pulse energy depends on wavelength; typically the energy available for ecperiments is a few microjoules (up to 50, depending on wavelength), while the beam diameter is 7-10 mm FWHM also depending on wavelength. Figure 4-8 shows the measured beam profiles of FELIX at 6.3 μm.

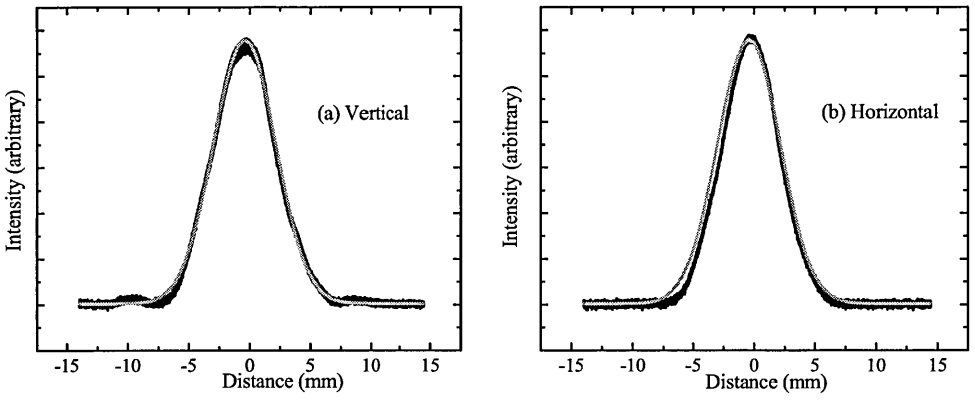

Figure 4-8 Measured FELIX profiles, at 6.3 μm wavelength. The grey lines are Gaussian fits, the same for both vertical and horizontal directions, proving an almost circular symmetry.

The beam profiles are Gaussian in shape and the distribution of intensity is almost circular. The dependence on wavelength of the beam profiles will be presented together with other measurements in Chapter 8, section 8.3.1.

4.4 Synchronization and delay

One of the requirements mentioned in the section 4.1 is a good temporal overlap between the signal and the pump pulses. For achieving a temporal overlap between the pulses, firstly the pulses need to be synchronised, and secondly a fine delay line is necessary. The delay line can be either optical or electronic. The allowed jitter, or synchronization accuracy is imposed by the longest pulse: the pump pulse, which is approximately 85 ps.

There are two major aspects related to the amplification experiments: the synchronization of the pump pulse (at 10 Hz) with the FEL macropulse, and the synchronization of the pump pulse with the FEL micropulse.

The synchronization between the FELIX macropulse and the pump pulse is done with a timer unit.

The different temporal structure of the seed laser of the regenerative amplifier and the micropulse FEL train repetition rates - 111 MHz and 1 GHz (25 MHz) for FELIX - makes difficult the pump pulse-FEL micropulse synchronization. The Pockels cell in the regenerative amplifier selects a pulse from a train with 111 MHz repetition rate, which is trapped in the cavity and amplified, leading the pump pulse. For synchronizing the pump pulse with FELIX micropulse, it is necessary to synchronize the 25 MHz of FELIX with the 111 MHz of the mode-locked pulse

train, which seeds the regenerative amplifier. The seed laser is synchronized with FELIX via an ultrastable rf clock (SMG 801.0001.52; Rhode & Schwarz, Munich, Germany). The Pockels cells in the regenerative amplifier are triggered synchronously with one micropulse in every FEL macropulse.

There are two basic ways of accomplishing temporal overlap between optical pulses: using an optical delay line, which can vary the path length of one of the pulses with respect to the other till the temporal overlap is achieved, or electronically. A computer controlled phase shifter can shift the phase of the 1GHz and the 25 MHz for the FELIX Gun with respect to the 25 MHz of the pump laser in steps of 1, 10, 100 ps and 1 ns. So, the system can vary the delay between the pump and the signal pulses in the parametric amplification experiment within 40 ns in steps of (minimum) 1ps. The temporal delay between FELIX and the pump laser has a jitter of a maximum of 5 ps, on a short time scale (minutes).

An additional shift, for delays greater than 40 ns, is realized by shifting the macropulse of FELIX with respect to the pump pulse, emerging from the regenerative amplifier.

4.5 Discussion

The laser sources described in this chapter are suitable for parametric amplification in a crystal which allows their phase matching. The crystal will be described in Chapter 5.

The pump pulse is provided by the Nd:YAG regenerative amplifier, and the signal by the mid-infrared FEL. The pump pulse has a fixed wavelength (1.064 μm), while the signal is tuneable in a chosen range of 4-11 μm. The beam profiles and temporal shapes of both pulses are Gaussian. The energies per pulse are ~ 80 mJ or more for the pump and ~ 10 μJ per pulse for the signal. The pump pulse duration is 85 ps FWHM. The signal pulse duration is adjustable in a range of a few ps [5]. The difference in pulse lengths between pump and signal pulses allowed a lengthening of the signal pulse, by stretching with a grating-stretcher, described in Chapter 8, section 8.2.1. More details about the FEL laser beam parameters are given in Chapters 7 (section 7.1) and Chapter 8 (section 8.3.1).

4.6 Bibliography

1. I. T. Sorokina and K.L. Vodopyanov, *"Solid Stated Mid-Infrared Laser Sources"*, Topics in Applied Physics, vol. 89, Springer Verlag, Berlin, 2003

2. L. J. Waxer, V. Bagnoud, I. A. Begishev, M. J. Guardalben, J. Puth, and J. D. Zuegel, *"High-conversion-efficiency optical parametric chirped-pulse amplification system using spatiotemporally shaped pump pulses"*, Opt. Lett. Vol. 28, No. 14, pp. 1245-1247, 2003

3. G. Datolli and A. Renieri, *"Experimental and theoretical aspects of the free-electron laser"* in *Laser Handbook* Vol. 4, edited by M.L. Stitch and M. Bass, North Holland, Amsterdam, pp. 1-133, 1985

4. G.M.H. Knippels, R.F.X.A.M. Mols, A.F.G. van der Meer, D. Oepts, P.W. van Amersfoort, *"Intense far-infrared free-electron laser pulses with a length of six optical cycles"*, Phys. Rev. Lett. Vol.75, pp. 1755-1758, 1995

5. www.rijnh.nl

Chapter 5 The Silver Gallium Sulphide Crystal

This chapter describes the general properties that makes silver gallium sulphide (silver thiogallate, $AgGaS_2$ or AGS) a suitable nonlinear medium for parametric amplification of FELIX with the Nd:YAG pump laser. A short historical overview of the crystal is presented, followed by calculation and measurements of the most important characteristics of the crystal used in the bexperiments: phase matching angles, refraction indices, nonlinear constant and absorption coefficient.

5.1 Introduction

The potential of silver thiogallate for nonlinear applications in mid-infrared was first suggested by Chemla et al. in 1971 [1]. This work predicted actually a whole class of crystals, with similar structure to AGS, namely chalcopyrite, compounds that can be generally represented as I-III-VI_2 or II-IV-V_2, as very promising candidates for nonlinear mid-infrared (MIR) applications. The birefringence of these compounds, which allows for phase matching in MIR, is due to the anisotropy of the crystal structure, caused by the occurrence of two kinds of atoms in the cation sublattice. In this pioneering work, the arguments brought by authors in favour of this class of crystals were based on the high nonlinear susceptibility coupled with the large birefringence of the compounds, and high transmission in mid-infrared (from 0.5-13 μm). These are necessary features for a material to be phase matchable for the desired MIR wavelength range of interaction, because the nonlinear coefficient is a crucial parameter for the efficiency of the nonlinear process, while the large birefringence allows for phase matching over a wide wavelength range, and very good transparency favours an optimal energy extraction from the pulses involved in the nonlinear interaction.

Still, as described in [1-3], in the beginning of the research on AGS crystal growth, only small sizes of twin-free regions samples up to several millimetres in length could be grown. (A twin is a compound crystal composed of two adjoining crystals or parts of the same crystal, sharing the same plane of atoms). The optical quality and transparency were limited by the growing technique and varied from sample to sample. Since then, a lot of effort has been dedicated to optimizing the quality of the samples and several growth techniques have been proposed. The most common are the melt growth: Bridgman-Stockbarger [1, 2, 4, 5], liquid encapsulated

Czochralski [3], vertical gradient freezing method (VGF) [6] and the chemical transport [7-9].

Only the melt growth was capable of producing large crystals without inclusions [6]. The first problems encountered with the growing technique were: crystal and ampoule cracking, bands of inclusions, compositional grading, twins, platelets, microcracks, voids, and low optical quality [1-3, 9-11]. The defects of the crystal have been studied by X-ray, photoluminescence, absorption, photoluminescence excitation spectroscopy and Raman scattering [8, 9, 12-16]. The most important discovery, that explained the difference between the theoretically high and experimentally low measured transmission of the AGS samples, and allowed for a substantially improvement of the growing techniques, was the anomalous thermal expansion along the c-axis, which created strain in the growing crystal, leading to cracking and twin formation [3]. Since then, due to the improvements in the growing processes, it has become possible to grow high-quality, long samples of AGS crystals, opening new fields for interesting non-linear experiments and applications. For example, a crystal as large as 28 mm in diameter and 60 mm in length has been grown by Bridgman-Stockbarger method [2].

Since 1974, AGS has been widely used in MIR applications like OPOs, OPGs and OPAs for nanosecond, picosecond and femtosecond pulses, and difference frequency generation spectrometers [21-24]. The first tunable infrared generation by down conversion in AGS was achieved in 1973 by Hanna et al. [21]. A power of hundred of milliwatts in pulses of 10 ns FWHM and a tunable range of 4.6-12 μm were reported. The wavelength range was extended to 18 μm, in 1976 by Seymour et al. as described in [25]. The first parametric generation of tunable picosecond pulses in MIR was reported by Elsaesser et al. [26], in 1984. The crystals used in their experiments were 3 and 1 cm long, while in [21] and [25] crystals of only 1.5 , 1.7 mm and 2.8 mm long have been used. The first report of a nanosecond OPO based on AGS is given in [27], with a wavelength range limited to 4 μm by the damage threshold of the crystal. The first synchronously pumped AGS OPO pumped by mode-locked Nd:YAG lasers is described in [28]. In that work, signal pulse widths ranging from 45-80 ps were obtained using 100 ps pump pulses length, a few mW power of for the idler pulses and 100 mW signal power.

5.2 Crystal properties

AGS is a negative uniaxial crystal belonging to the tetragonal -42m class of symmetry, with a chalcopyrite structure type. The crystal has a yellow pale color, other colours observed in the growing process (like greenish, orange) being attributed to changes in the stoichiometry or impurities [3]. From the point of view of nonlinear applications, a good knowledge of several crystal properties is very important for predicting the efficiency of the parametric process. In the case of OPA the most significant are the gain, wavelength range, spectral properties and energy of the amplified pulse, and the (optimum) configuration of interaction. The most important properties of the crystal from the point of view of nonlinear applications are the phase matching properties, transparency range, refractive indices, Fresnel losses, nonlinear constant, thermal effects and damage threshold.

The main properties making AGS attractive as nonlinear amplifying medium in our experiment, where the FEL pulses with wavelength between 4-11 μm are amplified via OPA using pump radiation with 1.064 μm wavelength, are:

- good transparency for both pump and signal wavelengths (in the wavelength range 0.5-13 μm [1, 29], a wavelength range including the one specific to the experiment: 4-10 μm. The high transparency in this range allows for pumping at 1.064 μm, a very common wavelength for powerful commercial lasers, which is not possible for example with crystals like $AgGaSe_2$, which has a similar structure and better nonlinear constant, but high absorption coefficient at 1.064 μm;
- possibility of (birefringent) phase matching with interacting wavelengths;
- (moderately) good nonlinear coefficient (d_{36}=13 ±2 pm/V)) [30];
- availability of large crystals, of the order of few centimetres (see for example [2, 31]);
- rather high damage threshold (see Table 5-1 and associated references).

5.2.1 Refractive indices and phase matching angles

Refractive indices are very important from the point of view of birefringence, which determines the wavelength range in which the crystal can be phase matched. The dependence on temperature provides useful information about temperature tuning.

The birefringence dispersion represents the dependence of the refractive index on wavelength. It has been extensively studied by different authors [30-34].

According to [29], the Sellmeier equations were obtained by Bhar and Smith [31] as expressed in Eq.(5-1).

$$\begin{aligned} n_o^2 &= 3.3970 + \frac{2.3982\lambda^2}{\lambda^2 - 0.09311} + \frac{2.1640\lambda^2}{\lambda^2 - 950} \\ n_e^2 &= 3.5873 + \frac{1.9533\lambda^2}{\lambda^2 - 0.11066} + \frac{2.3391\lambda^2}{\lambda^2 - 1030.7} \end{aligned} \tag{5-1}$$

Zondy et al. updated the coefficients [30]:

$$\begin{aligned} n_o^2 &= 3.40684 + \frac{2.40065\lambda^2}{\lambda^2 - 0.09311} + \frac{2.06248\lambda^2}{\lambda^2 - 950} \\ n_e^2 &= 3.60728 + \frac{1.94792\lambda^2}{\lambda^2 - 0.11066} + \frac{2.24544\lambda^2}{\lambda^2 - 1030.7} \end{aligned} \tag{5-2}$$

An important issue related to the birefringence is the temperature dependence of the refractive indices. The thermal effects together with the temperature tuning have been studied by different groups [30, 35, 36]. The equations giving the best fits with the experimental results for the temperature dependence are [29]:

$$\begin{aligned} \frac{dn_o}{dT} &= \frac{10^{-5}}{2n_o} \cdot \left[-\frac{39.88\lambda^2}{\lambda^2 - 0.0676} + \frac{112.20\lambda^2}{(\lambda^2 - 0.0676)^2} \right] \\ \frac{dn_e}{dT} &= \frac{10^{-5}}{2n_e} \cdot \left[\frac{25.50\lambda^2}{\lambda^2 - 0.107584} + \frac{45.72\lambda^4}{(\lambda^2 - 0.107584)^2} \right] \end{aligned} \tag{5-3}$$

The SNLO [37] code uses the Eqs. (5-1) and (5-3) for numeric simulations with the AGS crystal.

The phase matching curves for a certain configuration of interaction for the AGS crystal can be calculated using Eqs 3-12-13. The internal angles depend on the cut angle of the crystal and incidence angles, on the wavelengths of the interacting pulses and on the refractive indices.

One can use Eqs. (3-20-21) and the values of refractive indices given by SNLO code, or calculated with Eqs. (5-1) -(5-2), to determine the incidence, phase matching angles, and degree of noncollinearity for the signal and idler beams. In Figure 5-1 the degree of noncolinearity (angles β and γ) is shown as a function of the pump incidence angle α_p, for an AGS crystal cut at 41.5° for type I phase matching. The cut angle of the crystal and the type of interaction correspond to the crystal used

in the experimental setup, i.e. for OPA. It can be noticed that β increases strongly with α_p and also with the increasing signal wavelength, while γ maintains small values, less than few degrees.

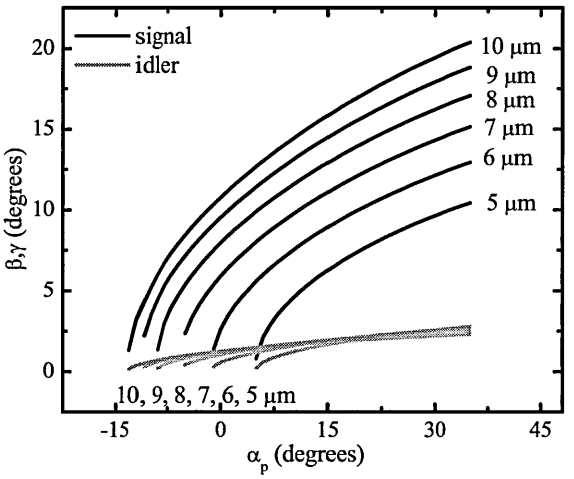

Figure 5-1 The degree of noncollinearity of the signal (β) and the idler (γ) beams relatively to the pump beam, as a function of the incidence angle of the pump beam on the crystal α_p, for a cut angle θ_c= 41.5°

The degree of noncollinearity should have a value lower then 5 degrees in order to get a good (acceptable) spatial overlap in the crystal. This condition restricts both the pump incidence angle and the angle between the signal beam and the pump. The incidence angles are restricted also by the reflection losses. Reflection losses can be reduced by antireflection coating. If that is optimized for normal incidence, the incidence angle should not exceed 10-15 degrees.

Figure 5-2 presents the dependence of the phase matching angles for the idler and signal (formed by the internal idler and signal with the optical axis of the crystal) as a function of wavelength, for θ_c=41.5° and normal pump incidence. It appears that the signal phase matching angle increases significantly with wavelength. This affects the overlap between the interacting beams.

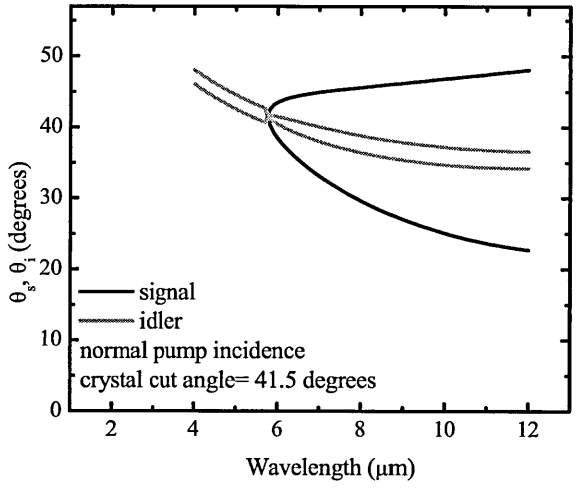

Figure 5-2 Phase matching angles as a function of wavelength for the signal and idler beams at normal pump incidence for θ_c=41.5°

In Figure 5-3 the dependence of the external angles on the pump incidence angle (α_p) for several values of FELIX wavelength is shown. The external and internal angles are optimised for a signal wavelength around 6 μm, that is why, for the other wavelengths in the range of 5-10 μm, correspond higher values of internal and external angles, leading to a worse spatial overlap in the crystal.

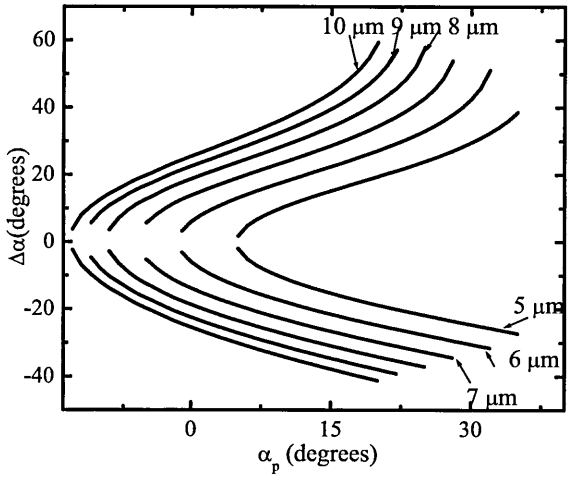

Figure 5-3 The external angle between FELIX and pump beams as a function of the incidence angle of the pump beam, for several signal wavelengths, shown in the figure. The curves are interrupted because the phase matching condition is not fulfilled for all angles

Figure 5-4 shows the dependence of $\Delta\alpha=\alpha_p-\alpha_s$ at two wavelengths -5 and 10 μm- as a function of the degree of noncollinearity of the signal (β).

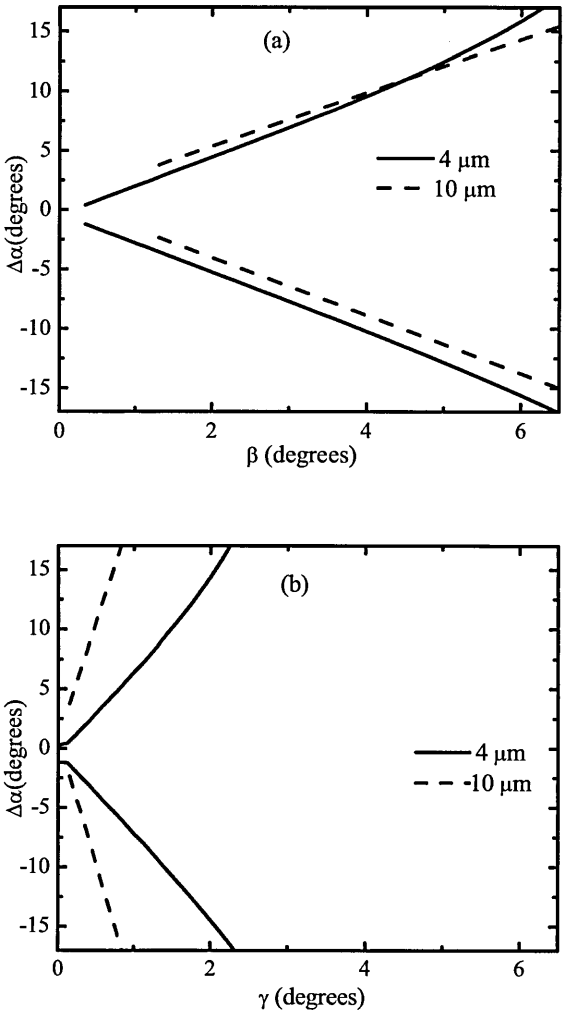

Figure 5-4 The external angle between signal and pump beam ($\Delta\alpha=\alpha_p-\alpha_s$) as a function of degree of noncollinearity of signal (β) (a) and idler (γ) (b) beams

In conclusion, for an external angle ($\Delta\alpha=\alpha_p-\alpha_s$) of about 5-6 degrees, the degree of noncollinearity between the signal and idler and the pump (respectively) expressed by the angles β and γ should not exceed few degrees. For a tunable parametric amplifier, with the signal wavelength varying between 4-10 μm, $\Delta\alpha$ is fixed by the incidence signal and pump beams, while the rotation of the crystals achieves phase matching at each signal wavelength. One can derive the rotation angle of the crystal for achieving a phase-matched interaction. This can be expressed as the variation of either α_s or α_p, because they are related by $\Delta\alpha$. Figure 5-5 shows the values of α_p and α_s for $\Delta\alpha$=5.6° for type I and type II interaction. It can be noticed that, for the type II, the phase matching condition is much less sensitive to the wavelength than in the case of type I. As plotted in Figure 5-4, at this external

angle, the angles β and γ have relatively small values in the whole wavelength range and this does not affect the spatial overlap of the interacting beams.

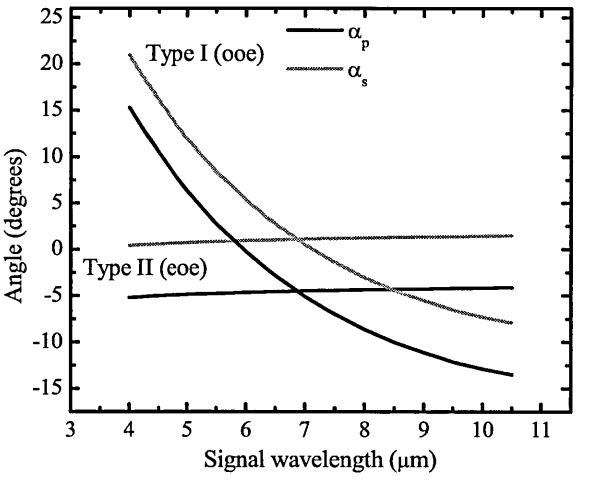

Figure 5-5 The incidence angles α_p, α_s, as a function of the signal wavelength for type I ooe and type II eoe interaction, for $\Delta\alpha$=5.6 degrees. For type II an optimum cut angle was determined to be 40 degrees, while for type I the angle was 41.5 degrees, the same as the crystal used in experiments

For AGS, due to the higher nonlinear coefficient and angular properties, the ideal cut angles of the crystal are θ=40° and φ=0°, corresponding to the maximum nonlinear constant at this type of interaction (eoe).

The type I ooe interaction allows for relative good efficiency and enables better operation at shorter wavelengths (less than 4 μm).

5.2.2 Nonlinear constant

The nonlinear constant is a fundamental characteristic of a crystal used in parametric processes. Still, the possibility of growing crystals with large size, good optical quality, high damage threshold and good transparency can balance a moderate or lower value of the nonlinear constant.

Because of symmetry considerations, the number of significant terms in the nonlinear tensor is reduced to one, namely d_{36}. Using the theory presented in Chapter 2, section 2.5, the effective nonlinear constant for type I ooe interaction, can be expressed as [29]:

$$d_{eff} = d_{36}\sin(\theta + \rho)\sin(2\varphi) \qquad (5\text{-}4)$$

The angles θ, ρ and φ are defined in Chapter 2. The value of d_{36}, has been determined by several authors [1, 17-20]. The measured values are spread over a range from 9 pm/V to 57 pm/V. The wide range is due to the poor quality and short length of first crystals used in measurements, to the method used in measurements, and also to some approximations assumed in calculations [38]. The nonlinear constant is a function of the interacting wavelengths, expressed by Miller's rule. The measurements performed by Zondy at al. [38] to determine the value of the nonlinear constant in AGS are generally accepted as the most accurate. The reported value of d_{36}, measured for three different interactions, was 13+/- 2 pm/V.

The Figure 5-6 shows a comparison between the calculated values of the effective nonlinear constant and the gain coefficient Γ as a function of wavelength, for the two possible types of interaction. The calculations were performed using the SNLO code, which applies the Miller scaling rule for determining the wavelength dependence of the nonlinear coefficient, but neglects the angular influence. The calculations show that the type II (eoe) interaction gives the highest nonlinear coefficient in the wavelength range 4-10 μm, while the oeo interaction is characterized by a higher d_{eff} and Γ in the wavelength range 2-4 μm. For example, for a signal wavelength of 7 μm, in type I ooe collinear interaction the d_{eff} is 10.3 pm/V, while for type II eeo, collinear d_{eff} is 15.8 pm/V, significantly higher.

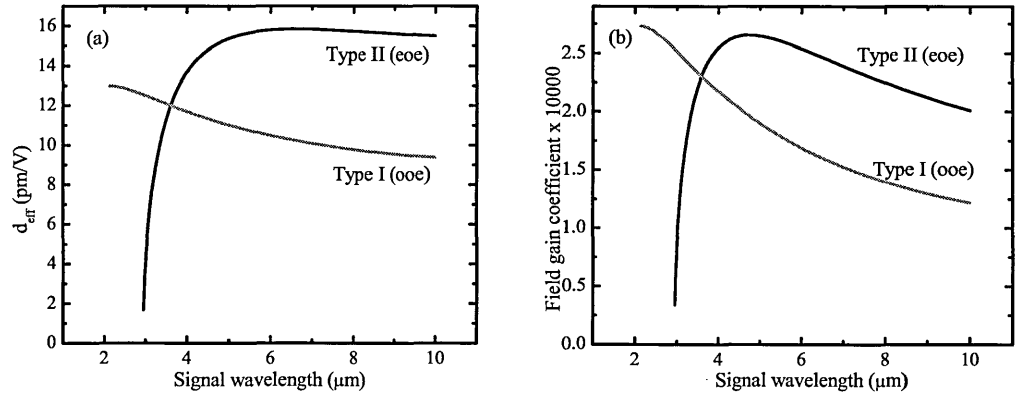

Figure 5-6 Effective nonlinear constant (a) and field gain coefficient (b) for type I and type II collinear interactions. While type II interaction is more convenient for higher wavelengths, type I can extend the wavelength range to lower values.

The characteristics of the crystal needed for amplification experiments were determined by simulations with the SNLO code [37]. The cut angle was calculated to optimise the nonlinear constant of the crystal and to get collinear interaction at 6 μm

signal wavelength. The optimum size of the crystal was found to be 14x17x17 mm^3. The length of the crystal was determined to be 17 mm, while the cross section resulted 14x17mm^2, with the long dimension in the rotation (horizontal) plane. The simulations performed to determine the crystal optimum size is described in Chapter 6, section 6.2. The crystal available for experiments was only 9x13x17 mm^3 in size, so the cross section was reduced. The crystal was required to be antireflection coated for the pump wavelength (1.064 μm) and for the mid-infrared range 3-12 μm, with a maximum reflectivity loss of 10 %.

The length was initially 17 mm. After amplification experiments, the crystal was damaged. The damaged layer was removed by the manufacturer, who repolished and recoated the crystal, with a loss in length of about 1mm. In the following, some optical properties of the crystal used in experiments are presented.

5.2.3 Transparency and damage threshold; transmission measurements and absorption losses

General facts

As mentioned above, the transparency of the crystal is a crucial parameter for the efficiency of the parametric process and for the damage threshold of the crystal. The transmission of the crystal is high in the range 0.5-9.5 μm and decreases around 10 μm due to a three-phonon absorption process (see Figure 5-7 and Figure 5-10). It is general accepted that at wavelengths higher than 12 μm, especially for long crystals, the absorption limits the efficiency of the parametric processes. Nevertheless, for wavelengths longer than 14 μm, the absorption decreases and it is possible to use AGS for wavelengths as long as 18.3 μm [25]. The transparency can vary from crystal to crystal due to possible defects, presence of twins, voids, etc.

AGS presents expansion coefficients with opposite signs for different crystallographic axes. The overheating caused by absorption can produce strains because of the opposite signs of expansion coefficients. The strains can damage the crystal and caused many problems with growing techniques. That is why an excellent transparency at the pump wavelength is required.

An overview of available data for damage threshold and linear absorption for the pump wavelength (1.064 μm) coefficient for the AGS crystal are given in Table 5-1.

Company	Damage threshold (MW/cm^{-2}) at 1.064 μm		Fresnel losses	Abs. Coeff. (cm^{-1}) at 1.064 μm
	Surface	Bulk		
Cassix [40]	25 (10 ns)	500	17%	0.01
Physcience Opto-electronics Co., Ltd., Beijing [41]	>500 (100ps) 20-30 (150ns)	>600 (150ns)		0.01-0.03
Russian Institute, Novosibirsk [43]	20-50 (10 ns)	500-750 (10 ns)		0.001-0.009
Cleveland [44]	25 (10 ns)	>500 (10 ns)		< 0.01
Novosibirsk, Russia (Moltech) [45]	-	350		-
Eksma [46]	10 (20 ns)			
MolTech [47]	10-20 (150 ns) for 10.6 μm			
Hanna at al. [21]	10 (10 ns)			
Elsaesser at al. [26]	3000 (20 ps) after several thousands pulses	25000 (20 ps) after 100 pulses		
Fan at al. [27]	10 (20 ns) after 1000 pulses	13 (20 ns) after 100 pulses		
Dimitriev at al. [29]	20-25 (35 ns) 10 (20 ns) 75-3000 ~20 ps			0.01

Table 5-1 Damage threshold and absorption coefficient for AGS

As shown in Table 5-1, the damage threshold is much higher for bulk than for surface. This can be associated with the general fact that the absorption coefficient on the surface is different than the one in the bulk, and in general the measured absorption coefficient includes the surface effect and represents an "effective absorption coefficient". Nevertheless, even if the damage threshold was expected to increase by applying AR coatings to the crystal, coating did not improve the damage threshold [27].

Another fact appearing from the data listed in Table 5-1 is the strong dependence of the damage threshold on the pump pulse duration. The damage thresholds are much higher for picosecond than for nanosecond pulses because of the stronger strain caused by heating effects for longer pulses.

Transmission measurements and damage of initial crystal

Initially, the crystal used in experiments had the size 13x9x17 mm^3. The crystal was required to be antireflection coated (ARC) for the pump wavelength and for the 3-12 μm with a reflectivity lower than 10% per face. Another important requirement was a high damage threshold, corresponding to pump energies up to 75 mJ in 85 ps pulses, with a beam diameter of 10-12 mm FWHM (500-730 MW/cm^2). These limits are dictated by the parameters of the pump laser pulse necessary for obtaining a high gain in the OPA process.

The transmission of the crystal was measured using FTIR and energy measurements. The incident and transmitted energies have been measured using the free electron laser available at FELIX, and a calibrated Molectron energy-meter head.

The first transmission measurements have been performed before any amplification experiments. The results are depicted in Figure 5-7 (black stars and squares represent energy measurements and the black line-FTIR measurements). For the pump wavelength (1.064 μm) the transmission and reflection losses have been determined, while for the wavelength range of 5-8 μm only transmission measurements have been performed.

The absorption coefficient of the crystal and the reflectivity of the ARC at the pump wavelength (λ=1.064 μm) have been evaluated, assuming no absorption in the coating. A low-power 20-ns Nd:YAG (Soliton-Thales) laser with a very small beam diameter (1mm) was used, in order to avoid crystal damage and errors introduced by the beam size. Energy measurements were performed with an energy meter with a calibrated head. A fast photodiode, placed in the front of the crystal at the reflection angle, was used for observing the reflections from the front and back ARC on the crystal faces. For that, an incidence angle of 22° was chosen, in order to be able to visualize separately the two reflections on the fast photodiode. The total transmission of the crystal was determined to be 80 % ± 1%, while the total reflected energy was determined to be 3%. The total-reflection losses and transmission were determined, and the ratio between the two reflections from the faces of the crystal was evaluated.

In an attempt to determine the reflectivity of the coating and the absorption coefficient of the crystal, it was considered that absorption takes place in the bulk, so that the coating itself does not introduce absorption losses.

The ratio of the two intensities can be expressed as:

$$\frac{I_2}{I_1} = (1-R)^2 e^{-2\alpha l} \tag{5-5}$$

with I_1 being the intensity of the reflection of the light reflected at the first face of the crystal, I_2 the intensity of the light reflected from the back-face of reflection, R the coating reflectivity, α, the absorption coefficient and l the path length of the light in the crystal. The transmission (T) can be expressed as:

$$T = (1-R)^2 e^{-\alpha l} \tag{5-6}$$

The absorption factor can be eliminated between Eqs. (5-5) and (5-6). First, the reflectivity of the coating can be determined by measuring the transmission of the crystal, the ratio of the reflected intensities and the total reflected energy at 22° incidence angle. Than, using Eqs. (5-5) and (5-6) the absorption coefficient can be calculated. The calculated value of the coating reflectivity (R) was 1.8 %, while the value of the absorption coefficient at the pump wavelength (before damage) is obtained as 0.11 cm^{-1}. The values of the absorption coefficient listed in Table 5-1, at the same wavelength, and for the best quality crystals are less than 0.005 cm^{-1}, and in general less than 0.01 cm^{-1}. Taking into account that the crystal was antireflection coated, with reflection losses of only 1.8% at 1.064 μm, the measured transmission showed much higher losses than the ones expected with absorption coefficients given in Table 5-1. The cause of the low transmission could be either a high absorption coefficient or absorption introduced by the coating.

After amplification experiments, some grey tracks appeared on the input face of the crystal. The crystal damage did not occur at the ARC, but in a thin layer between the coating and the crystal. The damage affected dramatically the transmission as shown in Figure 5-7. The damage was produced by the pump laser radiation (75 mJ in 85 ps pulses, with a beam diameter of 10-12 mm FWHM).

The results for transmission measurements after amplification experiments are illustrated in Figure 5-7, together with initial measurements. The crystal transmission in the wavelength range of 5-8 μm decreased from about 80% before amplification, to 40% after amplification.

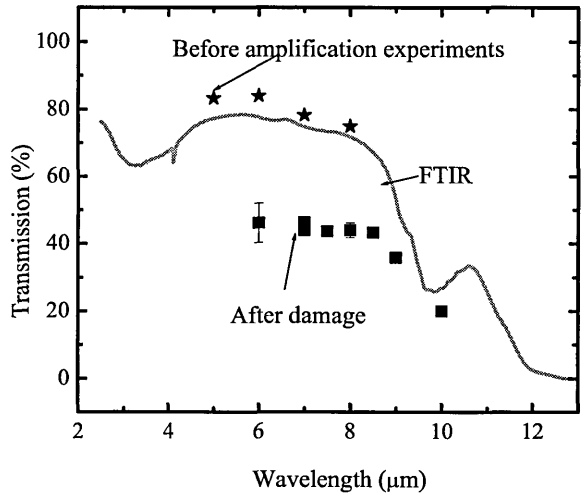

Figure 5-7 Transmission of the 17 mm long, ARC AGS crystal for the wavelength range 5-10 μm, normal incidence and FTIR measurements shown in the range of 2-13 μm

Assuming again (for the damaged crystal) that the loss is distributed in the bulk, the calculation with the corresponding value of the transmission (40%) yielded an absorption coefficient ~0.4 cm^{-1}. In the last calculation, it was considered that the reflectivity of the coating had not changed, as no damage appeared on the external surface of the coating.

Measurements with reconditioned crystal

After damage, the manufacturer (Russia, Novosibirsk) removed the antireflection coating from both faces and the damaged layer, and the crystal became 1 mm shorter. After re-conditioning, transmission measurements had been performed first in Russia (Novosibirsk) for the uncoated crystal and then for the antireflection-coated crystal. In our laboratory, (FOM-Rijnhuizen), the measurements were possible only for the antireflection coated crystal.

Figure 5-8 shows the coated crystal and the damaged layer at the interface between the crystal and the coating.

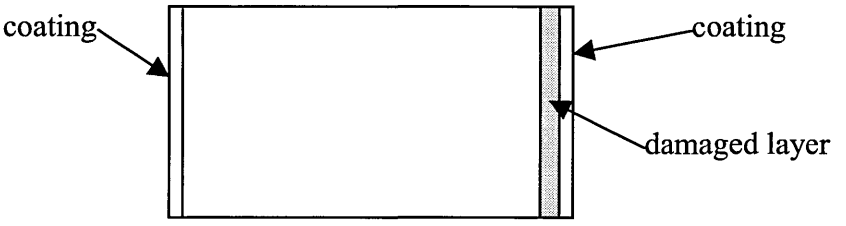

Figure 5-8 The damaged antireflection coated crystal. The damage appears in a layer between the crystal and the coating

Figure 5-9 shows the results of the transmission measurements performed in Novosibirsk with uncoated crystal for two different wavelength ranges: 0.6-1.6 μm, and 2.5-13 μm and for two different polarizations: ordinary and extraordinary. For comparison, the calculated curves of transmission assuming no absorption losses are added to transmission plots.

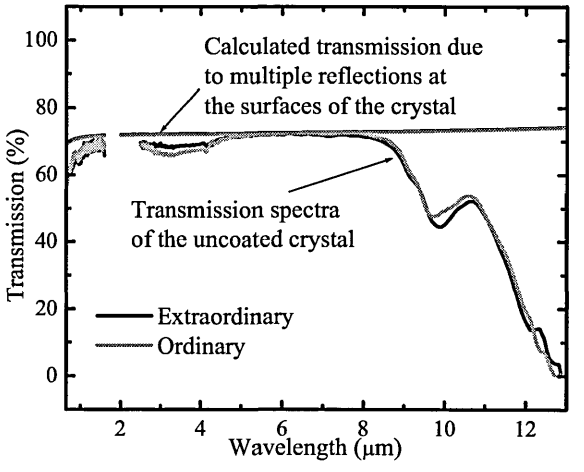

Figure 5-9 Transmission spectra for the uncoated crystal, recorded for two different polarizations: ordinary ($\vec{E}$ perpendicular to optical axis Z) - extraordinary (with $\vec{E}$ in the plane containing this axis and the direction of propagation). The calculated transmission in the case of no absorption in the crystal due to multiple reflections from the surfaces is shown together with the measured transmission. Data are provided by the Novosibirsk laboratory. The crystal thickness is 16 mm

Figure 5-10 shows the transmission of the uncoated crystal with multiple Fresnel reflection losses subtracted and adapted for 1 cm long crystal plotted together with the transmission curve given by the SNLO code [37]. The differences between the two curves are significant in the range 0.5-4 μm.

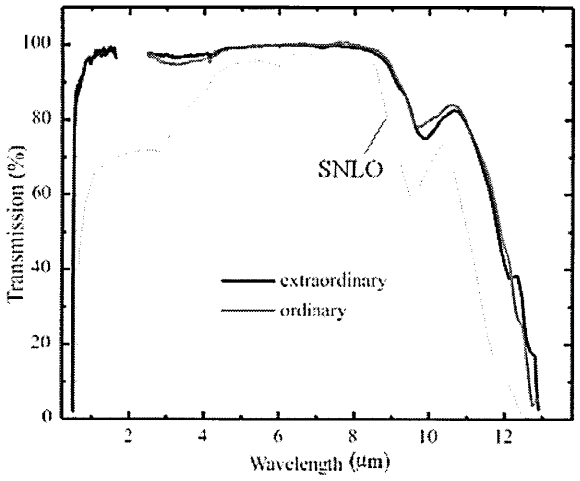

Figure 5-10 Comparison between the transmittance of the uncoated AGS crystal, adapted for 1 cm long crystal (dot lines) and the transmission plot given by SNLO code [37] (straight line) for the same crystal length.

A noticeable difference revealed by the comparison in Figure 5-10 is the shift of the three-phonon absorption in our crystal to longer wavelengths.

For calculating the absorption coefficient we used the following expression [50]:

$$T = \frac{(1-R)^2}{e^{\alpha d} - R^2 e^{-\alpha d}} \tag{5-7}$$

with T being the transmission of the crystal, R the reflectivity, α the absorption coefficient, and d the length of the crystal. It should be noted that for a birefringent crystal, the reflectivity depends on polarization, while for a long sample the optical activity can influence the values of the transmission.

R is given by Fresnel relations:

$$R = \left(\frac{n-1}{n+1}\right)^2 \tag{5-8}$$

Sellmeier equations (5-2) have been used in calculations for the ordinary and extraordinary refractive indices in Eqs. (5-7) and (5-8). The calculated absorption coefficient is shown in Figure 5-11 (a) and (b) for extraordinary polarization and Figure 5-12 (a) and (b) for ordinary polarization, with black lines for results corresponding to our laboratory (FOM Rijnhuizen) and grey lines for Novosibirsk.

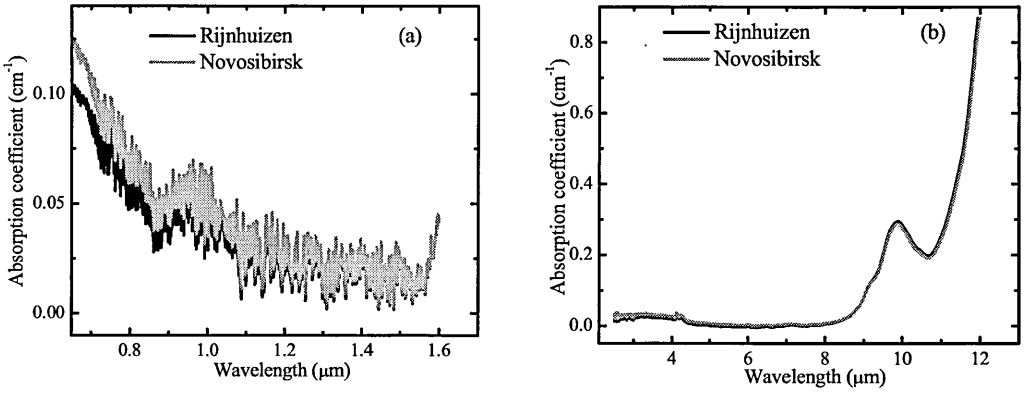

Figure 5-11 The absorption coefficient determined from Figure 5-9 (a) and (b) are absorption curves determined in our laboratory– black lines and Novosibirsk –grey lines for extraordinary polarization.

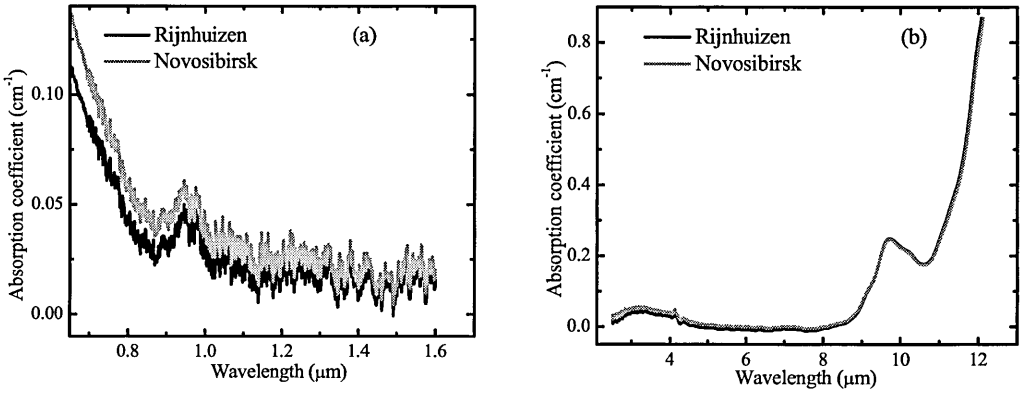

Figure 5-12 The same as Figure 5-11 for the ordinary polarization

The results of the calculations are similar, especially for the mid-infrared range, while a slight difference can be noticed for the lowest wavelength range in Figure 5-11 (a) and Figure 5-12 (a). Figure 5-13 presents a detail from Figure 5-11 (a) and Figure 5-12 (a) around the pump wavelength (1.064 μm), which is of special interest.

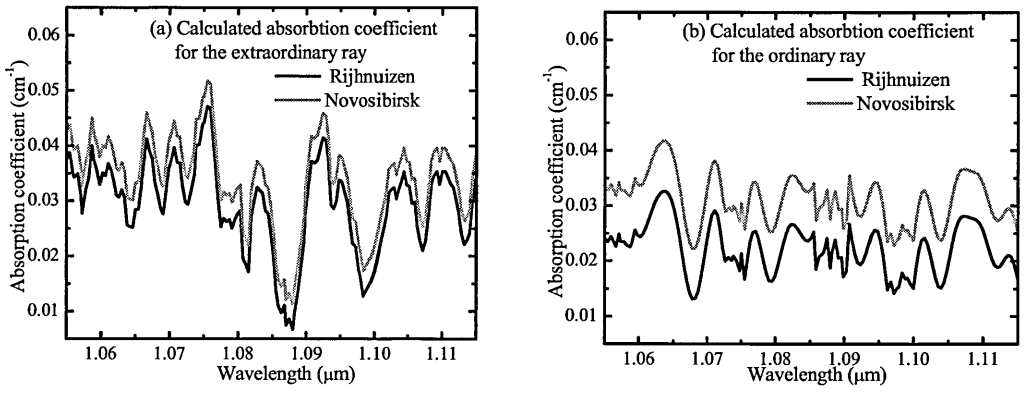

Figure 5-13 Black lines show the absorption coefficient for the AGS element, calculated taking into account multiple reflections on the crystal surfaces, using Eq. (5-7). The Fresnel losses are calculated using Eq. (5-8). The grey curves are obtained in Novosibirsk. The plots are scaled to show the calculated absorption coefficient for the pump wavelength (1.064 μm)

For the pump wavelength (1.064 μm) and extraordinary polarization (as used in amplification experiments), the plots suggested an absorption coefficient of about 0.035 ± 0.005 cm^{-1} (see again Table 5-1 for comparison). This corresponds to a transmission of 94% to 95% (if reflection losses are subtracted) for a 16 mm length crystal.

Figure 5-14 presents the transmission measurements performed after reconditioning and recoating the crystal. The data were recorded in Russia (Novosibirsk) for the wavelength range 0.4-2.5 μm. In order to highlight the contribution of the coating, the previous results for the transmission of uncoated crystal (see also Figure 5-9) are shown together with the transmission of the AR coated crystal. A significant improvement of the crystal transmission at the pump wavelength (1.064 μm) due to the antireflection coating is revealed.

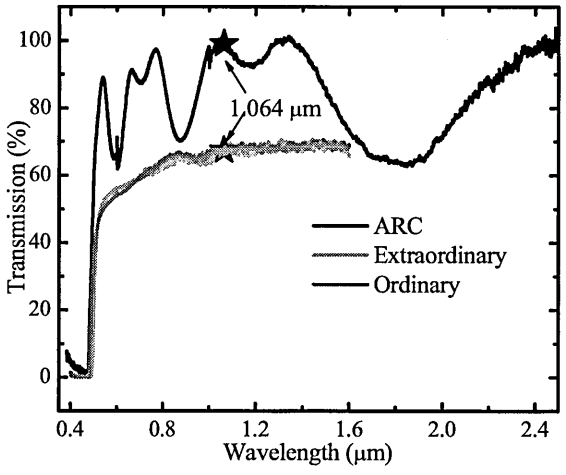

Figure 5-14 Comparison between the transmission of the uncoated crystal (dark grey and grey, for the two polarizations) and the AR coated crystal (black). The transmission at the pump wavelength (1.064 μm) is 99%, leading to a value of the absorption coefficient of 0.006 cm $^{-1}$. The values corresponding to the pump wavelength are marked with black stars

In Rijnhuizen laboratory, the transmission of new-ARC coated crystal was determined for the pump wavelength (1.064 μm) and in the mid-infrared (5-10.6 μm), using an FTIR spectrometer and energy measurements.

The results are shown in Figure 5-15 and Figure 5-17, respectively. A good transmission is observed for the range 5-8 μm, and not so good for longer wavelengths.

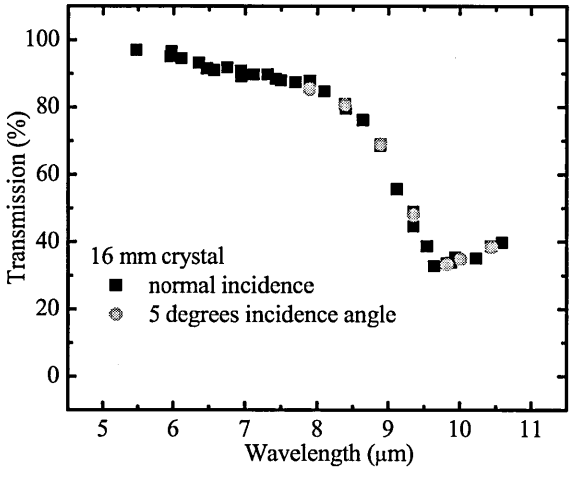

Figure 5-15 Transmission of the ARC crystal measured in Rijnhuizen laboratory. The squares represent results obtained for normal incidence and the circles are results for an incidence angle of 5 degrees

Assuming only reflection losses introduced by the coating (with no absorption or scattering), the transmission data of the uncoated (Figure 5-9) and

coated crystal (Figure 5-15) can be used to calculate the reflectivity of the coating. This is done by calculating the change in the transmission of the ARC crystal, introduced by the coating, while the absorption losses are estimated from data in Figure 5-9.

$$T_{ARC} = T_{ABS} \cdot R_{tot} \tag{5-9}$$

with T_{ARC} being the transmission of the ARC crystal and T_{ABS} the transmission loss due to absorption in the crystal, and R_{tot}, the reflection loss due to the coating, in the absence of other loss mechanisms.

$$T_{ABS} = \frac{T}{T_{FRESNEL}} \tag{5-10}$$

In Eq.(5-10), T is the measured transmission of the uncoated crystal (Novosibirsk) and $T_{FRESNEL}$ the estimated crystal transmission due only to Fresnel losses.

The results of calculations are shown in Figure 5-16, together with the Fresnel losses of the uncoated crystal and measured total reflection losses of the coated crystal. The total reflected power was measured only for a wavelength range longer than 8 μm, because for shorter wavelengths the reflected power was too low.

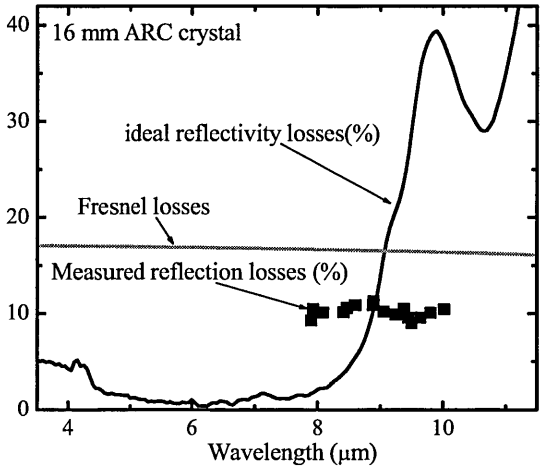

Figure 5-16 Calculated reflectivity losses using the transmission plots for the uncoated and ARC crystal, assuming no other losses. The grey line shows the calculated Fresnel losses. The squares show the measured reflection losses. The black line shows the calculated reflection losses considering only reflection losses at the coating and no absorption in the crystal. All data correspond to ordinary polarization. The discrepancy between the calculated reflection losses in the absence of other loss mechanisms and the measured total reflection losses indicates a strong absorption in the coating for wavelengths longer than 8.8 μm. This absorption might be a cause of damage at the interface crystal- AR coating.

In conclusion, the coating is effective only for wavelengths shorter than 9 μm, when the losses introduced by coating are smaller than Fresnel losses. The difference between the measured reflectivity and the losses shown by comparison of transmission measurements is obvious and is probably due to absorption losses introduced by the coating, or by the interface between the coating and crystal. Even if the measured reflectivity shows a value around 10 %, the absorption might be a cause of the damage produced at the interface between crystal and ARC.

Other measurements performed in our laboratory were FTIR measurements. They were performed for a wavelength range of 2.5-15 μm. Because of the sample size, FTIR measurements are useful only as a comparison, to check possible changes in the crystal transmission. The errors are due to the fact that background was not determined with a similar configuration. Moreover, the spectrometer is designed for measuring thin samples, with thickness of maximum few millimetres. As already mentioned, the crystal is 17 (16) mm long. The values of transmission determined by FTIR are lower with 2%- 5%than the ones measured with the energy measurements.

The measurements performed in Novosibirsk for the coated crystal covered the wavelength range of 0.6-2.5 μm, so that there is only one common wavelength (2.5 μm) with the wavelength range covered by measurements performed in

Riihjnuizen. However, as shown in Figure 5-17, the two plots obtained in the two different laboratories show similar results at 2.5 μm.

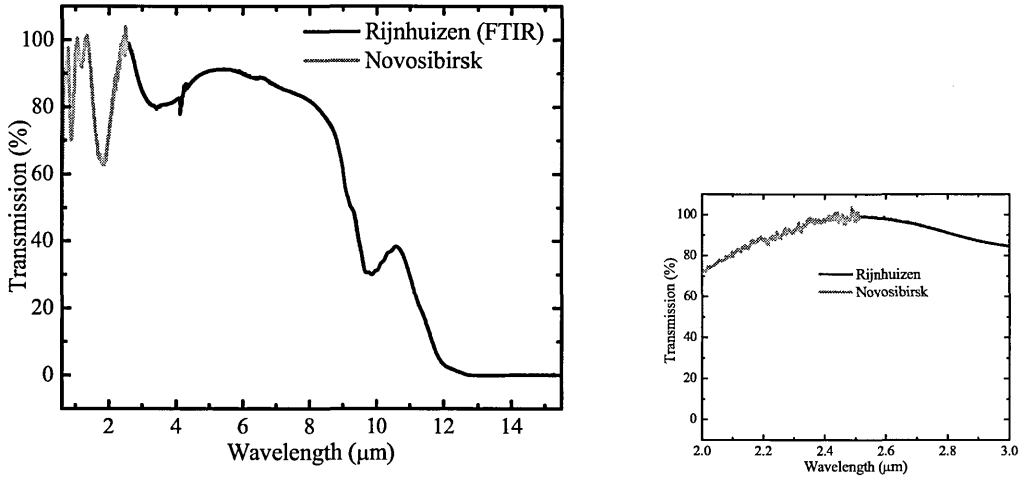

Figure 5-17 Transmission of the ARC crystal (16 mm). In the range 0.6-2.5 μm measurements are performed in Novosibirsk while in the range 2.5-13 μm, measurements are performed in our laboratory. The small plot shows the conjunction of the two measurements

Discussion

The measurements showed that crystal damage originated at the interface between the crystal and ARC.

Firstly, the grey tracks did not appear on the coating -which was not affected on the external surface- but in between the crystal and the coating. Secondly, the dramatic drop in the crystal transmission caused by the damage did not affect the bulk absorption coefficient. After reconditioning and recoating, a high transmission was retrieved.

The calculated absorption coefficient at the pump wavelength (1.064 μm) for the 17 mm- AR coated crystal, before damage, was 0.11 cm^{-1} a value much higher than the values given in literature (Table 5-1), which in general do not exceed 0.01 cm^{-1}. The calculation assumed only bulk absorption losses, and reflection losses at the coating. However, the discrepancy with data in literature (see Table 5-1) and later results obtained with the uncoated and recoated crystal did not confirm such high absorption coefficient. Thus, after removing the damaged layer and coatings, the absorption coefficient has been determined in Novosibirsk as 0.035 +/- 0.005 cm^{-1}. This suggested that the low transmission of the AR coated crystal is due to an additional loss mechanism, which does not take place in the bulk, neither on the

external surface of the coating, which was not damage, but probably, in a thin layer between the crystal and the ARC, or in the coating itself. The estimated loss at each interface ARC-crystal before damage is ~8%. After damage, this absorption coefficient increased dramatically, leading to an overall crystal transmission of only 40%.

Concerning the 16-mm AR coated crystal, the comparison between the plots presented in Figure 5-15 and the plot in Figure 5-9 for the uncoated crystal, shows that the ARC is not efficient for a wavelength greater than 8.8 μm, when the overall transmission decreases. The transmission measured for the uncoated crystal gives an extremely optimistic value for the absorption coefficient at around 10 μm, value cited in literature as being about 0.43 cm^{-1} [30, 38, 48] at 10.2 μm or 0.6 cm^{-1} [44] for 10.6 μm. However, as can be noticed from Figure 5-9, a value of only 0.24 cm^{-1} and 0.2 cm^{-1} resulted from both calculation (Novosibirsk and our laboratory) from the transmission plots (Figure 5-9) at 10.2 and 10.6 μm, respectively. Again, it appears a discrepancy with the measured reflected power, due (probably) to additional absorption losses introduced by the coating.

From our measurements, the transmission of the AR coated crystal at λ=1.064 μm is 95% ± 2%, which is in good agreement with an absorption coefficient of 0.01-0.04 cm^{-1} and a reflection loss of 1% at each face of the crystal. If the values measured in Novosibirsk are correct for both cases of coated and uncoated crystal, the transmission of the crystal at this wavelength is improved by the coating. As shown in Table 5-1, the value of 0.006 cm^{-1}, determined from measurements in Novosibirsk, corresponds to an excellent quality of the crystal, while 0.035 cm^{-1} is three times greater than the general accepted value of 0.01 cm^{-1}. This is not confirmed by our measurements, which give an overall transmission at 1.064 μm of 95%-97%.

A possible explanation of all discrepancies between measurements with uncoated/coated crystal, assuming all of them being correct, is related to the surface absorption .which influences the measurements results. The coating might also influence the level of the absorption at the surface. The measured absorption coefficients are in fact "effective bulk absorption coefficients", they include the surface effect [51]. The antireflection effect of the coating depends on wavelength,

and the coating is not efficient introducing absorption losses at wavelengths greater than 8.8 μm.

Because a slight decrease of the transmission in time can be noticed, a process of aging might take place for the coating, either a continuous damage due to irradiation under combined signal and pump beams.

Figure 5-18 shows an overview of the measurements taken with the 16 mm crystal. The measurements have been performed in different places and using different methods. In general they agree in the limits of the experimental errors (about 2% for FTIR and energy measurements).

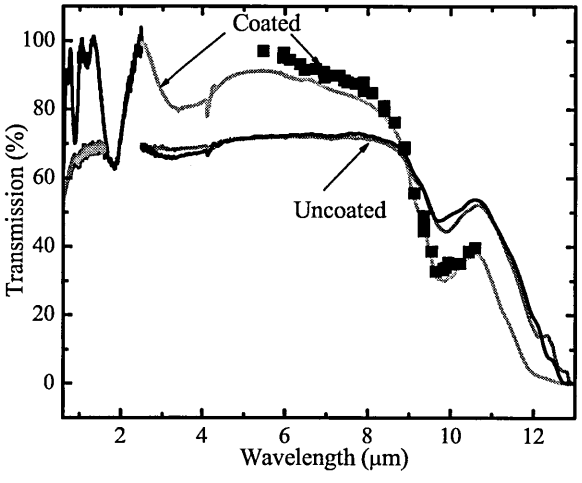

Figure 5-18 Overview of transmission curves for the uncoated and coated 16 mm long crystal. If measurements are correct, the antireflection coating is not effective for wavelengths greater than 8.8 μm

The coating is not effective for wavelengths longer than 8.8 μm, because the losses in the wavelength range 8.8-11 μm are higher than for the uncoated crystal. Moreover, the nonlinear constant is also higher for shorter wavelengths, so that the most efficient amplification is expected for the shorter wavelengths of the mid infrared range used in our experiments (4-11 μm).

5.3 Bibliography

1. D. S. Chemla, P. J. Kupecek, D. S. Robertson, and R. C.Smith, "*Silver thiogallate, a new material with potential for midinfrared devices*", Opt. Commun. Vol. 3, pp. 29, 1971

2. Re. S. Figelson and R. K. Route, "*Recent developments in the growth of chalcopyrite crystals for nonlinear infrared applications*", Opt. Eng., Vol. 26, pp. 113, 1987

3. P. Korczak and C. B. Staff, "*Liquid encapsulated Czochralski growth of silver thiogallate*", J. of Crystal Growth, Vol. 24-25, pp. 386-389, 1974

4. H. Matthes, R. Viehmann, and N. Marschall, "*Improved optical quality of $AgGaS_2$*", Appl. Phys. Lett., Vol. 26, No.5, pp. 237-239, 1975

5. O. Brisson, M. El Ganaoui, A. Simonnet and J. C. Launay, "*Experimental determination of physical parameters and analysis of the Bridgman–Stockbarger solidification for the growth $AgGaSe_2$ crystal in ampoule with conical shape*", J. of Crystal Growth, Vol. 204, pp. 201-212, 1999

6. E. Niwa, K. Masumoto, "*Growth of AgGaS2 single crystals by a self-seeding vertical gradient freezing method*", J. of Crystal Growth, Vol. 192, pp. 354–360, 1998

7. Ch. Power, S. Gilliland, A. Segura, and J. Gonzalez, "*Variation of the optical absorption edge in $AgGaS_2$ single crystals at high pressure*", Phys. Stat. Sol. (b) Vol. 235, No. 2, pp. 326–330, 2003

8. G. Brandt, A. Rauber, J. Schneider, "*ESR and X-ray analysis of the ternary semiconductors $CuAlS_2$, $CuInS_2$ and $AgGaS_2$*", Solid State Commun., Vol. 12, pp. 481-483, 1973

9. U. Kaufmann, A. Räuber and J. Schneider, "*ESR-analysis of 3d7 ions in IB---III---VI2 semiconductors*", Solid State Commun., Vol. 15, pp. 1881-1884, 1974

10. G. Massé and E. Redjai, "*Energy levels from lattice defects in $AgGaS_2$*", J. of Lumin., Vol. 33, pp. 369-376, 1985

11. In-Hwan Choi and Peter Y. Yu R. Koch, R. K. Route, R.S. Feigelson, "*Microscopic scattering centers in $AgGAS_2$*", Il Nuovo Cimento 2D Vol 6, pp. 767-1774, 1983

12. In-Hwan Choi and Peter Y. Yu, "*Optical investigation of defects in $AgGaS_2$ and $CuGaS_2$*", J. of Physics and Chemistry of Solids Vol. 57, pp. 1695-1704, 1996

13. B. Tell and J.L. Shay, "*Electroreflectance and Absorption-Edge Studies of $AgGaS_2$ and $AgGaSe_2$*", Phys Rev. B, Vol. 6, pp. 3008-3012, 1972

14. Zheng Wen-Chen, Wu Shao-Yi, Zhao Bei-Jun and Zhu Shi-Fu "*Studies of the substitutional site of Co^{2+} in $AgGaS_2$ crystal from EPR data*", Solid State Commun., Vol.109, pp. 83-86, 1998

15. O. Brisson, A. Simonnet, B. Darriet and J.-C. Launay, "*Transmission electron microscopy investigation of $AgGaSe_2$ single crystals and study of annealing efficiency by electrical conductivity measurements*", J. of Crystal Growth, Vol. 193, pp. 597-604, 1998

16. K. Mochizuki, E. Niwa and K. Masumoto "*Effects of heat-treatments on the photoluminescence spectra in $AgGaS_2$*", J. of Luminescence, Vol. 51, pp. 231-235, 1992

17. G. Yodh, H. W K. Tom, G. D. Aumiller, and R. S. Miranda, "*Generation of tunable mid-infrared picosecond pulses at 76 MHz*", J. Opt. Soc. Am. B., Vol. 8, pp. 1663, 1991

18. K. Kato, "*High power difference-frequency generation at 5–11 μm in $AgGaS_2$*", IEEE J. Quantum Electron. QE, Vol 20, pp. 698, 1984

19. P. Canarelli, Z. Benko, A. H. Hielscher, R. F. Curl, and F. K. Tittel "Measurement of nonlinear coefficient and phase matching characteristics of AgGaS2,'' IEEE J. Quantum Electron. 28, pp. 52, 1992

20. E. C. Cheung, K. Koch, and G. T. Moore, "*Measurement of second-order nonlinear optical coefficients from the spectral brightness of parametric fluorescence*", Opt. Lett. Vol. 19, pp. 168, 1994

21. D. C. Hanna, V. V. Rampal and R. C. Smith, "*Tunable infrared down-conversion in silver thiogallate*", Opt. Commun., Vol. 8, pp.151-153,1973

22. W. Kaiser and A. Seilmeier, "*Progress in the generation of ultrashort pulses in the IR*", Infrared Physics, Vol. 25, pp. 15-20, 1985

23. K. G. Spears, X. Zhu, X. Yang and L. Wang, "*Picosecond infrared generation from Nd: YAG and a visible, short cavity dye laser*", Opt. Commun., Vol. 66, pp. 167-171, 1988

24. T. Kelz, A. Schumacher, M. Nägele, B. Sumpf and H. D. Kronfeldt, "*Detection of co in air using diode laser pumped difference-frequency generation in a modular setup*", J. of Quantitative Spectroscopy and Radiative Transfer, Vol. 61, pp. 591-601, 1999

25. R.J. Seymour, F.Zernike, "*Infrared radiation tunable from 5.5 to 18.3 um generating by mixing in $AgGaS_2$*", Appl. Phys. Lett., Vol. 29, pp. 707, 1976

26. T. Elsaesser, A. Seilmeier, W. Kaiser, P. Koidl, and G. Brandt, "*Parametric generation of tunable picosecond pulses in the medium infrared using AgGaS2 crystals*", Appl. Phys. Lett. Vol. 44, pp. 383, 1984

27. Y. X. Fan, R. C. Eckardt, R. L. Byer, R. K. Route, and R. S. Feigelson, "*AgGaS2 infrared parametric oscillator*", Appl.Phys. Lett. Vol. 45, pp. 313, 1984

28. E. C. Cheung, Karl Koch, and G. T. Moore, "*Silver thiogallate, singly resonant optical parametric oscillator pumped by a continuous-wave mode-locked Nd:YAG laser*", Opt. Lett., Vol. 19, pp. 63, 1994

29. V. G. Dimitriev, G.G. Gurzadyan, D.N. Nikogosyan, Handbook of Nonlinear Optical Crystals, Springer Series in Optical Sciences, Vol. 64, 1999

30. J.-J. Zondy and D. Touahri, "*Updated thermo-optic coefficients of $AgGaS_2$ from temperature-tuned noncritical 3ω-$\omega \rightarrow 2\omega$ infrared parametric amplification*", JOSA B, Vol. 14, pp. 1331-1338, 1997

31. G. C. Bhar and R. C. Smith, "*Optical properties of II-IV-V2 and I-II-VI2 crystals with particular reference to transmission limits*", Phys. Status Solidi A, Vol. 13, pp.157–168, 1972

32. G. D. Holah, "*Infrared dielectric dispersion of silver thiogallate*", Opt. Commun., Vol. 5, pp. 10-13, 1972

33. I.-H. Choi S.-H. Eom and P. Y. Yu, "*Dispersion of birefringence in AgGaS2 and $CuGaS_2$*", J. Appl. Phys., Vol. 82, pp. 3104, 1997

34. C. Schwartz, D. S. Chemla and B. Ayrault, R. C. Smith, "*Direct measurement of the birefringence of $AgGaS_2$*", Opt. Commun., Vol. 5, pp. 244-247, 1972

35. G. C. Bhar, D. K. Ghosh, P. S. Ghosh, and D. Schmitt, "*Temperature effects in AgGaS2 nonlinear devices*", Appl. Opt., Vol. 22, pp. 2492-2494, 1983

36. E. Takaoka and K. Kato, "T*hermo-optic dispersion formula for $AgGaS_2$*", Appl. Opt. Vol. 38, pp. 4577-4580, 1999

37. SNLO nonlinear optics code, available from A. V. Smith, Sandia National Laboratories, Albuquerque, NM- 87185-1423

38. J.-J. Zondy, D. Touahri and O. Acef, "*Absolute value of the d_{36} nonlinear coefficient of $AgGaS_2$: prospect for a low-threshold doubly resonant oscillator-based 3:1 frequency divider*" JOSA B, Vol. 14, pp. 2481-2497, 1997

39. S. Haidar, K. Nakamura, E. Niwa, K.I Masumoto, and H.Ito, "*Mid-Infrared (5-12 μm) and limited (5.5 8.5 μm) single-Knob tuning generated by difference-frequency mixing in single-crystal $AgGaS_2$*", Appl. Opt.-LP, Vol. 38, pp. 1798-1801, 1999

40. Casix http://www.u-oplaz.com/crystals/crystals001.htm

41. Physcience Opto-electronics Co., Ltd., Beijing:

42. http://www.physoe.com/english/e-010404-AgGaSe2&AgGaS2/e010404.htm

43. United Institute of Geology, Geophysics and Mineralogy of SB RAS, laboratory of crystallization processes: http://www.monocrystal.ru/lc/ags.htm

44. Cleveland Crystals Inc. http://www.clevelandcrystals.com/AGSSE.shtml

45. Институт Минералогии и Петрографии
http://imp.uiggm.nsc.ru/lab443/Propertiese.htm

46. http://www.eksma.com/crystals.non/infra.htm

47. http://www.mt-berlin.com/charts/chart_01.htm

48. D. Touahri, O. Acef, and J.-J. Zondy, "30-THz upconversion of an AlGaAs diode laser with $AgGaS_2$: bridging the several-terahertz frequency gap in the near infrared", Opt. Lett., Vol. 21, No. 3, pp. 213, 1996

49. J.-J. Zondy, "*The effects of focusing in type-I and type-II difference-frequency generations*", Opt. Commun. Vol. 149, pp. 181–206, 1998

50. O., S. Kushmir, "*Effect of multiple reflections of light on the optical characteristics of crystals*", J. Opt. A: Pure Appl. Opt. Vol.5, pp. 478-488, 2003

51. http://www.cvdmaterials.com/literature.htm

Chapter 6 Simulations

This chapter presents the results of the simulations performed for configuring the experiments and characterizing the parametric-amplified pulse in the two cases (OPA) and (OPCPA). It consists of two main parts. In the first part, the calculations aim to predict the proper size of the crystal used in OPCPA experiments and the appropriate parameters for the pump and signal pulses (energy, beam diameters). For that, some preliminary results of OPA obtained with a 6 mm long AR AGS sample were used as a basis for simulations.

The second group of simulations deals with the most important experimental results obtained in the OPA and OPCPA experiments with a 16/17 mm long crystal. The characteristics of the used crystal were close to the ones calculated in the first part. Some simulations are added to highlight the influence of some important physical parameters like: nonlinear constant, crystal length, signal and pump energies, diameters, pulse durations, and delay between the pump and signal pulses. For each group of simulations, the results are presented in three main groups: the amplified energy, the spectra and the temporal shape. All these results are calculated by the code.

All simulations are performed using the SNLO code [1]. The results show reasonable agreement with experimental results, excepting the values of the amplified energy in OPA experiments.

6.1 Introduction

Chapter 3 of this thesis discusses the influence of several parameters, related to the pump and signal sources and of the nonlinear crystal properties on the parametric gain and hence on the value of the amplified energy. The nonlinear interaction in the AGS crystal is governed by Maxwell equations with nonlinear polarization, as described in the Chapter 2. It was pointed out that the calculations are extremely difficult if diffraction effects, group velocity and spatial walk-off, nonlinear effects and non-collinear interaction are considered. Moreover, if the spatial-temporal characteristics of the pulse are not Gaussian, or chirped pulses are involved, the task of determining the parametric gain, the amplified energy, the temporal and spectral characteristics of the amplified pulse becomes more difficult.

In this work, the mathematical tool used for simulations is the SNLO code [1]. The code enables diverse calculations, starting with the basic properties of a series of nonlinear crystals. Some simple functions allow a raw selection of the crystal for the desired application, while other functions are devoted to more precise calculations. Nevertheless, for some crystals (including AGS) not all parameters are known or published in the literature. Some parameters, like absorption coefficient, or nonlinear constant differ from crystal to crystal and are difficult to be determined experimentally. This is proven also by the wide range of values for the nonlinear constant of AGS, which can be found in literature [1].

6.2 Simulations for selection of the crystal size and configuration of nonlinear interaction in OPCPA experiments

This group of simulations was performed prior to the main experiments described in Chapter 7 and 8. Their goal was to estimate the optimum size of the nonlinear crystal for obtaining an output amplified energy of 2-2.5 mJ. As it is described in Chapter 5, the nonlinear crystal of choice was Silver Gallium Sulphide (AGS). The input energy of the signal pulse from FELIX is chosen to be 3-5 μJ. In order to optimise the parameters of the amplified pulse, one has to choose select a set of input parameters. Some of them are related to the crystal (cut angles, size, length, coating properties, type of phase matching), while others are related to the signal and pump input characteristics and include the beam diameters, pulse durations, angles of interaction and pulse energy. The crystal length has to be long enough to ensure high gain but short enough to avoid power losses due to the spatial and/or temporal overlap of the pulses. The cross-section has to be large enough to avoid beam losses at the crystal.

In order to select a crystal for OPCPA experiments, some preliminary experiments were performed. In these experiments, a sample crystal from Moltech (Germany) produced in Novosibirsk (Russia), was used in an OPA scheme. The sample was 6 mm long and AR coated. The pump and signal pulses were basically the same as used in the experiments and they are described in detail in Chapter 4.

The beam diameters, pulse durations input/output energies and absorption coefficient at pump wavelength were determined experimentally. The refractive indices were determined using the dispersion equations [Chapter 5] and calculating

the internal phase-matching angles for the extraordinary (pump) beam. The values of the nonlinear constant and absorption coefficient were estimated.

The results on the parametric gain served as a basis for calculations of the crystal suited to OPCPA experiments. The measurements performed on the parametrical gain, obtained with the 6-mm long crystal allowed an estimation of the size of the crystal and pump and signal properties, for obtaining amplified energies of about 2 mJ, at 6.25 μm.

In the earliest stage of the work, PW-MIX-SP (the Plane Wave Short Pulse Mixing) function was the only one performing calculations with chirped pulses, but diffraction effects could not be included. On the other hand, the function that allowed diffraction and group velocity mismatch effects (2DMIX-SP), could not take into account the chirp of the pulse, so simulations with chirped pulse and Gaussian-shaped beams using that function were not possible. Later on, in the version SNLO 3.6, the chirp was also introduced in the function as input parameter. Because in OPCPA experiments the chirp of the signal pulse was essential, the PW-MIX-SP function was used together with a calculation artifice, which allowed an estimation of the amplified energy but could not give information about spectral and temporal characteristics of the amplified pulse. However, later results showed a good agreement of the measured energy of the amplified pulse with predictions of the simulations.

The PW-MIX_SP function calculates –in- and –out- peak irradiances and on-axis fluences for the central rays of the corresponding three interacting beams (signal, idler, pump). The beams are assumed to have Gaussian shapes in space and time. Because bandwidth limitations are very important for a crystal length longer than 2-3 mm, in the range of pulse durations of 1-2 ps, the SNLO function 2D-mix-SP, which can calculate the total amount of energy while taking into account also diffraction effects cannot be used. For example, for estimating the amount of energy in the parametric-amplified pulse for pulse duration of 60 ps, this function will consider a transform-limited pulse, leading to a different pulse bandwidth than the one corresponding to an initial chirp-free pulse of 2 ps. Assuming no clipping of the spectrum in the stretcher system, the chirped pulse has the same bandwidth with the initial un-stretched pulse, considered to be 2 ps long. Consequently, using this function with the value of the stretched pulse duration only would overestimate the

output energy, giving also wrong results in the spectral characteristics of the amplified pulse.

Still, for estimating the output energy of the amplified pulse with the PW-MIX-SP function, one needs to evaluate the behaviour of the off-axis points. This can be done, by considering the spatial Gaussian distribution of the signal and pump beams. As previously mentioned, collinear propagation is assumed, with the maximum of the signal beam irradiance superimposed on the maximum beam irradiance of the pump beam. Thus, the initially Gaussian distribution of the signal beam intensity interacts with the Gaussian intensity of the pump. Because the interaction is nonlinear, and it depends on the intensities of the two beams, the parametric gain experienced in the transverse direction of the signal beam varies significantly with the distance from the maximum intensities. In a simplified calculation, (non-saturated regime, the intensity of the signal beam increases exponentially with the square of the pump intensity (see Chapter 3).

If the output fluence of the amplified pulse for a few (equidistant) points (or circles, in a cylindrical symmetry as it is the case) at different distances r_i from the axis, is calculated, then the total amount of energy is given by:

$$E_{out} = \sum_{i=1}^{n} 2\pi r_i \Delta r F_i \,, \tag{6-1}$$

where:

- r_i is the distance from the center of the signal beam to the "i" point
- Δr is the distance between two consecutive points
- F_i are the values of the output fluence at distance r_i
- n is the number of points considered in beam for the estimate.

The problem to be addressed is finding the appropriate values of the input parameters for the function of the code: the input energies for the pump and signal beams. For that, the formula for the irradiance of a Gaussian beam can be used:

$$I(r,t) = 4\ln(2)\frac{E}{\pi D^2}\sqrt{\frac{2a}{\pi}}\cdot 10^{11}\cdot \exp\left(\frac{-4\ln(2)\cdot r^2}{D^2} - 2at^2\right) \ \textbf{(W/cm}^2\textbf{)} \tag{6-2}$$

Where:

E= the pulse energy (mJ)

D= FWHM beam diameter (mm)

$$a = \frac{2\ln 2}{\tau^2}$$

τ = FWHM pulse duration, (ps)

The fluence is the time integral of *I(r,t)*. The integrals over time and space can be separated. Thus, the value of *I(r,t)* is the same with the peak irradiance of a pulse with a total energy of $E \cdot \exp\left(\frac{-4\ln(2)\cdot r^2}{D^2}\right)$. Because the code requires the value of the initial energy of the pulse, the equivalent values for the energy have to be calculated, and then introduced in the PWMixSP function. The code calculates the corresponding in-out, fluences and peak irradiances for the pulse, in each point, respectively.

With a good approximation (5.4% error), one can consider 5 points in the Gaussian distribution corresponding to five distances to the centre of the beam and then add their contributions, using the values of the output fluences given by the code. Each contribution to the total energy of the pulse will be a product of the output fluence given by the code with the elementary area between two points in the beam. As an illustration of the different intensity distributions in the two beams, Figure 6-1 and Figure 6-2 show the input/output fluences for different positions in the beam, for the second set of simulations:

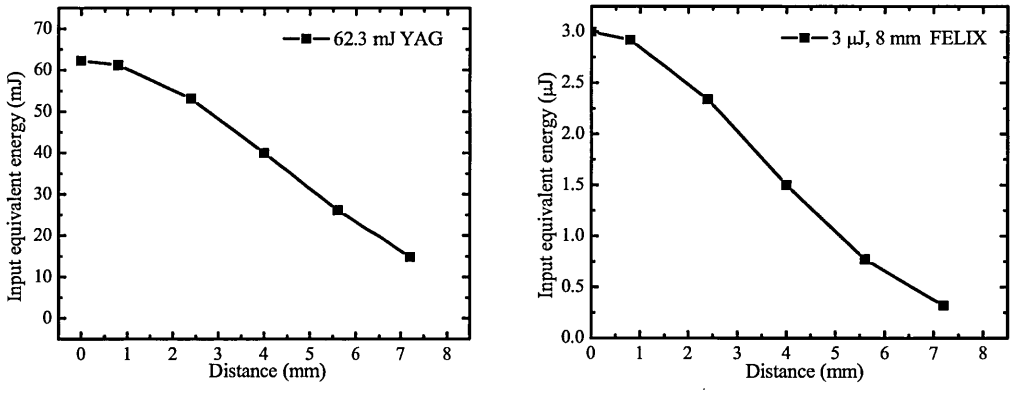

Figure 6-1 The values of input energies used in simulations for the FELIX beam, and pump beam, respectively: 8mm FHWM diameter (FELIX), 10 mm FHWM diameter (pump), 3μJ input energy, for different distances from the axis, line= Gaussian fit.

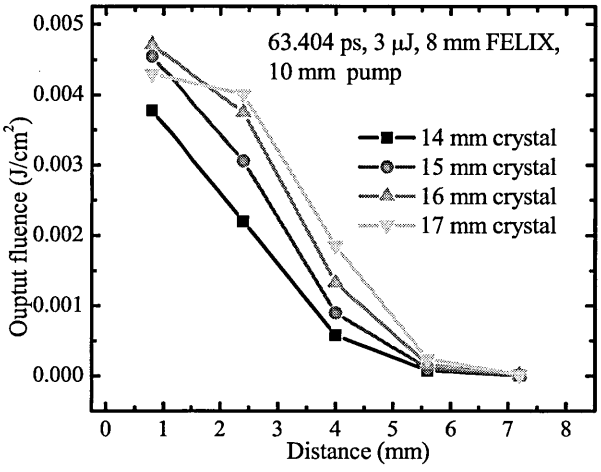

Figure 6-2 Output fluence as a function of distance to the centre of the FELIX beam for pulse durations of 63.404 ps, and for different crystal lengths.

The pulse duration is varied by stretching an initially near transform-limited pulse of 2 ps length. Thus, in all simulations the pulses with different durations have the same bandwidth, but different durations and chirps.

The micropulse is stretched using the dispersive effect in a simple stretcher system, which is described in Chapter 8. The stretched pulse durations are calculated using the well known formulas for propagation of Gaussian pulses through dispersive media [3,4]:

$$a(z) = \frac{a_0}{(1 + 2\beta'' z b_0)^2 + (2\beta'' z a_0)^2} \tag{6-3}$$

and

$$b(z) = \frac{b_0(1 + 2\beta'' z b_0) + 2\beta'' z a_0^2}{(1 + 2\beta'' z b_0)^2 + (2\beta'' z a_0)^2} \tag{6-4}$$

The parameter *a(z)* gives the pulse duration after passing the medium:

$$\Delta\tau(z) = \sqrt{\frac{2\ln(2)}{a(z)}} \tag{6-5}$$

while the parameter *b(z)* gives the pulse chirp. This is defined by the equation:

$$\omega_i(t) = \omega(t) + 2bt \tag{6-6}$$

a_0 and b_0 are the values of the parameters *a(z)* and *b(z)* for $z=0$ (the parameters of the input Gaussian pulse). For a transform-limited pulse $b_0=0$

The second order dispersion term introduced by a pair of parallel gratings, at the distance *z* apart is:

$$\beta'' = -\frac{\lambda^3 m^2 c}{4\pi c d^2 \cos^3 \gamma} z \qquad (6\text{-}7)$$

with:

m= the diffraction order

λ= the central wavelength

z= the distance between gratings

γ= the diffraction angle

d= grooves spacing

c= the speed of light

The stretcher/compressor systems are equivalent to a pair of parallel gratings placed at a distance $z=2\Delta z/\cos(\gamma)$. The distance Δz is expressed in different ways for the stretcher and the compressor. For the stretcher, Δz is the displacement of the grating from the focal point of the concave mirror, and the distance is negative). For the compressor Δz is the distance between the grating and the horizontal retroreflector (see Chapter 8).

One has also to consider the fact that the stretcher/compressor are traversed twice. The resulting stretched-pulse duration, defined by $a'(z)$, and the final chirp, given by $b'(z)$, can be determined by considering the functions of $a(z)$ and $b(z)$after the first pass as input parameters for the second pass.

The final stretched pulse duration is given by:

$$\Delta\tau(z) = \sqrt{\frac{2\ln(2)}{a'(z)}} \qquad (6\text{-}8)$$

6.2.1 Input parameters

This section discusses the input parameters used in calculations using the function PWMIXSP. The input parameters required for the function PW-mix-SP [1] are shown in Table 6-1. The signal wavelength was chosen to be 6.25 μm, because preliminary measurements have been performed at this wavelength. The pump wavelength is 1.064 μm and the idler wavelength results from the conservation of energy (see Chapter 3). The refractive indices, group velocity indices and group velocity dispersion parameters are calculated using some additional functions of the SNLO code applied for the interacting wavelengths in the AGS crystal. The nonlinear parameter (n2) and the two-photon absorption are not known.

	Signal	Idler	Pump
Wavelengths [nm]	6250	1282.3	1064
Index of refraction	2.389	2.438	2.430
Group velocity index	2.434	2.503	2.527
Group velocity dispersion (cm/sec-cm-1)	1.12E5	-1.21E5	-1.56E5
Phases [rad]	0	0	0
N2 signal [sq cm/W]	0	0	0
N2 idler [sq cm/W]	0	0	0
N2 pump [sq cm/W]	0	0	0
Beta signal [cm/W]	0	0	0
Beta idler [cm/W]	0	0	0
Beta pump [cm/W]	0	0	0
Crystal input reflectivity	0	0	0
Crystal output reflectivity	0	0	0
Crystal absorption [1/mm]	.001	.001	.008
Pulse energy (J)	5E-6	0	45
Beam diameters [mm]			
Pulse duration [ps]			85
Pulse chirp (THz/ps)			
Pulse delay relative to pump [ps]	0	0	
Crystal length [mm]	7		
$D_{effective}$ [pm/V]	9.78		
Delta k [1/mm]	0	0	0
z integration steps	100		
Time steps	4096		

Table 6-1 The input parameters for the PW MIX SP function

For these preliminary estimations, the input/output reflectivities of the crystal were not taken into account. The crystal absorption coefficient value was taken from literature to be 0.001/mm (see also the detailed discussion in Chapter 5, section 5.2.3).

In the first set of simulations the diameters of FELIX beams and of the pump beam were chosen to be 6 and 8.5 mm respectively, FHWM (full width at half maximum). The input energy was taken 3 μJ for FELIX and 45 mJ for the pump.

In a second set of simulations slightly different beam diameters were chosen: 8 mm FWHM for FELIX and 10 mm FWHM for the pump beam. The pump pulse input energy was modified to 62.3 mJ, such as the peak irradiance is about the same as in the first set of simulations.

In the third set, the pump peak irradiance was lowered, and the beam diameter was taken 12 mm. The pump pulse energy was chosen 80 mJ. The FELIX diameter was taken to be first 8 and then 6 mm.

The beam diameters were varied in order to evaluate the influence of these parameters on the overall gain energy and saturation limit. For example, in the first and second set of simulations the same peak irradiance for the pump beam was set, for different values of the beam diameters.

In the third set of simulations, the crystal length was set to 17 mm, the pump beam diameter and energy were fixed, and only the FELIX diameter and energy were varied.

The values of the input parameters used in simulations for the signal and pump beams are summarized in Table 6-2.

Input energy (FELIX) (μJ)	FELIX diameter (mm)	pump diameter (mm)	pump Energy (mJ)	pump Peak Irradiance (MW/cm^2)	Crystal length (mm)
3	6	8.5	45	607.5	14-17
3/5	8	10	62.3	608	14-17
3/5	6/8	12	80	541.9	17

Table 6-2 Values of the input parameters for the signal and pump beams (used in simulations)

The nonlinear constant, d_{eff}, was set to 9 pm/V, because this value gave the best fit for the experimental results on the parametric gain obtained with preliminary experiments.

The duration of the stretched pulse, as a function of the grating displacement and for an initial (transform-limited) pulse of 2 ps, at a wavelength of 6.25 μm, and a deviation angle of 22 degrees is shown in Table 6-3.

Displacement (m)	Stretched pulse duration (ps)	Chirp (THz/ps)
0.1	9.271458	0.023237
0.2	18.21647	0.012039
0.3	27.23306	0.00808
0.4	36.26788	0.006074
0.5	45.31003	0.004865
0.6	54.35584	0.004056
0.7	63.40376	0.003478
0.8	72.45299	0.003044
0.9	81.5031	0.002706
1	90.55382	0.002436

Table 6-3 The values of the signal pulse duration and the frequency chirp after stretching as a function of the grating displacement

6.2.2 Results

A synthesis of the results of the three sets of simulations is given in Figure 6-3 and Figure 6-4. In Figure 6-3 (a) and (b) the dependence of the output energy on the stretched pulse duration for different crystal lengths, specified in the plots, is plotted. In Figure 6-3 (a), corresponding to the first set of simulations, one can notice the optimum value of the stretched pulse duration. The energy has a maximum because that is the "point" where two opposite effects balance. The two effects are described also in Chapter 8, section **Spectral and temporal features of the amplified pulse**.

First, the parametric gain is an exponential function of the square root of the pump beam irradiance (in the plane-wave fixed-field approximation corresponding in fact to the non-saturated regime). In a simplified view, one effect is the increase of the parametric gain due to the "de-saturating" effect of stretching – a longer pulse decreases the signal-peak irradiance, at the same input signal energy. The overall energy gain increases due to the higher gain experienced by the stretched signal pulse. This happens in the saturated regime. The second effect is the decrease of the overall gain due to the temporal shape of the pump pulse. Similar to spatial effects, but in the time domain: in different moments of the signal pulse, the irradiances of the pump pulse experienced by the corresponding parts of the signal pulse are different, and this effect is decreasing the value of the energy gain. This effect is important especially for stretched pulses longer than the pump. For the total energy

of the amplified pulse, the overall effect takes into account the spatial distribution of the two interacting beams.

Figure 6-3 (b) shows some plots derived from the second set of simulations, for an input FELIX energy of 3μJ and a wavelength of 6.25 μm; it is obvious that the energy of the output pulse is not saturated for a crystal length shorter than 17 mm. The energy of the amplified pulse are higher compared with the similar values obtained with the first set of simulations, shown in Figure 6-3 (a), but they start to decrease at longer signal pulse durations. For a crystal length of 17 mm, the energy can reach a value of 2.5 mJ but cannot increase anymore for pulses longer than 70 ps.

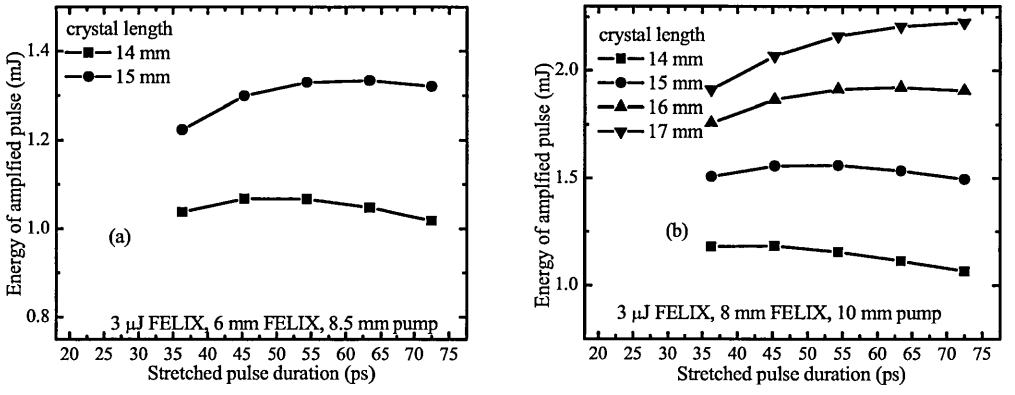

Figure 6-3 (a), (b) The dependence of the amplified pulse energy on the stretched pulse duration for different crystal lengths and different beam diameters of the interacting beams, for 3 μJ input energy (FELIX). The energy of the stretched and amplified pulse is higher for the second set of input parameters, and can reach a value of 2.5 mJ for a crystal length of 17 mm, and pulse duration of ~ 70 ps.

The results obtained with the third set of input parameters are shown in Figure 6-4. The crystal length is fixed to 17 mm and the pump beam diameter to 12 mm. Different values of the FELIX beam diameter (6 and 8 mm) are combined with two different values of the FELIX input energy (3-5 μJ).

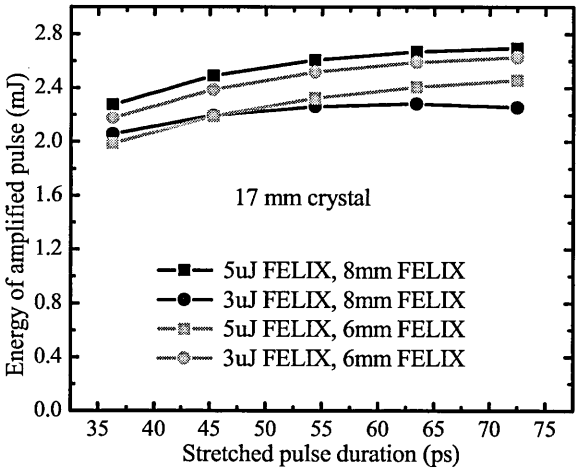

Figure 6-4 The output energy as a function of the stretched pulse duration for different values of the input energy of FELIX and different diameters. The pump beam diameter is 12 mm and the energy 80 mJ.

For a signal beam diameter of 8 mm, the output energy is not deeply saturated, and an increase of the signal input energy still leads to a higher energy of the amplified pulse. It can be noticed that, the maximum value of the amplified energy corresponds to pulse durations of about 60 ps.

For a 6 mm signal diameter, the pulse energy shows deep saturation (the value of the output energy for an input of 5 μJ is lower than the one corresponding to 3 μJ). Nevertheless, a larger signal beam diameter requires a larger aperture of the crystal. The interaction is non collinear and the refraction of the FELIX beam inside the crystal, as well as the incidence angle, requires a bigger size for the crystal aperture. Taking into account the spatial distortions in the beam profile of the output pulse, it is better to choose a smaller beam diameter for the FELIX beam (6 instead of 8 mm). As the calculations did not take into account the non collinear interaction of the pump and signal beams, a lower saturation is expected to take place.

6.2.3 Discussion

Simulations described in this section show that the optimal crystal length for a 6.25 μm wavelength of the signal beam is 17 mm, for an input energy of FELIX (3-5 μJ).

This estimation is valid assuming the values given for the optical properties of the crystal, and the energy of the amplified pulse is close to 2.5 mJ. For this crystal length, the simulations show deep saturation of output energy: the energy of the amplified pulse for 5 μJ input signal energy is less than the value corresponding

to 3 μJ input FELIX energy. Saturation of the pulse is convenient because, in the saturation regime, the energy stability of the amplified pulse is improved.

The optimum configuration of interaction is given by a pump diameter of 12 mm; this value is limited by the amount of energy necessary to get a high gain (80 mJ corresponding to a peak irradiance of 520 MW/cm^2) and by the damage threshold of the crystal. A thorough discussion of the AGS damage threshold, is given in Chapter 5, section 5.2.3. The damage threshold of other optical components is also important. In the experiment, the optical path of the pump beam is about 16 mm and its diameter can become small and causing, at energies of ~ 100 mJ, the damage of mirrors, waveplates, etc.

Concerning the diameter of the FELIX beam, this should be small compared to the pump diameter (so the pump can be considered to be top-hat compared to the signal intensity profile) in order to get a high gain for the signal beam; on the other hand; if the beam diameter is too small the saturation effect is strong and limits the amount of energy of the amplified pulse. The optimum value is around 6 mm, close to the measured value of the beam diameter at this wavelength (as presented in Chapter 8.

The results of simulations show that, for each crystal length and a given geometry of interaction, it correspond an optimum stretched pulse duration. For this pulse duration the maximum energy of the amplified pulse can be obtained. The pulse duration is limited by the saturation effect (in the lower limit) and by the pump pulse duration (in the upper one). For a 17 mm crystal length, the value of the stretched pulse duration can go close to the pump pulse duration. It means that the saturation effect is still stronger than the effect of the pump pulse duration. For a 72.5 ps pulse length the corresponding value of the displacement of the grating is 80 cm.

An alternative is to split the pump beam and use the first crystal (6.7 mm) as a preamplifier. The setup will still need an optical delay line in order to adjust the temporal overlap of the pre-amplified pulse and the corresponding pump beam in the second crystal. Another possibility is to use the transmitted pump beam through the first crystal in the second one. A possible difficulty is the instability of the pre-amplified pulse, in case the saturation is not reached, but this might be overcome by strong saturation in the second crystal, with properly choice for the beam diameters and pulse duration of the signal pulse.

The simulations were performed based on the previous experimental results. A new crystal might have slightly different optical characteristics, so the results are only an estimate. The value of d_{eff} was taken to be 9 pm/V. In literature there is a wide range for this parameter. Usually the value is higher, the one given in the SNLO code for collinear interaction is 11.7 pm/V, which makes a big difference for the parametric gain and for the overall efficiency. In the simulations the nonlinear effects were neglected, because the values of the nonlinear index and two-photon absorption coefficient for this crystal are not available. The pump beam peak irradiance was considered about 6 GW/cm^2. The damage threshold of the crystal is 3 GW/cm^2. In future experiments it might be possible to increase the pump irradiance, but for a long-term use, it is desirable to operate at a "safe" value in order not to initiate any damage on the crystal.

The spectral effects induced by parametric amplification on the output pulse were also neglected, and this might be the most important approximations. The procedure described in the beginning of the section 6.2 could not take into account such effects. The improved version of the SNLO code was used for describing such effects and their influence in section 6.3, showing the important influence on the output pulse duration and consequently on the output power of the amplified pulse.

For a long crystal, there are several effects that can reduce the parametric gain. Some of them, such as group velocity walk-off, can be taken into account by the code itself. From this point of view, collinear interaction can be not really the best choice. The bandwidth acceptance, which is directly related to the difference in the group velocities of the idler and signal beam, can be improved by properly choosing the degree of non-collinearity, but this might severely affect the good spatial overlap of the beams.

Other possible sources of errors (neglected in simulations) are the diffraction effects and assumption of collinear interaction. These effects, due to the low angular acceptance (less than 0.5 degrees/cm) can drastically reduce the gain. For longer crystal, the spatially overlap can become poor (depending on the angles and beam diameters). The poor spatial overlap can lead to distortion of the beam profile of the amplified pulse. Still, if one chose the parameters mentioned above, the spatial overlap of the two beams for a degree of non-collinearity (the angle between signal and pump inside the crystal) of less than 6 degrees is still good. This corresponds to a displacement of less than 2 mm at the exit of the crystal, in the transversal plane.

Consequently, the optimal crystal aperture is estimated to be 14x17 mm^2 and the length ~ 17 mm, the diameters of the beams 6 and 12 mm respectively, the signal pulse length about 72 ps. As seen from the plots, the pulse duration can vary in a quite wide range, without a significant influence on the output energy. These estimations are valid for a signal wavelength of 6.25 μm.

6.3 Simulations and experimental results. Amplified energy and amplification factor for the OPA and OPCPA experiments. Spectral and temporal changes in the amplified pulse

The second set of simulations was performed for checking the concordance of the experimental results with the predictions of the SNLO code. Excepting the section describing the influence of the crystal length, they were performed for the distinct situations of the 17-mm length and 16-mm length crystal (after recovering from damage).

The simulations allow a better understanding of the crystal properties (the influence of the nonlinear constant). They are useful for predicting the energy of the amplified pulse, but also from the side of the expected spectral and temporal pulse characteristics after amplification.

Only the behaviour of the signal pulse was investigated, because of its major interest in the experiments. The function of the code used for this set is 2DMIX-SP, which had been in the meantime upgraded by the author to include as input parameter the chirp of the pulse. This made possible a more flexible use of the code and did not require the artifice mentioned in the first part of this chapter. A typical set of input parameters for the 2DMIX_SP function is shown in Table 6-4. The nonlinear coefficient n_2 and the two-photon absorption coefficient β are not known.

The nonlinear constant can be estimated by using other functions of the code, as well as the refractive indices. The beam diameters, the pulse durations and the input pulse energy are determined experimentally.

	Signal	Idler	Pump
Wavelengths [nm]	5384.08	1326.05	1064
Index of refraction	2.39518	2.438	2.428443
Group velocity index	2.429687	2.494907	2.52601
Group velocity dispersion (cm/sec-cm^{-1})	5.89E4	-1.16E5	-1.57E5
Input face reflectivity	0.05	0.01	0.08
Output face reflectivity	0.05	0.01	0.08
Crystal absorption [1/mm]	.001	.001	.008
Pulse energy (J)	1.9E-5	0	7E-2
Pulse duration [ps]	2.459	3	85
Pulse delay relative to pump [ps]	0	0	
Pulse chirp (THz/ps)	0	0	0
Beam diameters [mm]	6	8	11
Walkoff angle [mrad]	-44	9.26	21.77
Radius of curvature [mm]	1.00E12	1.00E12	1.00E12
Number of t,x,y points	1024	32	32
Size of the crystal/grid [mm]	16	13	9
$D_{effective}$ [pm/V]	10.6		
Delta k [1/mm]	0		
z integration steps	100		

Table 6-4 Typical set of input parameters for the 2DMIX_SP function

A custom version of the code, available with the courtesy of its author, allows variable input parameters, and writes output files with the signal, pump and idler intensity distributions against frequency and time. The data make possible calculations of the output pulses energy, by integrating the intensity distributions. The data can be analysed and the FWHM of spectra and temporal distributions can be calculated.

The influence of several variable parameters on the energy, spectrum and temporal pulse shape of the amplified pulse is discussed. These parameters are of great interest for the parametric process, because they determine its efficiency, the spectral and temporal properties of the amplified pulse and they influence the wavelength selectivity and stability of the amplified pulse.

These factors can be grouped by considering the effects related to the laser sources (like wavelength, irradiance, beam diameter, pulse duration), effects related to the properties of the nonlinear medium (nonlinear constant, size, bandwidth acceptance) and effects generated by phase mismatch, pulse chirp and relative delay of the interacting pulses.

In the absence of the spatial or temporal chirp, and in the case of perfect temporal and spatial overlap, the pump and signal irradiances influence the spectral properties of the amplified pulse in a symmetric way. The chirp and phase mismatch can introduce asymmetry in the amplified spectrum. In the case of the stretched

pulses, the delay between the pump and signal sources perturbs the spectrum of the amplified pulse, shifting the central wavelength and distorting the spectrum.

The main parameters considered as input variables in simulations are the input pump/signal energy, signal wavelength, beam diameters and pulse durations. The relative delay between the pump and signal pulse, the initial signal chirp and the phase mismatch are later taken into account. The crystal length and nonlinear constant are also discussed. The values of the signal wavelength, signal and pump pulse duration, beam diameters were chosen to match their experimental values.

A special attention is given to saturation effects. The saturation and the parameters, which contribute to enhancing this effect, (the pump and signal irradiances (pump/signal energy, pulse durations and beam diameters), the crystal length, the nonlinear constant, the degree of noncollinearity and the signal wavelength) have been discussed in Chapter 3. The impact of saturation on the properties of the amplified pulse is highlighted for each parameter under consideration. The basis of choosing the variable parameters in simulations is given by the expression of the single pass gain, as described in Chapter 3:

$$\frac{I_s}{I_0} = G = 1 + \sinh^2(\Gamma_{eff} l)\left(1 + \left(\frac{\Delta k}{2\Gamma_{eff}}\right)^2\right) \text{(3-3)} \qquad \text{(6-9)}$$

$$\Gamma^2 = \frac{2deff^2}{n_p n_s n_i} \cdot \frac{2\omega_s \omega_i I_p}{\varepsilon_0 c^3} \text{ (3-4)} \qquad \text{(6-10)}$$

The nonlinear effect influences the spectrum of an input signal, unless the pump and signal propagate collinearly and have both top-hat intensity distributions (situation that is not practically encountered).

The influence is stronger with increasing chirp/phase mismatch and also depends on the pump pulse energy.

The dependence of the amplified energy and amplification factor on these parameters is not unitary. It can be noticed for example, that under strong saturation, the dependence of the amplified energy (or irradiance) on several parameters, which contribute in the non-saturated case to a sensitive increase in the parametric gain, is much weaker, or very different. Such effects, together with comparisons with experimental results, will be illustrated in the next sections.

6.3.1 The crystal length

The length of the nonlinear medium is an essential parameter for the optimisation of the gain and amplified energy. However, as it happens for most of the parameters of interest, the optimum crystal length is a function of other parameters, usually dictated by the specific conditions of the experiment. The main of those are the wavelengths involved in the interaction, the pulse durations (and bandwidths) and the crystal damage threshold. The beam irradiances can be adjusted in a large range, limited by damage threshold and saturation.

Table 6-5 shows the main set of parameters used for investigating the influence of the crystal length on the amplified energy of the signal pulse and on the spectral and temporal shapes. The simulations were performed for variable crystal length, while the other parameters are kept constant. The values chosen for the input parameters are correspond to the ones used in experiments. A pump energy of 60 mJ was chosen because this value was the typical used for measurements. The simulations are performed for a signal wavelength of 5.384 μm and three values of the input signal energy are considered: 1, 10 and 19 μJ.

	Signal	Idler	Pump
Wavelengths [nm]	5384.08	1326.05	1064
Index of refraction	2.39518	2.438587	2.428443
Group velocity index	2.429687	2.494907	2.52601
Group velocity dispersion (cm/sec-cm-^{1})	5.89E-4	-1.16E-5	-1.57E-5
Input face reflectivity	0.05	0.1	0.08
Output face reflectivity	0.1	0.1	0.08
Crystal absorption [1/mm]	.001	.003	.001
Pulse energy (J)	1.E-6	0	6E-2
Pulse duration [ps]	2.459	3	85
Pulse delay relative to pump [ps]	0	0	
Pulse chirp (THz/ps)	0	0	0
Beam diameters [mm]	6	8	11
Walkoff angle [mrad]	0	0	21.77
Radius of curvature [mm]	1.00E12	1.00E12	1.00E12
Number of t,x,y points	1024	32	32
Size of the crystal/grid [mm]	1-19	13	9
$D_{effective}$ [pm/V]	10.6		
Delta k [1/mm]	0		
z integration steps	100		

Table 6-5 The set of parameters for simulations performed for revealing the role of the crystal length. The crystal length is varied between 1 and 19 mm.

The results are presented in Figure 6-5 and Figure 6-6 and Figure 6-7 (a-d). The saturation of the amplified energy is apparent in Figure 6-5. This takes place at

about 15 mm for an input energy of 1 μJ and at shorter crystal lengths for 10 and 19 μJ respectively.

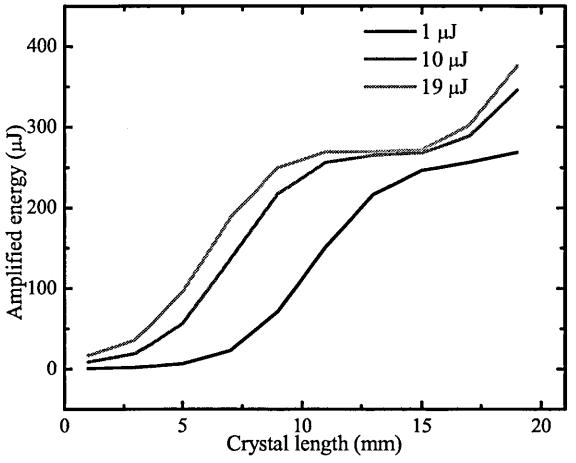

Figure 6-5 The dependence of the amplified energy on the crystal length for three different values of input signal energy, at 60 mJ pump energy. Saturation manifests at shorter crystal lengths for high input signal irradiance, and at longer crystal lengths for lower input signal irradiance

Figure 6-6 and Figure 6-7 (a)-(c) present the influence of the amplification process on the spectra and pulse shapes for the three input signal energies 1, 10 and 19 μJ, respectively. The spectral and temporal changes are much stronger for higher input signal energy and longer crystal lengths. For comparison, Figure 6-6 (d) and Figure 6-7 (d) present the spectra and pulse shape of the amplified signal for the extreme values considered in simulations for the crystal length: 1 mm and 19 mm and for the three input signal energies: 1, 10 and 19 μJ.

The plots show a strong influence of the crystal length on the spectral and temporal shapes of the amplified pulses; but this influence also depends on the input signal irradiance (at the same pump irradiance). It can be noticed that the first tendency of the spectra when increasing the crystal length is a slight narrowing, till 15 mm for 1 μJ input energy, and about 13 mm for the others. For longer lengths, the spectra are distorted and strong saturation takes place. The spectra remain symmetric, but under strong saturation the Gaussian shape is lost. The temporal shift of the amplified pulse depends on the crystal length, but also on the input signal energy.

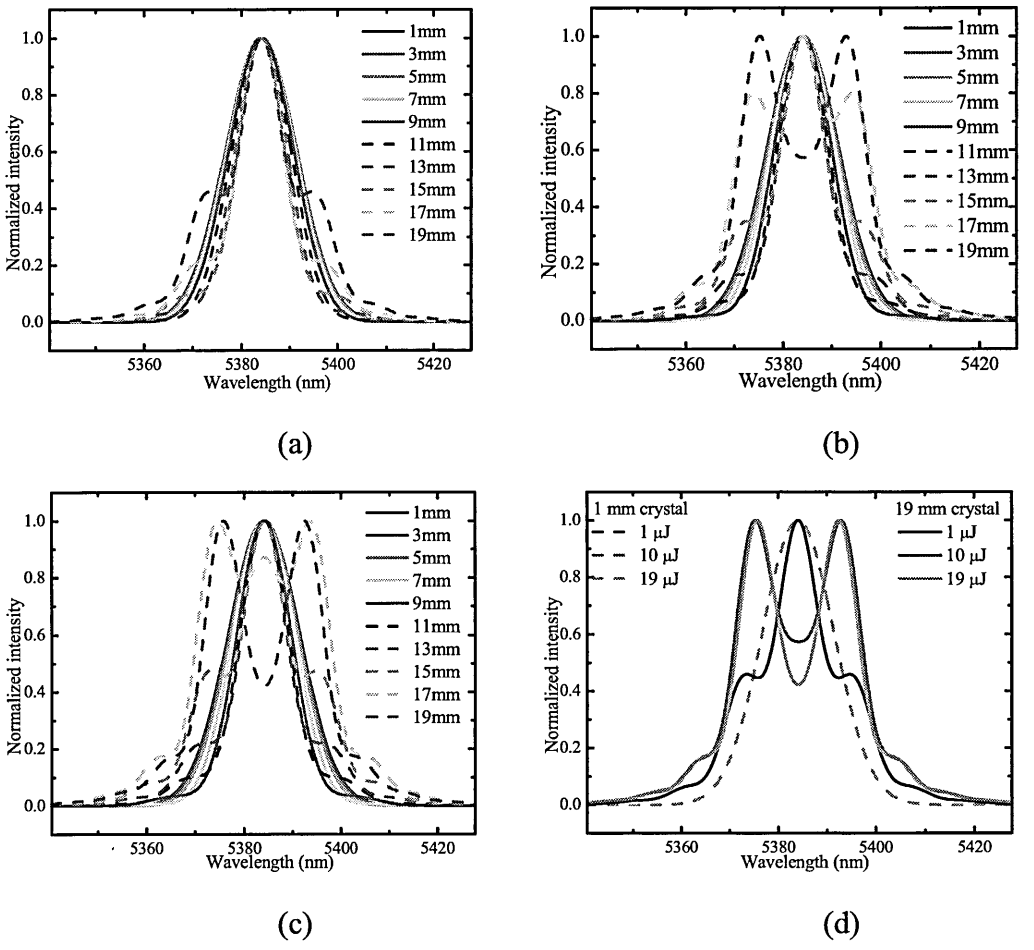

Figure 6-6 (a), (b), (c) Spectra of the amplified pulses as a function of crystal length (d) Comparison between spectra of the amplified pulses for 1 mm and 19 mm length, for three different signal input energies, 1, 10 and 19 μJ

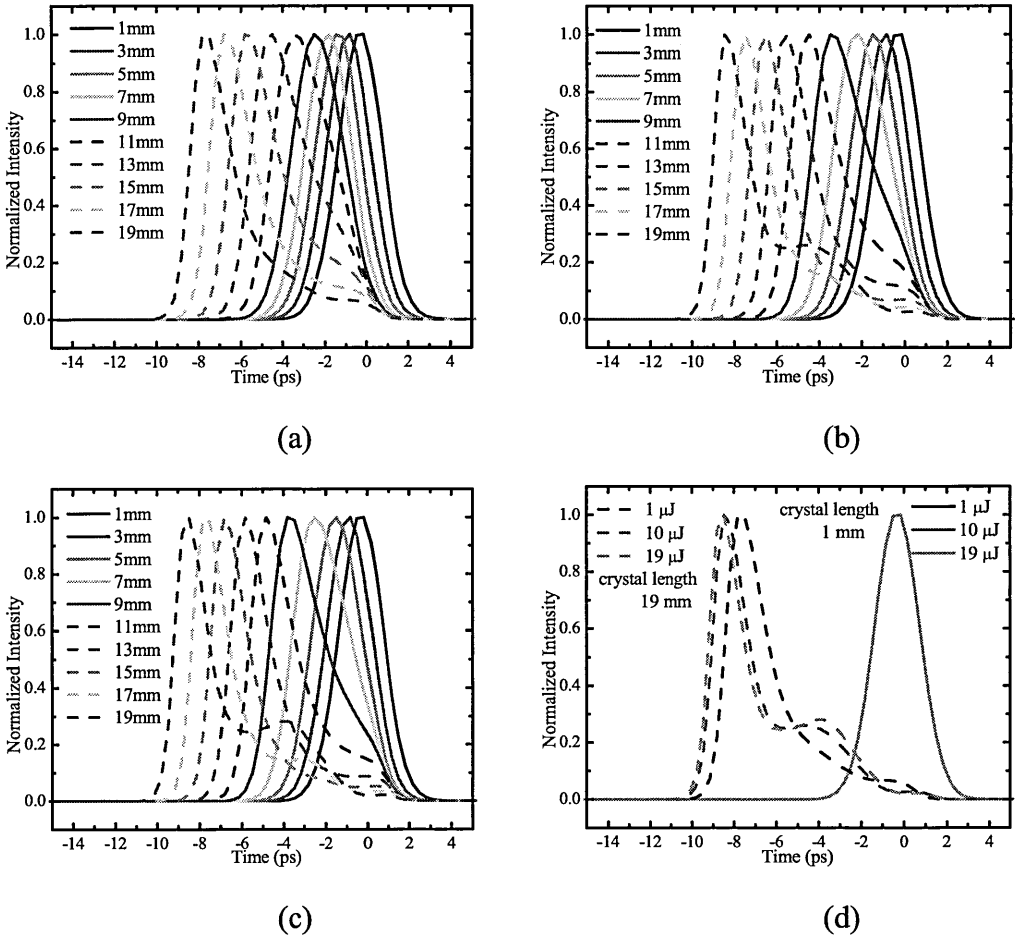

Figure 6-7 The temporal shape of the amplified pulse as a function of the crystal length for an input signal energy of (a) 1μJ, (b) 10 μJ and (c) 19 μJ - (d)-Comparison between the temporal shape of the amplified pulse for 1 mm and 19 mm length, for three different signal input energies, 1, 10 and 19 μJ.

The dependence on the amplified energy on the crystal length in the cases of parametric amplification and stretched-pulse amplification is useful from the point of view of experiments. A set of simulations is dedicated to the comparison of the un-stretched and stretched amplification for different crystal lengths. Table 6-6 presents the set of parameters used for this comparison. Two cases have been considered: input signal energy of 1 and 10 μJ respectively for a pulse length of 3.5 ps and the same for the pulse stretched to 35 ps (with un-stretched pulse duration of 3.5 ps, so that the initial pulse bandwidth is the same). The chirp of the amplified pulse was 0.0358 Thz/ps.

	Signal	Idler	Pump
Wavelengths [nm]	6310	1279.8	1064
Index of refraction	2.388	2.437	2.427
Group velocity index	2.434	2.504	2.527
Group velocity dispersion (cm/sec-cm-^{1})	-1.16E-5	-1.21E-5	-1.57E-5
Input face reflectivity	0.05	0.1	0.018
Output face reflectivity	0.1	0.1	0.018
Crystal absorption [1/mm]	.001	.003	.001
Pulse energy (J)	10.E-6	0	6E-2
Pulse duration [ps]	3.5	3	85
Pulse delay relative to pump [ps]	0	0	
Pulse chirp (THz/ps)	0	0	0
Beam diameters [mm]	5	6	11
Walkoff angle [mrad]	0	0	21.76
Radius of curvature [mm]	1.00E12	1.00E12	1.00E12
Number of t,x,y points	1024	32	32
Size of the crystal/grid [mm]	1-19	13	9
$D_{effective}$ [pm/V]	10.6		
Delta k [1/mm]	0		
z integration steps	200		

Table 6-6 Set of parameters used in comparing the dependence of the energy, spectral and temporal shape of the amplified pulse for parametric amplification and chirped-pulse parametric amplification

The results of the simulations are shown in Figure 6-8-Figure 6-10.

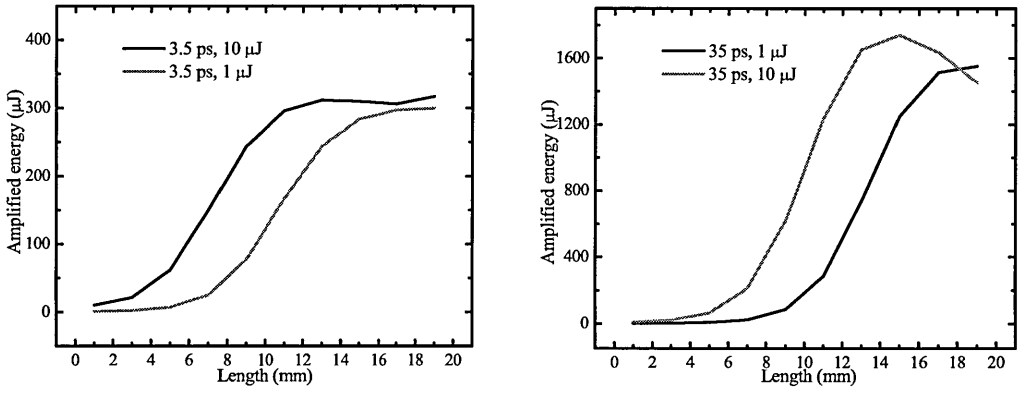

(a) (b)

Figure 6-8 The amplified energy as a function of the crystal length for the un-stretched parametric amplification (a) and for the stretched parametric amplification (b), for 1 and 10 μJ input signal energy and the other parameters shown in Table 6-6. The saturation develops faster for the un-stretched pulse, and at higher input signal energy. The maximum amplified energy differs is ~ 1.6 mJ for the stretched pulse amplification and only ~ 300 μJ for the un-stretched amplification

Figure 6-8 presents a comparison between the dependences of the energy of the amplified pulses in the cases of (a) un-stretched and (b) stretched input signal pulses. According to the results, for typical input signal energies of few microjoules, the maximum energy obtainable by un-stretched amplification is limited to 300 μJ, while the stretched amplification leads to values of more than 1600 μJ. Because

saturation manifests at crystal lengths ~ 14 mm, for input energy of 10 μJ, further increase of stretching can result in higher amplified pulse energy. A longer crystal length is useful for lower input signal energies; if high energies are available, the increase in the crystal length is not useful in terms of amplified energy. The only way to make advantage from long crystal length is to decrease the signal irradiance by enlarging the beam diameter or lengthening the pulse.

Figure 6-9 and Figure 6-10 put together the results of spectra and temporal shapes, for the extreme cases: the shortest and longest lengths considered by simulations, for the un-stretched and stretched pulse durations.

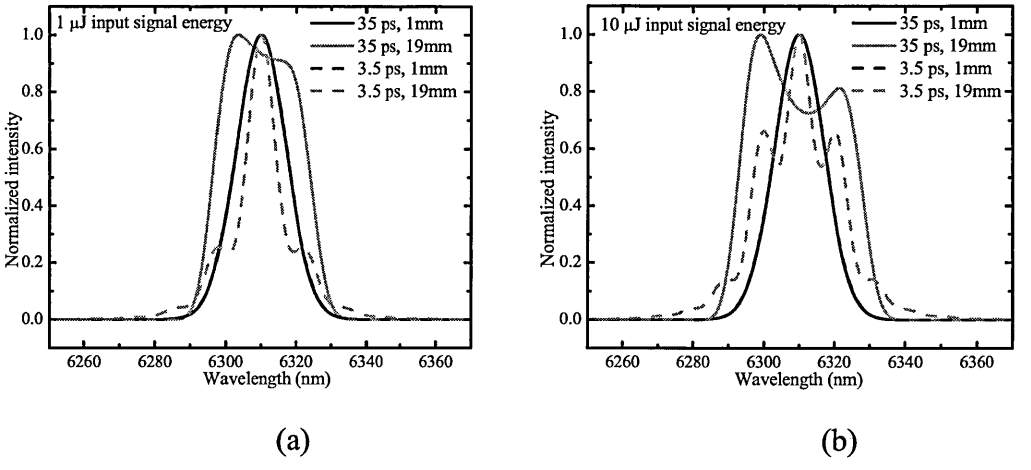

(a) (b)

Figure 6-9 The spectral changes for 1 mm crystal length (black lines) and for 19 mm crystal length (grey lines) for 1 μJ (a) and 10 μJ input signal energy (b), for 35 ps (straight lines) and 3.5 signal pulse duration (dashed lines). The higher input signal energy results in stronger distortions of the amplified pulse.

In Figure 6-9 (a) and Figure 6-10 (a) the results for 1 μJ input signal energy are plotted, while Figure 6-9 (b) and Figure 6-10 (b) present the results for 10 μJ input signal energy.

For 1 mm crystal length, there is no visible difference between the results for two different input signal energies. For the maximum crystal length (19 mm), due to saturation, both spectra of the amplified and stretched-amplified pulses are distorted. The differences in the way this happens are due to the temporal wavelength distribution present in the input chirped pulse spectrum. The distortions of the (initially) un-chirped pulse are symmetric, while for the stretched pulse, the distortions are asymmetric. The asymmetry is due to saturation and wavelength distribution in the chirped pulse.

The plots in Figure 6-10 (a) and (b) show the saturation effect starting to develop for the stretched-amplified pulses at 1 μJ input energy and 19 mm crystal length, and deep saturation at 19 mm crystal length and 10 μJ input energy. For the un-stretched pulse, the developing of the second pulse manifests for both input signal energies.

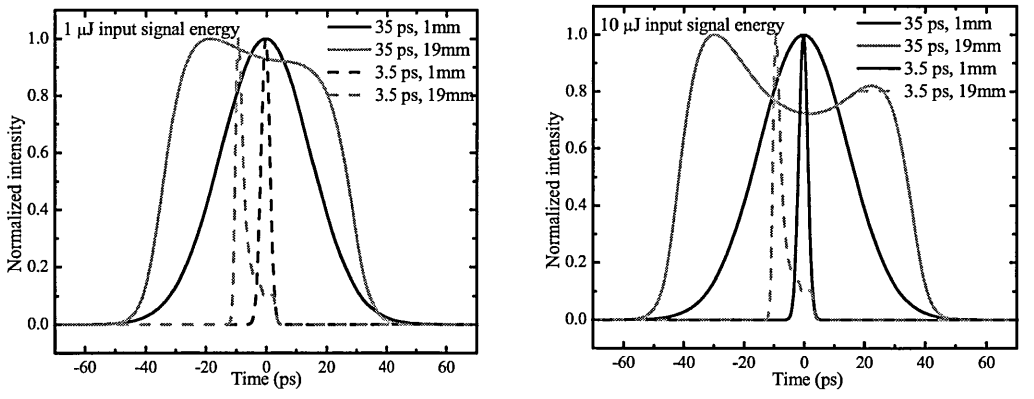

(a) (b)

Figure 6-10 The temporal changes for 1 mm crystal length (black lines) and for 19 mm crystal length (grey lines) for 1 μJ (a) and 10 μJ input signal energy (b), for 35 ps (straight lines) and 3.5 signal pulse duration (dashed lines). The 10 μJ input signal energy results in more important temporal changes compared to the 1 μJ input signal energy.

The behaviour of un-stretched amplification in the three figures show the limitations imposed by the short pulse duration on the output power, and the comparison with the features of the stretched- amplification shows the possibility of improved output power with a proper choice of the input parameters, and of the crystal length. A crystal length of 17 mm and input energies of few microjoules, can result, for stretched pulse durations and 60 mJ pump energy in more than 1.6 mJ of amplified energy. Adjusting back the pulse duration to few picoseconds restores the high peak power.

6.3.2 The value of the nonlinear constant

Another important parameter of the crystal is the nonlinear constant. In Chapter 2 has been explained the importance of the value of the effective nonlinear constant, which is not an intrinsic value, but depends on the orientation of the crystal and on the wavelengths involved in interaction. The set of parameters used in simulations for illustrating the importance of the nonlinear constant and some aspects related to its influence is shown in Table 6-7.

	Signal	Idler	Pump
Wavelengths [nm]	5384.08	1326.05	1064
Index of refraction	2.39518	2.438587	2.428443
Group velocity index	2.429687	2.494907	2.52601
Group velocity dispersion (cm/sec-cm-^{1})	5.89E4	-1.16E5	-1.57E5
Input face reflectivity	0.05	0.1	0.08
Output face reflectivity	0.1	0.1	0.08
Crystal absorption [1/mm]	.001	.003	.001
Pulse energy (J)	1.9E-10	0	7E-2
Pulse duration [ps]	2.459	3	85
Pulse delay relative to pump [ps]	0	0	
Pulse chirp (THz/ps)	0	0	0
Beam diameters [mm]	6	8	11
Walkoff angle [mrad]	-44	9.26	21.77
Radius of curvature [mm]	1.00E12	1.00E12	1.00E12
Number of t,x,y points	1024	32	32
Size of the crystal/grid [mm]	16	13	9
$D_{effective}$ [pm/V]	6-12		
Delta k [1/mm]	0		
z integration steps	100		

Table 6-7The set of parameters for simulations performed for investigating the influence of the nonlinear constant. Two situations were considered: low input signal energy (0.00019 μJ) and high input signal energy (10 μJ)

Figure 6-11 presents the results of the simulations performed with varying the nonlinear constant value in a wide range (6-12 pm/V). Two different situations were considered: low input signal energy (0.00019 μJ) and high input signal energy (10 μJ). These two values correspond to a non-saturated and to the saturated regimes, respectively. The plots related to the non-saturated regime reveal the sensitive dependence of the parametric gain and amplified energy at low signal intensity.

The situation is different for the saturated regime. In this case the value of the amplified energy (Figure 6-11 (b)) varies slightly with the nonlinear constant, while the amplification factor is correspondingly almost constant.

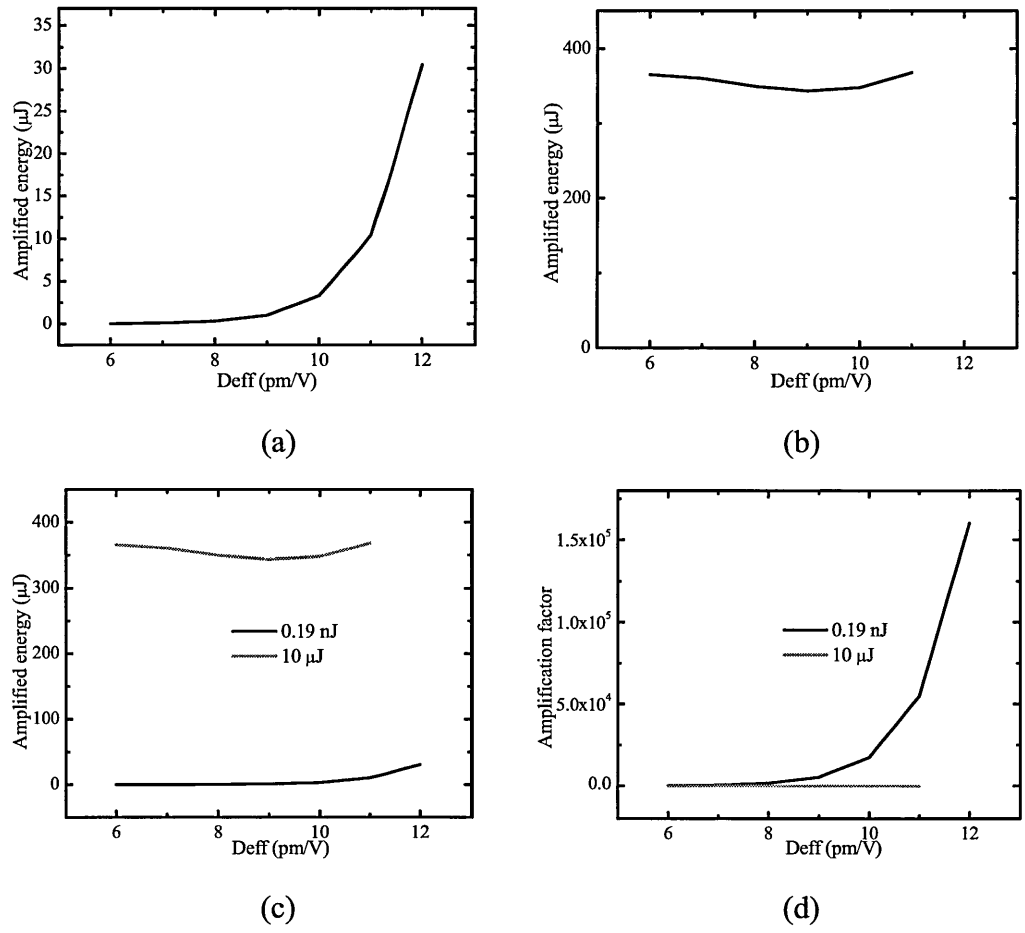

Figure 6-11 (a) The amplified energy as a function of d_{eff} at 0.19 nJ; (b) The amplified energy as a function of d_{eff} at 10 μJ; (c) Comparison between the two plots presented at (a) and (b); (d) The amplification factor for the two situations presented at (a) and (b)

Regarding spectra and temporal shapes of the amplified pulse, for low input signal energy, shown in Figure 6-12, one can notice show significant changes.

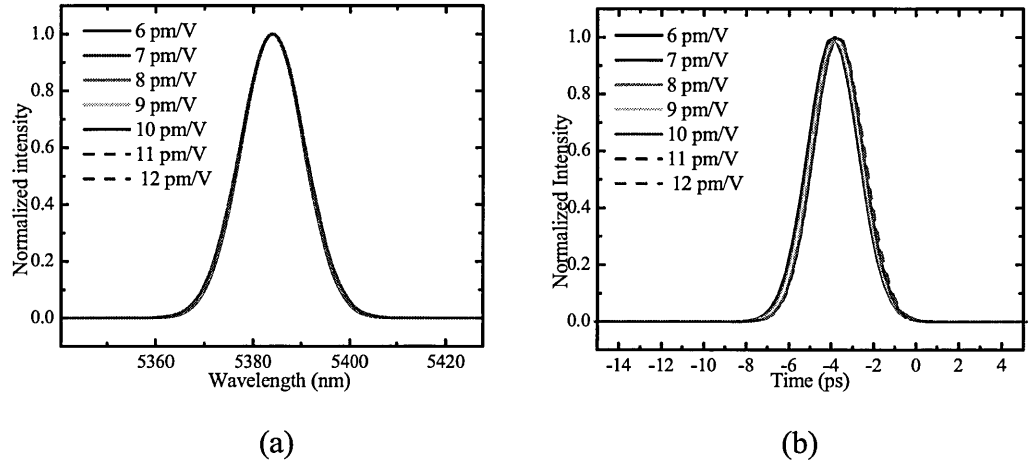

Figure 6-12 The influence of the nonlinear constant on the spectrum (a) and temporal shape (b) of the amplified pulse at high pump energy (70 mJ) and low input signal energy (0.19 nJ). The corresponding values of the nonlinear constant are shown in the plots.

Figure 6-13 (a) and (b) show a different situation, corresponding to the input signal energy of 10 μJ. The modifications of the spectra (and of associated temporal shapes) are caused by saturation effects. Besides the distortions and double pulse formation, one can notice also the temporal shift of the amplified pulse, increasing with the value of *deff*. Figure 6-13 (b) shows the amplified pulse early by a few picoseconds compared with the nonsaturated regime.

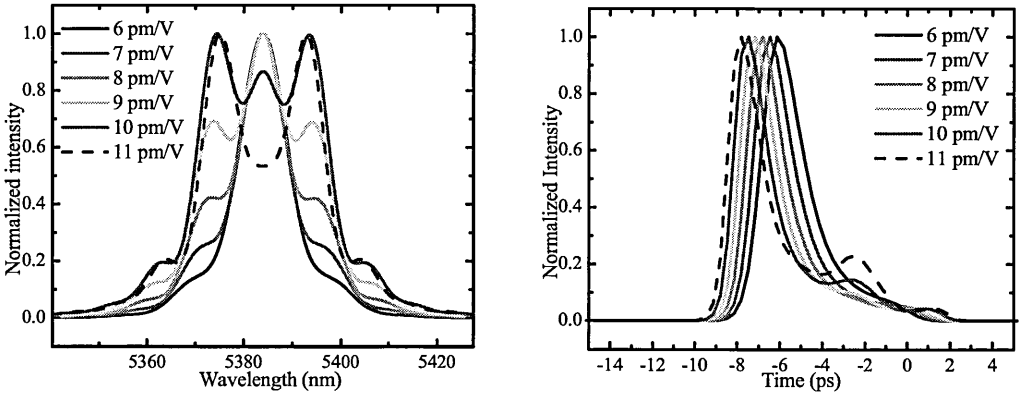

(a) (b)

Figure 6-13 The influence of the nonlinear constant on the spectrum (a) and temporal shape (b) of the amplified pulse at high pump energy and high input signal energy (10 μJ), for different values of the nonlinear constant.

The major differences between the two regimes illustrate the difficulty of estimating the correct value of the nonlinear constant. Using Eq. (6-10) as expression of the parametric gain, besides the assumption of no spatial and diffraction effects, can lead to large errors for the saturated regime. This explains the wide range of the values obtained in literature for the nonlinear constant [2]. For a correct estimation several factors have to be taken into account: precise evaluation of the beam irradiances, and verifying the correspondence between the approximations and assumptions of the model used for determining the nonlinear constant.

6.3.3 The influence of the pump irradiance

The pump irradiance is a fundamental parameter for the efficiency of the parametric amplification process as shown by Eq. (6-10)). This is because, in the parametric process, the pump pulse energy is redirected to the signal and idler pulses. For an efficient parametric transfer, the pump irradiance has to be high, at the limit of the damage threshold of the crystal. However, to maximize efficiency, one should also optimise the crystal length. The limits for the crystal length are the

bandwidth limit (estimated also from the approximations given by Eqs. (6-9) and (6-10)) and explained in Chapter 3), and the available crystal length.

Table 6-8 (a) presents the input parameters and results of simulations performed at a signal wavelength of 5.384 μm and 2.6 μJ input energy. The parameters used in simulations were chosen close to the ones determined experimentally, excepting the pump beam diameter.

	Signal	Idler	Pump
Wavelengths [nm]	5384.08	1326.05	1064
Index of refraction	2.39518	2.438587	2.428443
Group velocity index	2.429687	2.494907	2.52601
Group velocity dispersion (cm/sec-cm-^{1})	5.89E4	-1.16E5	-1.57E5
Input face reflectivity	0.0	0.1	0
Output face reflectivity	0	0.1	0
Crystal absorption [1/mm]	.001	.0	.001
Pulse energy (J)	2.6E-6	0	8E-2
Pulse duration [ps]	2.459	3	85
Pulse delay relative to pump [ps]	0	0	
Pulse chirp (THz/ps)	0	0	0
Beam diameters [mm]	4	8	6
Walkoff angle [mrad]	-44	9.26	21.77
Radius of curvature [mm]	1.00E12	1.00E12	1.00E12
Number of t,x,y points	1024	32	32
Size of the crystal/grid [mm]	16	13	9
$D_{effective}$ [pm/V]	14		
Delta k [1/mm]	0		
z integration steps	50		

Table 6-8 The set of input parameters for simulations at 5.384 μ, for simulations in Figure 6-14

In Figure 6-14 (a) the plots obtained as results of simulations and the experimental results are compared. The comparison with experimental results does not show a good agreement, because the simulations cannot explain the high values of the energy obtained in the amplification process. For the pump pulse, the parameters in simulations were changed to lower input diameter (6 mm FWHM) and higher pump energy (80 mJ), but even with increased pump irradiance, the results show lower amplified energies. The change aimed to see if the increased pump irradiance can explain the higher values of the amplified pulse energy, but even with much smaller beam diameter (6 mm compared to 11 mm determined experimentally), the experimental data could not be fitted.

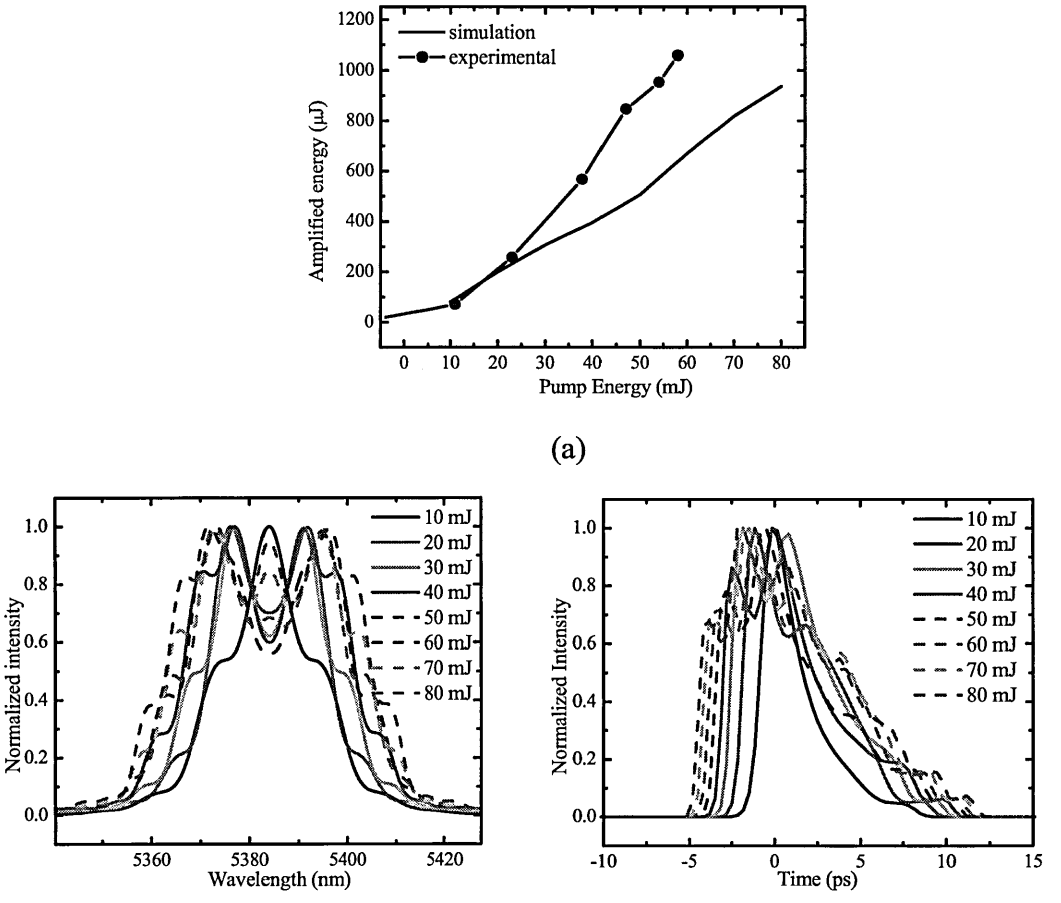

Figure 6-14 Simulations at 5.384 μm (a) The dependence of the amplified energy on the pump energy Comparison with experimental results (b) The modifications of the spectra with the pump energy (c) The modification of the temporal shape with the pump energy The results of simulations do not fit very well with experimental results, even in the simulations the pump irradiance was increased in comparison with the experimental values

The simulations show strong distortions in the amplified pulse, as appearing in Figure 6-14 (b) and (c).

The influence of pump beam diameter is presented in Figure 6-15. The simulations take into account an initial high energy of the signal (19 μJ) and high pump energy (~70 mJ). The set of input parameters are contained in Table 6-9.

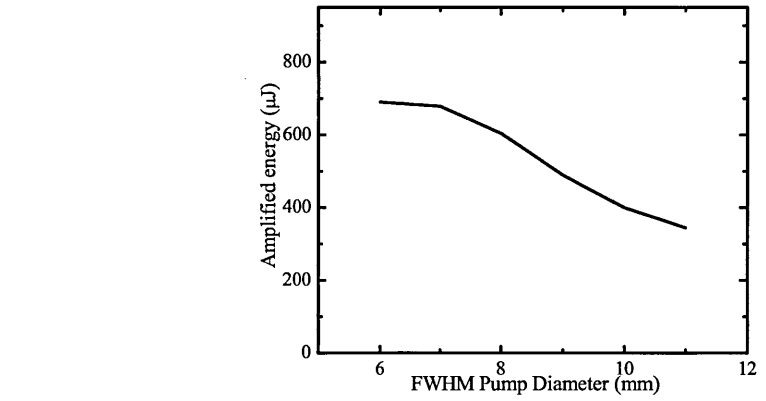

(a)

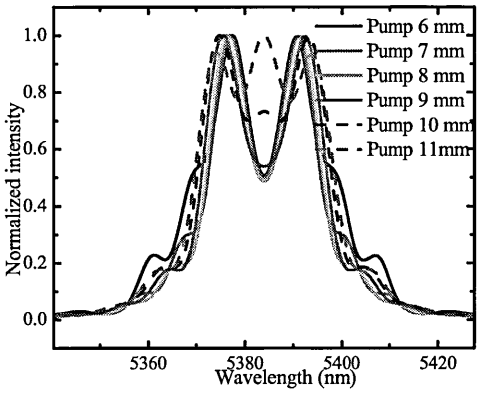

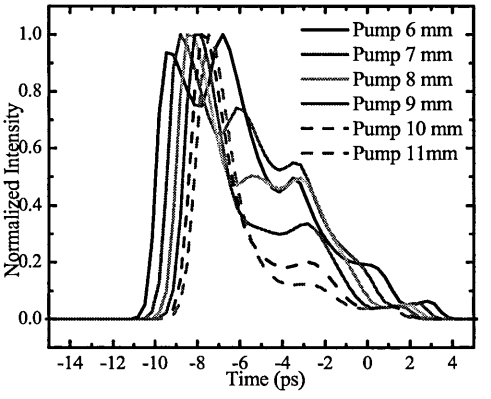

(b) (c)

Figure 6-15 The set of parameters (a), the amplified energy (b), spectra (c) and temporal shapes (d) for different pump beam diameters at 5.384 μm. The maximum amplified energies are obtained at shorter pump diameters, but the increased irradiances are much above the damage threshold. The increase in energy is accompanied by strong pulse distortions.

Figure 6-15 (a) shows the dependence of the amplified pulse energy on the pump beam diameter. The maximum amplified energy is obtained for smaller beam diameter, which is explained by the much higher irradiance in this case. However, as shown in Figure 6-15 (b) and (c), this is accompanied by strong modifications of the spectral and temporal shapes.

	Signal	Idler	Pump
Wavelengths [nm]	5384.08	1326.05	1064
Index of refraction	2.39518	2.438587	2.428443
Group velocity index	2.429687	2.494907	2.52601
Group velocity dispersion (cm/sec-cm-^{1})	5.89E4	-1.16E5	-1.57E5
Input face reflectivity	0.05	0.1	0.08
Output face reflectivity	0.1	0.1	0.08
Crystal absorption [1/mm]	.001	.006	.001
Pulse energy (J)	1.9E-5	0	7E-2
Pulse duration [ps]	2.459	3	85
Pulse delay relative to pump [ps]	0	0	
Pulse chirp (THz/ps)	0	0	0
Beam diameters [mm]	6	8	11
Walkoff angle [mrad]	-44	9.26	21.77
Radius of curvature [mm]	1.00E12	1.00E12	1.00E12
Number of t,x,y points	1024	32	32
Size of the crystal/grid [mm]	16	13	9
$D_{effective}$ [pm/V]	10.6		
Delta k [1/mm]	0		
z integration steps	100		

Table 6-9 Set of parameters used by simulations for characterizing the influence of the pump diameter

Next, Table 6-10 presents the input parameters used in simulations for fitting the experimental results obtained at 6.31 μm signal wavelength and input energy of 10 μJ and pulse duration is 3.5 ps. The pump diameter is taken to be 11 mm, and crystal length of 17 mm.

	Signal	Idler	Pump
Wavelengths [nm]	6310	1279.8	1064
Index of refraction	2.388	2.437	2.427
Group velocity index	2.434	2.504	2.527
Group velocity dispersion (cm/sec-cm-^{1})	-1.16E-5	-1.21E-5	-1.57E-5
Input face reflectivity	0.05	0.1	0.02
Output face reflectivity	0.1	0.1	0.02
Crystal absorption [1/mm]	.001	.003	.001
Pulse energy (J)	10.E-6	0	7E-2
Pulse duration [ps]	3.5	3	85
Pulse delay relative to pump [ps]	0	0	
Pulse chirp (THz/ps)	0	0	0
Beam diameters [mm]	6	8	11
Walkoff angle [mrad]	20.9	4.1	21.76
Radius of curvature [mm]	1.00E12	1.00E12	1.00E12
Number of t,x,y points	1024	32	32
Size of the crystal/grid [mm]	17	13	9
$D_{effective}$ [pm/V]	10.6		
Delta k [1/mm]	0		
z integration steps	200		

Table 6-10 The set of input parameters for simulations in Figure 6-16, at 6.31 μm signal wavelength

Figure 6-16 (a) shows the comparison between the experimental results and simulations for the energy of the amplified pulse.

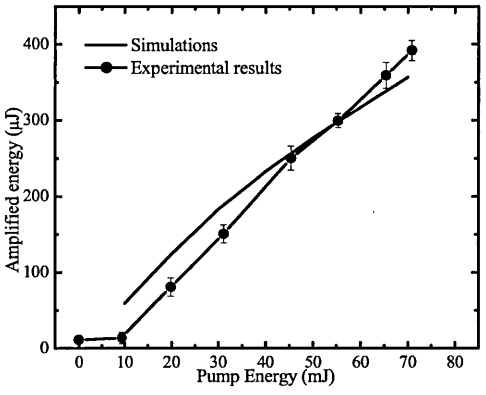

(a)

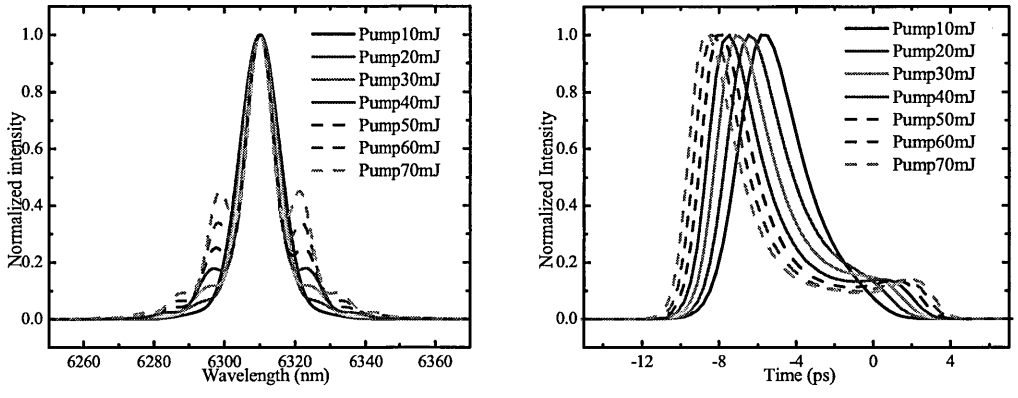

(b) (c)

Figure 6-16 Simulations at 6.31 μm (a) (b) The dependence of the amplified energy on the pump energy Comparison with experimental results (c) The modifications of the spectra with the pump energy (d) The modification of the temporal shape with the pump energy. The results show a rather good agreement with the experimental ones.

The energy of the amplified pulse obtained by simulations show a rather good agreement with the experimental results. For lower pump energies, the values predicted by simulations are higher than the ones obtained experimentally, while at higher pump energies (higher than 50 mJ), the situation reverses. This shows that the gain is higher at lower pump wavelengths and saturates faster, so the experimental situation looks less "saturated" than the one shown by simulations.

Similar conclusions regarding the comparison between simulation and experimental results can be drawn from Figure 6-17. Table 6-11 presents the set of input parameters used for these simulations. Here the chirped-pulse amplification is considered, for a pulse duration of ~35 ps, stretched from an initial pulse duration of 3.5 ps, at the signal wavelength of 6.31 μm.

The experimental results in panel (a), and in (b) and (c) the spectra and temporal shapes, for different pump energies, are plotted. One can notice the spectral/temporal broadening with increasing pump energy, and an apparent shift of the central wavelength.

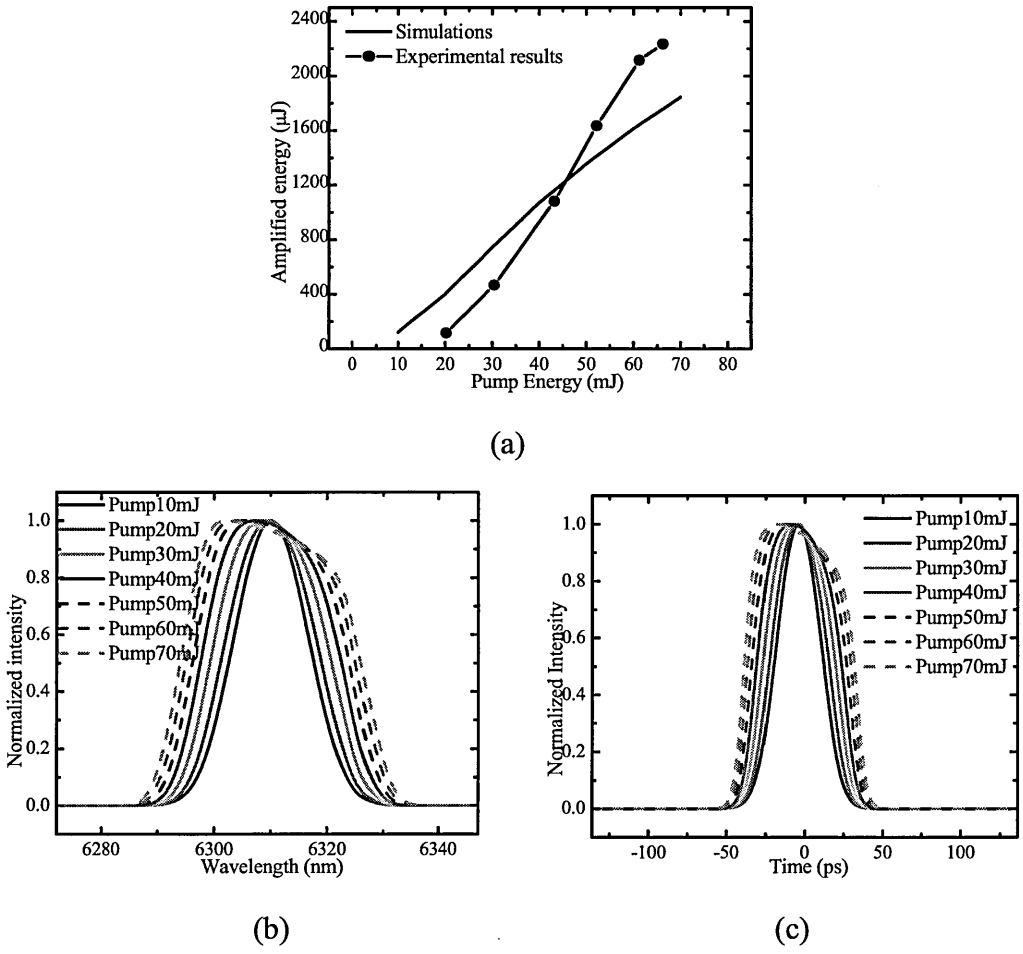

Figure 6-17 Simulations at 6.31 μm (a) The dependence of the amplified energy on the pump energy (b) The modifications of the spectra with the pump energy (c) The modification of the temporal shape with the pump energy

	Signal	Idler	Pump
Wavelengths [nm]	6310	1279.8	1064
Index of refraction	2.388	2.437	2.427
Group velocity index	2.434	2.504	2.527
Group velocity dispersion (cm/sec-cm-^{1})	-1.16E-5	-1.21E-5	-1.57E-5
Input face reflectivity	0.05	0.1	0.02
Output face reflectivity	0.1	0.1	0.02
Crystal absorption [1/mm]	0.001	.003	.001
Pulse energy (J)	10.E-6	0	7E-2
Pulse duration [ps]	35.08008	16	85
Pulse delay relative to pump [ps]	0	0	
Pulse chirp (THz/ps)	0.00358	0	0
Beam diameters [mm]	5	6	11
Walkoff angle [mrad]	0	0	21.76
Radius of curvature [mm]	1.00E12	1.00E12	1.00E12
Number of t,x,y points	1024	32	32
Size of the crystal/grid [mm]	17	20	20
$D_{effective}$ [pm/V]	10.6		
Delta k [1/mm]	0		
z integration steps	100		

Table 6-11 The set of input parameters for simulations presented in Figure 6-17 (a)-(c)

The simulations presented in Figure 6-18 and Figure 6-19 aim to fit the experimental results at signal wavelengths of 8.8 μm and 9.98 μm. The input parameters are listed in Table 6-12 and Table 6-13.

	Signal	Idler	Pump
Wavelengths [nm]	8800	1210.3	1064
Index of refraction	2.368	2.443	2.434
Group velocity index	2.453	2.516	2.531
Group velocity dispersion (cm/sec-cm-^{1})	3.66E5	-1.29E5	-1.56E5
Input face reflectivity	0.1	0.1	0.08
Output face reflectivity	0.1	0.1	0.08
Crystal absorption [1/mm]	.03	.001	.001
Pulse energy (J)	2.4E-6	0	8E-2
Pulse duration [ps]	4	3	85
Pulse delay relative to pump [ps]	0	0	
Pulse chirp (THz/ps)	0	0	0
Beam diameters [mm]	9	8	11
Walkoff angle [mrad]	0	0	21.77
Radius of curvature [mm]	1.00E12	1.00E12	1.00E12
Number of t,x,y points	1024	32	32
Size of the crystal/grid [mm]	17	13	9
$D_{effective}$ [pm/V]	9.86		
Delta k [1/mm]	0		
z integration steps	100		

Table 6-12 The set of input parameters for simulations in Figure 6-18

	Signal	Idler	Pump
Wavelengths [nm]	9980	1191	1064
Index of refraction	2.355	2.518	2.433
Group velocity index	2.464	2.518	2.53
Group velocity dispersion (cm/sec-cm-^{1})	5.47E4	-1.31E5	-1.55E5
Input face reflectivity	0.15	0.1	0.02
Output face reflectivity	0.15	0.1	0.02
Crystal absorption [1/mm]	.006	.006	.001
Pulse energy (J)	2.5E-5	0	7E-2
Pulse duration [ps]	6	3	85
Pulse delay relative to pump [ps]	0	0	
Pulse chirp (THz/ps)	0	0	0
Beam diameters [mm]	9	8	12
Walkoff angle [mrad]	0	0	0
Radius of curvature [mm]	1.00E12	1.00E12	1.00E12
Number of t,x,y points	1024	32	32
Size of the crystal/grid [mm]	16	13	9
$D_{effective}$ [pm/V]	8.5		
Delta k [1/mm]	0		
z integration steps	100		

Table 6-13 The set of input parameters for simulations presented in Figure 6-19

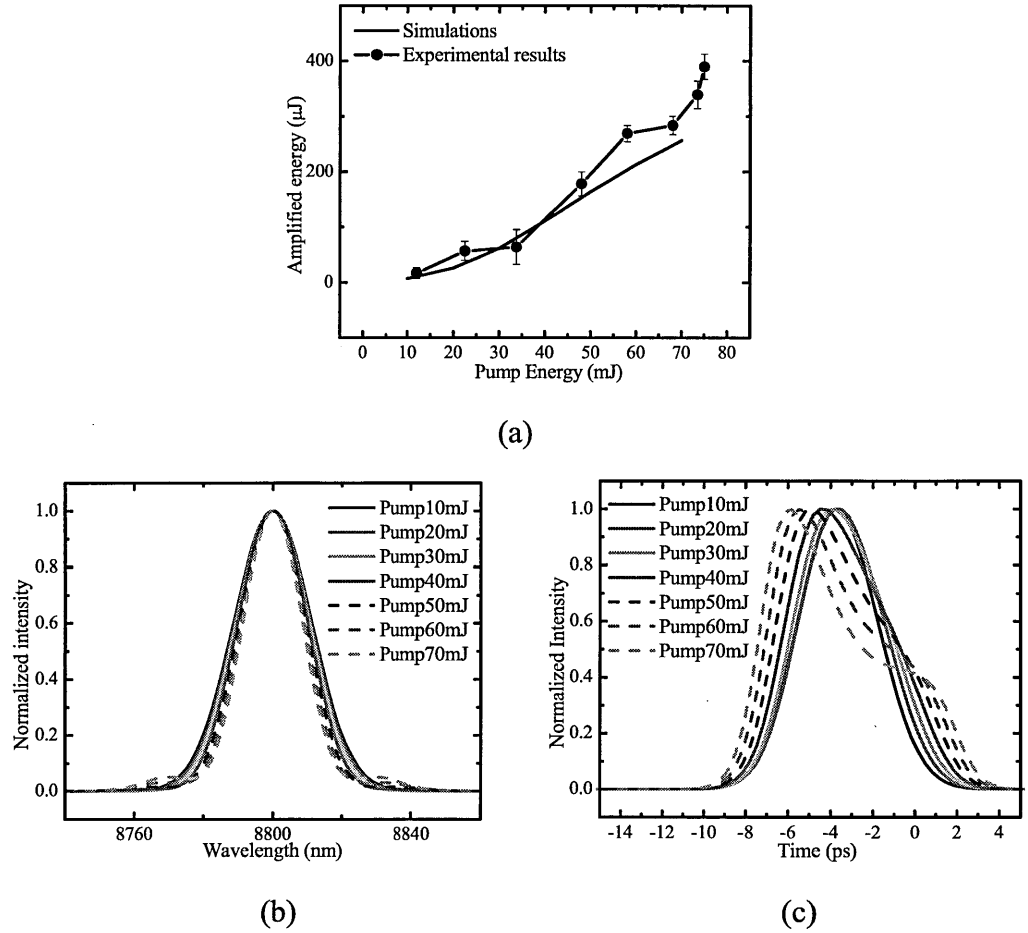

Figure 6-18 Simulations at 8.8 μm and 17 mm crystal length (a The dependence of the amplified energy on the pump energy Comparison with experimental results (b) The modifications of the spectra with the pump energy (c) The modification of the temporal shape with the pump energy

In Figure 6-19 (b), together with the spectra of the amplified pulses for different input pump energies, the measured input spectrum of the signal pulse is plotted.

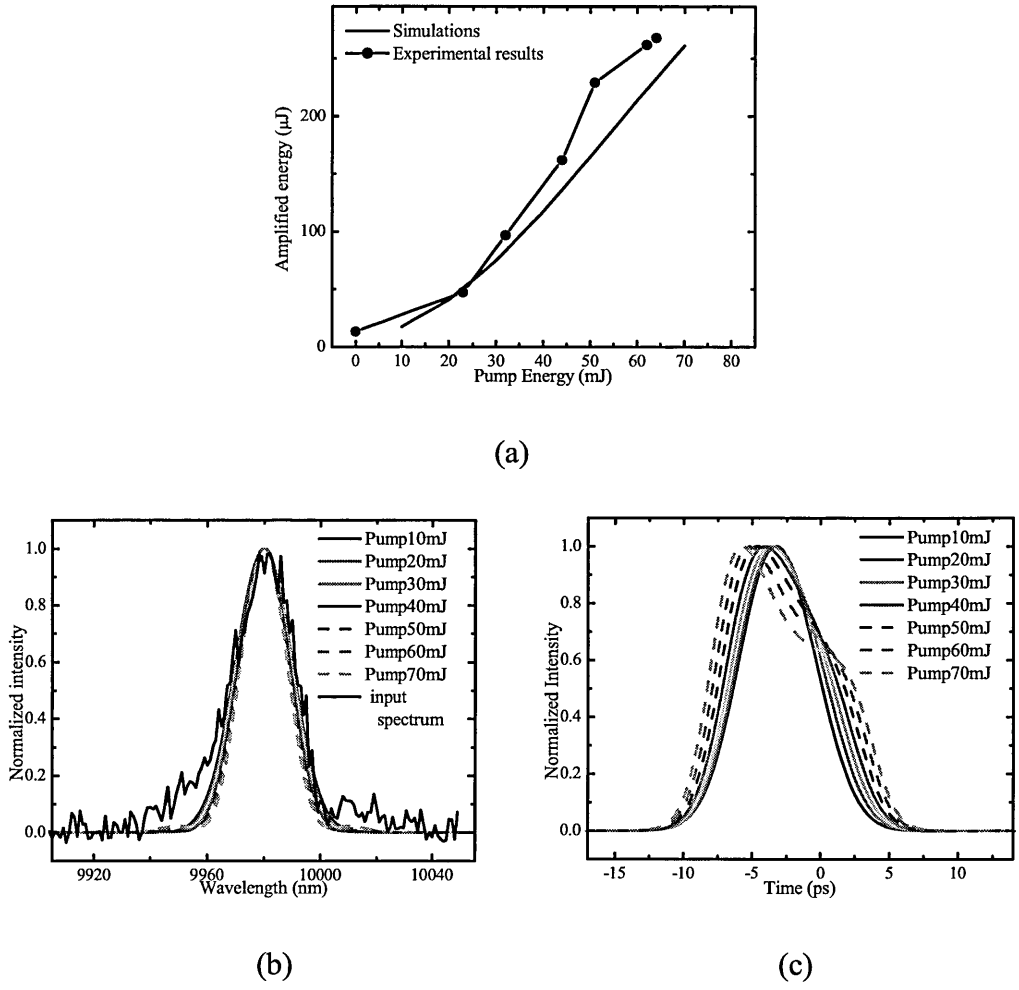

Figure 6-19 Simulations at 9.98 μm (a) The dependence of the amplified energy on the pump energy Comparison with experimental results (b) The modifications of the spectra with the pump energy together with the input pulse spectrum (c) The modification of the temporal shape with the pump energy

When comparing with shorter signal wavelengths, a common feature of the simulation results illustrated in Figure 6-18 and Figure 6-19 is the better fit with experimental results for the dependence of the amplified pulse energy on the pump pulse energy. A weaker influence on the spectra of the amplified pulse can be noticed in Figure 6-18 (b) and Figure 6-19 (b). This is probably due to the lower value of the nonlinear constant at longer wavelengths, which decrease the saturation level and thus the influence of the amplification process on the spectral and temporal characteristic of the amplified pulse.

6.3.4 The influence of the signal irradiance

Three factors can influence the signal irradiance: the signal beam diameter, the pulse energy and the pulse durations. In experiments, the pump pulse duration is not deliberately changed, but the signal pulse duration can be adjusted to optimise the output power. As mentioned in Chapter 4, which is dedicated to the laser sources used in the experiments, the pulse duration of the FEL pulse (the signal) can be adjusted, together with its bandwidth. Chapter 8 describes the means for stretching the signal pulse duration, but in this case, ideally, the bandwidth is not changed.

In this section the three factors are considered as variable parameters for simulations: pulse duration, input energy, and beam diameters. The basic set of parameters is shown in Table 6-14. The pulse durations and frequency chirps used in the simulations with variable input signal energy listed in Table 6-15.

	Signal	Idler	Pump
Wavelengths [nm]	6310	1279.8	1064
Index of refraction	2.388	2.437	2.427
Group velocity index	2.434	2.504	2.527
Group velocity dispersion (cm/sec-cm-^{1})	-1.16E-5	-1.21E-5	-1.57E-5
Input face reflectivity	0.05	0.1	0.02
Output face reflectivity	0.1	0.1	0.02
Crystal absorption [1/mm]	.001	.006	.001
Pulse energy (J)	9.001E-6	0	6E-2
Pulse duration [ps]	3.5	3	85
Pulse delay relative to pump [ps]	0	0	
Pulse chirp (THz/ps)	0	0	0
Beam diameters [mm]	6	8	12
Walkoff angle [mrad]	20.9	4.1	21.76
Radius of curvature [mm]	1.00E12	1.00E12	1.00E12
Number of t,x,y points	1024	32	32
Size of the crystal/grid [mm]	16	13	9
$D_{effective}$ [pm/V]	10.6		
Delta k [1/mm]	0		
z integration steps	100		

Table 6-14 The set of input parameters for the simulations with variable input signal energy

Pulse duration (ps)	Frequency chirp (THz/ps)
3.5	0
10.02361	0.01179
20.00125	0.00621
29.5601	0.00424
45.01839	0.00279
59.98062	0.0021
85.45982	0.00147
100.39207	0.00126

Table 6-15 Pulse durations and frequency chirps used in the simulations with variable input signal energy

Figure 6-20 shows the dependence of the amplified pulse energy as a function of the input signal energy, for the pulse durations and chirps listed in Table 6-15.

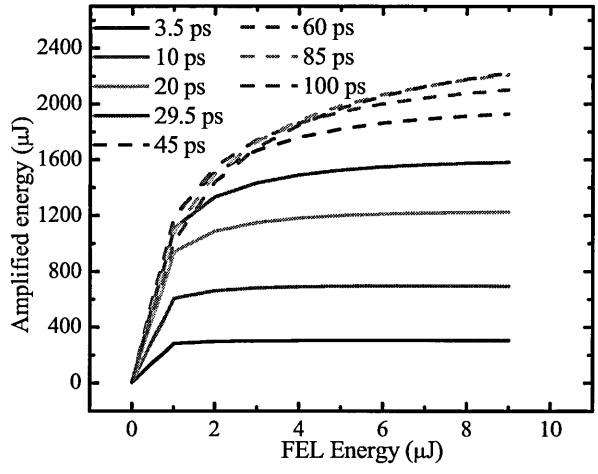

Figure 6-20 The amplified energy for different stretched pulse duration at 6.310 μm signal wavelength, for different stretched pulse durations, listed in the figure. The un-stretched pulse duration is in all cases 3.5 ps. The pump energy is 60 mJ , and the FWHM beam diameter is 12 mm.

The pulse lengthening leads to a more efficient parametric amplification, due to the overcoming of the saturation effect. It is noticeable that the pulse lengthening has a more significant effect for shorter stretched-pulse durations. This is due to saturation, which is stronger at shorter signal pulse duration and to the pump pulse duration, limited to 85 ps.

For the same set of simulations, the changes in spectrum and temporal shape of the amplified pulse are presented in Figure 6-21-Figure 6-28 (a) and (b). Figure

6-21-Figure 6-28 (a) show the spectral modifications induced by the parametric amplification for the pulse lengths, listed in Table 6-15.

There are several aspects that can be noticed. For the unstretched pulse (Figure 6-21 (a)), the central wavelength of the amplified pulse does not vary with the input signal energy. The spectral bandwidth decreases with the increasing input signal energy. For the stretched pulses (Figure 6-22-Figure 6-28), the central wavelength shifts (the sign of the chirp determines the direction of this wavelength shift). The amount of shift and the change in the spectrum depend on the input stretched pulse duration and energy. For pulse durations longer than about 60 ps, and for maximum input signal energy in simulations, about 9 μJ, the spectra approach a Gaussian shape, and the central wavelength reaches the value of the input signal wavelength (compare for example Figure 6-23 (a) with Figure 6-28 (a)).

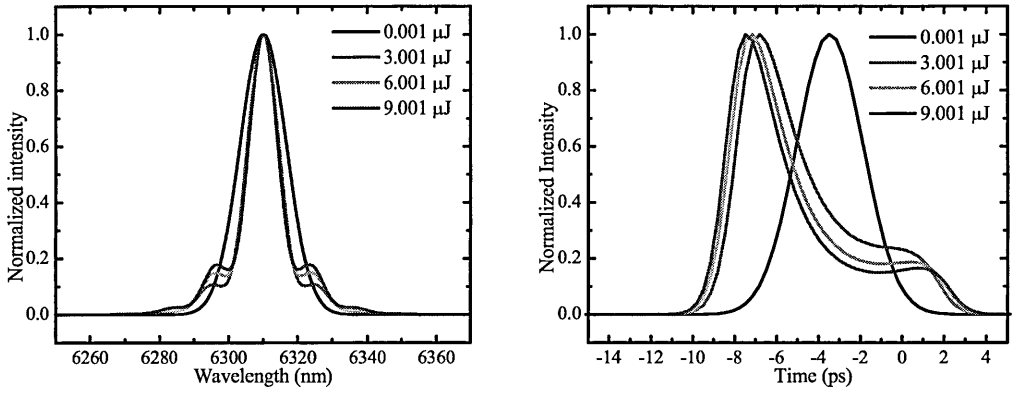

Figure 6-21 The spectra (a) and temporal shape (b) of the amplified pulse for a pulse duration of 3.5 ps, for different input signal energy

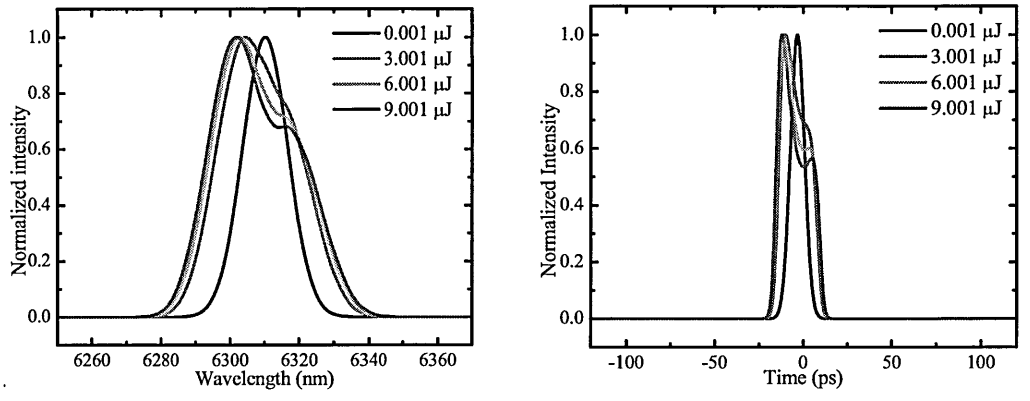

Figure 6-22 The spectra (a) and temporal shape (b) of the amplified pulse for a stretched pulse duration of 10 ps, for different input signal energy

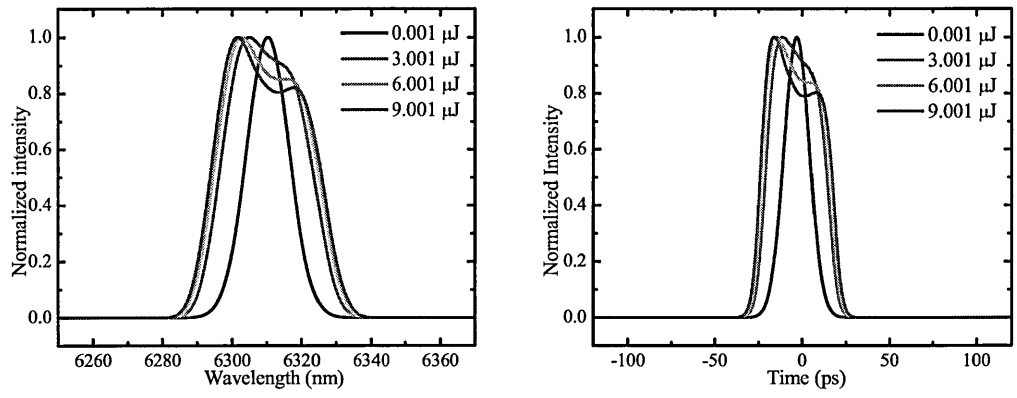

(a) (b)

Figure 6-23 The spectra (a) and temporal shape (b) of the amplified pulse for a stretched pulse duration of 20 ps

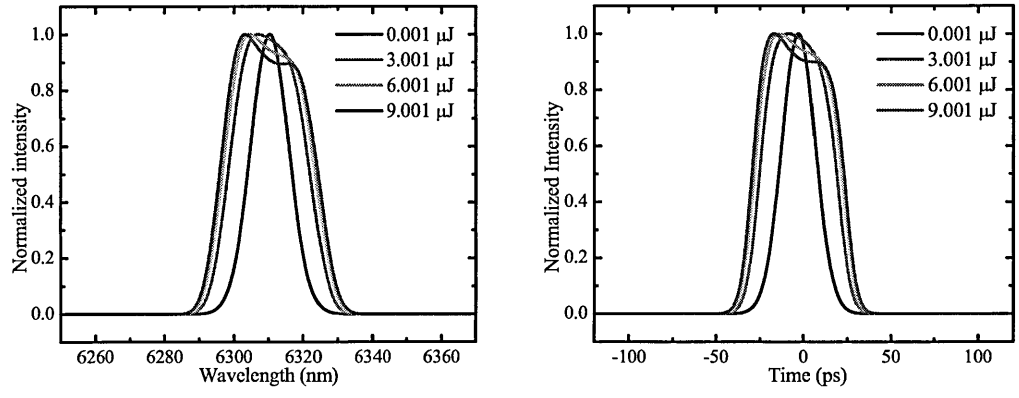

(a) (b)

Figure 6-24 The spectra (a) and temporal shape (b) of the amplified pulse for a stretched pulse duration of 29.5 ps, for different input signal energy

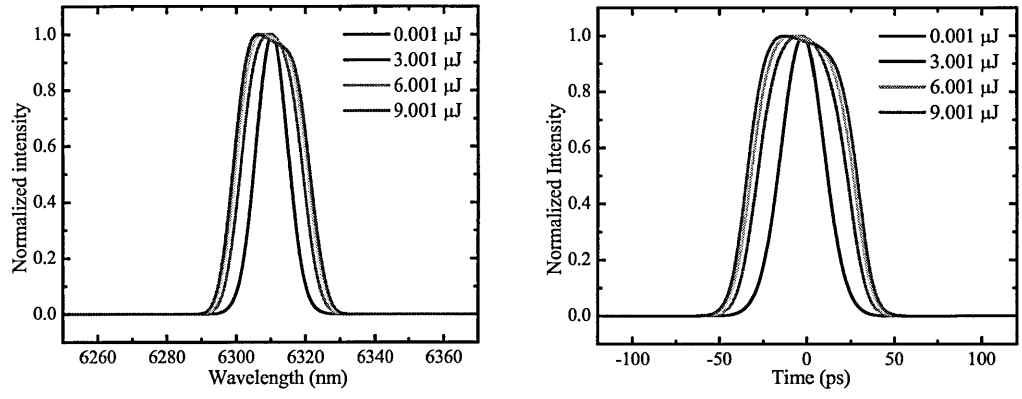

(a) (b)

Figure 6-25 The spectra (a) and temporal shape (b) of the amplified pulse for a stretched pulse duration of 45 ps, for different input signal energy

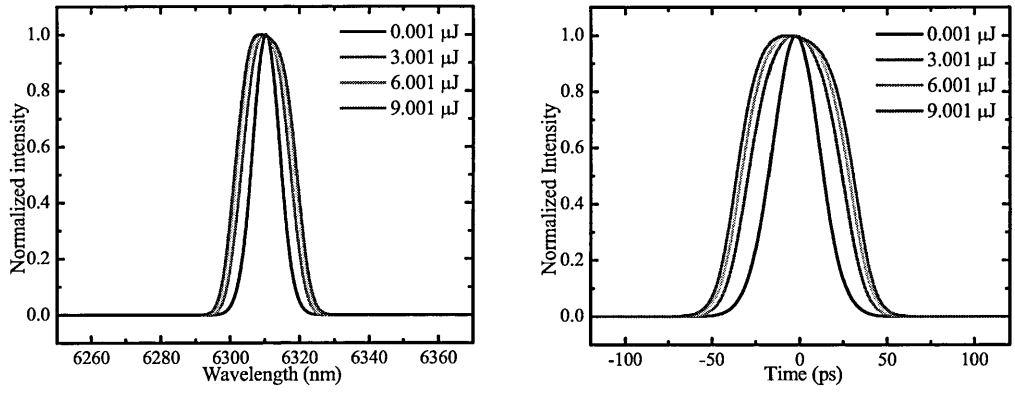

(a) (b)

Figure 6-26 The spectra (a) and temporal shape (b) of the amplified pulse for a stretched pulse duration of 60 ps, for different input signal energy

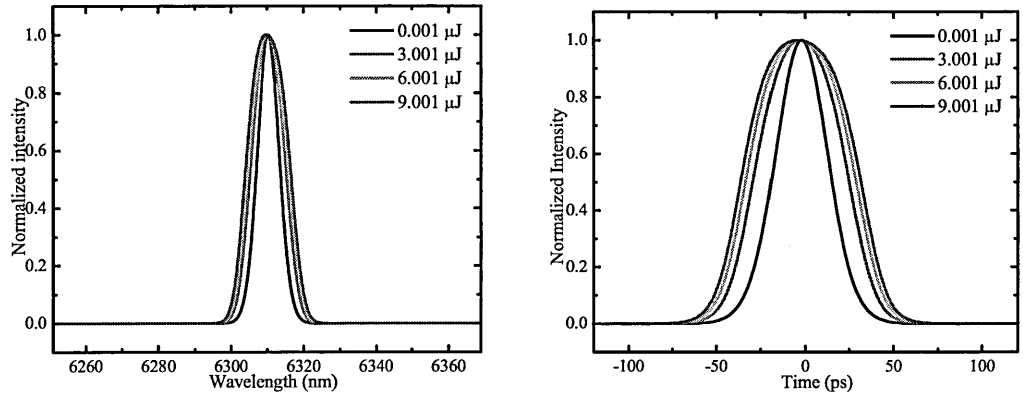

(a) (b)

Figure 6-27 The spectra (a) and temporal shape (b) of the amplified pulse for a stretched pulse duration of 85 ps, for different input signal energy

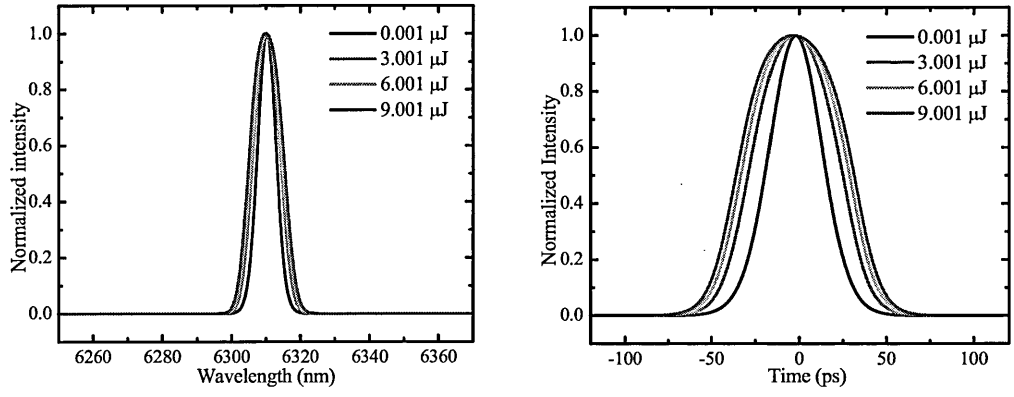

(a) (b)

Figure 6-28 The spectra (a) and temporal shape (b) of the amplified pulse for a stretched pulse duration of 100 ps, for different input signal energy

The spectral changes are more significant for the highest input signal energy. The amplified pulse duration is also modified with the input signal energy and initial pulse duration. The evolution of the amplified and stretched-amplified pulses is shown in Figure 6-21-Figure 6-28 (b). The pulse length increases together with the bandwidth broadening, contrary to the situation of the un-stretched pulse. However, with increasing pulse duration and hence with weaker saturation, the stretched amplified spectra and pulse shapes approach a Gaussian shape.

The comparison of the spectra of the amplified pulse, for the maximum input signal energy considered in simulations (9 μJ) and for different pulse duration is shown in Figure 6-29. The spectrum of the input signal pulse is plotted, for better comparison.

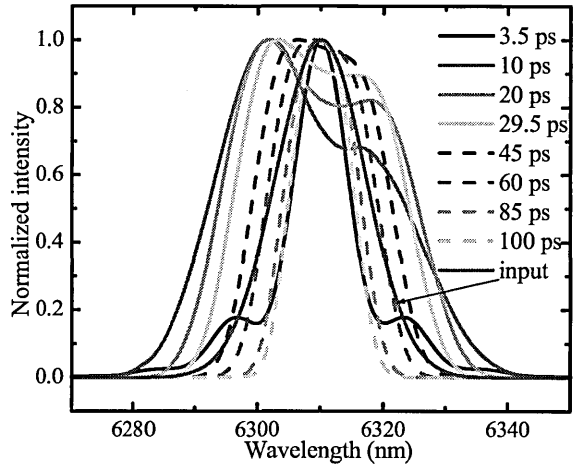

Figure 6-29 Spectra of the amplified pulse at 9μJ signal energy and 60 mJ pump energy, for different pulse durations. The initial spectrum, common for all pulses, is presented for comparison

It appears that, for stretched pulse durations longer then ~ 60 ps, the pulse spectrum of the amplified pulse narrows significantly compared with the initial pulse. As already mentioned, from the similar plots presenting the comparison of the amplified energy in Figure 6-20, one can notice that the amplified energy does not increase significantly any more on behalf of the stretching, for pulse durations longer than 60 ps. The reason lies in the pump pulse duration, of only 85 ps. Stretching the signal pulse longer than that, leads to excluding the marginal wavelengths from amplification process. This narrows the pulse bandwidth and limits the amplified energy.

Another factor related to the signal irradiance is the signal beam diameter. To show its influence on the output parameters of interest, simulations have been performed for the signal wavelength of 5.384, at two pump energies: 30 and 70 mJ respectively. The set of parameters is shown in Table 6-16, while the results on the amplified energy are plotted in Figure 6-30.

	Signal	Idler	Pump
Wavelengths [nm]	5384.08	1326.05	1064
Index of refraction	2.39518	2.438587	2.428443
Group velocity index	2.429687	2.494907	2.52601
Group velocity dispersion (cm/sec-cm-^{1})	5.89E4	-1.16E5	-1.57E5
Input face reflectivity	0.05	0.1	0.08
Output face reflectivity	0.1	0.1	0.08
Crystal absorption [1/mm]	.001	.006	.001
Pulse energy (J)	1.9E-5	0	7E-2
Pulse duration [ps]	2.459	3	85
Pulse delay relative to pump [ps]	0	0	
Pulse chirp (THz/ps)	0	0	0
Beam diameters [mm]	12	8	11
Walkoff angle [mrad]	-44	9.26	21.77
Radius of curvature [mm]	1.00E12	1.00E12	1.00E12
Number of t,x,y points	1024	32	32
Size of the crystal/grid [mm]	16	13	9
$D_{effective}$ [pm/V]	10.8		
Delta k [1/mm]	0		
z integration steps	100		

Table 6-16 The set of parameters for simulations performed for investigating the influence of the signal beam diameter. Two situations were considered: (relatively) low input pump energy (30 mJ) and high input pump energy (70 mJ)

The results for amplified pulse energy, shown in Figure 6-30, reveal that, for the input signal and pump parameters considered in simulations, the value of the amplified pulse energy does not depend much on the signal beam diameter. This is due to the limited transversal size of the crystal (9x13) mm^2 and to saturation. The increase of the signal beam diameter, which reduces the saturation and favours higher amplified energy, is compensated by the loss at the crystal.

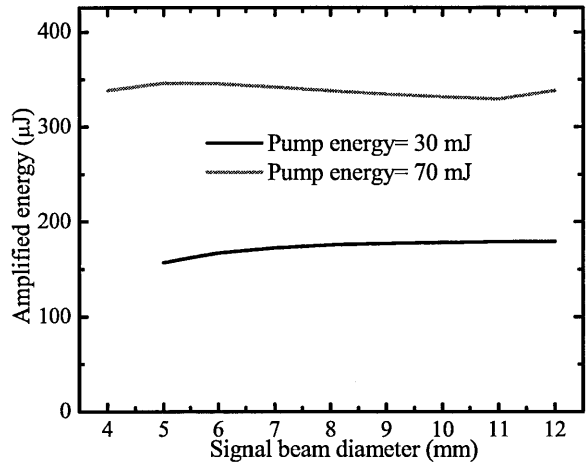

Figure 6-30 The dependence of the amplified energy on the signal beam diameter at 30 and 70 mJ input pump energy, for the input parameters in Table 6-16. The amplified pulse energy is not very sensitive to variations of the input signal energy

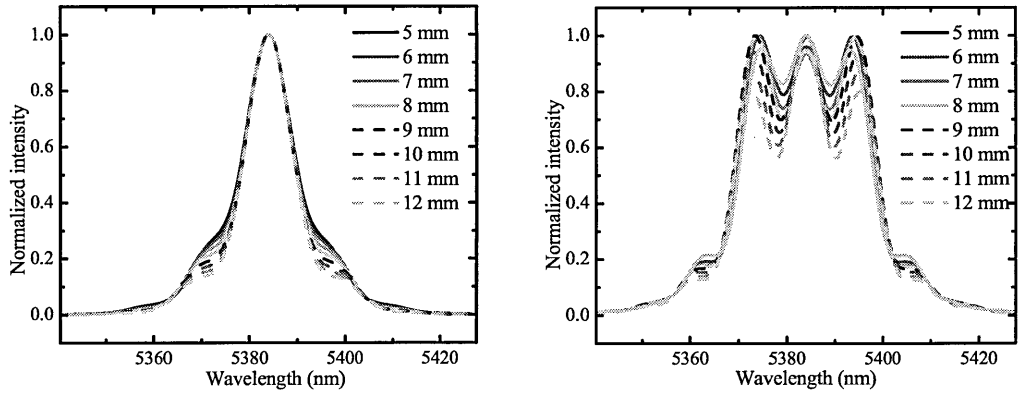

(a) (b)

Figure 6-31 The spectra of the amplified pulse for input pump energy 30 mJ (a) and 70 mJ pump (b). Important distortions appear for the maximum signal beam diameter.

The stronger distortion present at low saturation (longer signal beam diameter), for both values of the pump energy, as presented in Figure 6-31 (a) and (b), seem also to be caused, in simulations, by the comparable diameters of the pump and signal beams.

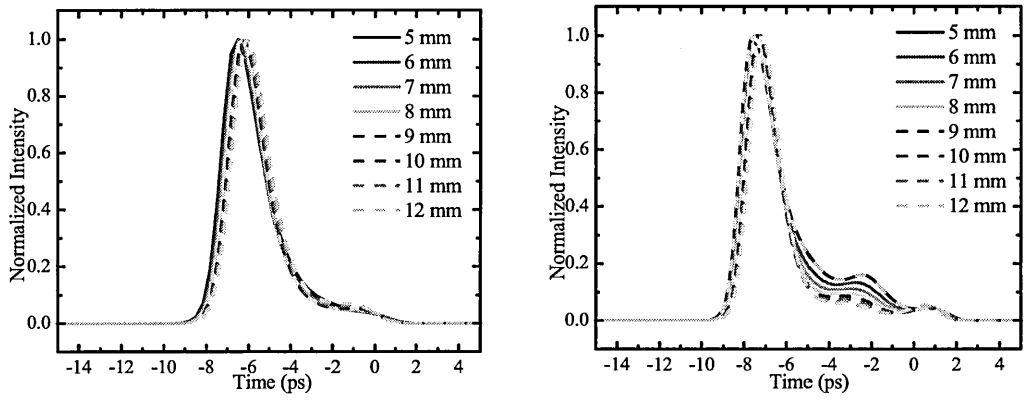

Figure 6-32 The temporal pulse shape of the amplified pulse for input pump energy 30 mJ (a) and 70 mJ pump (b)

Regarding the changes in the temporal shape, it can again be noticed that for low pump energy, shown in Figure 6-32 (a), the dependence on the signal beam diameter is weak, while for the high pump energy, the changes are more pronounced and, as expected from the higher signal irradiance at shorter diameters, they are more important for shorter beam diameters.

6.3.5 Chirp and phase mismatch

The simulations considering the presence of (signal pulse) chirp and phase mismatch are useful in explaining the distorted shape of the spectra measured for the un-stretched amplified pulse (Chapter 7). The influence of the initial phase mismatch on the spectra and pulse shape is the chirp present in the amplified pulse [5,6].

The similar effects of input signal pulse chirp and phase mismatch are shown in Figure 6-33 and Figure 6-34. The input parameters are shown in Table 6-17 and Table 6-18 respectively.

	Signal	Idler	Pump
Wavelengths [nm]	5384.08	1326.05	1064
Index of refraction	2.39518	2.438587	2.428443
Group velocity index	2.429687	2.494907	2.52601
Group velocity dispersion (cm/sec-cm-^{1})	5.89E4	-1.16E5	-1.57E5
Input face reflectivity	0.05	0.1	0.08
Output face reflectivity	0.1	0.1	0.08
Crystal absorption [1/mm]	0.001	.001	.001
Pulse energy (J)	1.9E-5	0	8E-2
Pulse duration [ps]	2.459	3	85
Pulse delay relative to pump [ps]	0	0	
Pulse chirp (THz/ps)	0.01	0	0
Beam diameters [mm]	6	8	11
Walkoff angle [mrad]	-44	9.26	21.77
Radius of curvature [mm]	1.00E12	1.00E12	1.00E12
Number of t,x,y points	1024	32	32
Size of the crystal/grid [mm]	16	13	9
$D_{effective}$ [pm/V]	10.6		
Delta k [1/mm]	0		
z integration steps	100		

Table 6-17 the set of input parameters in Figure 6-33

	Signal	Idler	Pump
Wavelengths [nm]	5384.08	1326.05	1064
Index of refraction	2.39518	2.438587	2.428443
Group velocity index	2.429687	2.494907	2.52601
Group velocity dispersion (cm/sec-cm-^{1})	5.89E4	-1.16E5	-1.57E5
Input face reflectivity	0.05	0.1	0.08
Output face reflectivity	0.1	0.1	0.08
Crystal absorption [1/mm]	.001	.001	.001
Pulse energy (J)	1.9E-5	0	8E-2
Pulse duration [ps]	2.459	3	85
Pulse delay relative to pump [ps]	0	0	
Pulse chirp (THz/ps)	0	0	0
Beam diameters [mm]	6	8	11
Walkoff angle [mrad]	0	0	21.77
Radius of curvature [mm]	1.00E12	1.00E12	1.00E12
Number of t,x,y points	1024	32	32
Size of the crystal/grid [mm]	16	13	9
$D_{effective}$ [pm/V]	10.6		
Delta k [1/mm]	0.2		
z integration steps	100		

Table 6-18 The set of input parameters for simulations in Figure 6-34

Both figures show, apart from the set of input parameters, the dependence of the amplified pulse energy, spectra and temporal shapes of the input pump energy. Excepting the chirp and the phase mismatch, all the other input parameters are the same. It can be noticed that the main feature introduced by the initial chirp and phase mismatch is the amplified pulse distortion. Regarding the influence of the chirp on the amplified pulse spectra, Figure 6-33 (b) shows significant distortion for input pump energies higher than 40-50 mJ.

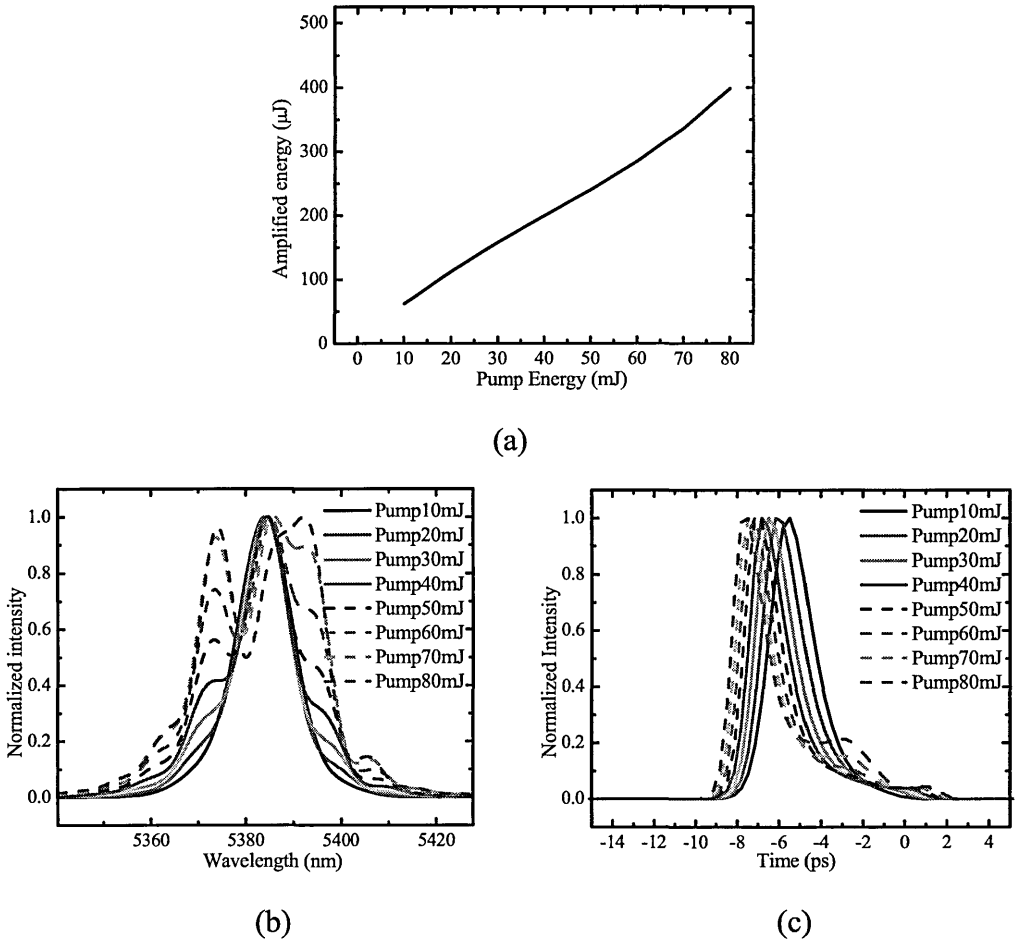

Figure 6-33 Influence of the input signal chirp (0.01 THz/ps) on the amplified pulse parameters (a) the dependence of the amplified pulse energy on the input pump energy; (b) Spectra and (c) temporal pulse shapes, for different input pump energies. The presence of the input chirp in the pump pulse determines distortions in the amplified pulse spectra

The pulse distortions are more pronounced with increasing input chirp. In Figure 6-34 (b), the measured and normalized spectrum of the amplified pulse at ~75 mJ input pump energy is compared with the (normalized) spectra obtained as result of simulations. Even if for the spectrum at the maximum pump energy does not perfectly reproduce the measured one, the presence of a phase mismatch of 0.2-0.3/mm can explain the modifications induced by parametric amplification in the amplified pulse spectrum.

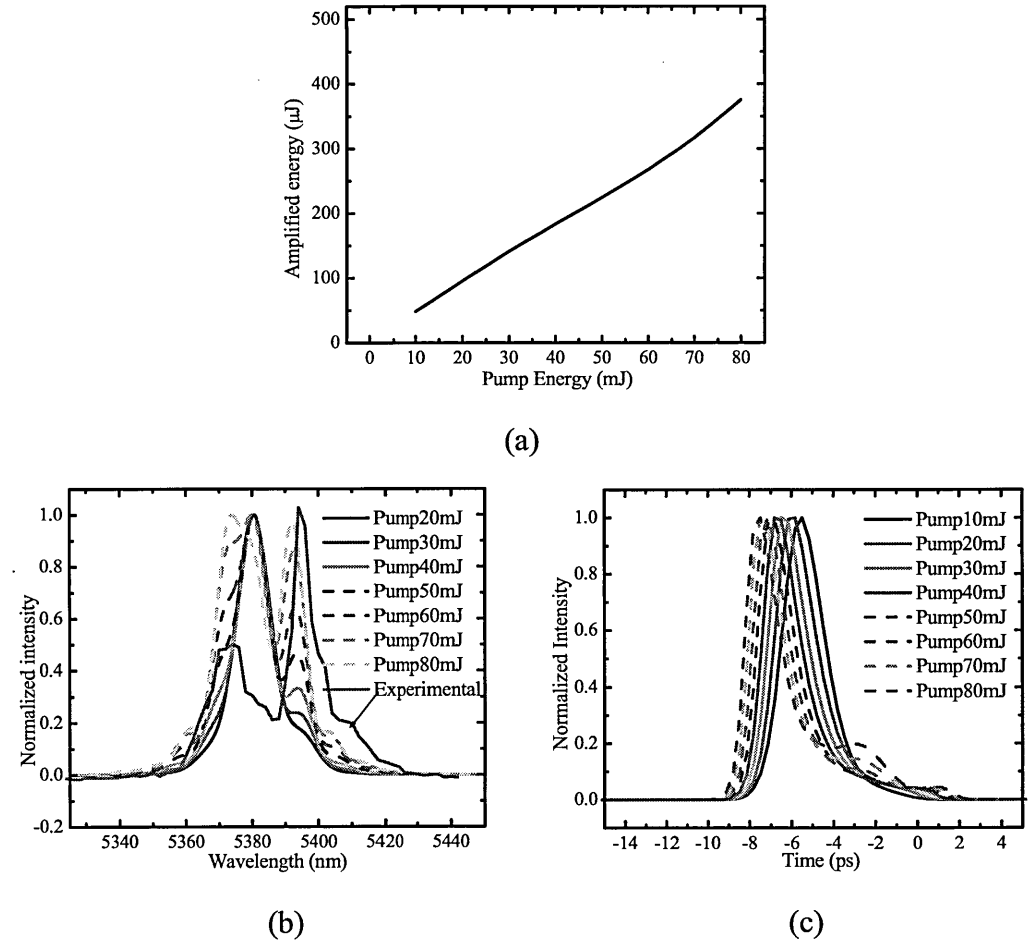

Figure 6-34 The influence of the phase mismatch Δk=0.2/mm. (a) the dependence of the amplified pulse energy on the input pump energy; (b) Comparison of the spectra of the amplified pulse for different input pump energies and the measured spectrum, at ~20 μJ input signal energy, and 75 mJ pump energy; (c) The temporal shapes of the amplified pulses in the presence of the phase mismatch, for different input pump energies.

As in the case of the input signal chirp, the significant distortions appear at pump energies higher than 40 mJ.

The developing of the pulse distortions in the presence of the input chirp, as a function of the input signal energy is shown in Figure 6-35. The distortions increase with the signal pulse energy and they start to manifest (for the 0.01THz/ps) at ~ 3 μJ input signal energy.

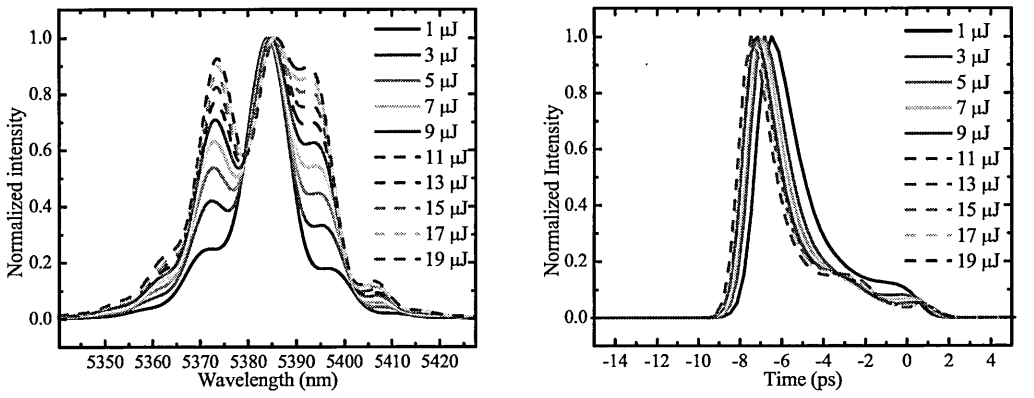

(a) (b)

Figure 6-35 Spectra (a) and pulse shape (b) of the amplified pulses, for chirped-input signal pulses, as a function of input signal energy. The pump energy is 75 mJ, and all the other parameters are the same as in Table 6-17. The values of the input signal energies are listed in the plots. At this level of high pump energy (75 mJ) the distortions start to develop at ~3 μJ input signal energies

Figure 6-36 presents similar results with Figure 6-35. Instead of pulse chirp, (considered 0 this time), it is the phase mismatch (0.2 mm^{-1}) causing the distortions. The pump energy was 70 mJ, and the values of the input signal energies corresponding to each plot are listed in the figure.

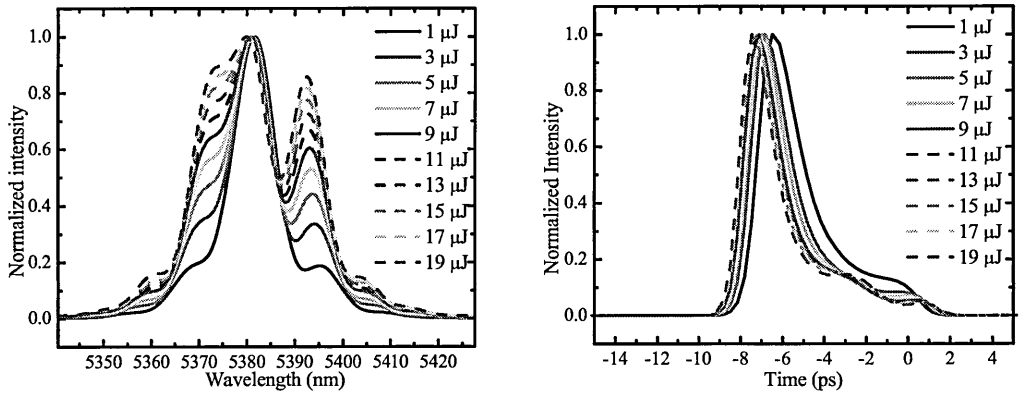

(a) (b)

Figure 6-36 Spectra (a) and pulse shape (b) of the amplified pulses, for an input phase mismatch of 0.2/mm, for different input signal energies. The pump energy is 70 mJ, and all the other parameters are the same as inTable 6-18). The values of the input signal energies are listed in the plots. At this level of high pump energy (70 mJ) the distortions start to develop at an input signal energy ~3 μJ

The simulations show a similar behaviour of the spectra and temporal shapes if an initial chirp and phase mismatch are considered. In both cases the distortions are influenced by the saturation level.

The evolution of pulse distortions with increasing phase mismatch is shown in Figure 6-37.

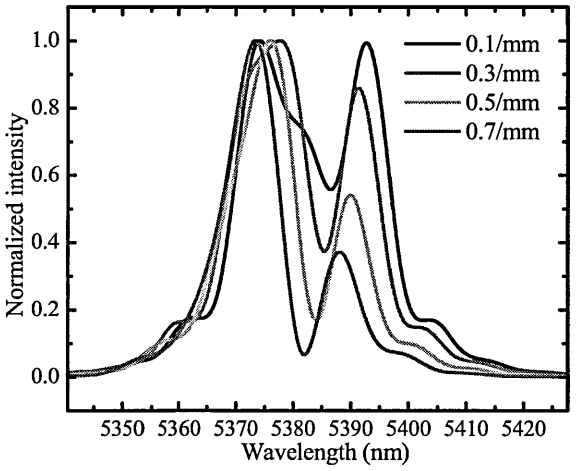

Figure 6-37 The spectral distortions for several values of the phase mismatch, listed in the plot, the input pump energy of 80 mJ and input signal energy of 19 μJ. Due to the high values of both pump and signal energies, the distortions manifest for all values of the phase mismatch, but they increase with the value of the phase mismatch. The initial pulse is Gaussian, centred at 5.384 μm.

The plot shows the transformation induced by the phase mismatch on an initial Gaussian spectrum centred at 5.384 μm, under the conditions of high input pump and signal energies (strong saturation). The input parameters are similar to the ones in Table 6-18, but the pump energy is fixed at 80 mJ, and the signal energy is 19 μJ. Because the input pump and signal energies are high, the distortions are already considerable for the lowest value of the phase mismatch (0.1/mm).

6.3.6 The delay between the pump and signal pulses

In Chapter 8, the influence of the delay for the OPCPA experiment is discussed in detail; it is shown that the delay between the pump and signal pulses can influence the amplified energy, spectra, stretched-amplified pulse duration, central wavelength of the amplified pulse. For comparable pump and stretched signal pulse duration, the jitter between the pulses can create energy and spectral instabilities.

A comparison between the simulations and experimental results with variable delay can give in principle useful information about pulse durations (both stretched-signal and pump) and about the accuracy of the delay itself. The central wavelength shift in the stretched-amplification process, measured and simulated for different delays, can also be simulated and comparison of the results reflects the accuracy of the (real) delay between the pump and signal pulses.

However, because the simulations with variable input pump and signal energies did not fit very well the experimental results for the energy of the amplified pulse, the same situation holds for the simulations with variable delay. By varying the delay, the stretched pulse interacts with different pump intensity distributions, and all the properties of the amplified pulse are affected.

Figure 6-38 shows a comparison between experimental results for the amplified pulse energy at 9.98 μm, presented in Chapter 8. The measurements were taken with the signal pulse passing through the stretcher system, but for no displacement (ideally no stretching of the input pulse). Several simulations have been performed for different pump pulse durations, because the pump pulse length estimated from the autocorrelation traces in Chapter 4, did not give satisfactory results. It can be seen that an 85 ps pulse length predicts notable amplification of the input pulse even for delays of 50 ps, while experimentally this has not been observed. The maximum energy corresponding to a 0 delay predicted by simulations is also about one half of the maximum measured energy of the amplified pulse.

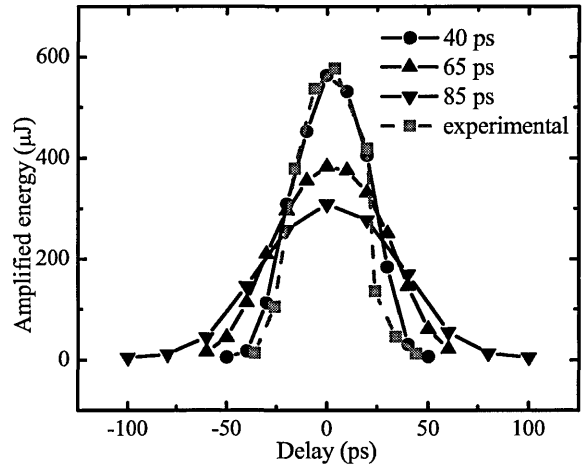

Figure 6-38 The energy of the amplified pulse for 15 μJ input signal energy and 5.49 ps pulse duration, at 9.98 μm signal wavelength as a function of the delay. The pump energy was considered 70 mJ, the FWHM pump beam diameter 9 mm and the different pump pulse durations are listed in the plot. The comparison with the experimental results show a best fit for a pump pulse duration of ~ 40 ps, while the autocorrelation measurements (Chapter 4) suggest a pump pulse length of 85 ps.

The pump pulse length giving the best fit with experimental results is 40 ps. But this conclusion was not supported by the comparison between experimental results and simulations for other two pulse durations: 14.4 ps and 17.5 ps. As shown

in Figure 6-39 (a) and (b), the 85 ps pump pulse length give a better agreement with the experimental results.

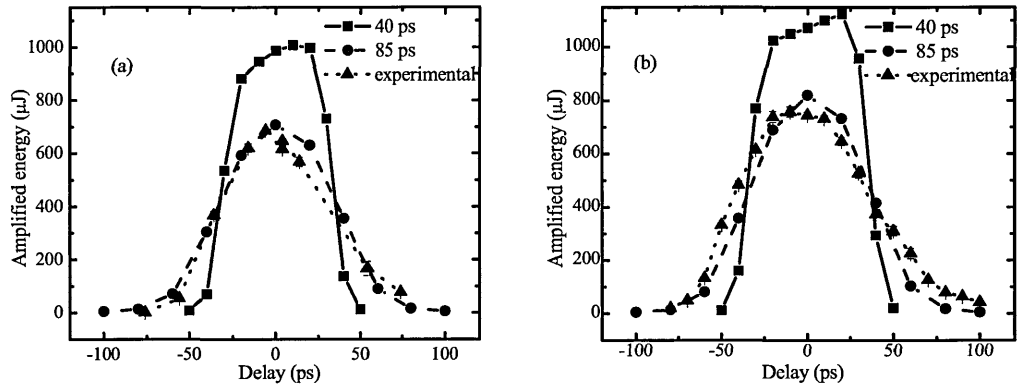

Figure 6-39 The energy of the amplified pulse for 15 μJ input signal energy and (a) 14.4 ps and (b) 17.5 ps pulse duration, at 9.98 μm signal wavelength as a function of the delay. In simulations, the pump energy was 70 mJ, the FWHM pump beam diameter 9 mm and the different pump pulse durations are listed in the plot. The comparison with the experimental results show a good fit for a pump pulse duration of ~ 85 ps.

For simulations performed with un-stretched pulses, as is the case of the results shown in Figure 6-38, no central wavelength shifts have been predicted. The situation is different for the stretched pulses, where the presence of the chirp and the increased pulse durations lead to spectral distortions and shifts of the central wavelength.

These effects are discussed in detail in Chapter 8, in the **Spectral measurements** section, where the measured central wavelength shift for different delays has been determined and compared with the simulations results. The comparison showed good agreement between simulations and measurements.

On the other hand, it has been mentioned that the effects depend on the value of the delay, and all the input parameters related to input irradiances and parametric gain. Figure 6-40 shows the spectra and the temporal shapes for the same parameters used in Figure 6-39, for the pump pulse length of 85 ps. One can notice that the distortions are more significant for short delays, corresponding to the high pump and signal irradiances, and so, to a saturated gain.

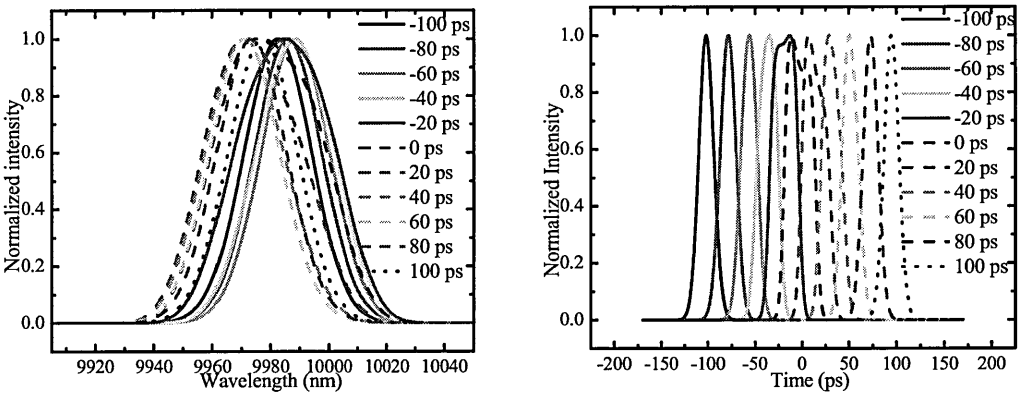

(a) (b)

Figure 6-40 (a) Spectra and (b) temporal shapes corresponding to the simulations in Figure 6-39 for 85 ps pump pulse duration.

More significant distortions are shown in Figure 6-41, where the pump irradiance is higher (70 mJ in 40 ps FWHM pulse duration) and the pump pulse duration is comparable to the delay and about twice the stretched pulse duration.

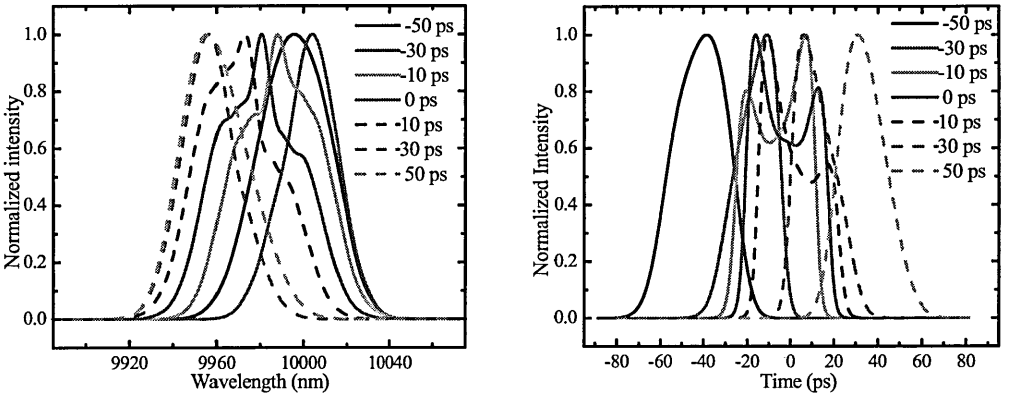

(a) (b)

Figure 6-41 (a) Spectra and (b) temporal shapes corresponding to the simulations in Figure 6-39 (b) for 40 ps pump pulse duration. The distortions increase because of saturation.

The distortions at the same delay depend also on the input signal irradiance and they increase with it.

For shorter wavelengths, the higher gain for the same pump irradiance increases also the distortions. This is shown by the results of two sets of simulations performed for 6.31 μm signal wavelength, for an input energy of 10 and 1 μJ respectively, in Figure 6-42 and Figure 6-43. The input parametersare listed in Table 6-19.

	Signal	Idler	Pump
Wavelengths [nm]	6310	1279.8	1064
Index of refraction	2.388	2.437	2.43
Group velocity index	2.434	2.504	2.527
Group velocity dispersion (cm/sec-cm-^{1})	-1.16E5	-1.21E5	-1.57E-
Input face reflectivity	0.05	0.1	0.02
Output face reflectivity	0.05	0.1	0.02
Crystal absorption [1/mm]	0.001	.006	.001
Pulse energy (J)	10.E-6	0	6E-2
Pulse duration [ps]	29.5601	16	85
Pulse delay relative to pump [ps]	0	0	
Pulse chirp (THz/ps)	0.00424	0	0
Beam diameters [mm]	6	8	12
Walkoff angle [mrad]	20.9	4.1	21.76
Radius of curvature [mm]	1.00E12	1.00E12	1.00E12
Number of t,x,y points	1024	32	32
Size of the crystal/grid [mm]	16	13	9
$D_{effective}$ [pm/V]	10.6		
Delta k [1/mm]	0		
z integration steps	100		

Table 6-19 The set of input parameters for simulations with variable delay. The delay is varied between -80 to 80 ps

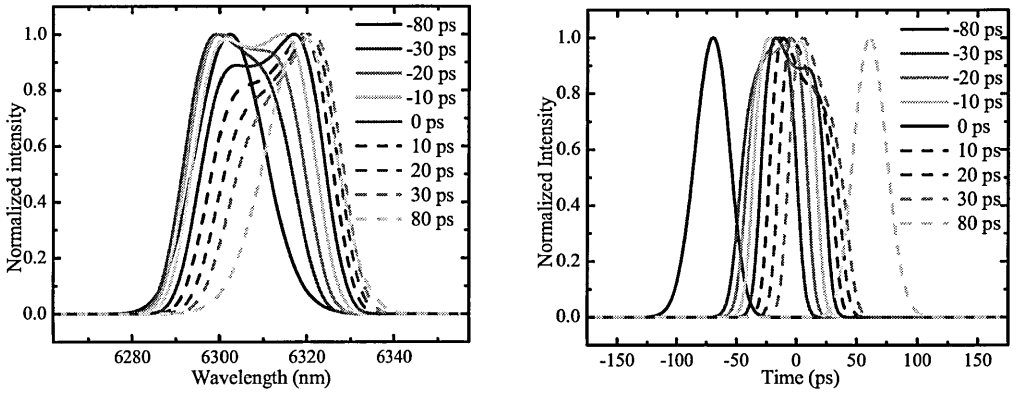

(a) (b)

Figure 6-42 Simulations at 6.31 μm for the stretched pulse (a) The modifications of the spectra due to the change in the delay (b) The modification of the temporal shape with the pump energy

Even if the pump irradiance is much lower than for the results obtained in Figure 6-40, the distortions are more pronounced due to the wavelength dependence of the gain. For 1 μJ input signal energy, the only effect of the variable delay on the spectral properties of the amplified pulse is the wavelength shift. The results are shown in Figure 6-43.

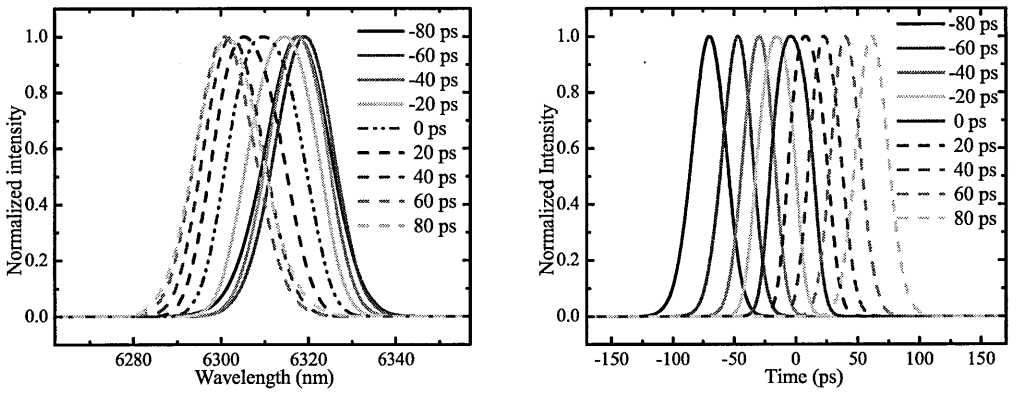

(a) (b)

Figure 6-43 Simulations at 6.31 μm for the stretched pulse (a) The spectra of the amplified pulses against the delay between the pump and stretched signal pulses (b) The temporal shapes as a function of delay. The input parameters are the same as in Table 6-19, but for 1 μJ input signal energy

6.3.7 Conclusions

The simulations presented in section 6.3 of this chapter aimed to explain the dependence of the amplified pulse energy and the spectral/temporal changes induced by the parametric process, on the most important input parameters: crystal length, nonlinear constant, input pump and signal irradiance. Other simulations took into account the phase mismatch or chirp of the input signal pulse, and the delay between the pump and signal pulses.

All sets of input parameters considered the type I ooe interaction of a pump wavelength of 1.064 μm with several signal wavelengths in the range of (5-10 μm), in an AGS crystal of either 17 or 16 mm length, when a variable crystal length was not considered.

The simulations presented in sections 6.3.1-6.3.4 revealed the influence of saturation on the amplified pulse parameters and spectral/temporal shape and the beneficial influence of stretched pulse amplification for surmounting the power limits of OPA. These effects are important because they can introduce power limitations, by spectral narrowing at excessive stretching, (Figure 6-29), although the amplified energy increases with the stretched pulse length (Figure 6-20). They also pointed out other spectral effects that can appear when using this method: central wavelength shifts and distortions, which are important in applications where the selectivity of the signal wavelength is considered.

When appropriate, the results of simulations were compared with the experimental ones (section 6.3.3, 6.3.4). A better fit of the amplified energy was noticed for longer wavelengths (Figure 6-18 and Figure 6-19) than for shorter ones, where the simulations predict much stronger saturation effects than the experimental results (Figure 6-14, Figure 6-16).

When investigating the importance of the crystal length, the results could not be compared with experimental ones, because this parameter could not be varied. Nevertheless, they offered a useful picture of the developing of saturation effects for several input parameters.

The simulations accounting for phase mismatch and chirp for the unstretched (section 6.3.5) pulses could explain pulse distortions observed in OPA experiments.

The influence of the delay was investigated mainly for the stretched-pulse amplification (section 6.3.6). For pulse durations of the order of the ones used in experiments, the central wavelength shifts induced by stretched-amplification depend on the saturation level, they do not vary linearly with the delay, and they are of the order of tens of nanometres for delays of 20 ps. This shows the great importance of a low jitter for the synchronization electronics between the pump and signal pulses for obtaining a stable powerful spectroscopic source, under the conditions imposed by our experiment (pump and stretched pulse lengths of 85 ps and tens of picoseconds respectively).

6.4 Bibliography

1. SNLO nonlinear optics code available from A.V. Smith, Sandia National Laboratories, Albuquerque, NM 87185-1423, USA

2. J.-J. Zondy, D. Touahri, and O. Acef, "*Absolute value of the d_{36} nonlinear coefficient of $AgGaS_2$: prospect for a low-threshold doubly resonant oscillator-based 3:1 frequency divider*" JOSA B,Vol. 14, pp. 2481-2497,1997

3. E. Siegman, *Lasers*, University Science Books, Mill Valley, California, 334-335 1986

4. E. B. Treacy "*Optical pulse compression with diffraction gratings*", IEEE J. of Quantum Electron., Vol. 5 , pp 454-458, 1969

5. L. J. Qian, X. Liu, and F. W. Wise, "*Femtosecond Kerr-lens mode locking with negative nonlinear phase shifts*", Opt. Lett., Vol 24., pp. 166-169, 1999

6. A. V. Smith and M. S. Bowers, "*Phase distortions in sum- and difference-frequency mixing in crystals*", J. Opt. Soc. Am. B, Vol. 12, pp.49-57, 1995

Chapter 7 The optical parametric amplifier

Optical parametric amplification (OPA) is an efficient technique of amplifying short optical pulses. As described in detail in Chapter 3, the main advantages are the design simplicity, large gain and broad tunability. This chapter describes the experimental setup and results obtained with an OPA scheme which amplifies the tunable signal from FELIX in the range of 5-10 μm in the field of a powerful beam provided by a Nd:YAG regenrative amplifier at 1.064 μm. The pump pulse energy can reach 70-80 mJ, a limit imposed by the damage threshold of the crystal. The nonlinear crystal used is $AgGaS_2$ (AGS). The results show amplified energies of several hundreds microjoules for the signal wavelength range, with a maximum energy of about 1.4 mJ at 5 μm, and about 200 μJ at 10 μm. The amount of amplified energy is limited by the difference in the pulse durations of the pump and signal pulses, which does not allow an efficient energy transfer from the pump to the signal pulse. Strong saturation of the amplified pulse energy and modification of the spectral-temporal characteristics are observed. An increase in the amplified energy and improvement of spectral and temporal characteristics is possible, by introducing the chirped-pulse amplification technique. The chirped-pulse amplification scheme and related results are presented in Chapter 8.

7.1 Experimental setup

The experimental set-up of the optical parametric amplifier is shown in Figure 7-1. Its main parts are the signal and pump lasers and the nonlinear crystal. The signal pulses are provided by the free electron laser at FELIX and the pump is delivered by a Nd:YAG regenerative amplifier, as described in Chapter 4. The signal interacts with the pump pulse in the nonlinear crystal (AGS), described in Chapter 5, and the third (idler) beam is generated (not shown in the figure). The amplifying process is the OPA, which is discussed in Chapter 3. The interaction in the nonlinear crystal is type I (ooe). Therefore, the pump beam is horizontally polarized (extraordinary polarization), while FELIX and the generated idler are vertically polarized (ordinary polarization). The crystal is mounted on a rotation stage, and can be rotated around an axis perpendicular to its principal plane with a minimum step

size of 0.02 degrees. The rotation stage itself is mounted on a xyz stage for fine adjustment of the position.

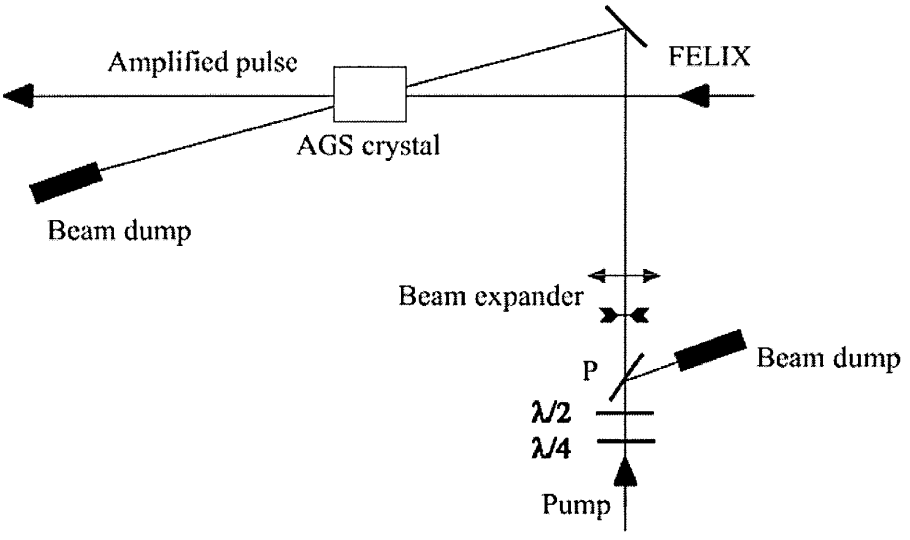

Figure 7-1 Experimental setup for the OPA experiment. Pump and signal beams (FELIX) are incident on the AGS crystal under an angle Δα= 5.6 degrees. The quarter λ/4 plate renders a linear polarization to the pump, while the λ/2 plate can rotate the polarization vector. The polarizer P reflects the vertical polarization component which is dumped by the beam dump, and transmits the horizontal one to the setup. The amount of transmitted energy vary with the orientation of the λ/2 plate. The beam expander increases the beam diameter to 11 mm diameter. The crystal is mounted on a motorized rotation delay stage, which allows rotation for adjusting the phase matching, with a minimum step size of 0.02 degrees. A xyz stage is used for precise alignment of the crystal with the signal and pump beams. After the crystal, the remaining pump energy is dumped in a second beam dump.

The main parameters of FELIX (wavelength and pulse length, polarization, energy) are adjusted at the FELIX console. It is only possible to adjust the beam direction and diameter on the optical table. The beam diameter at the crystal depends on wavelength; because the beam diameter is comparable with the crystal size, a resizing of the FELIX beam is not done. The diameter of the pump is adjusted with a beam expander to the value of 11 mm FWHM, while the pump energy is varied using a half wave plate and a polarizer. Before the half waveplate and polarizer, a quarter wave plate is used to render the polarization of the pump beam linear. The external angle between the pump and the signal beam (the difference of pump and signal incidence angles on the crystal) is about 5.6 degrees, allowing for good separation of the beams after amplification. The necessary synchronization between pump and signal pulses and the variable delay between them are described in section 4.4.

The output beam can be directed to the spectrometer (TRIAX 320, from Jobin-Yvon) [1] and to the autocorrelation setup, for characterizing the spectral and temporal features of the input and amplified pulses, or to the energy-meter, in order to determine the energy of the input and amplified pulses.

7.1.1 The temporal overlap

A major problem for the experiments is finding the time overlap between the interacting pulses. Still, within 1 ns, the pulses can be superimposed temporally by observing the signal from the room temperature-MCT detector on a 500 MHz Tektronics oscilloscope. The pulses can be overlapped by varying the delay till, on the scope, they appear superimposed. Because the pump pulse and FELIX pulse are 85 ps and few picoseconds long (respectively) a more precise method has to be used in order to achieve the correct time overlap.

Simply scanning the delay for achieving parametric amplification is not effective, because of the small angular acceptance of the crystal. A rotation of about 0.5 degrees can significantly reduce the amplification factor to very low values, even in the case of perfect overlap of the pump and signal pulses, thus reducing the chance to observe the parametric effect, while scanning the delay. Firstly, for a short wavelength (and thus for a high parametric gain, which makes easier the detection of the parametric signal), the crystal is positioned close to the calculated phase-matched position. This is done by using the plots in Chapter 5, section 5.2.1. After that, the AGS crystal is replaced by a silicon plate, which is used for finding the time overlap between the pump and signal pulses within time scales shorter than 1 ns, of the order of the pump pulse duration. The transmission of the silicon plate decreases rapidly with the pump intensity, in few ps. The silicon plate has a high transmission for the micropulse train arriving before the pump pulse, while the pulses arriving after the pump pulse experience a significantly lower value of the transmission. The temporal overlap is found by varying the delay between the pump pulse and FELIX, till the "moment" when the transmission experienced by the individual micropulse, which has to be superimposed on the pump pulse, changes suddenly. The micropulse is then roughly superimposed on the pump, on a time scale of tens of picoseconds. Then the crystal is put back in its place, close to the expected phase matching position. By slightly varying the delay and the angle, the parametric effect is easily observed and optimised. In applying this procedure one has to take into account the

pump pulse structure, (prepulses appear in any regenerative amplifier), and the second pulse revealed by the autocorrelation trace (see Chapter 4). A delay scan and energy measurements can easily determine the main peak, containing the maximum pump energy. The advantage of the silicon plate is that the unnecessary heating of the crystal is avoided during the process of overlapping the pulses.

7.1.2 Measuring energy

The energy of FELIX macropulse is measured with a calibrated Molectron energy meter, with pyroelectric probes models J8LP or J50LP-3 [2], before and after the crystal. They feature a flat spectral response between 0.1 to 12 μm, so include the mid-infrared range of interest. A filter is used to avoid the possible reflections to the energymeter from the idler and pump beams. The energy meter head measures the total energy in the macropulse Because of the temporal structure of the pump and signal radiation, only one micropulse in the train is amplified. The difference between the macropulse energy after the crystal with and without amplification determines the value of the amplified pulse energy. For evaluating the amplification factor, it is important to determine the initial FELIX pulse energy. The measured energy of the macropulse before the crystal gives an indication about the input pulse energy. Knowing the macropulse duration, the total energy and the micropulse train frequency at 25 MHz, the energy of one micropulse can be evaluated. This can be done, for example, by recording the macropulse trace with an oscilloscope. The time integral over the whole macropulse is proportional with the macropulse energy, while the time integral over one macropulse is proportional with the energy of an individual pulse. The energy of the individual pulse is given by the product of the ratio of the two integrals and the macropulse energy.

7.1.3 Recording spectra

Spectral measurements are performed for the input and amplified FELIX pulses, in order to observe the changes induced by the parametric process on the amplified pulse spectrum.

Due to the temporal structure of FELIX macropulse, the spectrum can be recorded simultaneously for the direct and amplified pulses, because the different micropulses can be resolved on a room-temperature MCT detector (PEM-L, Vigo System). The pulses are separated by 40 ns, and because they are close in the

macropulse, their properties do not differ essentially. In this way, the possible differences or errors that can appear in successive measurements, - as for example a backlash at the grating rotation stage in the spectrometer that can lead to a false central wavelength shift - are avoided.

At the entrance of the spectrometer, the power transmission through the entrance slit is optimised by adjusting the beam alignment, and the slit size is reduced till the transmitted power starts to decrease and the alignment cannot improve it anymore. For an optimum transmitted beam, the input beam is focused on the entrance slit using a lens with the focal length that matches the f-number of the spectrometer (4.1), for the whole wavelength range. a slight adjustment of the longitudinal position is necessary when changing the wavelength, because the focal length varies with wavelength due to the dispersive properties of its material. This is done by placing the lens on a translation stage. The power transmission is optimised by adjusting the position of the lens in both transversal and longitudinal directions. At the exit slit, a lens focuses the light on a room-temperature MCT detector. The size of the exit slit of the spectrometer is adjusted on the same size with the entrance slit, normally to 0.08 mm. The resolution of the whole system is limited by the largest slit [1].

A Labview code is used to record spectra. The code can automatically align the grating for the desired central wavelength, and rotate it with steps as small as 0.06 nm. In experiments the step was chosen to be 1 nm. The measurements are usually averaged on 16 pulses.

7.1.4 Autocorrelation traces

The autocorrelation measurements aimed to determine the input and amplified FELIX pulse duration. For that, a purpose-built autocorrelator [3] has been used, which is represented schematically in Figure 7-2. The pulses are assumed to be Gaussian in time.

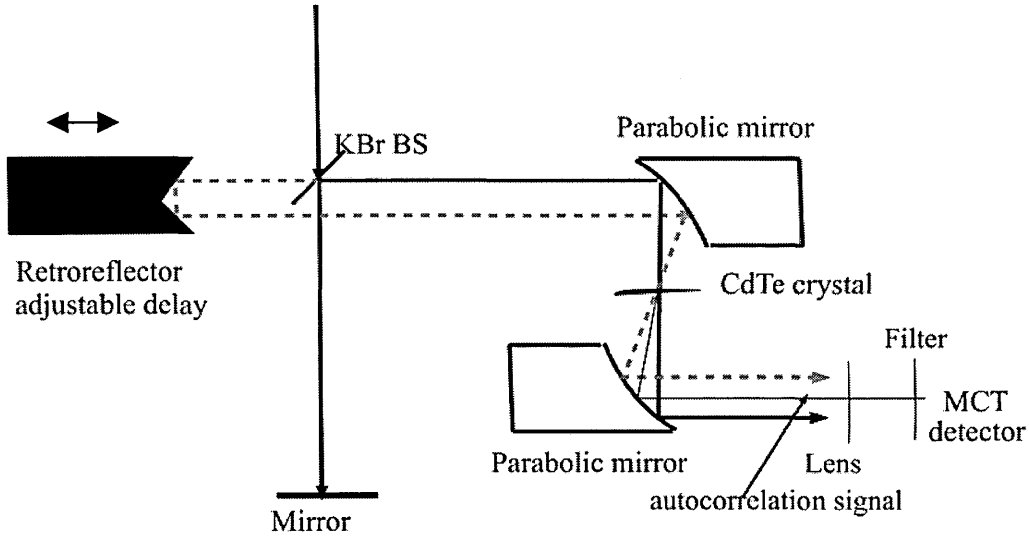

Figure 7-2 Autocorrelation setup. The signal beam is split at the beam splitter BS in two beams. One is reflected back to the beamsplitter and the other is directed to the retroreflector mounted on a delay stage. The two beams are aligned parallel to the axis of the first parabolic mirror. The crystal is positioned in the focus of the two mirrors. The two beams resulting from splitting and focused on the crystal generate separately second harmonic generation signals. When spatial and temporal overlap between the two split pulses takes place, an autocorrelation second harmonic generation signal is generated in the crystal. The signal is focused on the MCT detector and a filter eliminates the influence of the fundamental beam signal from the detector.

In the FELIX pulse, the fundamental wavelength is accompanied by harmonics (see Eq. 4.4). At the entrance of the autocorrelator, they are eliminated by a filter. The pulse is split by the KBr beam splitter. A part is transmitted to a mirror, reflected back to the beam splitter and then to the first parabolic mirror, which focuses the light on the crystal, and another part is directed to a retroreflector. The retroreflector is positioned on a variable delay stage. The first parabolic mirror focuses the beams to the CdTe crystal, where the second harmonic is generated. If the pulses are temporally and spatially overlapped, an autocorrelation signal is generated. The autocorrelation signal is detected and optimized on a cooled MCT detector. Before that, a confocal parabolic mirror renders the beams parallel. A lens focuses the second harmonic autocorrelation intensity on the detector, and the aperture blocks the second harmonics generated independently by the two crossed-beams. A filter in the front of the detector blocks the fundamental wavelength, but transmits the second harmonic, so that only the autocorrelation signal is detected. The signal is visualised on a Tektronics oscilloscope. The detector is not able to resolve the micropulses of FELIX, but only the macropulse. The delay is scanned by moving the retroreflector parallel to the beam direction. The traces for different

positions of the delay stage can be grabbed, using a Labview code. In the code one can establish gates for collecting data only at specific instants in the macropulse.

7.1.5 Absorption in water vapours in the atmosphere

Absorption by water vapour in the atmosphere can pose serious problems for the energy and spectral measurements and interpretation of autocorrelation traces. Figure 7-3 presents the air-transmittance, in percentages per metre, for the wavelength range interesting for amplification experiments. A strong absorption peak at 4.3 μm, can be observed, together with a lot of others in the wavelength range of 5-7.8 μm.

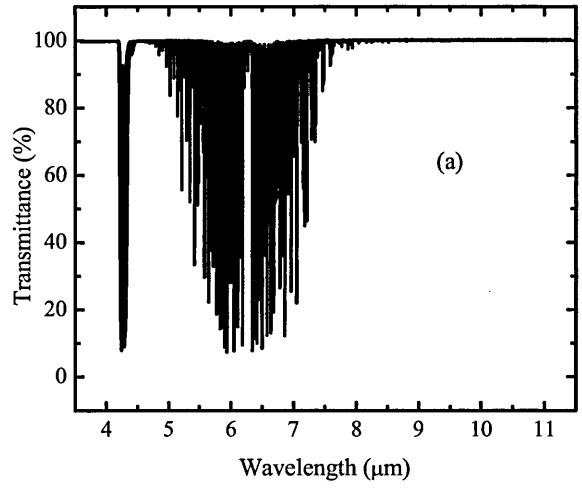

Figure 7-3 Air transmittance at normal atmospheric pressure in the wavelength range of 4-11 μm. The strong absorption around 4.3 μm and 5-7.8 μm can distort the input and amplified pulses. Moreover, the autocorrelation traces are affected by absorption of radiation.

Because the OPA experiment involves distances of a few metres, the values of absorption at certain wavelengths can affect the input spectra at the crystal and seriously influence the spectral characteristics of the amplified pulse. Purging the path with dry nitrogen can circumvent the problems created by water vapour absorption in the atmosphere. Experiments were performed without purging with dry nitrogen, so the wavelength and its bandwidth had to be carefully chosen, in order to avoid the strong absorption peaks.

7.2 Experimental results and discussion

First experiments have been performed with the 17 mm long crystal. After damage occurred between the antireflection coating and the surface of the crystal

(see complete description in Chapter 5), the crystal was polished and recoated, resulting in a shorter length of 16 mm. First, results with the longer crystal are presented, followed by results with the reconditioned and recoated crystal. The two sets of results do not differ too much in energy, because the initial crystal had additional losses at the interface between the antireflection coating and its surface.

The measurements aimed to characterize the amplified pulse energy, pulse duration and spectrum.

7.2.1 Experimental results with crystal length of 17 mm

The experimental results obtained with the OPA scheme utilizing the 17 mm long AGS crystal are divided in two groups. The first group of measurements deals with the amplified energy of the FELIX pulse. The energy of the amplified pulse is determined for several wavelengths. The second group includes the spectral and temporal measurements for the input and amplified pulses at 6.3 μm.

Energy measurements

In this section the dependence of the amplified pulse energy on two parameters: the pump energy and the signal energy is described. These dependences are determined for several signal wavelengths in the range 5-10 μm.

Most measurements were performed at 6.3 μm, a wavelength close to 6 μm for which the crystal was optimised for type I ooe interaction. At 6.3 μm there is a small gap in atmospheric absorption. The transmittance in the vicinity of 6.3 μm is shown is Figure 7-4, which is just a detail from Figure 7-3.

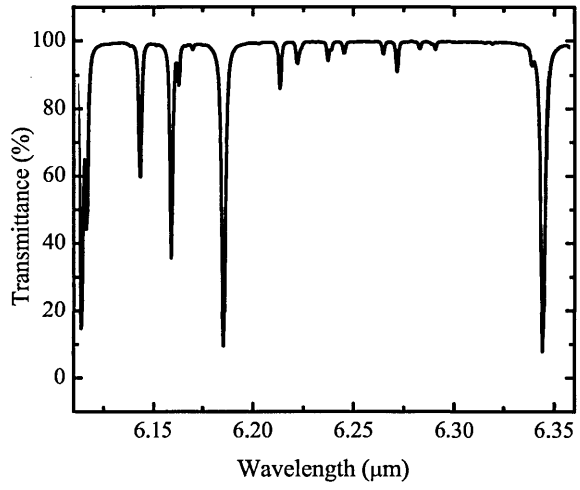

Figure 7-4 Transmittance in air at normal atmospheric pressure around 6.3 μm. The wavelength was chosen in the small gap present between two strong absorption peaks

Other measurements in this section were performed around 8, 9 and 10 μm, where the absorption in water vapours in the atmosphere is not present.

The dependences of the amplified energy on the pump energy for different input signal energies, at 6.3 μm, are plotted in Figure 7-5 and Figure 7-6.

Figure 7-5 (a)-(f) shows the amplified energy of the FELIX micropulse as a function of the pump energy. In the presented plots, a comparison is made between the experimental results (squares) and the calculated values in the non-saturated regime, in the fixed-field plane wave approximation, described in Chapter 3, section 3.2. The circles show the simulation for the calculated energy, for each input signal pulse energy. For all curves, the same gain was considered, the one that approximates the best is the lowest input energy used in the experiment (1.5 μJ). The case of the lowest input signal energy (a) is the best approximation of the un-saturated regime (even if it does not fit perfectly to it, due to saturation effects). For higher input signal energies, the departure from the un-saturated regime is more significant as it appears from the comparison between the experimental data and the simulations.

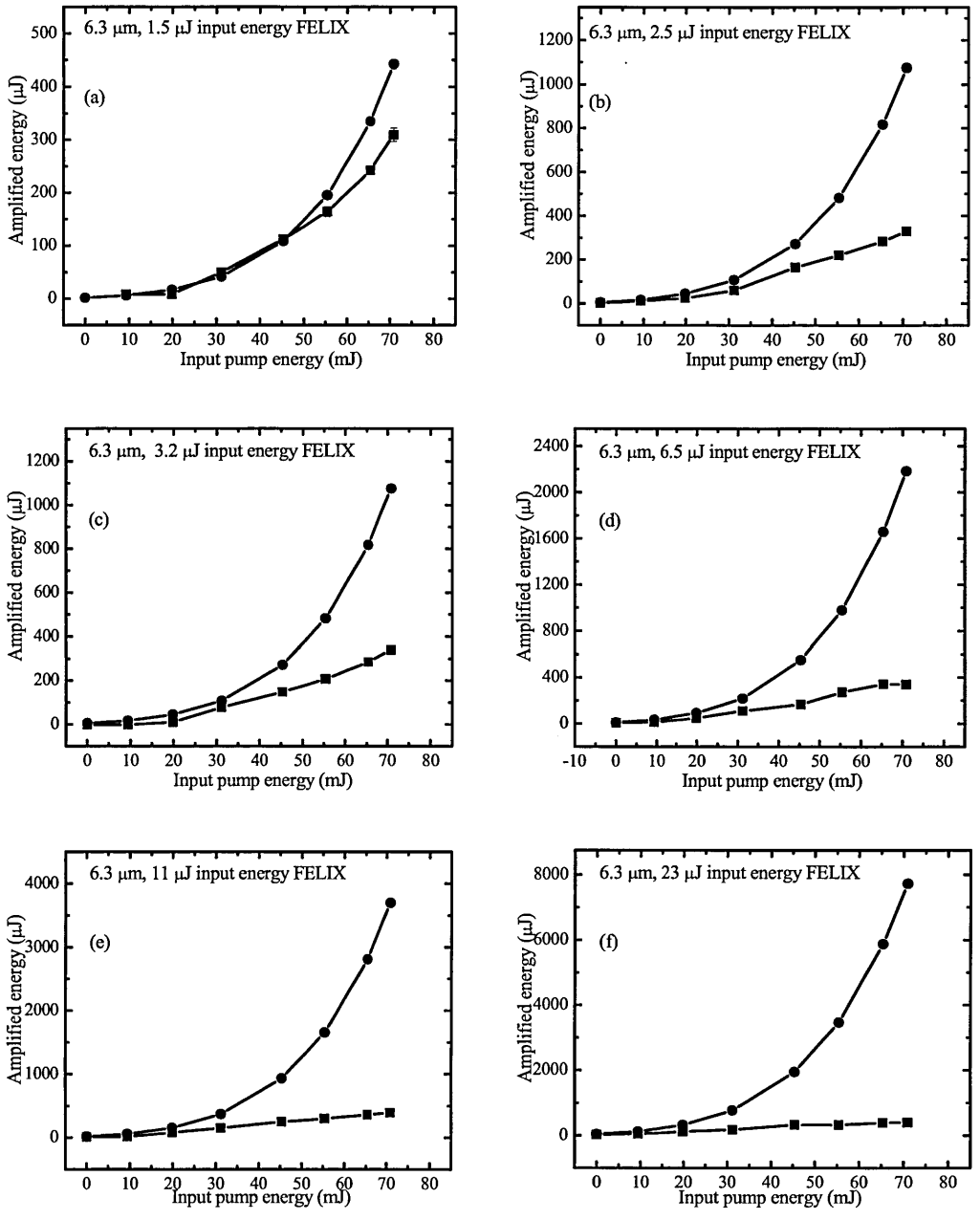

Figure 7-5 (a)-(f) Amplified energy as a function of the pump energy for different input FEL pulse energies, mentioned on each figure. The squares show the experimental results, while the circles present the results of simulations, in the plane-wave, fixed-field approximation described in Chapter3, section 3.2. The visible departure of the experimental data from the ideal case indicates the influence of the transverse intensity distribution in the two beams and the saturation effect. Saturation is revealed by the decrease of the gain with the increasing signal energy, while the influence of the beam size is related to the low value of the parametric gain compared to the expected one, in the case of the lowest input signal energy, and is caused by the variable pump intensity in the cross section of the signal beam.

The gain is expressed in the form given by Eq. 3-5. A field gain coefficient (defined in Chapter 3, Eq. 3.7) can be evaluated with this low input signal energy. With an 85 ps pump pulse length and 11 mm FWHM beam diameter for the pump it

results g=8.702x10^{-5} $\sqrt{\text{Watt}}$. The field gain coefficient g can be alternatively calculated with Eqs. 3.6 and 3.7. For the gain coefficient the SNLO code gives a value of 1.71x10^{-4} $\sqrt{\text{Watt}}$. The difference between the two values is due mostly to the Gaussian profiles of the two beams. The parametric gain is a ratio of two intensities, none of them spatially uniform. As a result, the overall amplification factor cannot be expressed as a ratio of two intensities and it necessitates much more complicated calculations. Nevertheless, the comparison for different input signal energies with the values calculated with the same amplification factors gives a clear indication of the increased saturation effect in the amplification gain: the curves with increased signal intensity are farther from the fix-field approximation.

A possible cause of low value of the field gain coefficient used for simulations in Figure 7-5 can be the fact that the amplification is already saturated at the input signal energy of 1.5 μJ, and Eqs. 3.6 and 3.7 used for calculating the field gain coefficient are valid for the unsaturated regime.

Saturation is also revealed by Figure 7-6 (a) and (b). In Figure 7-6 (a), the dependence of the amplified energy shows only a slight increase with the input signal energy, while the amplification factor sensitively decreases with the signal input intensity. As expected, the saturation effect is also determined by the pump beam intensity. The saturation effect is much more pronounced for high pump energies than for the low ones as shown in Figure 7-6.

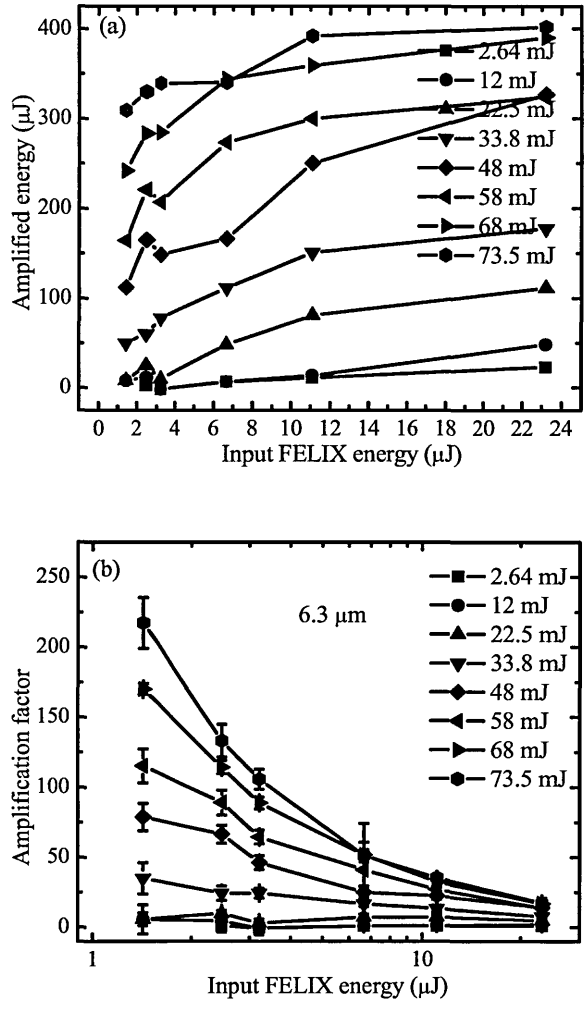

Figure 7-6 Amplified energy (a) and amplification factor (b) as a function of the input pulse energy of FELIX, at 6.3μm, for different pump energies. The signal bandwidth for these measurements was ~18 nm. The saturation effect is more pronounced for higher input signal energy and higher pump energy, and is shown by the decrease of the amplification factor with the input signal energy.

In Figure 7-7 (a) and (b) and Figure 7-8 the experimental results and simulations at 8.8 μm and 10 μm signal wavelength are plotted, as a function of the pump energy. In this case, the simulations have been performed with the 2D_MIX_SP function of the SNLO code [4]. The simulations are described in Chapter 6. The input parameters for the simulations presented in Figure 7-7 (a) and (b) are listed in Table 7-1.

	Signal	Idler	Pump
Wavelengths [nm]	8800	1210.3	1064
Index of refraction	2.368	2.443	2.434
Group velocity index	2.453	2.516	2.531
Group velocity dispersion (cm/sec-cm-^{1})	3.66E5	-1.29E5	-1.56E5
Input face reflectivity	0.1	0.1	0.08
Output face reflectivity	0.1	0.1	0.08
Crystal absorption [1/mm]	.03	.001	.001
Pulse energy (J)	2.4E-6	0	8E-2
Pulse duration [ps]	4	3	85
Pulse delay relative to pump [ps]	0	0	
Pulse chirp (THz/ps)	0	0	0
Beam diameters [mm]	9	8	11
Walkoff angle [mrad]	0	0	21.77
Radius of curvature [mm]	1.00E12	1.00E12	1.00E12
Number of t,x,y points	1024	32	32
Size of the crystal/grid [mm]	17	13	9
$D_{effective}$ [pm/V]	9.86		
Delta k [1/mm]	0		
z integration steps	100		

Table 7-1 The main input parameters for simulations presented in Figure 7-7 (a) and (b).

The amplified energy reaches values of hundreds of microjoules, but the simulations do not confirm the dependence of the amplified signal energy on the pump energy. The saturation level of the experimental results seems to be less than the one shown by simulations. Thus, for low pump energies, simulations predict a higher amplified energy, indicating a higher gain, while for high pump energies, the gain is saturated and the high values of amplified energy obtained in experiments could not be explained.

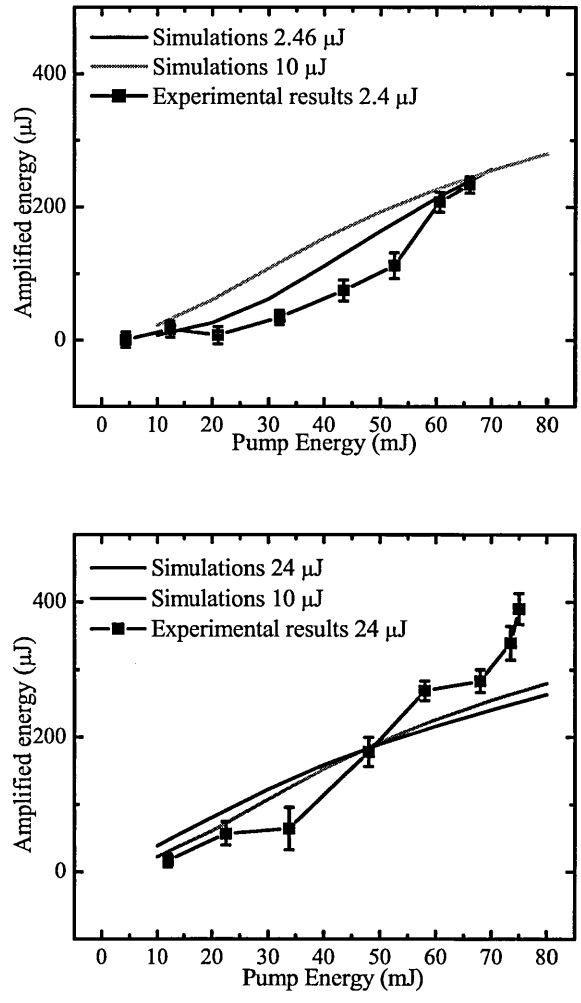

Figure 7-7 Amplified energy against the pump energy at 8.8 μm and input energy of ~2.4 (a) and 24 μJ (b). Simulations are presented for the same input signal energies and for an intermediate value of 10 μJ. The simulations show a higher gain (or amplification factor), that determines higher amplified energies at lower pump energies than the ones determined experimentally, and a stronger degree of saturation that limits the value of the amplified energy at higher pump energies.

This lack of agreement between simulations and experimental results of the amplified energy is consistently shown for OPA, but they are more pronounced at lower wavelengths. An example is given in Figure 7-7. More detailed simulations are presented in Chapter 6.

Figure 7-8 presents the experimental results for the amplified energy obtained using a signal wavelength of 10 μm and three different input signal energies, and compares these results with two simulated plots. The plots show the dependence of the energy of the amplified pulse on the pump energy. The simulated plots show higher gain than the experimental ones.

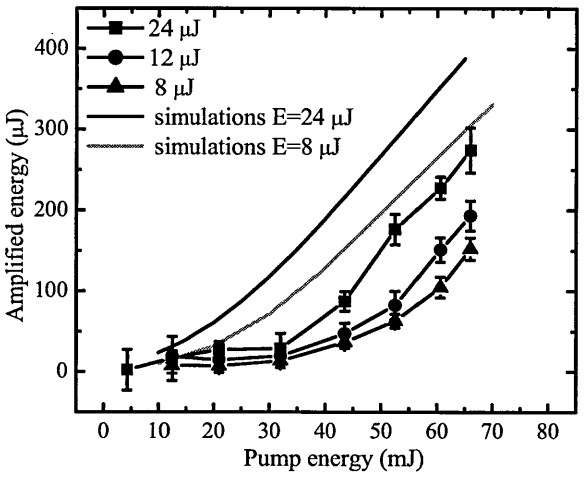

Figure 7-8 Measured energy of the amplified pulse against the pump energy at 10 μm at three different input signal energy: 24 μJ, 12 μJ and 8 μJ. Values as high as few hundreds microjoules are obtained for high input pump energy and signal input energy of 24 μJ. The simulations show higher gain than the experimental results

A common feature of the plots presenting the results of the amplified energy as a function of wavelength is the gain saturation for the maximum input pulse energy. The saturation is not as strong as the one shown by simulations. As can be understood from crystal properties (the nonlinear constant is higher for shorter wavelengths), and from experimental results, the level of saturation is stronger at shorter wavelengths. This is generally due to the higher values of the gain at shorter wavelengths as described in Chapter 3 (Eq. (3-5)). The crystal transmission (see Chapter 5 for more details) is also very much dependent on wavelength, with the lowest transmission of ~ 25% at around 9.6 μm and the highest transmission of about 80 % at 5-6 μm.

Spectral measurements and autocorrelation traces

As shown by Knippels et al. [5], FELIX micropulses are transform-limited with a temporal shape close to Gaussian. The spectral-temporal properties of the micropulses can be adjusted by varying FEL parameters like cavity length. Nevertheless, the spectral and temporal features of the micropulse are not identical in the micropulses train, but they depend on the position in the train. Depending on the level of the parametric gain, the parametric amplification can strongly influence the properties of the pulse being amplified. This influence depends on factors like the bandwidth acceptance of the crystal, crystal length, initial bandwidth of the pulse,

the level of saturation, the initial irradiance of the signal pulse and pump irradiance, phase matching angles. Not all of these factors are independent. For example, the bandwidth acceptance and the length of the crystal are related to the initial bandwidth of the pulse; a broad bandwidth is narrowed in a long crystal with a small bandwidth acceptance; on the other hand the bandwidth acceptance depends on the phase matching angles, and on the degree of noncollinearity between the signal and the idler beams. Because the parametric gain is higher at shorter wavelengths, the effects of saturation are more pronounced for shorter wavelength measurements; moreover, in our experiments the beam diameter increases with wavelength, leading to higher intensities for shorter wavelengths.

In this section, only experimental spectra of the incident and amplified pulses measured at a central wavelength of 6.3 μm are presented. More relevant results will be shown for the reconditioned crystal, in one of the next sections (Spectral and temporal measurements).

The spectral measurements taken at 6.3 μm did not show significant changes of the pulse spectrum. The results are presented in Figure 7-9. The spectral bandwidth tends to decrease, showing the effect of gain narrowing. This spectral narrowing is due to the low pump energy of the pump pulse. The influence of the amplification process is enhanced by the pump energy. At high pump energy, the effects of saturation manifest by spectrum broadening and distorted lineshape, as it will be proven by the later results. In a regime with a low gain the main influence is due to the initial pulse bandwidth. If this bandwidth is comparable to the bandwidth acceptance of the crystal, the amplification process does not show a strong effect. The narrowing effect is due to the fact that the wavelengths close to the peak are more amplified than the wings because of the nonlinear character of the process, and the amplification is not strongly saturated.

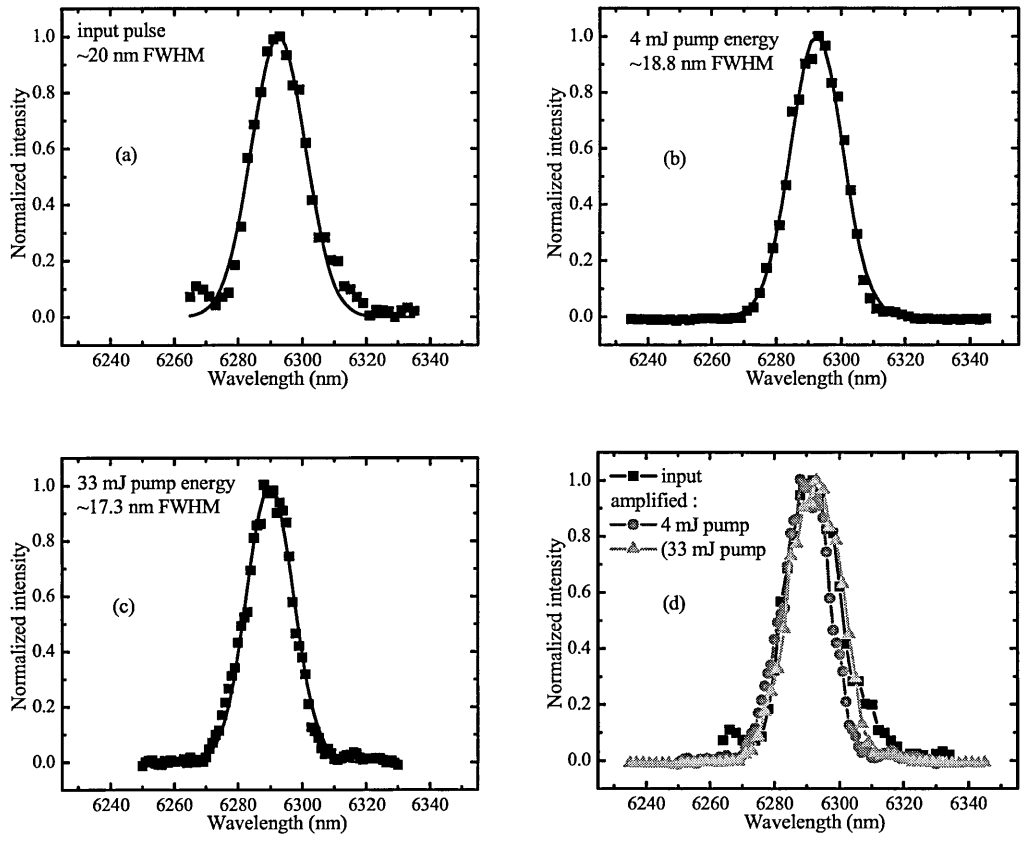

Figure 7-9 Normalized spectra of the not-amplified and amplified pulses at 6.29 μm for 17 mm crystal length. (a) The input, not-amplified pulse; (b) The amplified pulse at 4 mJ pump energy; (c) The amplified pulse at 33 mJ pump energy (d) A synthesis of (a), (b), (c) showing the slight narrowing with increasing energy. The squares show the experimental points, while the continuous lines are Gaussian fits of the spectra.

The influence of the amplification process on the output power of the amplified pulse is due not only to the value of the amplified energy, but also to the value of the pulse duration. The spectral modifications induce also modifications of the pulse shape. Assuming transform-limited pulses, the spectral narrowing is accompanied by pulse lengthening as can be seen in Figure 7-10 and Figure 7-11. Such effects are detrimental to the output pulse power. The effect depends on the pump pulse energy, initial pulse energy and initial bandwidth (pulse duration) so mainly on the gain and its dependence on wavelength, and on saturation level. The spectral modifications are due to the preferential amplification determined by the finite bandwidth acceptance of the crystal. The effect is more pronounced for shorter initial pulses (with broader spectra) and tends to narrow the spectral bandwidth and thus enlarge the pulse duration, as shown in Figure 7-10 and Figure 7-11. The relative broadening of the autocorrelation trace is more pronounced for shorter initial pulse duration, due to the larger bandwidth associated with it.

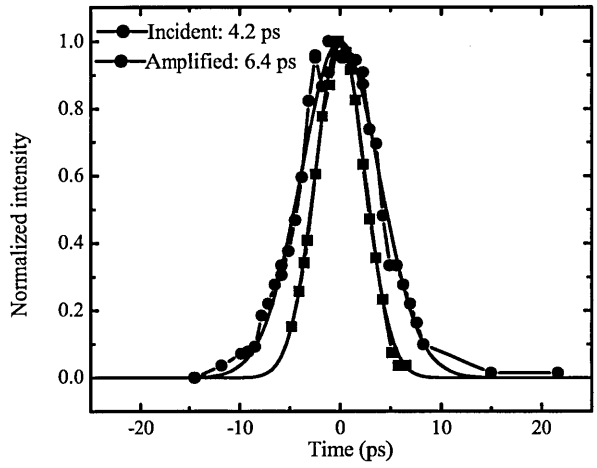

Figure 7-10 Autocorrelation traces for input and amplified pulses, at 6.3 μm and pump energy of 33 mJ. An initial pulse duration of approximately 4 ps increases to 6.5 ps due to the amplification process

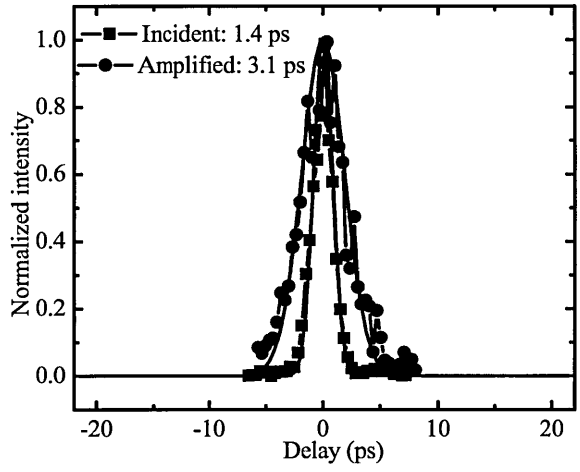

Figure 7-11 Autocorelation traces. Initial pulse duration is 1.4 ps. Amplified pulse duration at 30 mJ pump energy is 3.1 ps.

Because the spectra in Figure 7-9 were recorded independently from the traces in Figure 7-10 and Figure 7-11, a conclusion about the influence of the OPA process on the time-bandwidth product (defined as the product of the pulse duration with the bandwidth at FWHM) cannot be drawn. A spectral narrowing in the case of the initially transform-limited pulse can mean only a lengthening of the amplified pulse and this is also shown by autocorrelation traces.

7.2.2 Experimental results with the 16 mm long crystal

In this sub-section the experimental results obtained after reconditioning the crystal are presented. The values of the amplified energy obtained with the 16 mm

crystal did not differ very much from the ones obtained with the 17 mm crystal, mainly due to the improved transparency of the input/output antireflection coatings, which compensated for the loss in the length of the crystal. The results of the amplified signal energy are presented as a function of input signal energy and as a function of pump energy. A special attention is given to shorter wavelengths, were the saturation phenomenon in stronger than for the longer wavelengths, due to the increased value of the small-signal parametric gain.

Energy measurements

In this section the results obtained in OPA experiments for the amplified energy, at several wavelengths are presented.

Firstly, the results at wavelengths around 5.3 μm are presented. From reasons presented earlier in this chapter, the wavelengths were chosen in a range where water absorption is small. The transmission through air for 1m path length is presented in Figure 7-12, which is a detail of Figure 7-3.

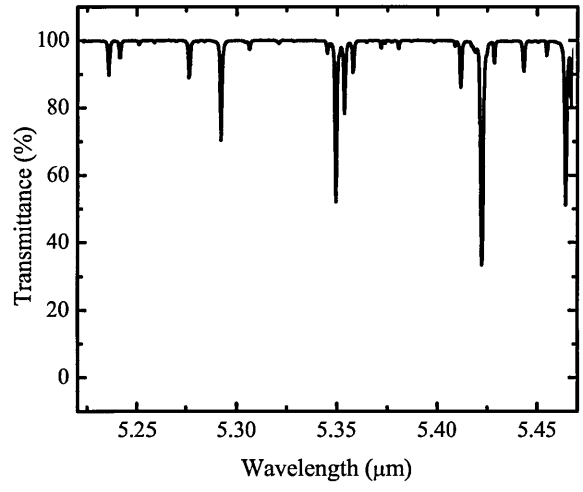

Figure 7-12 Absorption in air around 5.30 μm

Figure 7-13 and Figure 7-14(a) present the results obtained for the amplified energy at 5.33 μm, and 5.4 μm (respectively) as a function of pump energy. The values of the input energy (FELIX micropulse) are listed in each plot and they reflect the fact that the signal energy is varied in steps given by the available attenuators (3 dB, 10 dB, etc). They also reflect a different input FELIX energy, because results were measured with different FELIX settings. From both these plots, it can be noticed that, with increasing input signal energy, the dependence on the pump energy

evolves from an almost exponential shape to a linear one. As described in Chapter 3, the exponential increasing of the gain is characteristic to the non-saturated regime, while the almost linear regime is characteristic to the saturated one (the low gain approximation in Eq. 3.3). In Figure 7-13 and Figure 7-14 (b) the dependence of the energy of the amplified pulse as a function of the input signal energy, for several values of the pump energy, are shown. The values of the pump pulse energy are mentioned in the plot.

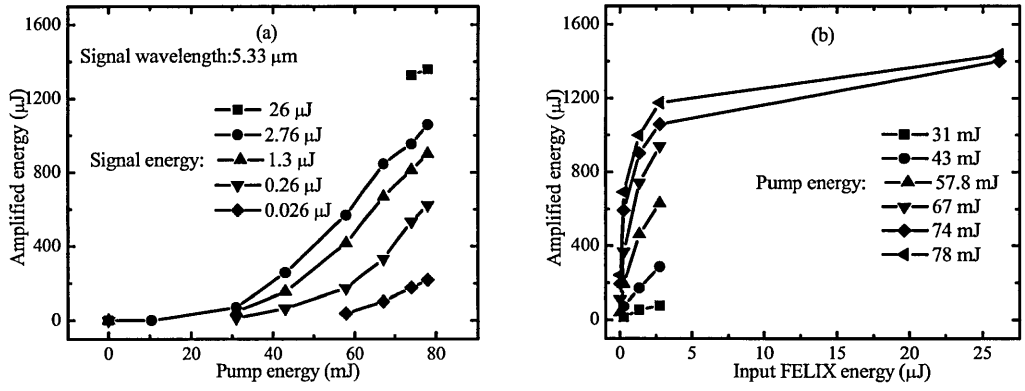

Figure 7-13 (a) The amplified energy as a function of pump energy at different FELIX input pulse energies, and 5.33 μm wavelength. Less experimental points were measured at 26 μJ input signal energy (b) Amplified energy as a function of FELIX input pulse energy for different pump energy at 5.33 μm wavelength

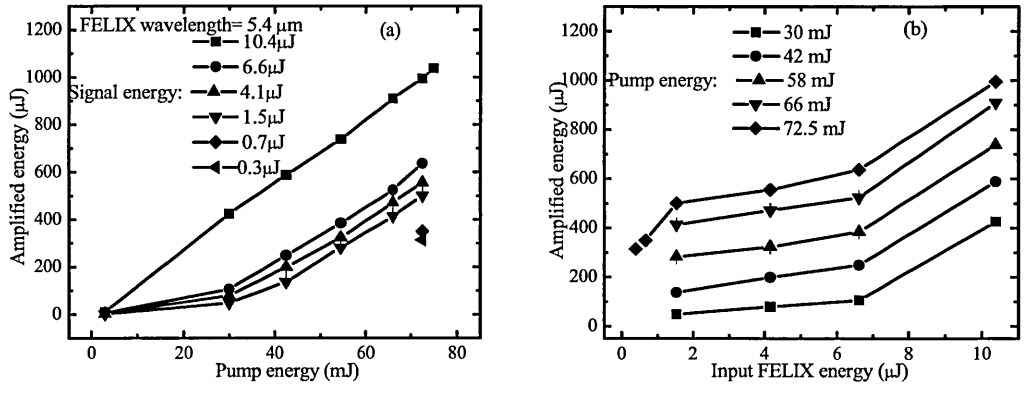

Figure 7-14 (a) The energy of the amplified pulse as a function of the pump energy and input signal energy for a not optimised temporal delay (10-15 ps off) at 5.4 μm wavelength. (b) is the same as a function of the input signal energy. In the plots are listed also the values of the signal and pump energies, respectively

A comparison between Figure 7-13 and Figure 7-14 reveals some differences in the behaviour of the amplified energy in the same conditions. In the plots presented in Figure 7-14, the delay between the pump and the signal pulses is not optimised and the energy of the amplified pulses are lower than in the case of Figure

7-13. That is why the maximum obtainable energies differ significantly, as well as the amplified pulse energy dependence on the input signal energy for the two cases.

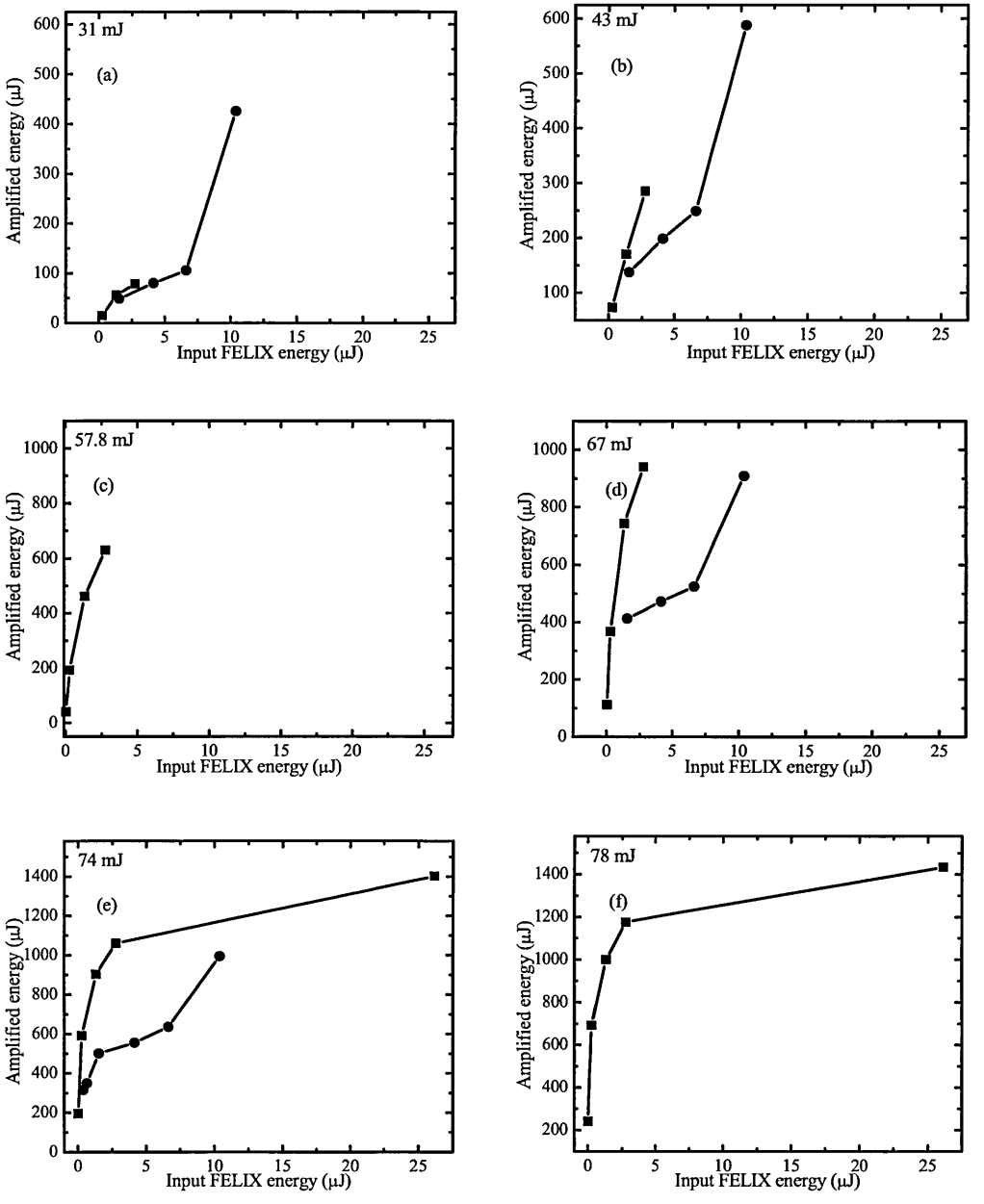

Figure 7-15 (a)-(f) Amplified energy as a function of FELIX input energy at 5.33 μm signal wavelength and different pump energies. With increasing pump energy the saturation effect is enhanced: the increase of the amplified energy is limited. For comparison, results obtained at 5.4 μm signal wavelength, but not optimised delay between pump and signal are plotted together, (when possible). The influence is very important at high pump energy and low input signal energy, and still significant (few hundred microjoules) at high signal input energy

It can be noticed a dramatic influence of the delay between the interacting pulses on the energy of the amplified pulse, even in the conditions of heavy saturation. The plots of the amplified pulse energy against the input signal energy are detailed in Figure 7-15. The differences are greater at low signal energies and high

pump energies, because the gain is higher at high pump intensities and less saturated at low energies. Due to the delay, the signal pulse interacts not with the maximum pump intensity, but with a lower pump intensity (the pulses have Gaussian temporal shape). The parametric gain is more sensitive to pump intensity variations when the signal intensity is low, because the process is not saturated. When both the signal and pump intensities are high, the saturation is stronger, and the parametric gain variation is less sensitive to the pump intensity changes.

Generally, the results show a strong saturation obtained for the 5.33-5.4 μm signal wavelength and high pump energy. Strong saturation is observed also for the 4.6 μm wavelength. Several values of the amplified pulse energy for three different values of the pump energy are shown in Figure 7-16 (a), while the dependence on pump energy is plotted in Figure 7-16 (b) for few values of the input signal energy. In Figure 7-16 (a) it can be noticed an almost flat dependence, proving the gain saturation.

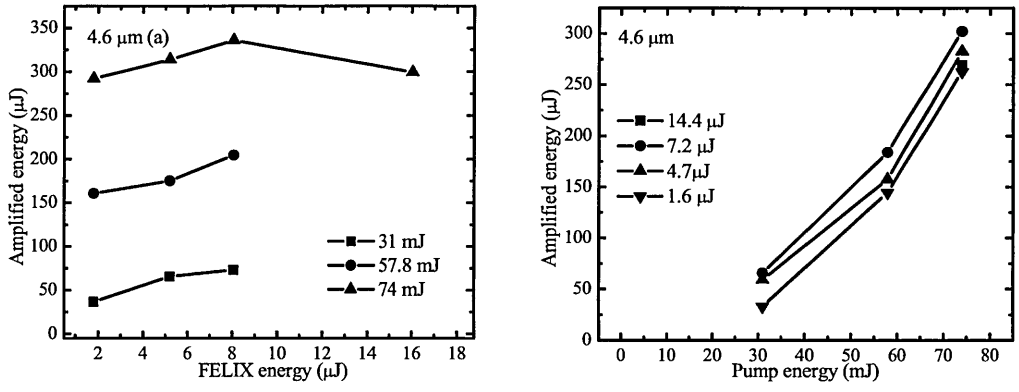

Figure 7-16 The energy of the amplified pulse as a function of input signal energy (a) and of the pump pulse energy (b) at 4.6 μm signal wavelength

Additional results of amplified energy as a function of the pump energy at other wavelengths are plotted in Figure 7-17-Figure 7-19. These measurements have been performed at longer wavelengths of the signal pulse (6.3 μm, 9 μm and 10 μm respectively). Input signal energies are 12 μJ, 14 μJ and 18 μJ respectively.

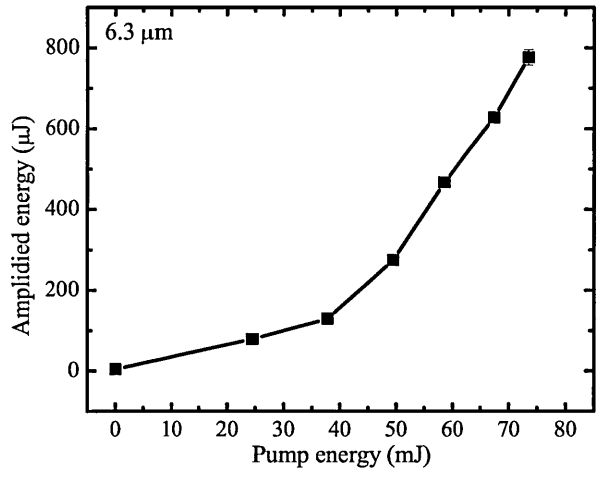

Figure 7-17 The amplified energy as a function of the pump pulse energy at 6.3 μm and 12 μJ input signal energy

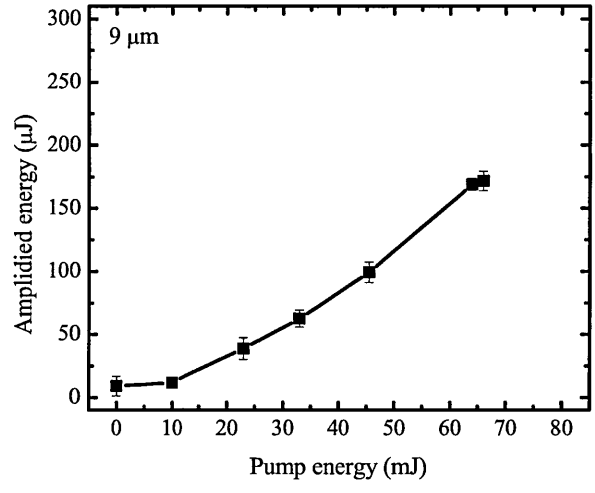

Figure 7-18 The amplified energy as a function of the pump pulse energy at 8.8 μm and 14 μJ input signal energy

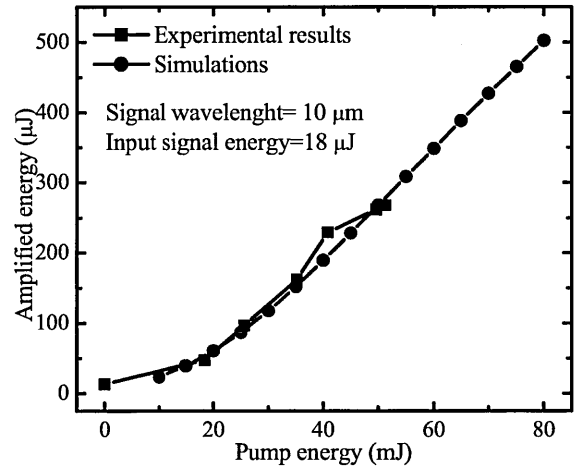

Figure 7-19 The amplified energy as a function of the pump pulse energy at 10 μm. The experimental results are shown together with the simulations.

The maximum energy of the amplified pulse decreases at longer wavelengths. The plots do not show deep saturation (the energy of the amplified pulse increases almost linearly with the pump irradiance only in Figure 7-19). This can be due to a not optimized delay between the pump and signal pulses, or to unstable behaviour of the seeding laser of the regenerative amplifier. In Figure 7-19 simulation performed with the SNLO code are presented together with the experimental results, showing a very good agreement.

In Figure 7-20, the maximum amplified energy is plotted as a function of wavelength.

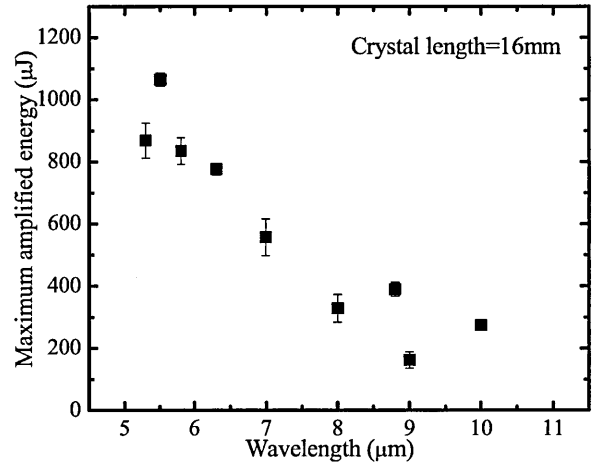

Figure 7-20 Energy of the amplified pulse as a function of the signal wavelength, at a pump power of 66 mJ. Beam diameters and input signal energies are different for each wavelength, but spectral width is 2%-3% from the central wavelength (respectively). The results are taken by scanning the FELIX wavelength and rotating the crystal for phase matching

There are various factors contribute to the picture of the dependence of the amplified pulse energy on the signal wavelength. As mentioned in Chapter 3, the parametric gain depends on the wavelengths involved in the nonlinear interaction and is higher for shorter wavelengths. The input energy and the beam diameters also depend on wavelength and on the FEL settings. The transmission of the crystal and the reflectivity of the coating are function of wavelength as shown in Chapter 5. The energy of the amplified pulses is very sensitive to the stability of the pump laser. A good operation involves efficient seeding of the regenerative amplifier and correct dumping of the amplified pulse from its cavity.

Spectral and temporal measurements

Spectra of the amplified pulses at short wavelengths showed pronounced effects of saturation and were distorted. In Figure 7-21, the spectra of the input and amplified pulses, at different input signal energies are presented. Even if the input pulse energy is decreased one thousand times, the spectrum is still is very much distorted; for the maximum input pulse energy (20 μJ) the distortion of the amplified pulse spectrum is the most pronounced and the formation of the double pulse is visible.

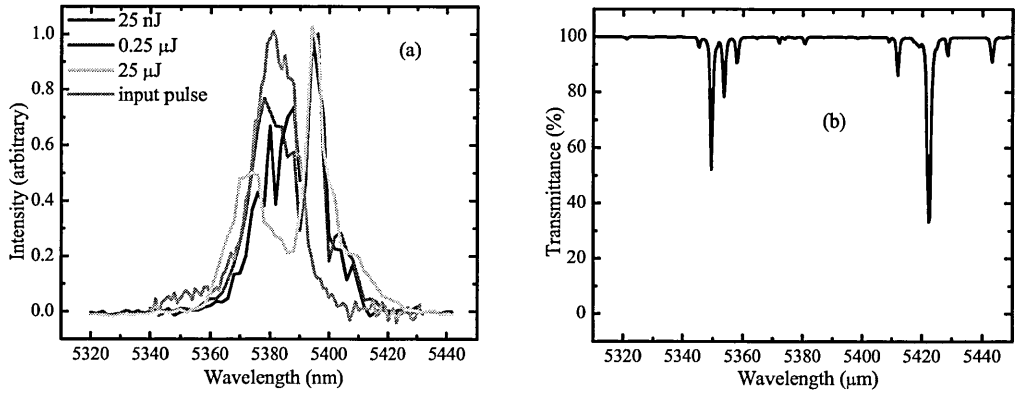

Figure 7-21 (a) Normalized spectra of the input (not amplified) pulse and of the amplified pulses for different input FELIX energy and a pump energy 74 mJ at an input central wavelength ~5380 nm (b) Transmittance in air around the central wavelength (5380 nm)

There are possible reasons for the observed asymmetry of the spectra: an initial chirp of the signal pulse, the phase mismatch, and the noncollinear character of the parametric interaction; the simulations performed with the SNLO code show symmetric spectra relatively to the central wavelength only in the case of the absence of the pulse chirp and no phase mismatch. Figure 7-22 presents the results with

simulations performed at a signal wavelength of 5.384 μm, pump energy 70 mJ, and different input signal energies, for a phase mismatch of Δk=-0.3 mm^{-1}. The pulse duration was taken ~2.5 ps, which is the transform-limited value of the measured FWHM spectrum width of the input pulse, shown in Figure 7-21.

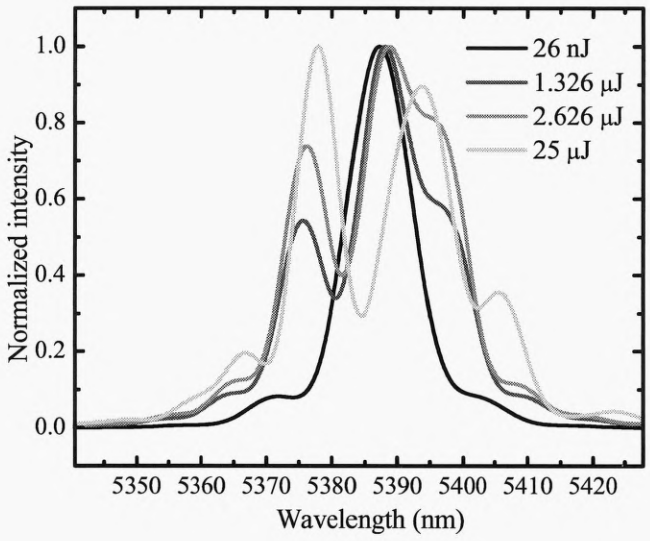

Figure 7-22 Simulations with SNLO code, with phase mismatch of Δk=-0.3 mm^{-1}. The pump energy is taken to be 70 mJ. The different curves show the spectral shape for different input signal energy: 26 nJ, 1.326 μJ, 2.626 μJ and 25 μJ

Because the path lengths for the input and amplified pulses are exactly the same, a linear absorption in atmosphere cannot cause such spectral effects. We did not investigate nonlinear absorption at this wavelength. When comparing simulation results in Figure 7-22 and normalized experimental spectra, shown in Figure 7-21 (a), one can notice similar (even if not-identical) distortions present in the amplified pulse, so that the phase mismatch is a possible cause of the pulse distortion during the OPA. The position of the dip created in the amplified spectra with phase mismatch depends on the value of the phase mismatch, on the input signal energy and on the pump energy.

In Figure 7-23 (a) shows a comparison between the (normalized) measured amplified pulse and normalized simulated pulse spectrum at 25 μJ input energy, and Δk=-0.3 mm^{-1}. Figure 7-23 (b) presents the corresponding simulated-pulse shape, revealing the presence of the multiple pulses. This results in a decrease of the amplified pulse peak power.

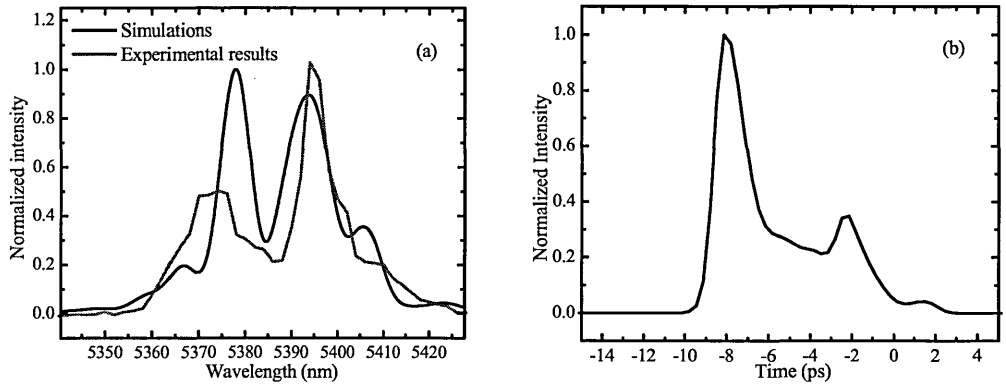

Figure 7-23 (a) Comparison between normalized experimental spectrum of the parametric amplified pulse and simulations for the input signal energy of 25 μJ. The pump energy is 70 mJ. Even if not identical, the shape of the spectrum obtained by simulations can explain the distortion present in the measured spectrum. The phase mismatch considered in simulations is Δk=-0.3 mm^{-1}. (b) The simulated pulse shape for the simulated-spectrum in (a) The developing of multiple pulse is visible

Figure 7-24 (a) presents spectral measurements at an input central wavelength of 4.580 μm. Figure 7-24 (a) illustrates the same behaviour (distortion) for input pulse energy of 15 μJ at a central wavelength of 4580 nm. The main difference between the spectra in Figure 7-21 (a) and Figure 7-24 (a) consists of the position of the first peak in the amplified pulse

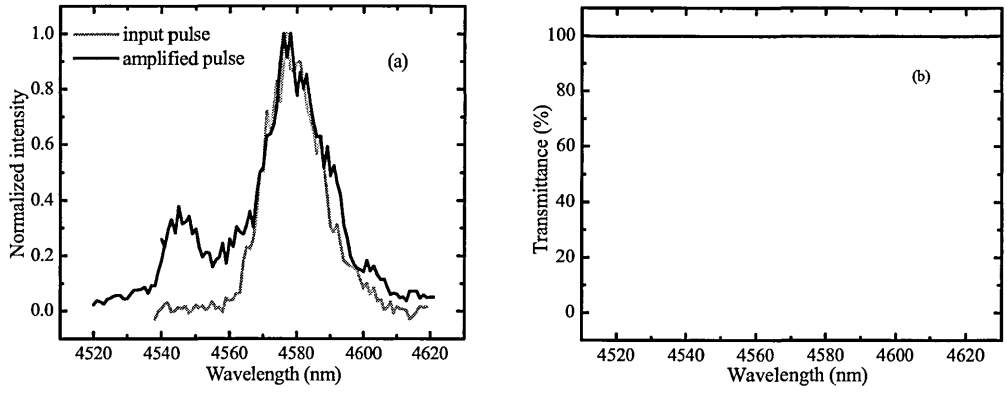

Figure 7-24 (a) Spectra of the input and amplified pulses for a pump energy 74 mJ at an input central wavelength ~4.580 μm and input energy of ~15 μJ. (b) The air-transmittance around the central wavelength (4580 nm), showing almost no (linear) absorption

In Figure 7-25, presenting similar measurements as Figure 7-21 (a) and Figure 7-24 (a), but performed at a central signal wavelength of 7.54 μm, a quite different situation can be noticed. Almost no difference between the spectra of the input and amplified pulses can be distinguished, even if they are measured at high pump energy (58-68 mJ).

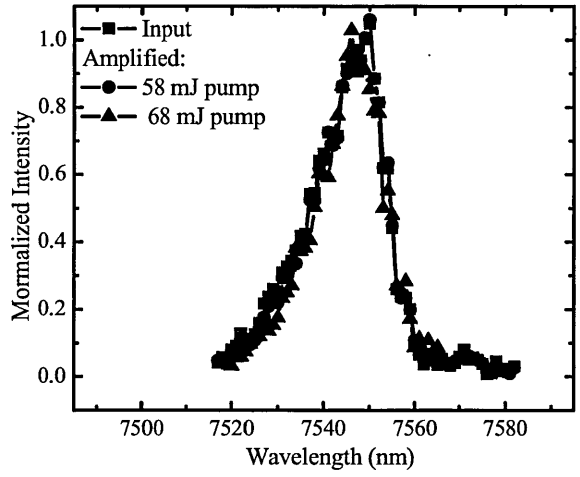

Figure 7-25 Normalized spectra of the input and amplified pulses at 7. 54 μm. The spectra of the amplified pulses do not show significant changes

As a conclusion of these results, the distortion effects increase with the increasing pump and signal irradiances, and they limit the peak power of the amplified pulse. The pulses are distorted by the amplification process mainly at short wavelengths. Because the gain at short wavelength is higher than at longer wavelengths, the same effects are not pronounced with increasing wavelength. The distortions in the pulses observed at short wavelengths can be explained by the phase-mismatch.

Bandwidth acceptance

The bandwidth acceptance is usually defined with respect to the parametric gain (see Chapter 3, Eq.3.11). As shown also in section 7.2.1, the parametric gain cannot characterize the overall behaviour of the amplified pulse. When spatial effects (or the transverse distribution of intensity) cannot be neglected, the parametric gain, which refers to a ratio of intensities, has a spatial distribution, and it cannot be used to characterize the overall energy gain. A more practical parameter can be the energy gain, or the energy amplification factor. Figure 7-26 (a) and (b) shows the measurements of the bandwidth acceptance of the signal at a central wavelength of 5.29 μm.

Using a Labview code available at FELIX facility, the signal wavelength was scanned, while the position of the crystal was fixed at the phase-matched position for the central wavelength 5.29 μm. The data measured with an energy meter head were recorded for each value of the signal wavelength. The input signal bandwidth was

approximately 10.4 nm, while the measured bandwidth acceptances were 31.6 nm (a) and 30.3 nm (b). This small difference is not significant, but it indicates the effect of (deep) saturation.

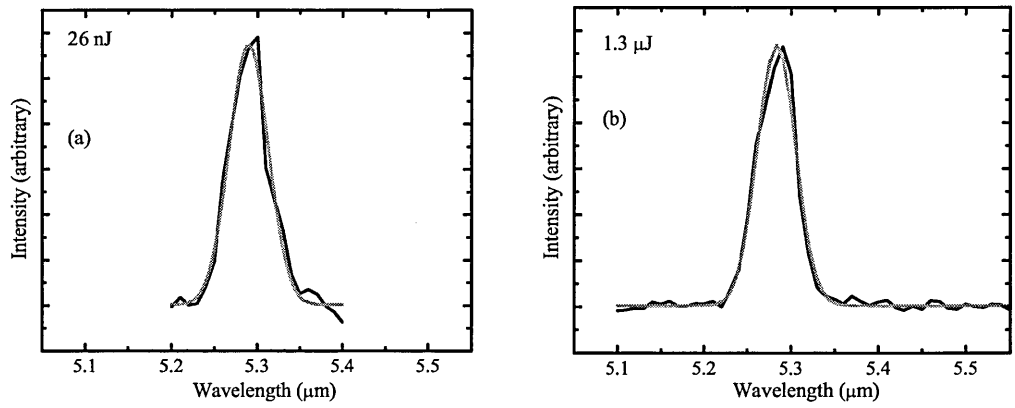

Figure 7-26 The energy gain (arbitrary units) for a signal wavelength at 5.29 μm. The measurements were taken for a pump energy of 74 mJ, and the signal pulse energy of (a) 26 nJ and (b) 1.3 μJ. The dashed lines represent the experimental results and the continuous lines Gaussian fits. It results an acceptance of ~31 nm

Autocorrelation traces

In this section, several autocorrelation traces, recorded at signal wavelengths of 6.3 μm and 7.52 μm are presented. The same procedure as described in 7.1.4 was applied. The results are presented in Figure 7-27 -Figure 7-30. The autocorrelation traces can be modified due to the bandwidth acceptance of the crystal or due to saturation. In Figure 7-27, the initial pulse is shorter than in Figure 7-28, so the bandwidth acceptance narrows the spectrum of the amplified pulse and the pulse will be consequently longer, yielding a broadened autocorrelation trace. In Figure 7-28, this effect is not visible because the input signal bandwidth is narrower, and the narrowing the bandwidth acceptance does not influence the duration of the amplified pulse. Both autocorrelation traces are recorded for relatively low input pump energy, 25 mJ.

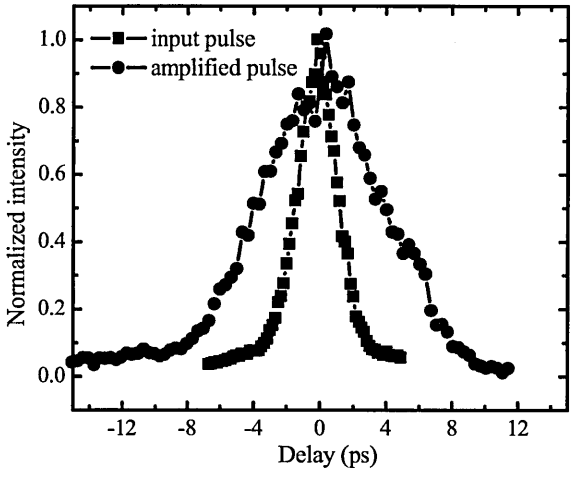

Figure 7-27 Autocorrelation traces of the input and amplified pulses at signal wavelength 6.3 μm and 25 mJ pump energy. The broadening of the autocorrelation trace indicates a lengthening of the amplified pulse, due to the gain narrowing

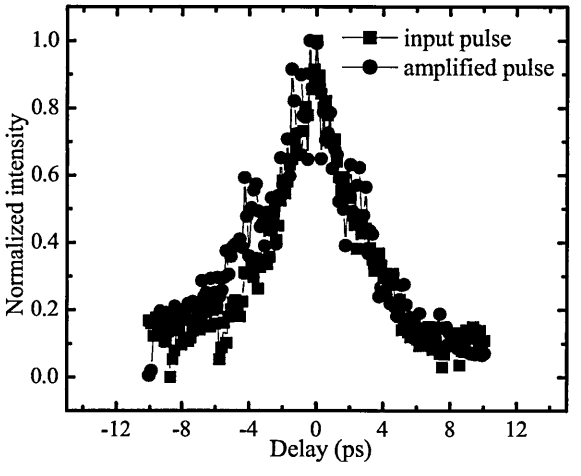

Figure 7-28 Autocorrelation traces of the input and amplified pulses at signal wavelength 6.3 μm and 25 mJ pump energy

A similar broadening effect as in Figure 7-27 can be observed in Figure 7-29. The measurements are performed at 7.52 μm signal wavelength, 4 μJ input signal energy, and 15 mJ pump energy.

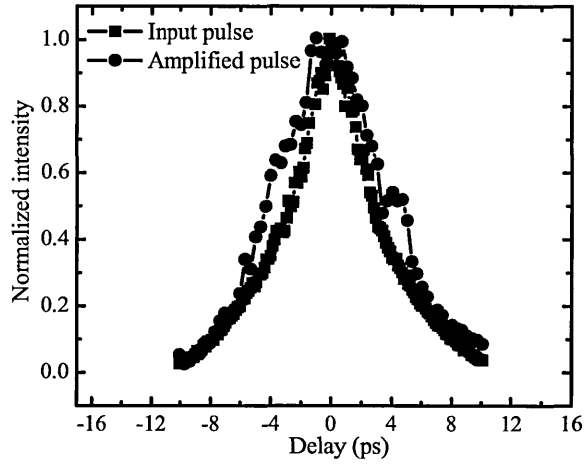

Figure 7-29 Normalized autotcorrelation traces of the input and amplified pulses, at 7.52 μm and 4 μJ input energy, and 15 mJ pump energy

If the spectrum of the input pulse has a bandwidth smaller or comparable to the bandwidth acceptance of the crystal, the main phenomenon influencing the autocorrelation trace is saturation. This is not present in Figure 7-27 because the pump energy was too low, but is noticeable in Figure 7-30, where the pump energy is 50 mJ.

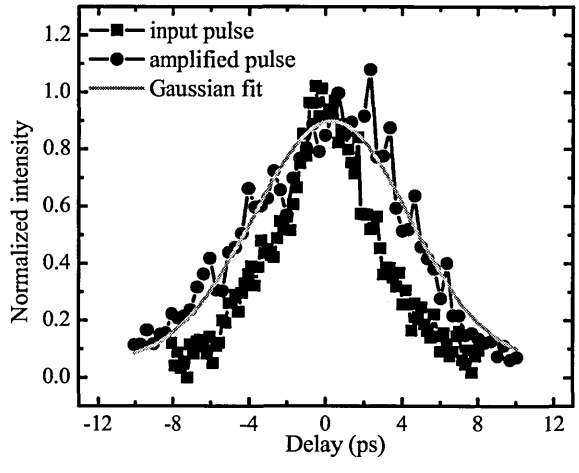

Figure 7-30 Autocorrelation traces at 6.3 μm, input signal energy 9 μJ and 50 mJ pump energy.

Measurements with variable delay

Measuring the intensity of the amplified signal as a function of the delay between the pump and signal pulses permitted to get information about the temporal shape of the pump pulse, without performing autocorrelation measurements. Thus, as appearing from Figure 7-31, the pump pulse contains a first peak at about 145 ps

before the main peak. The signal was recorded with a room-temperature MCT detector.

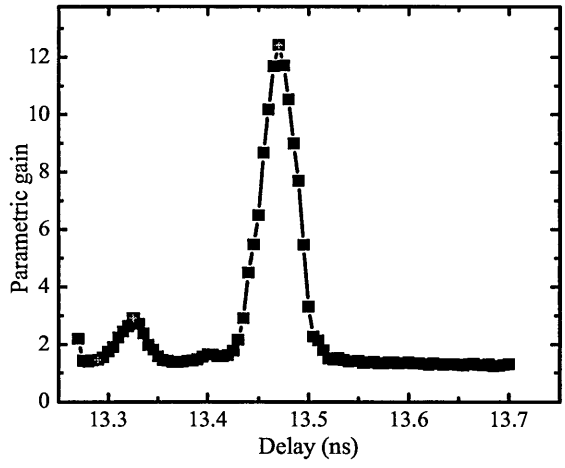

Figure 7-31 The parametric gain of the amplified signal as a function of the delay at 10.06 μm signal wavelength and 25 mJ pump energy, and 2 μJ input FELIX energy.

Similar measurements have been performed at 5.4 μm, but the MCT detector was replaced by the energy meter head. The delay was scanned around the maximum peak. The results are shown in Figure 7-32 and Figure 7-33. Figure 7-32 presents a comparison of the amplification factor for two different input energies of the input FELIX pulse. The different by a factor of ~ 15 dB and they are estimated to be 0.63 and 0.02 μJ respectively. The pump energy was 70 mJ, a value that shows indeed a strong saturation of the signal even for less than 1 μJ input. This is due to the decrease of the amplification factor with increasing pump intensity.

The FWHM in the three figures presenting the results of the energy or parametric gain measurements when scanning the delay differ considerably. For the main peak in the plot shown in Figure 7-31, the FWHM is 41.3 ps, for the 0.02 μJ input FELIX energy in Figure 7-32, the FHWM is 50.2 ps and for the 0.63 μJ input FELIX energy in are 46 ps for 30 mJ and 62 ps for 70 mJ pump energy. These variations show the highest value for the most saturated situation and the lowest for the less saturated one.

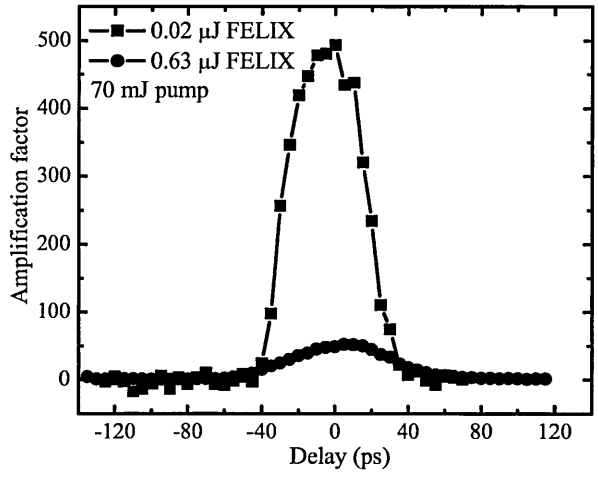

Figure 7-32 The amplification factor determined for two input energies of FELIX (0.02 μJ and 0.63 μJ) and 70 mJ pump energy. The amplification factor is almost 10 higher for the lower input energy

In Figure 7-33 the amplification factors at low pump energy (30 mJ) and high (70 mJ) pump energy are compared. The maximum values differ by a factor of 5.

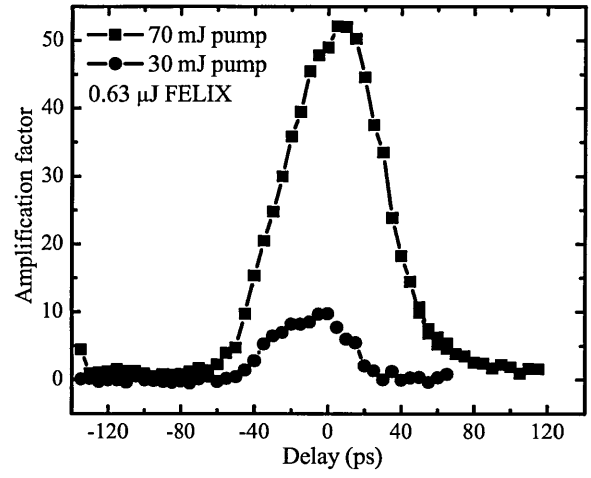

Figure 7-33 The amplification factor determined for two pump energies (30 mj and 70 mJ) FELIX (0.63 μJ) and 70 mJ pump energy

7.3 Conclusion

The experimental results presented in this chapter show strong saturation of the parametric amplified pulse. The degree of saturation is higher for the shorter wavelengths of the signal pulse. For shorter wavelengths, the amount of energy that can be obtained can exceed one millijoule, while for longer wavelengths, the amplified energy is limited to few hundreds microjoules. The measured spectra show

strong distortions for high amplified energies, i.e. in the first part of the range, while autocorrelation traces reveal enlargement of the pulse. These effects are not so pronounced for higher wavelengths. The strong saturation observed suggests a possible improvement of the amplified energy, because the saturation phenomenon limits the amplification factor. In a simple picture, if the initial signal pulse has the same input energy as in the strong-saturation situation and the same beam diameter, but longer pulse duration, the amplification factor could increase because longer pulse durations decrease the peak intensity of the incoming beam. Still, for a transform limited pulse, this can mean a decrease of the total available power (because of the longer pulse duration).

Because the pump pulse duration (85 ps) is much longer than the signal pulse duration (typically several picoseconds), a method of circumventing the saturation effects, with maintaining high output power, is stretching the signal pulse before amplification and compressing the amplified pulse after amplification. This method is called optical-chirped pulsed parametric amplification (OPCPA) and is presented in the next chapter, together with the experimental results.

7.4 Bibliography

1.http://www.jobinyvon.com/usadivisions/Mono/triax320322.htm

2.http://www.coherent.de/laserzubehoer/download/Molectron/MolectronProductCatalog.pdf

3.J. Xu, G.M.H. Knippels, D. Oepts, and A.F.G. van der Meer, "*A far-infrared broadband (8.5-37 μm) autocorrelator with sub-picosecond time resolution based on cadmium telluride*", Opt. Commun., Vol. 197, pp. 379-383, 2001

4.SNLO nonlinear optics code, available from A. V. Smith, Sandia National Laboratories, Albuquerque, NM- 87185-1423

5.G.M.H. Knippels, R.F.X.A.M. Mols, A.F.G. van der Meer, D. Oepts and P.W. van Amersfoort,"*Intense far-infrared free-electron laser pulses with a length of six optical cycles*", Phys. Rev. Lett., Vol. 75, pp.1755-1758, 1995

Chapter 8 Optical Parametrical Chirped-Pulse Amplification

This chapter describes a technique introduced to enhance the power of the parametrically-amplified FELIX pulse. It was shown in Chapter 6, that the power of the amplified pulse is limited by saturation. The method presented in this chapter (the optical chirped pulse amplification) is introduced to overcome the un-wanted saturation effects and improve the amplified energy. Firstly, the principle is described, followed by the experimental set-up, experimental results and discussion. Using the optical chirped pulse amplification technique, energies of the stretched amplified pulse of more than two milijoules have been obtained. For the compressed pulse the energy decreased to 1 milijoule due to reflection losses in the compressor. The maximum amplified energy varies with the maximum available energy from FELIX, transmission properties of the stretcher/compressor the nonlinear crystal and with the efficiency of the nonlinear process.

8.1 Introduction

The Optical Chirped Pulse Amplification (OPCPA) is a technique of amplification of optical pulses, which applies the Chirped Pulse Amplification (CPA) to optical parametric amplification (OPA). The scheme of OPCPA principle is shown in Figure 8-1.

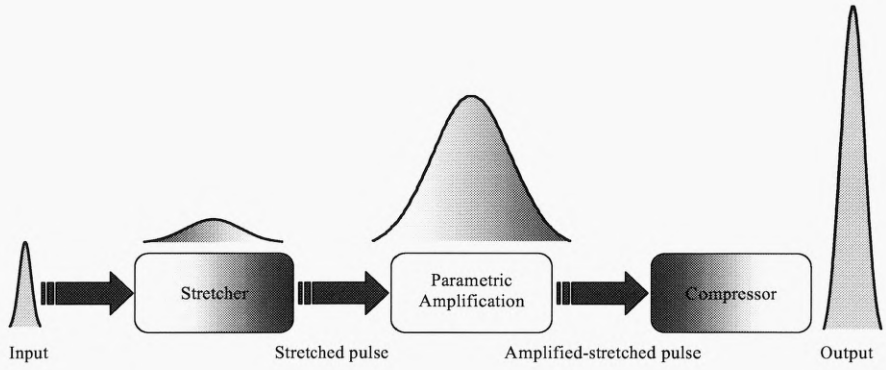

Figure 8-1 The OPCPA scheme. The signal pulse is first stretched in a stretcher, then amplified, and finally compressed in a compressor

CPA is used to improve the features of the amplified pulse, by overcoming the effects of strong saturation in the amplifying medium. If a short signal interacts with a long pump pulse, the pump is not effectively depleted. This is achieved by enlarging the duration of the pulse to be amplified, which in turn decreases the intensity of the signal pulse. The method is effective if the pump pulse is much

longer than the signal, and the stretched signal, in the whole frequency range, still interacts with high pump intensity. The pulse is first chirped in a device called optical stretcher, then amplified in an optical amplifier (a nonlinear crystal in the case of OPCPA, by parametrical interaction with a strong pump beam), and compressed back to a short pulse duration in a pulse compressor. A higher amplified energy and much better spectral, spatial and temporal features of the amplified pulses can be achieved using CPA. Thus, this method was a revolutionary technique for the performances of regenerative amplifiers and was first proposed by Mourou et al. [1], while the use of OPCPA was first suggested by Dubietis et al [2]. CPA is aplicable to tabletop-size systems as well as to large laser chains. In the case of OPCPA, the laser amplifier is replaced by an OPA stage. OPCPA was extensively used by different other groups [3-15]. Theoretical (numerical) studies for describing and optimising the OPCPA process have been performed in several publications [3, 4, 8-10, 12 - 14, 16].

However, the method has never been applied to the mid-infrared, using an AGS crystal. In our experiments, the OPCPA technique is used for the first to time to amplify FEL pulses. A great advantage is the rapid tunability of the FEL without any change in the alignment of the incoming pulse on the optical table, which makes the method easy to use and to adapt for different wavelengths; the only necessary adjustments are the rotation of the crystal and of the gratings in the stretcher-compressor system.

The choice of this method for increasing the amplified energy of the FELIX micropulse is based on several considerations related to the need of surmounting the saturation effect. Basically, there are three ways to do this: attenuating the energy, enlarging the beam-size, or/and stretching the pulse duration. The size of the crystal can limit the efficiency of enlarging the beam diameter. The initial diameter of the FELIX beam is already comparable to the size of the crystal. If the beam diameter becomes too large the losses at the crystal can reduce the amplified energy. On the other hand, a large signal beam requires an enlargement of the pump beam and corresponding increase in the pump power, which can cause damage at the optics transporting the pump pulse to the experimental table. In addition, large crystals are difficult to obtain and hence less available. The temporal stretching of the pulse (and consequently the use of the OPCPA technique) seemed to be the best choice for increasing the extracted amplified energy. Even if accompanied by a decrease in the

(stretched) pulse energy due to the inherent losses at the optics of the stretcher, this inconvenience is compensated by the increased amplification factor in the nonlinear crystal leading to maximum amplified energies of more than 2 mJ and energies of the compressed pulse of 1 mJ.

8.2 The experimental setup

The experimental setup, following the scheme presented in Figure 8-1, is presented in Figure 8-2. It consists of a setup similar to the one used for the OPA experiments, already described in Chpater 6. The main difference between the OPCPA and OPA schemes resides in the presence of the stretcher (before the OPA setup) and the compressor (after OPA set-up).

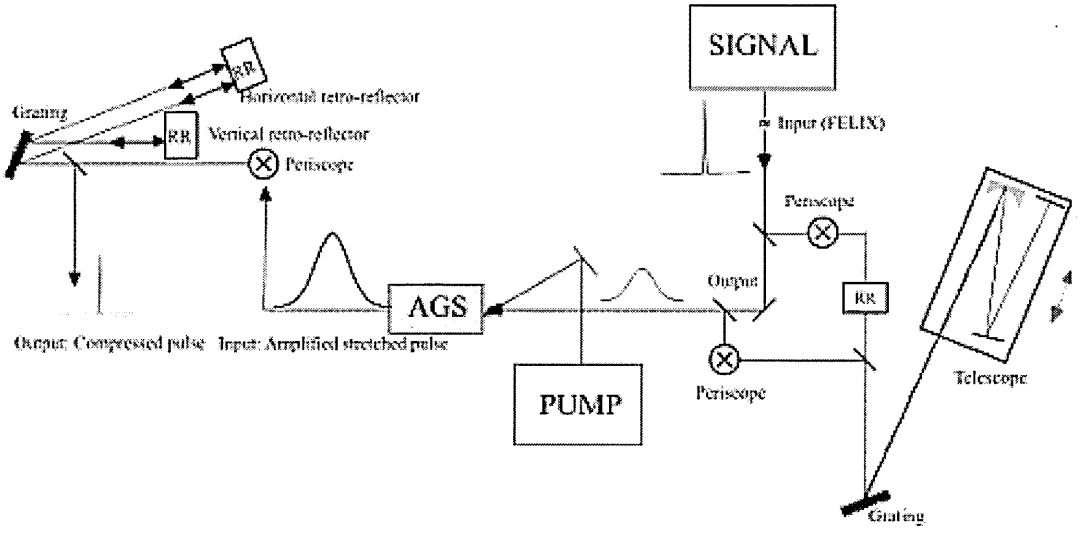

Figure 8-2 Experimental setup. The signal pulse provided by the FEL is first stretched in an all-reflective grating stretcher. The stretched pulse duration can be adjusted by moving the telescope in the horizontal plane, while the grating can be rotated to ensure the correct alignment for different values of the signal pulse wavelength. After amplification in the nonlinear crystal (AGS) the pulse is compressed in the pulse compressor, similar to the stretcher, but the telescope is replaced with an horizontal retroreflector.

Because the OPA setup has already been described, including the lasers and the crystal, only the specific parts of the OPCPA scheme are described in the following section: the stretcher and the compressor.

Before interacting with the pump pulse in the nonlinear crystal, the signal pulse provided by FELIX, enters the stretcher and passes it twice. In the stretcher the pulse duration is lengthened. The polarization of the input beam is flipped by 90 degrees at both entrance and exit of the stretcher. This is done because in the

experiment a vertical polarization of the mid-infrared pulse is required for type I ooe interaction with the pump pulse in the crystal, while the diffraction grating is more efficient for the horizontal polarization. In the mean time, some flip mirrors (not shown in the figure) can alternatively direct the beam to the crystal, for the OPA experiment. Redirecting the beam path directly to the crystal is also necessary for measuring the input pulse spectrum and recording autocorrelation trace, because the autocorrelator and spectrometer are situated after the crystal. Even though it is possible to automatically control the polarization of the FEL pulse, it is preferable to maintain the same polarization of the input FELIX pulse for both schemes because the automatic change can result in a slight misalignment of the beam on the optical table. This is due to the backlash effects and is enough to create problems for the long paths of the mid-infrared beam in the stretcher/compressor system.

After passing through the stretcher, the pulse is amplified in the nonlinear crystal by nonlinear interaction with the pump pulse and it passes to the compressor in order to regain short pulse duration. The beam can be alternatively directed to the autocorrelator, or spectrometer. A more detailed description of the stretcher and compressor is given in the following sections.

8.2.1 The stretcher and the compressor

The stretcher and compressor are both classical all-reflective, one-grating stretcher devices. They chirp the incoming pulse in opposite ways. A transform limited pulse which passes the stretcher will have at the output a frequency distribution which varies in time: the "redder" light comes first and the "bluer" light comes later; the delay introduced between different wavelengths lengthen the initial pulse duration. The compressor acts in an opposite way: for an incoming transform-limited pulse, at the output of the compressor the blue light comes earlier than the red light.

In our experiment, the stretcher leads to a longer pulse, because at the input, the signal pulses from FELIX are transform limited, while the compressor restores the chirped (and amplified) pulse to a short pulse length, by compensating the delay between wavelengths of different colours.

The dispersing effect used by the stretcher and compressor to modify the pulse length (and ideally maintaining the spectrum) is based on the principle of two gratings.

The grating pair

The concept of the grating pair used for varying the pulse length in the stretcher and compressor is illustrated in Figure 8-3:

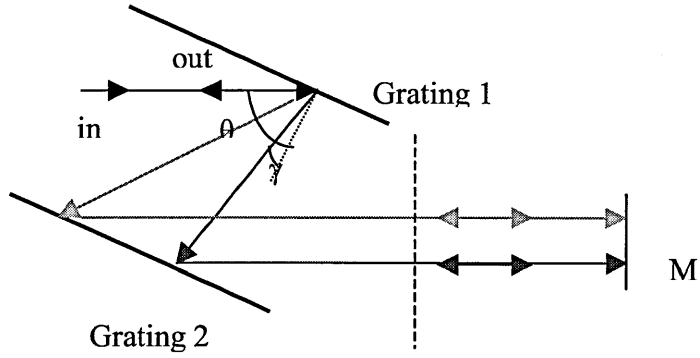

Figure 8-3 The principle of two diffraction gratings. The "red" light is delayed at the exit of the two gratings, due to the dispersive properties of the gratings. If the pair of gratings is passed only once, a spatial chirp appears at the exit (a colour distribution at the dashed line). The spatial chirp is removed by introducing the flat mirror M. For separating the input and output beams, the mirror can be replaced with a vertical retroreflector

The diffraction grating is a dispersive system, because, at the same incidence angle θ, the diffraction angle γ after the grating depends on the wavelength, according to the grating equation:

$$d(\sin(\theta) + \sin(\gamma)) = m\lambda \tag{8-1}$$

with m being the diffraction order, d the distance between the grooves and λ the wavelength. It is obvious that, because of different diffraction angles, the path lengths for different wavelengths passing through the grating system are different.
The optical frequency of a chirped-Gaussian pulse varies in time according to [17]:

$$\omega_i(t) = \omega_0(t) + 2bt \tag{8-2}$$

with $\omega = \frac{2\pi c}{\lambda}$ and b being the chirp parameter.
The electric field can be then expressed as:

$$E(t) \approx \exp(-at^2)\exp(j\,(\omega_0 t + bt^2)) \tag{8-3}$$

and the intensity:

$$I(t) \approx exp(-2at^2) \tag{8-4}$$

where a is the parameter of the Gaussian function and is related to the FWHM pulse duration $\Delta\tau$ by:

$$a = \frac{2\ln(2)}{(\Delta\tau)^2} \tag{8-5}$$

This formula can be easily derived from Eq.(8-4).

The problem of calculating the influence of the pair of gratings on the chirp and pulse duration of a Gaussian pulse reduces to calculation of parameters a and b after passing through the grating system. For a Gaussian pulse, after propagating through a dispersive medium, the parameters a and b vary with the propagation distance z according to [17]:

$$a(z) = \frac{a_0}{(1+2\beta'' z b_0)^2 + (2\beta'' z a_0)^2} \tag{8-6}$$

and:

$$b(z) = \frac{b_0(1+2\beta'' z b_0) + 2\beta'' z a_0^2}{(1+2\beta'' z b_0)^2 + (2\beta'' z a_0)^2} \tag{8-7}$$

with β'' the chirping parameter (the second order dispersion term), $\beta=k(\omega)$, $\beta'' = \frac{\partial^2\beta}{\partial\omega^2}$ a_0 and b_0 the input values for a and b and c the speed of light.

In the case of a pair of gratings, the chirping parameter is given by [18]:

$$\beta'' = -\frac{\lambda^3 m^2}{4\pi c d^2 \cos^2\gamma} \tag{8-8}$$

For an input transform-limited Gaussian pulse ($b_0=0, a_0 = \frac{2\ln(2)}{(\Delta\tau_0)^2}$), Eqs.(8-5) and (8-6) lead to:

$$a(z) = \frac{a_0}{1+(2\beta'' z a_0)^2}, \text{ or}$$

$$\Delta\tau(z)^2 = \Delta\tau_0^2 + \left(\frac{4\beta'' z \ln(2)}{\Delta\tau_0}\right)^2 \qquad (8\text{-}9)$$

$$b(z) = \frac{2\beta'' z a_0^{\,2}}{1 + (2\beta'' z a_0)^2} \qquad (8\text{-}10)$$

The relation between z and the distance between gratings, Δz, is expressed by: $z = \Delta z / \cos\gamma$

Eqs.(8-9), (8-10) express the dependence of the stretched pulse duration and chirp, after passing through the pair of gratings, on grating parameters, distance between gratings, angle of incidence and pulse characteristics (initial pulse duration, wavelength). For a given pulse duration and wavelength, the incidence angle and the diffraction grating can be chosen to obtain a desired stretched pulse length. However, if efficiency is an issue, the incidence angle cannot be arbitrary chosen, and has to be close to the Litrow configuration. An additional increase of the stretched pulse duration is achieved by multiple passing through the pair of gratings. In this case, calculations have to take into account the values of parameters a and b after each pass and consider them as input values for the next pass.

The stretcher

The stretcher is designed to stretch pulses of few picosecond in length in the wavelength range of 4-11 μm, to values comparable to the pump pulse length (85 ps) or more. The construction of the stretcher is equivalent to the pair of gratings, described above, but introducing a total positive chirp.

A schematic view of the stretcher is presented in Figure 8-4.

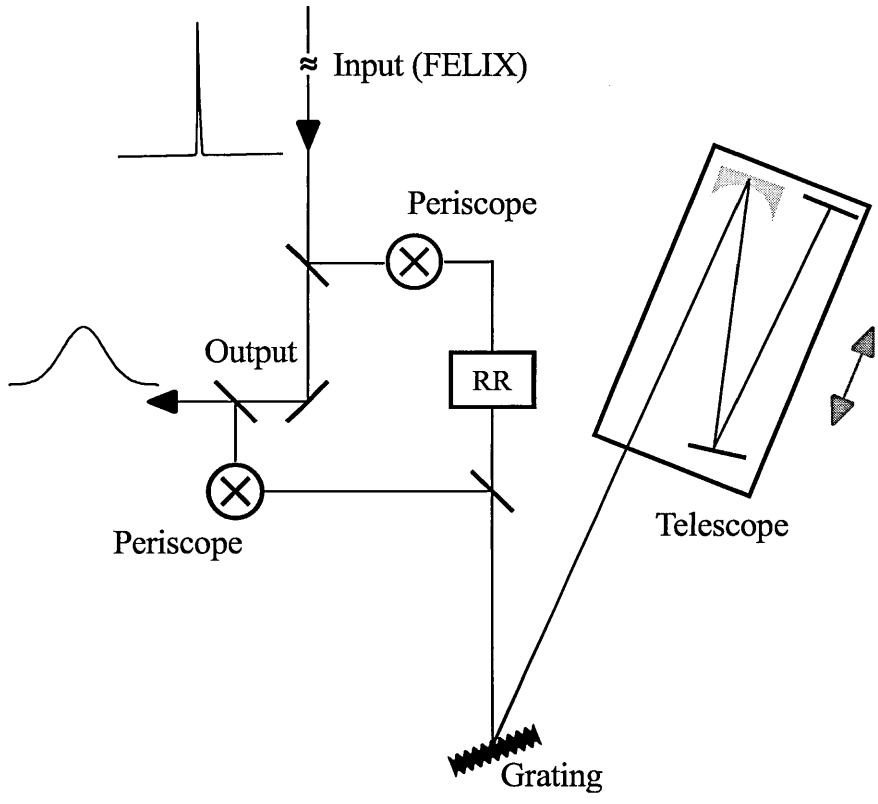

Figure 8-4 The stretcher consists of the grating and the telescope with magnification –1. The telescope consists of a concave mirror and a flat mirror in the focus of the concave one, and a folding mirror in between. The grating can be rotated around the vertical axis to adjust the diffraction angle for each incoming wavelength. RR is a vertical retroreflector used for redirecting the outgoing beam to the stretcher. The mirrors of the vertical RR are displaced in the vertical plane, such as the input pulse can pass through. After two ways through the stretcher, a flat gold mirror directs it to a periscope and amplification experiment. The first periscope at the entrance of the stretcher flips the polarization for the most efficient regime of the grating (s-polarization). The second periscope restores the polarization to vertical, as necessary for amplification experiment.

The stretcher consists of a diffraction grating (150 gr/mm, 26.7° blaze angle, Richardson Gratings Laboratory (Spectra Physics)) and a telescope with magnification –1. The telescope contains a concave mirror with a focal length of –1 m or –1.25 m, a flat mirror in the focus of the concave one, and a folding mirror in between. The diameter of the concave mirror is 10 cm, in both cases. Only one grating is used but the beam is redirected to it via the telescope in such a way that the beam path and dispersion effects are similar to an anti-parallel pair of gratings, with a "negative" distance in between, leading to a positive chirp (see Eqs.(8-8) and (8-10)).

The vertical retroreflector consists of two flat mirrors, gold plated, 4x6 cm^2 in size, with the largest length in the horizontal plane. They are positioned at 90 degrees with respect to each other with a tolerance of less than 1 degree in 8 m. When the

grating is positioned in the focus of the concave mirror, the pulse is ideally not stretched (z=0). If the distance from the grating to the mirror is greater than the focal length (z>0), the chirp is negative, and if is shorter (z<0), the chirp is positive. The distance between the grating and the curved mirror can be varied without changing the alignment of the outgoing beam by moving the telescope in the horizontal plane parallel to the direction of the diffracted beam. The movement in the horizontal plane (variable z) is necessary to adjust the stretched pulse duration, by taking into account the initial pulse duration and wavelength.

The telescope can be moved in the vertical plane, and this is necessary for alignment and adjusting the separation of the incoming-outgoing beams. The configuration of the beam on the diffraction grating is shown in Figure 8-5.

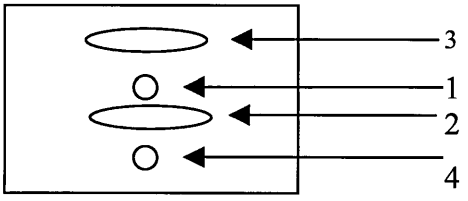

Figure 8-5 The configuration of the beam on the diffraction grating. 1 = incident beam, 2= after the first round-trip through the stretcher, 3 – after vertical RR, 4-after two round trips through the stretcher

The different size of the beams is due to the dispersion of the grating and reflects also the spatial chirp mentioned above. The separation of the beams 2 and 3 is due to the retroreflector RR, which shifts the beam up and redirects it to the stretcher.

As mentioned before, in the brief description of the experimental setup, at the entrance and exit of the stretcher, the polarization is flipped with the aid of two periscopes, in order to take advantage of the higher diffraction efficiency of the grating in the s-plane for the wavelength range of 5-10 μm. A vertical retro-reflector is used to pass the stretcher twice, in order to remove the spatial chirp and to enhance the stretching.

The diffraction grating

The diffraction grating is a crucial element for the stretcher/compressor design. Its parameters influence the amount of light transmitted by the stretcher and on the stretching effect itself. Consequently, there are two main requirements for the

grating: high diffraction efficiency and appropriate stretching factor for the FELIX wavelength range used in experiments (4-11μm).

The diffraction efficiency is defined as the fraction of incident monochromatic light diffracted into a specific order [20]. It depends on several factors like: wavelength, diffraction order, polarization, blaze angle, departure from Littrow. An appropriate choice of the grating should take into account all the parameters.

In order to achieve a high efficiency over a wide wavelength range, it is preferable to use s-polarized light (perpendicular to the grooves), and blaze angles larger than 25 degrees, for which the efficiency in the s-plane shows a large plateau with a value higher than 80%. The Littrow configuration generally gives the highest diffraction efficiency. For s-polarization, the departure from Littrow shifts and shortens the useful wavelength range, but the peak efficiency remains high, close to 100%. The blaze angle and diffraction efficiency are related in the sense that the shortening of the wavelength range is more pronounced for high values of the blaze angle and is very important for big deviation angles (i.e. the angle between the incident and diffracted beams), greater than 15 degrees. Due to the configuration of the stretcher-compressor system, and also to the requirement of high stretching factor, (favoured by a high diffraction angle), the departure from Littrow is about 23 degrees. This experimental fact plays a role in choosing the right grating. In conclusion, the best compromise between a large wavelength range and small influence on this range at departure from Litrow is a blaze angle of 26.7 degrees. This value is a standard one, and efficiency curves are available for deviation angles of 8 and 45 degrees [22]. The plots are very often given as a function of λ/d [21]. Thus, a groove density can be chosen for the desired wavelength range, for which λ/d shows a large efficiency value for the entire range.

Taking into account the above-mentioned considerations and the standard available gratings, the best choice for the diffraction grating resulted to be 150 gr/mm, 26.7° blaze angle with a ruled area of 64 x 64 mm (Richardson Gratings). Figure 8-6 presents the diffraction efficiency of the grating as given by the catalogue [19].

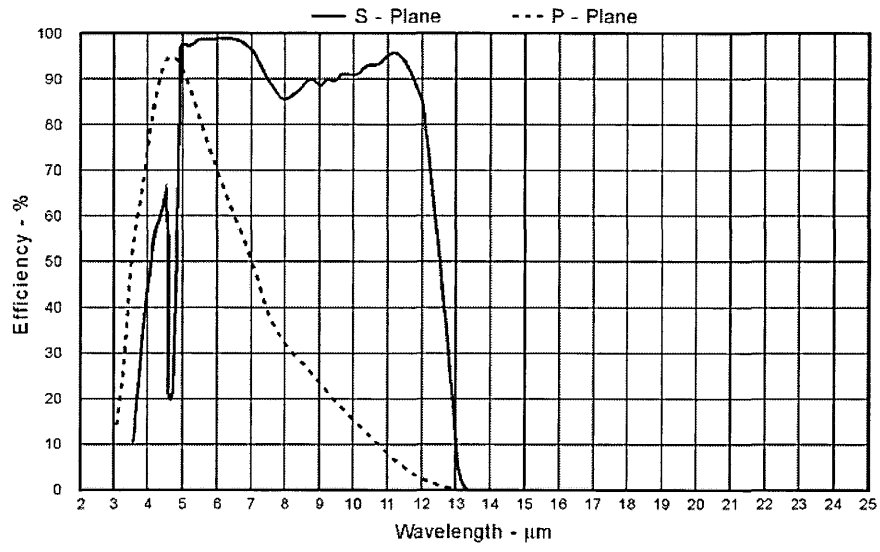

Figure 8-6 Diffraction efficiency of the grating used in experiments [19] The dashed curve is the diffraction efficiency for the p-plane, while the continuous one is for the s-plane, both for the first order (m=1). Because in the mid-infrared range the losses at the metal are negligible, the absolute diffraction efficiency (measuring the diffracted power in a certain order relatively to the incident one) is equivalent with the relative diffraction efficiency, which determines the amount of light diffracted in a certain order, without accounting for losses.

More information about the diffraction efficiency of the grating used in experiments and a comparison with the measured efficiency, together with its influence on the stretcher compressor efficiency is presented in the section 8.3.1 (The efficiency of the stretcher and the compressor), where is treated the efficiency of the stretcher and the compressor.

The FELIX beam position does not change with wavelength. That is why the incident beam on the grating does not change its alignment when scanning the wavelength. Because the incidence/diffraction angles on the grating vary as a function of the wavelength. According to Eq.(8-1), the grating rotation is necessary in order to preserve the deviation angle and the stretcher alignment. For a constant deviation angle and varying wavelength, the corresponding incidence and diffraction angles can be determined using Eq.(8-1).

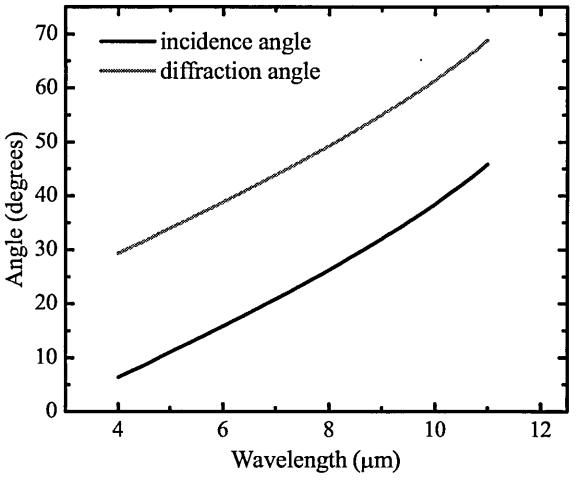

Figure 8-7 Incidence and diffraction angles for 23 degrees departure from Littrow, as a function of wavelength

The angles, as a function of the input wavelength, are plotted in Figure 8-7. The knowledge of the incidence angles is necessary for the correct alignment of the stretcher when the FEL wavelength is scanned. The values of the diffraction angles are necessary in evaluating the stretching factor, according to Eq.(8-8). As one can notice, the incidence and diffraction angles are interchangeable, due to the symmetry of Eq.(8-1). The configuration with higher diffraction angles is chosen for a more efficient stretching effect, as shown by Eq.(8-8).

How pulses are stretched

The Eqs.(8-6) and (8-7) consist the basis for estimation of pulse durations after the stretcher. Because of the stretcher construction, the displacement of the grating from the focus of the concave mirror leads to a double distance z in Eq.(8-9) As already pointed out, the stretching effect depends strongly on the initial pulse duration (spectrum) of the incoming pulse; because FELIX micropulse bandwidth and pulse duration are adjustable in a wide range, the settings of the stretcher for a fixed wavelength and output pulse duration are not unique.

Figure 8-8, Figure 8-9 show some characteristics of the stretcher calculated with the parameters of the grating used in experiments. Two input pulse durations of 1 and 5 ps respectively are chosen and the corresponding stretched pulse durations are plotted as a function of displacement for five different wavelengths are plotted.

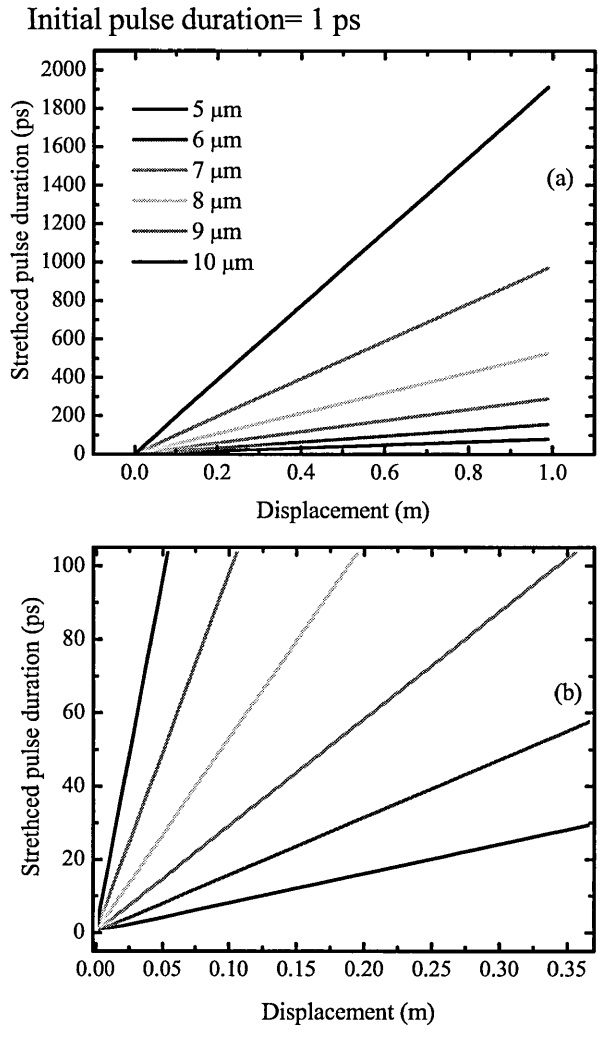

Figure 8-8 Calculated stretched pulse duration against the displacement of the grating from the focal point of the mirror for different wavelengths and for 1 ps input pulse duration. (b) is a detail of (a) for stretched pulse durations in a range up to 100 ps and displacements up to 35 cm.

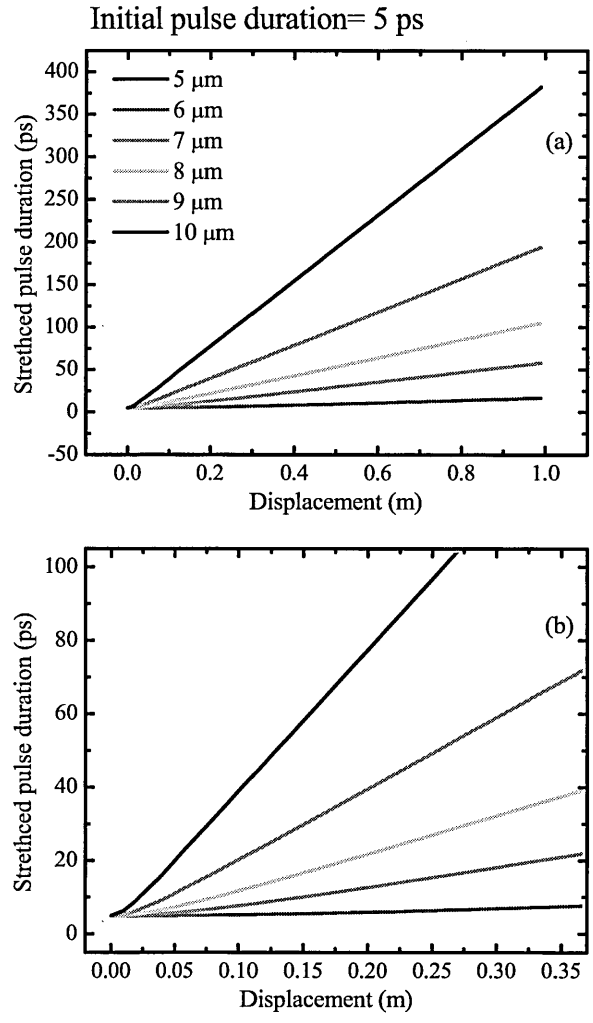

Figure 8-9 Calculated stretched pulse duration against the displacement of the grating in the focal point of the mirror for different wavelengths and for 5 ps input pulse duration. (b) is a detail of (a) for stretched pulse durations in a range up to 100 ps and displacements up to 35 cm.

Figure 8-8 and Figure 8-9 characterize the ability of the stretcher to enlarge pulse durations for several different wavelengths, with different input characteristics. As can be noticed, the range in which the pulse duration can be stretched is quite large, and strongly depends on the input characteristics. While for the wavelength of 10 μm, and initial pulse duration of 5 ps, a displacement of 10-25 cm is enough to stretch the pulse to about 100 ps, for the wavelength of 5 μm, and 1 ps pulse length, a displacement of 1 m is necessary for obtaining the same pulse duration.

The compressor

The role of the compressor is to restore the short pulse duration for the amplified pulse; ideally the same as the incoming one. A scheme of the compressor is presented in Figure 8-10. The compressor operates on the same principle as the stretcher but has a different construction, which provides a positive chirp. It consists of a grating (similar to the one in the stretcher) and a horizontal retroreflector, which replaces the telescope with –1 magnification in the stretcher. The retroreflector is mobile to insure the adjustment of the minimum compressed pulse duration, at each wavelength. Thus the compressor becomes equivalent to the pair of gratings depicted in Figure 8-3. The role of the horizontal retroreflector is similar to the telescope in the stretcher, but the chirp has an opposite sign - the temporal delay between different wavelengths increases with wavelength. This crucial difference between the stretcher and compressor makes possible pulse compression. The vertical retroreflector has the same role as in the stretcher setup: it provides a double pass of the device, removing the spatial chirp, which appears after the first pass through the compressor, and enhances the chirp. Unlike in the stretcher setup, the input beam passes close to the vertical retroreflector to the compressor. In the compressor, the beam is displaced horizontally by the horizontal retroreflector. After the second incidence on the grating, the beam meets the vertical retroreflector and is redirected to the compressor to a lower height, the distance between the spots on the grating being the same as in the stretcher.

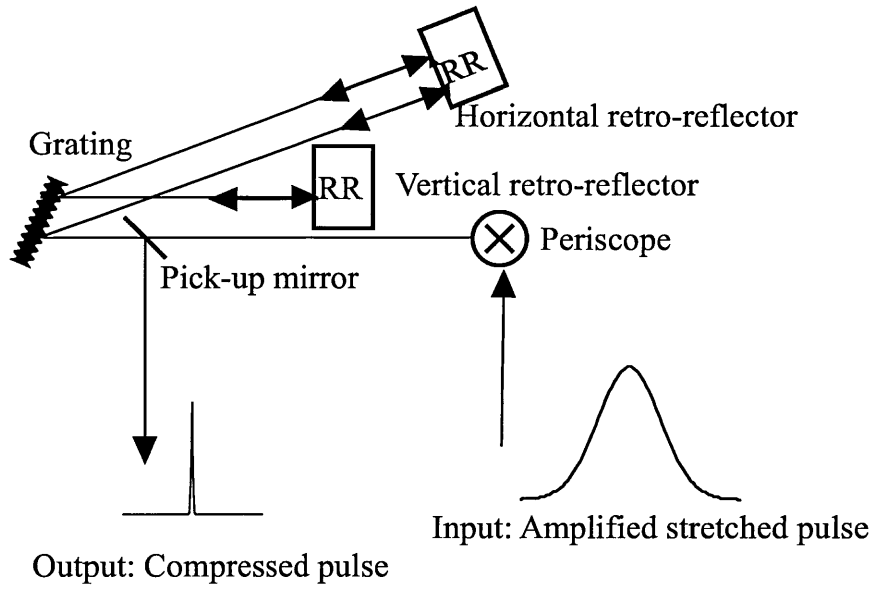

Figure 8-10 Schematic view of the compressor setup. The periscope flips the polarization of the input (amplified) stretched pulse. After diffraction, the beam is redirected to the grating by a horizontal retroreflector. After hitting the grating second time, the vertical retroreflector lowers the position of the beam and allows the second pass through the compressor. At the exit, a mirror picks up the beam. The position of this mirror is low, and does not intercept the incident beam, which passes to the grating parallel with the exit one but in a higher position.

Figure 8-11 shows the positions of the beams on the compressor grating. Each round trip in the compressor takes place in the horizontal plane. The first round trip is the upper one, the incident beam is displaced to the right by the horizontal retroreflector. The vertical retroreflector simply shifts the beam path in a lower plane, which makes possible also the pick up of the beam at the exit of the compressor.

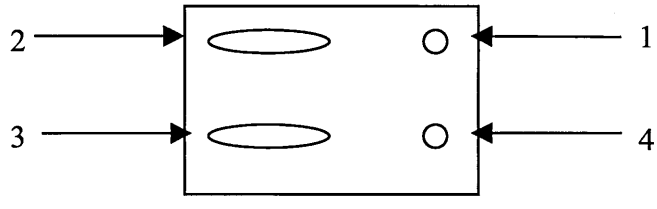

Figure 8-11 The configuration of the beams at the diffraction grating in the stretcher; 1- the incident beam on the grating, 2- the beam after one-round through the compressor, after hitting the horizontal retrorefelctor 3- the beam after being redirected to compressor by the vertical retroreflector 4- the beam after second round through the compressor

The efficiency of the stretcher and compressor systems is an essential parameter, because is strongly influencing the value of the output energy extracted after OPCPA takes place. The stretcher efficiency is not as important as compressor efficiency, because it can be compensated by a high amplification factor in the

amplification stage; while the compressor is the final stage of the OPCPA and represents a serious and unavoidable limit of output pulse energy.

For optimising the overall efficiency, the compressor contains less optics than the stretcher; it can be seen from Figure 8-4 and Figure 8-10 that the construction of the stretcher is adapted to give a positive chirp, while the compressor introduces a negative one. With this arrangement, the alignment of the compressor is easier than the stretcher alignment, which is important again because the compressor is the final stage and needs to be realigned more often than the stretcher.

8.3 Experimental results

The experimental results are divided in two main parts: the first part presents the measurements performed without amplification: temporal, spectral and spatial measurements are performed for the incoming and out coming beam in the stretcher/compressor system. The aim of these measurements is to provide information about the influence of the system itself on the spectral, temporal and spatial characteristics of the input pulse. The second part is dedicated to the chirped-pulse amplification experiment. It presents the results of the amplified energy for several wavelengths as a function of the pump pulse energy, autocorrelation traces spectral measurements showing the possibility of improvement of the results presented in Chapter 6.

8.3.1 Measurements without amplification

The experimental results have been obtained by measuring beam diameters, autocorrelation traces and spectra before and after the stretcher- compressor system. The characteristics were also investigated for the stretcher and compressor alone, in order to compare the individual influence on the pulse properties. The results are presented starting with the beam diameters and continuing with the spectra an autocorrelation traces. In the end of the section a small subsection is dedicated to the efficiency of the stretcher and compressor systems.

Beam diameters

Beam diameters and divergence of the interacting beams are very important for an efficient energy transfer in OPA process. A low divergence is significant for the ability of the stretcher/compressor to stretch/compress the pulse with minimum

pulse distortions, because the angular dispersion existing in a nonparallel beam results in un-wanted dispersion effects. An additional negative effect consists of the losses that can occur at the optics, leading to spectral narrowing.

In an ideal case, the pump diameter is larger than the signal (like top-hat, or supergaussian profiles) [13,14]. The objective of achieving high power densities with OPCPA systems involves a uniform spatial profile of the amplified signal, which can then be focused to a small diameter after compression takes place. The beam diameter at the crystal is also a factor contributing to the saturation level and is limited by the available (transverse) size of the crystal, and by the issue of spatial walk-off with pump for comparable pump-beam diameters. For long crystals, small beam diameters of pump can be affected by spatial walk-off and consequent spatial gain modulation. In our experiment, the beam diameter is limited to the crystal size.

The beam diameters have been measured using a Spiricon linear array, with 256 elements/inch. The array is positioned at the peak intensity in the horizontal and vertical planes, and the profile is visualised on a Tectronix oscilloscope. The traces are grabbed and recorded with the aid of a Labview code available at FELIX facility.

In Figure 8-12 (a) and (b), the FWHM (full-width at half maximum) beam diameters of the FELIX beam at the entrance of the stretcher and at the crystal are shown.

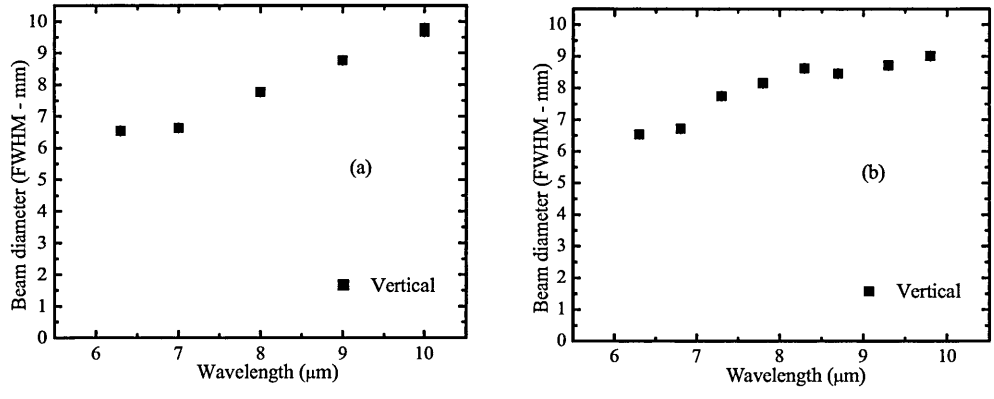

Figure 8-12 Beam diameters (FWHM) at two different positions, showing a wavelength dependence of the beam diameter and a low beam divergence. The two positions are separated about two metres. The first beam corresponds to the entrance in the stretcher and the second to the position of the crystal

The separation between the positions is two metres. The values of the beam diameters show a dependence on wavelength, the beam diameters at the crystal increase with wavelength. Figure 8-13 presents the measured values of the beam

diameters as a function of the distance at the entrance of the stretcher, at 6.3 μm wavelength. The diameters are determined inside the stretcher compressor system, and not at free propagation of the beam along the whole distance, and they show a slight convergence of the beam at the exit of the compressor (the longer distance in the figure).

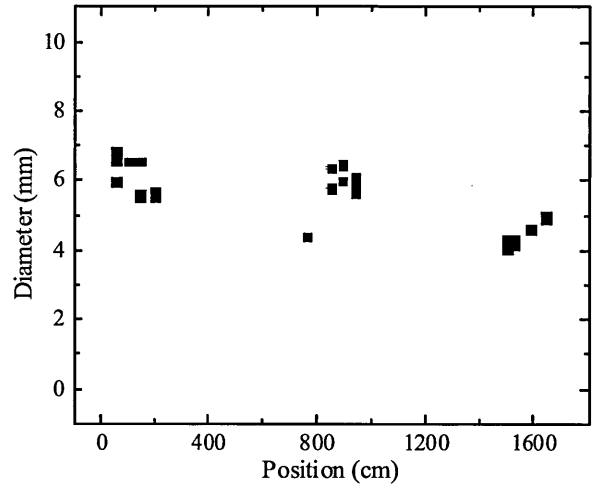

Figure 8-13 The FWHM beam diameter (FELIX) as a function of distance at 6.3 μm. The reference distance is considered at the entrance of the stretcher. The measurements show a slight convergence of the beam at the exit of the compressor (the longer distance in the figure)

For FELIX, the beam diameters on the table are influenced not only by wavelength, but also by the settings of the out-coupling mirror. This affects the value of the macropulse energy for a certain wavelength range. The beam diameters (at the crystal, after passing through the stretcher) in the case of optimised energy in the range 8-10 μm are shown in Figure 8-14.

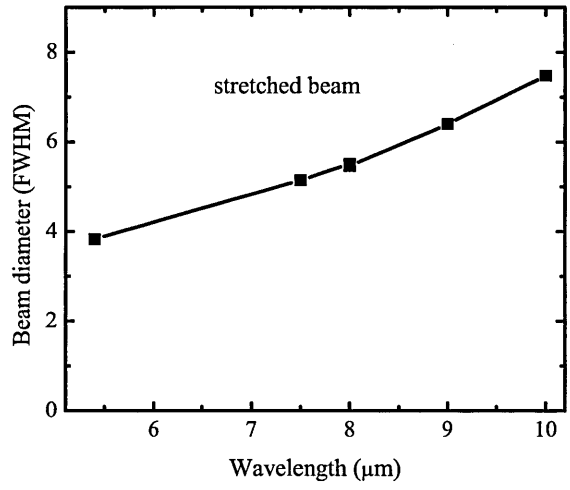

Figure 8-14 Beam diameter for the stretched beam at the crystal, for FELIX settings for optimum FELIX energy in the range 8-10 μm

In conclusion, the beam diameters depend on wavelength, and vary between 4 mm and 8 mm in the case of the stretched beam and between 5 mm and 10 for the unstretched case. A major impediment for modifying the beam diameter before the crystal is this dependence on wavelength; using an all-reflective telescope would modify all the diameters to the same extent. Using refractive optics would bring a focal length dependence on the wavelength, which in turn can bring the difficulty of adjusting the lens positions for each wavelength. The possibility of adjusting the beam diameter after the stretcher is limited by the unavoidable small difference in the directions of the output beams. Lenses also introduce additional losses.

The solution is to avoid the use of any telescope before the stretcher or before the crystal, because the measured beam diameters at the crystal have still convenient values for the experiments, in the sense that they are comparable to the crystal size, they do not vary dramatically, and they are also comparable to the size of the pump beam diameter at the crystal.

Spectral measurements and autocorrelation traces

In this section, the influence of the stretcher and compressor on the spectral and temporal characteristic of the signal pulse is investigated. Firstly, it is shown how the spectral-temporal characteristics of FELIX micropulses vary along the macropulse. This is important because the amount of stretching depends on the input spectral bandwidth of the pulse. Secondly, some spectra and autocorrelation traces of the input pulse in the stretcher, and pulses out of the stretcher and compressor are

presented, showing a not significant influence of the stretcher/compressor system on the spectral and temporal characteristics of the signal pulse. Most of the measurements are performed at 6.3 μm, a signal wavelength most often used in the amplification experiments.

In Figure 8-15 (a) the spectral bandwidth, calculated as a FWHM from the recorded spectra is plotted against temporal position of the FELIX micropulse in the macropulse. The position in the macropulse is indicated by the overlapped macropulse trace. The knowledge of these properties is important for characterizing the stretching effect on the micropulse selected for amplification. It can be noticed that the spectral bandwidth is larger for the leading edge and decreases monotonically to the trailing edge. Correspondingly, the pulse duration derived from autocorrelation traces is shorter on the leading edge of the macropulse. The calculated pulse durations from the autocorrelation traces, assuming Gaussian shape, are plotted in Figure 8-15 (b), also as a function of the position of the micropulse in the macropulse. Because the Felix micropulse is selected close to the maximum energy, its bandwidth is narrow (can be even more than twice or smaller than the bandwidth of the micropulse in the leading edge of the macropulse). Consequently, the stretcher acts differently on micropulses at different moments in the macropulse, because the stretching effect is affected by the different input bandwidths. From the experimental point of view, the relevant behaviour is that corresponding to the micropulses with highest energy, because the selected micropulse for parametric amplification lies in that region.

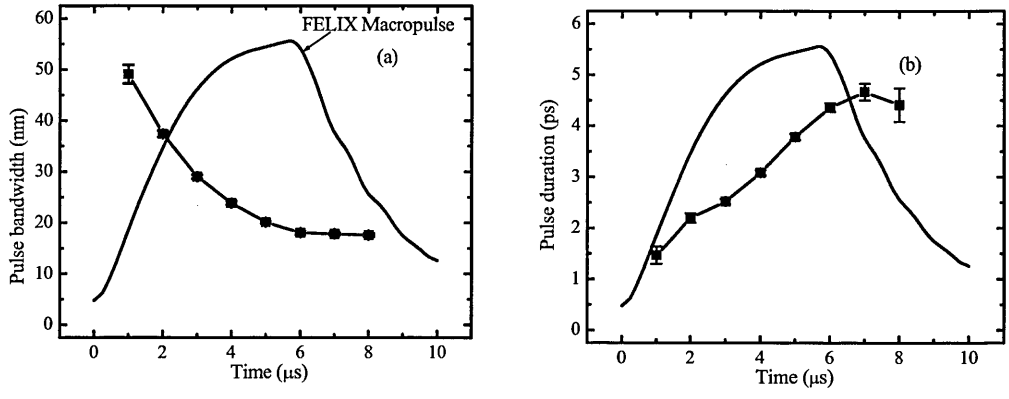

Figure 8-15 Bandwidth (a) and pulse durations (b) for different moments in the macropulse. The stars mark the position of the micropulse in the macropulse. The measurements are performed at 6.3 μm wavelength of FELIX

An important feature of the stretcher-compressor system is the possibility of compressing the pulse back to short pulse durations, ideally to the same pulse duration of the unstretched pulse. In the particular case of amplifying FELIX micropulses, this is valid for the micropulse involved in the parametric amplification. The overall spectral changes of the other pulses in the macropulse train are not important from the point of view of parametric amplification.

Losses can take place because the grating is a dispersive system and the sizes of the beams can exceed the size of the optical components for short pulses and large bandwidth. Misalignments of the stretcher can lead to similar effects. If part of the spectrum is lost in the system, it is not possible to compress back the pulse to the initial pulse duration. However, the measurements performed at different wavelengths showed the same bandwidth of the pulse before and after stretching. Figure 8-16 shows the values of the FWHM bandwidths for the FEL pulses at the input of the stretcher/compressor system compared to the bandwidth of the pulses at the output of the stretcher compressor system, at a wavelength of 6.3 μm. From this figure, it appears that the bandwidth is unchanged after passing the stretcher and the compressor, excepting the region at the beginning of the FEL macropulse. This can be due to a spectral loss at the stretcher components.

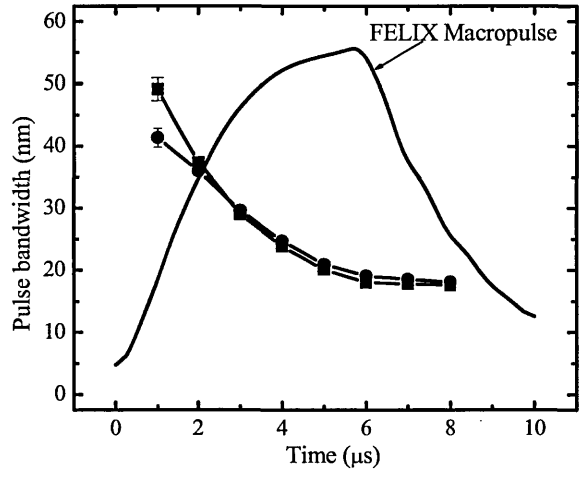

Figure 8-16 The spectra of the input (black squares) and output pulses, after stretching and compressing (circles), at different moments in the macorpulse of FELIX

In Figure 8-17 the spectra of the un-stretched and stretched and compressed pulses are compared. No essential modification is observed between the spectrum of the input and output pulses at the stretcher/compressor system. The measurements

are performed around 6.3 μm. Figure 8-18 presents the spectra of the pulses at the input and output of the stretcher, for a central wavelength of approximately 10 μm. The conclusion is similar with the one deriving from Figure 8-17: the stretcher does not influence the bandwidth of the input pulse.

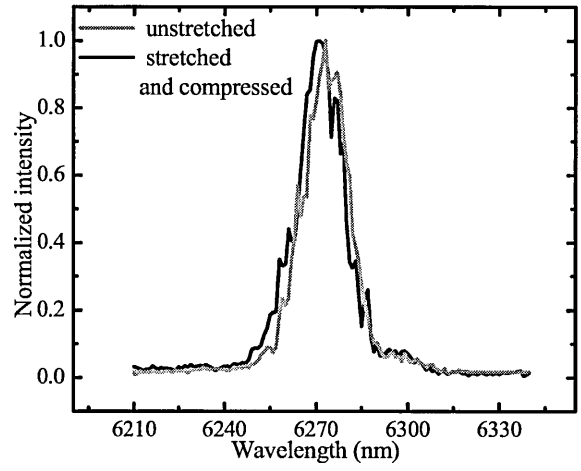

Figure 8-17 Spectra of the un-stretched and stretched-compressed pulse, for the peak-power in the macropulse, usually selected in amplification experiments. The figure shows not significant modification of the spectrum after passing the stretcher-compressor system

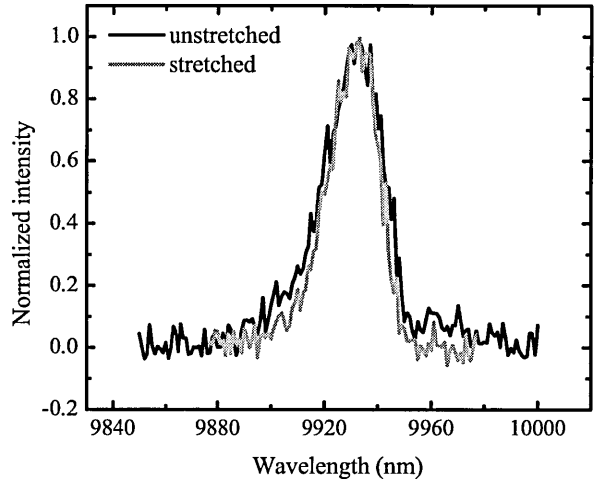

Figure 8-18 Spectra of the unstretched and stretched pulses, at a central wavelength ~ 9.92 μm

The autocorrelation traces bring similar conclusions. An example is shown in Figure 8-19. The figure presents the autocorrelation traces for the input (unstretched) pulse and the output pulse, which passed successively through the stretcher and the compressor. The measurements show the ability of the whole system to recompress the pulse to the initial pulse duration, in the absence of the amplification process.

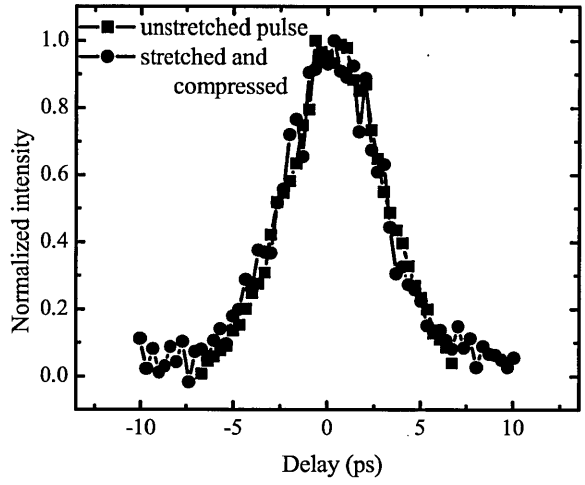

Figure 8-19 Autocorrelation traces for incident pulse and stretched and compressed at 6.3 μm, for the micropulse, which is selected for amplification

In Figure 8-20 the results of the measurements on the stretched pulse durations for two different (but close) configurations of the stretcher are plotted. The expected pulse durations are determined by using the measured pulse duration of the input pulse and the stretcher configuration and Eqs.(8-9) and (8-10). The calculated values are plotted together with the ones determined from autocorrelation traces, assuming Gaussian shapes. The results show a precision of several picoseconds at a wavelength of 6.3 μm. At this wavelength, a variation of several centimetres in the displacement of the stretcher (the position of the grating with respect to the concave mirror in the telescope) does not significantly influence the stretched pulse duration. For longer wavelengths (9-10 μm), the variation of the stretched pulse duration with the distance between the diffraction grating of the stretcher to the focus of the concave mirror is much more dramatic, as presented in the section 8.2.1.

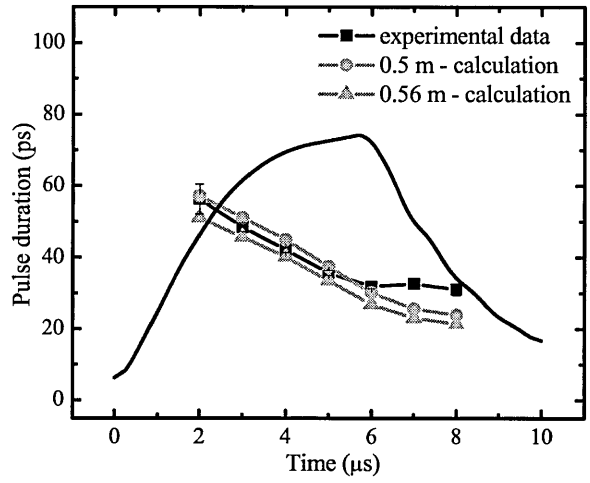

Figure 8-20 Measured and calculated stretched pulse durations. The expected pulse durations are determined by using the measured pulse duration of the input pulse, assuming Gaussian shape, the stretcher configuration (the displacements) and (8-9) and (8-10). The circles and triangles correspond to calculated pulse durations for stretcher displacements of 0.5 and 0.56 m.

In Figure 8-21 the pulse durations for the input un-stretched and output stretched-compressed pulses are presented, as resulting from the autocorrelation traces, and assuming Gaussian pulse shape.

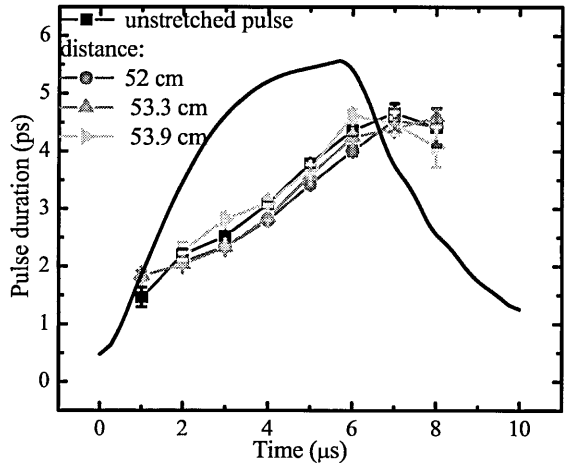

Figure 8-21 Pulse durations calculated from autocorrelation traces,a assuming Gaussian shape. A comparison is made between the unstretched and stretched-compressed pulses for the shortest compressed pulses.

The different distances represent the distance from the horizontal retroreflector in the compressor to the diffraction grating (see Figure 8-10). The displacement in the stretcher (the distance between the focus of the concave mirror and the grating) was 52 cm.

The efficiency of the stretcher and the compressor

In the configuration of the stretcher, a concave silver mirror with –1 m focal length and a silver pick-up mirror at the exit were initially used. They were replaced by a concave gold-coated mirror, with a longer focal length of -1.25 m and the same diameter of the silver one (10 cm), and with a gold-coated pick-up mirror, respectively. The change in the focal length of the concave mirror aimed the possibility of longer stretched pulses in the range of low wavelengths (5-6.5 μm). The stretcher efficiency for both configurations has been determined and is shown in Figure 8-22. It can be noticed a slight improvement of the efficiency with the gold-coated mirrors, and some particular wavelengths where the efficiency dropped when using silver mirrors.

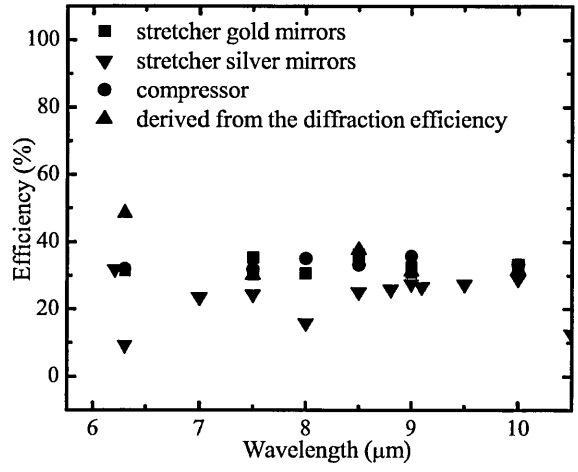

Figure 8-22 Efficiency of the stretcher and compressor as a function of wavelength. For the stretcher, the efficiency is measured with using different concave mirrors and different pick-up mirrors. For the gold plated mirrors, the experimental values of efficiency are plotted with square symbols, while for the silver mirrors they are plotted as triangles. The circles represent the experimental data available for the efficiency of the compressor. For comparison, the ideal efficiency derived as a fourth power of the diffraction efficiency is added

The efficiency of the compressor system has been also determined for several wavelengths. Figure 8-22 shows the measurements of the stretcher and compression efficiency for a set of wavelengths and using two different concave-mirrors in the stretcher telescope. The reflectance of silver and gold in the mid-infrared is typically 97-99%. However, the low efficiency (only around 40%) is due mainly to the diminished grating efficiency after a long use. This can be seen in Figure 8-23 (a), which shows some measurements of the grating efficiency before and after experiments.

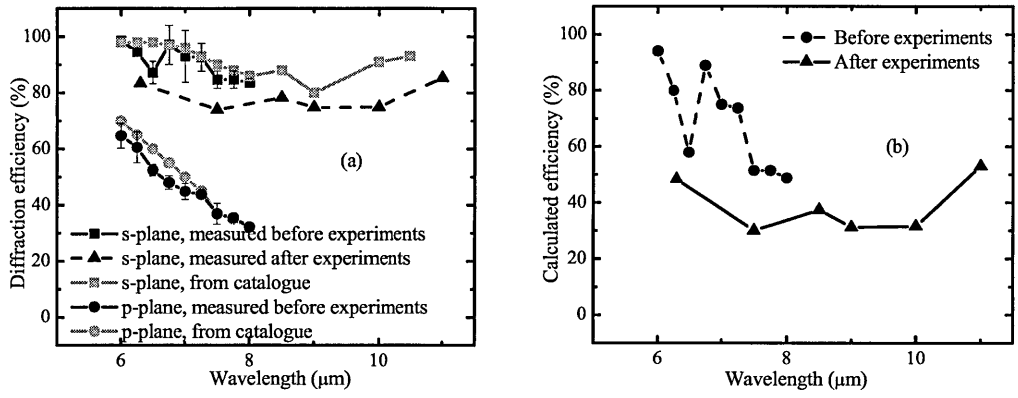

Figure 8-23 (a) The measured (relative) efficiency of the diffraction grating before starting amplification experiments and after few months of experiments (hundreds of hours of grating use, with an incident power of several milijoules) (b) The calculated efficiency of the stretcher/compressor, with two round-trips, neglecting other losses in the systems, with data from the diffraction efficiency before and after performing experiments (only in the s-plane)

Figure 8-23 (b) presents the expected efficiency of the optical system in case the diffraction grating is hit four times (as it is the case of the stretcher and compressor with two round trips). The efficiency of the stretcher/compressor systems is sensitive to any decrease of the diffraction efficiency because this is enhanced with a power of four. A measure of this drop is expressed by the plots in Figure 8-23 (b).

When comparing the measured efficiency of the stretcher and compressor with the one calculated from the measured diffraction efficiency after a long use of the gratings, the values appear to be very close, revealing no substantial influence of the gold-coated mirrors in the stretcher and the compressor.

As a conclusion of the section 8.3.1, it can be stated that the stretcher/compressor system does not change the input temporal/spectral characteristics of the FELIX pulse. This happens when the bandwidth of the input pulse does not exceed 40 nm. In this case the efficiency of the stretcher and of the compressor does not exceed 40%. The optical element responsible for that is the diffraction grating.

8.3.2 Amplification experiment

This section presents the experimental results obtained with the OPCPA method. The methods used are the ones described in Chapter 6. The measured amplified energy versus pump and signal input energy are firstly presented for the two crystal lengths: 17 mm and 16 mm. A small subsection is dedicated to the

energy of the compressed pulse. In the next section the variation of the amplified energy as a function of the delay between the pump and signal is studied. The last section is treating the factors that induce changes of the spectral and temporal characteristic of the pulse undergoing OPCPA.

Energy measurements

Measurements at 17 mm crystal length

First experiments were performed using the 17 mm long crystal. The most important results are related to the values of the amplified energy and amplification factor. The measurements were performed at the wavelength of 6.3 μm.

Figure 8-24 and Figure 8-25 show the amplified energy and amplification factor at a stretched pulse duration of approximately 35 ps length at 6.3 μm central signal pulse wavelength. The experimental values show amplified energies of more than 2.4 millijoules, which correspond to a compressed pulse energy of more than one milijoule. The pump energy was 73 mJ. The curves show also a good stability of the amplified pulse energy, due to the stability of the pump pulse and to the saturation regime. The saturation starts to manifest at input signal energy of few microjoules.

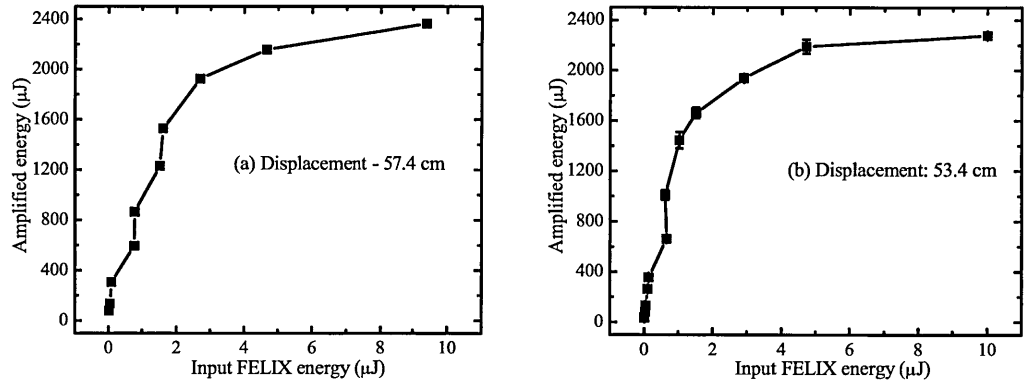

Figure 8-24 The amplified energy against the input FELIX energy (at the crystal) for a stretched pulse duration of 35 ps, at 73 mJ pump energy and 6.3 μm central signal pulse wavelength

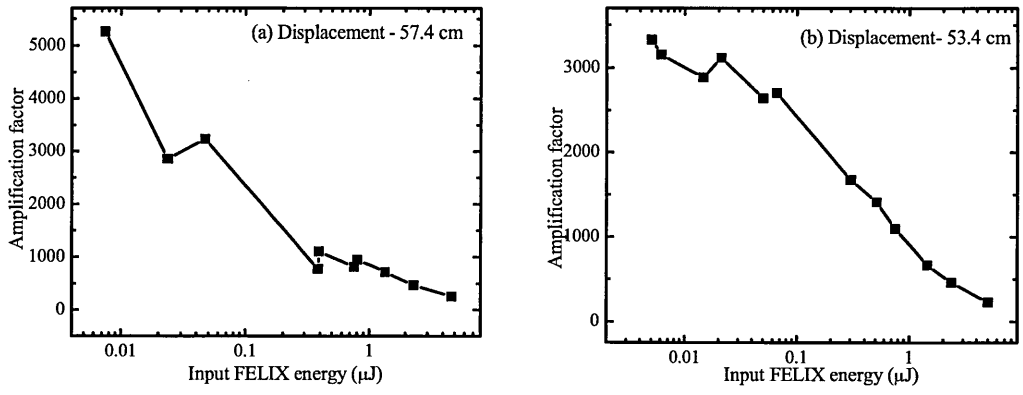

Figure 8-25 the amplification factor against the input FELIX energy for a stretched pulse duration of ~ 35 ps at 6.3 μm central wavelength and 73 mJ pump energy. In (a) the displacement in the stretcher is 57.4 cm and in (b) the displacement is 53.4 cm

Thus, the maximum amplified energy depends strongly on the input FEL energy, if the micropulse energy on the crystal is less than 5 μJ. The value of the input signal energy of the FELIX micropulse can be optimised for a narrow spectrum of the micropulse, which must not exceed the bandwidth acceptance of the crystal. The saturation effect appears also from Figure 8-25. It can be noticed that the amplification factor decreases with the signal energy, from few thousands to few tens.

These considerations about saturation effect are valid for the maximum pump energy of about 73 mJ on the crystal, because the amplified energy strongly depends also on the pump energy. Figure 8-26 shows this dependence.

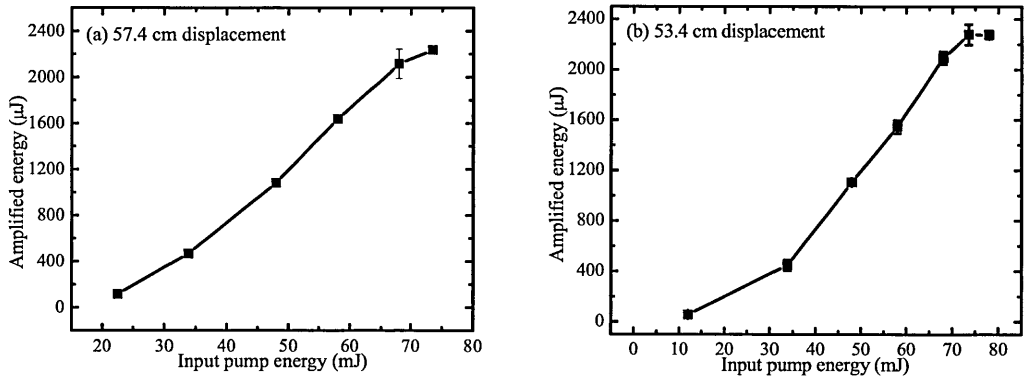

Figure 8-26 Amplified energy against the pump pulse energy for a stretched pulse duration of 35 ps. The input energy of the micropulse, at the crystal, was 10 μJ. In (a) the displacement in the stretcher is 57.4 cm and in (b) the displacement is 53.4 cm

Measurements were taken in the same conditions with the plots presented in Figure 8-24 and Figure 8-25. The usual fluctuations of ~ 1% in the pump energy lead

to a good stability of the amplified pulse energy (less than 5 %). The drop in the pump energy that can happen after a long use of the laser or the malfunction of the seed laser leading to strong fluctuations in the pump power, could lead in turn to high fluctuations of the amplified pulse. For example, according to Figure 8-26, a fluctuation of 10%-20% of the pump energy leads to fluctuations of several hundreds of microjoules in the amplified pulse. The temporal fluctuations causing a bad temporal effects and the pointing stability of the pump laser usually associated with the un-seeded regime increase the fluctuations of the amplified energy.

Measurements at 16 mm crystal length

After polishing and recoating the crystal, its length decreased to 16 mm. It was still possible to extract an energy of about 2 mJ at 6.3 μm (depending on the input FEL pulse energy). The influence of the crystal length is more important at low pump energies than for the high pump energies (close to the limit of 70-80 mJ). This is due to the fact that at low pump energies, the level of saturation is not high and, consequently, the relative influence on the amplified energy is more sensitive to any factor decreasing the gain (crystal length and nonlinear constant). At high pump energies, the saturation is strong and the variations of the same factors do not have the same impact on the amplified energy.

The dependence of the amplified energy for different pump energies is plotted at various wavelengths and some different stretched pulse durations. Figure 8-27 (a) and (b) presents the dependences of the energy of the stretched-amplified pulse, at 5.4 signal wavelength, for two different displacements of the stretcher, leading to (estimated) pulse durations of 23 and 44.7 ps respectively.

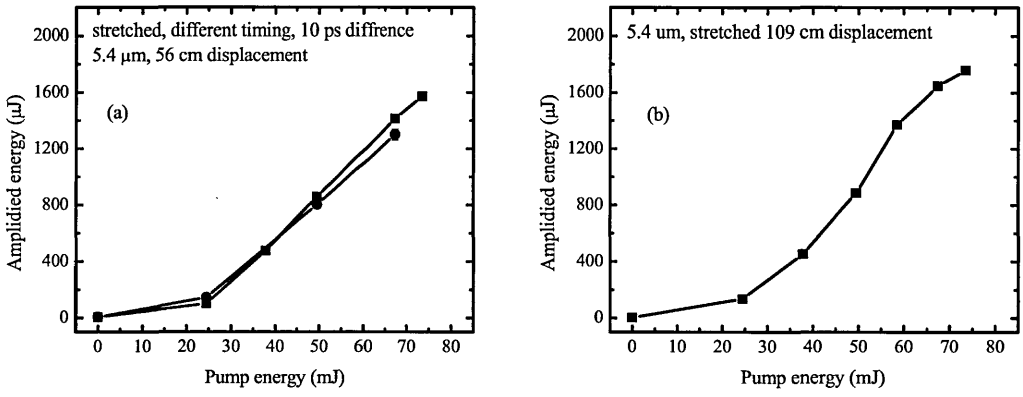

Figure 8-27 Amplified FEL energy against the pump energy at 5.4 μm signal wavelength for two different stretched pulse durations. The input signal energy at the crystal is 3.15 μJ (a) and 2.5 μJ in (b) The corresponding calculated pulse durations are 23 ps in (a) and 44.7 ps in (b). In (a) the two curves represent measurements of the amplified energy with a delay between pump and signal of 10 ps.

The maximum amplified energies, corresponding to pump energies of about 73 mJ are comparable to the maximum ones obtained in the OPA experiments, but with higher input signal energy (~20 μJ). Because of the low efficiency of the grating around 5 μm and horizontal polarization, the energy of the amplified pulse obtainable at this wavelength is not improved, and even decreased if considering the similar loss introduced by the compressor. A better efficiency with the same grating could be obtained, for wavelengths between 4-5.5 μm, with p-polarization (parallel to the grooves) of the signal electric field, but such experiments have not been performed. Figure 8-27 (a) presents results for similar measurements, the only difference being the 10 ps delay between the pump and signal pulses. Adjusting the delay can slightly improve the value of the amplified energy at high pump energy, but, as it will be shown later in this chapter (section 8.3.2, (*Spectral measurements*)) this can lead to a central wavelength shift and spectral narrowing of the stretched-amplified pulse.

Figure 8-28 presents some experimental results obtained for the stretched-pulse amplification at signal wavelengths around 6 μm. Figure 8-28 (a) presents the experimental results of the energy of the amplified pulse against results for 6 μm signal wavelength, while (b) and (c) refer to measurements taken at 6.3 μm signal wavelength, for two different settings of FELIX, but at the same displacement in the stretcher. In Figure 8-28 (b), the two measurements correspond to a 10 ps difference in the delay between the pump and signal pulses.

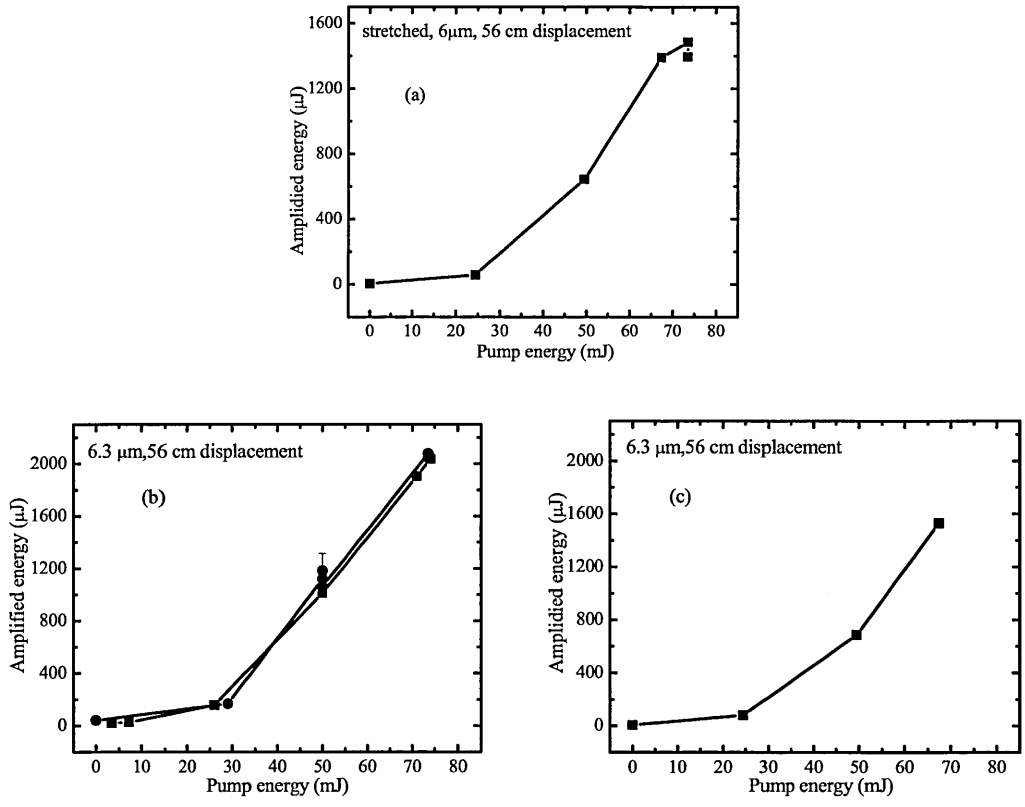

Figure 8-28 (a)Amplified energy of FEL at 6 μm signal wavelength, 2 μJ input signal energy and against the pump energy, (b)same as (a) with 6.3 μm signal wavelength, 3.5 input signal energy and (c) the same as (b) with 4 μJ input signal energy, and different FEL settings

The difference in the values of the amplified energy is due to the different input signal energy, or to the delay between the pump and signal pulses.

Figure 8-29 presents similar results for a signal wavelength of 10 μm, and 5 μJ input signal energy. The stretched pulse duration is estimated to be 25 ps. Values as high as 700 μJ of the amplified energy are obtained, for pump energy of ~ 66 mJ.

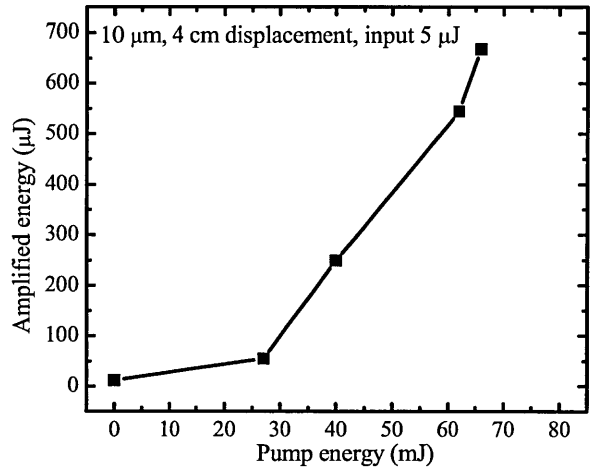

Figure 8-29 The amplified energy as a function of pump energy at 10 μm signal wavelength, 5 μJ input signal energy and 4 cm displacement, corresponding to ~ 25 ps stretched pulse length

The wavelength dependence of the maximum stretched-amplified pulse energy is exemplified Figure 8-30. The two plots were obtained for different FEL settings, yielding different beam diameters and different input pulse energy, but approximately the same bandwidth. The pump energy was ~ 65 mJ. The amplified energy decreases with wavelength because the efficiency of the nonlinear process depends on the nonlinear constant, which is a function of wavelength.

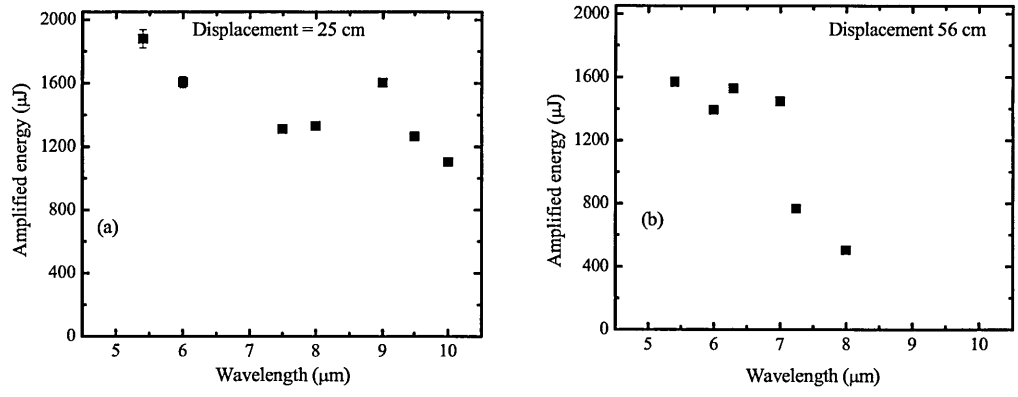

Figure 8-30 Stretched-amplified pulse energy as a function of wavelength for FEL settings optimized for 8-10 μm and displacement of the stretcher of 25 cm (a) and 56 cm (b), input bandwidth 0.2% and pump energy ~ 64 mJ

The amplified energy depends also on the stretched pulse duration. Stretching is effective in terms of power if two conditions are fulfilled: surmounting of saturation effect and preserving of the short pulse duration after compressing. In the stretched pulse duration exceeds the pump pulse duration, the spectrum of the

amplified pulse can be modified (becomes narrower than the initial one). Considering only this effect, after compression it is not possible to reach the initial pulse duration. As discussed in the section 8.2 when describing the experimental setup, the influence of the displacement on the stretched pulse duration depends on the wavelength. For short wavelengths (4-5.5 μm), the displacement necessary to produce pulses of tens of picoseconds approaches 1 m. For long wavelengths (around 10 μm), the displacement is of the order of 1 cm. A consequence is that the sensitivity of the stretched pulse duration to the variation of the stretcher configuration is much higher at long wavelengths than at short ones. That is why, in Figure 8-30, the high values of the amplified energy at longer wavelengths (8.5-10 μm is due both to spectral narrowing and high signal input energy.

As can be observed from spectral measurements, presented in section 8.3.2, (*Spectral measurements*), the optimum stretched pulse duration is conditioned not only by the maximum obtainable energy, but also by the delay between the stretched-signal with respect to the pump pulse. The stretching and the relative delay can determine a narrowing of the output pulse, due to the comparable lengths of the two pulses. Thus, despite a high energy in reality the power can be affected. For pump pulses much longer than the stretched pulse durations, the influence of the delay and its jitter is minimized, eliminating also the spectral effect associated with them.

Because in our experiment the stretched signal and the pump pulses have comparable lengths, the delay between the pulses is also important and superimposing the peak intensities has to be accurate (in 5 ps) in order to preserve the central wavelength and the high power of the amplified pulse.

Figure 8-31 and Figure 8-32 present the amplification factor and the amplified energy as functions of stretched pulse duration at two different wavelengths: 8.8 μm and 10 μm. For 9 μm it is possible to identify a stretched pulse length for which the amplified energy reaches a maximum. This is around 30 ps. For 10 μm, the measurements were taken at pulse lengths shorter than 30 ps.

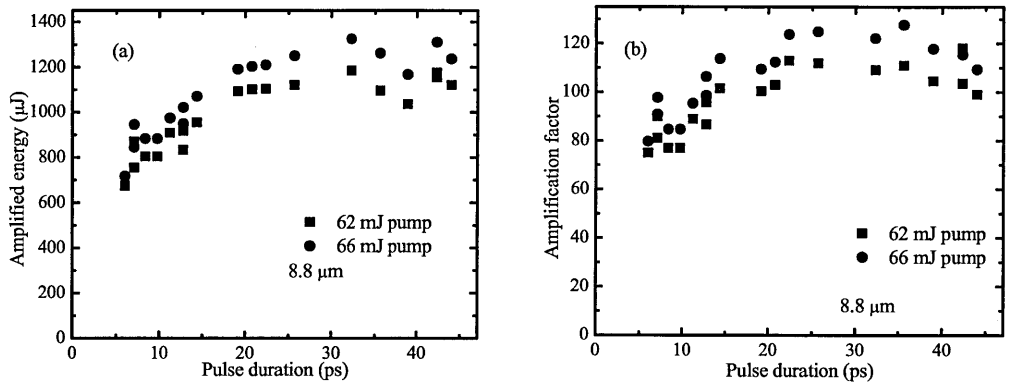

Figure 8-31 The dependence of amplified energy (a) and amplification factor (b) on the stretched pulse duration, as calculated from the displacement of the grating in the stretcher, at 8.8 μm, crystal length= 16mm. Because the input energy of FELIX varies slightly with varying the delay, and delay has to be adjusted for each different configuration of the stretcher, (a) and (b) are not completely equivalent

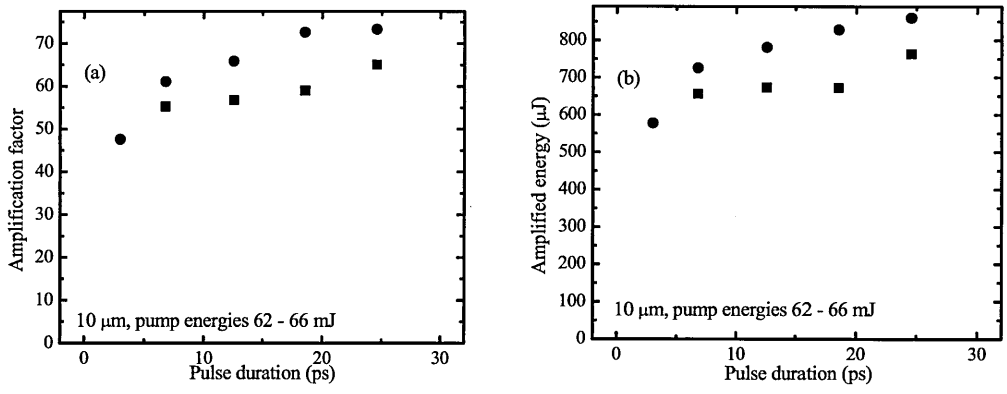

Figure 8-32The dependence of amplified energy (a) and amplification factor (b) on the stretched pulse duration, as calculated from the displacement of the grating in the stretcher, at 10 μm signal wavelength, crystal length= 16mm

The compressed pulse

The energy of the compressed pulse has been also measured at the exit of the compressor. The results are presented in Figure 8-33. The amplified energy at the output of the compressor is plotted against the pump energy, at 6.3 μm signal wavelength. For these measurements, a value as high as 800 μJ amplified energy was determined.

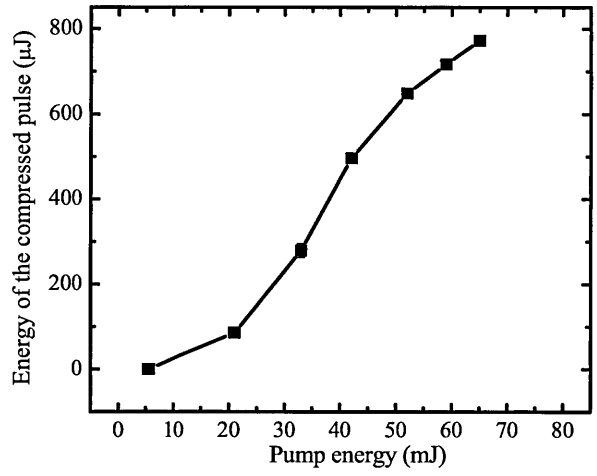

Figure 8-33 Energy of the compressed pulse against the pump energy at 6.3 μm wavelength and 10 μJ input energy of the FEL pulse

Measurements with variable delay between the pump and signal pulses

The temporal overlap between the pump and signal pulses is an important issue for the amplification process. Not only the amplified energy is affected by a poor synchronization, but also the stability and the temporal and spectral characteristics of the amplified pulse. The delay between the pump and signal pulse which can lead to significant modifications of the characteristics of the amplified pulse depends on the pulse durations and irradiances of the interacting pulses. An important feature is the jitter between the two pulses; this has to be much less than the duration of the pump pulse.

In the OPA case, because the pump pulse is much longer than the signal, the effect is not as noticeable as for the OPCPA case, particularly in our experiment. Other systems use nanosecond pump pulses and several hundreds picoseconds stretched pulses, so the conditions are very different from the point of view of relative length of the interacting pulses and the acceptable jitter between them.

The effects of the wrong temporal overlap on the spectral characteristics of the amplified pulse are presented in section 8.3.2, (*Spectral measurements*).
Because in the experiments presented in this thesis, the pump and signal pulse durations are comparable, the delay influence on the amplified energy and spectral characteristics is prominent.

In Figure 8-34 a comparison between the parametric gain in the case of OPA and OPCPA is shown. The measurements are taken at low pump energy (25 mJ) at an input energy of the stretched pulse of 1 μJ. The signal wavelength is 10.06 μm.

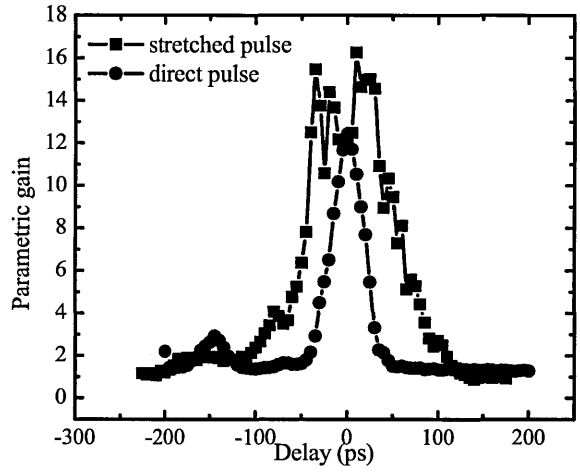

Figure 8-34 Measurements of the parametric gain with varying the delay between the pump and the signal pulses, at 10.06 μm. Comparison between the unstretched and stretched-amplified pulses. Pump energy is 25 mJ, while the signal pulse energy is 1 μJ

The plots reveal the existence of the second peak in the pump pulse (or, better said, of a prepulse). The presence of the peak was also shown by the autocorrelation traces of the pump pulse, presented in Chapter 4. The peak appears to be here at a distance of 150 ps from the main one. The peak separation in the autocorrelation trace was determined to be 200 ps. Other measurements with time delay variation showed also a value of 200 ps. It is not clear if the separation of the two pulses in the structure of the pump pulse indeed varied, or is a "bug" in the phase shifter, which varies the delay.

The instabilities present in the stretched amplified pulse in comparison with the un-stretched pulse measurements, are due to the fact that the stretched pulse does not saturate the amplification process at this level of the pump energy.

Figure 8-35 shows three measurements corresponding to three different stretched pulse durations at 10 μm.

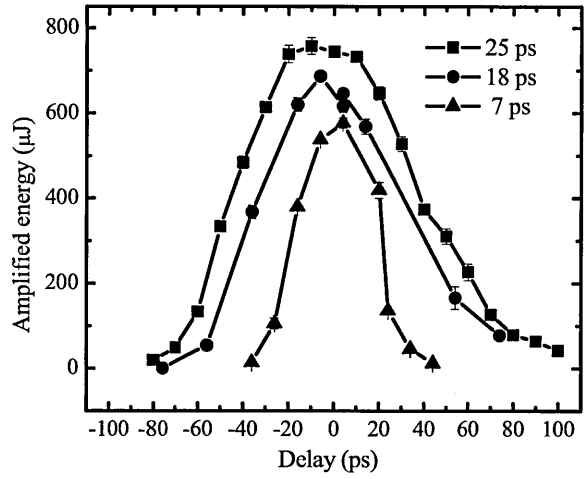

Figure 8-35 Measurements with temporal delay at 10 μm for different stretched pulse durations

The different pulse duration at this wavelength were obtained by only 1 cm difference in the displacement of the stretcher. The comparison of the plots shows the "de-saturation" of the amplification process at longer stretched signal pulse durations, while the other conditions remain similar. The energy of the amplified pulse is higher for longer stretched pulses.

In addition to the problem related to the separation of the pulses in the pump structure, an intriguing fact is that the data corresponding to the shortest stretched pulse duration do not fit with simulations considering a 85 ps pump pulse length, but they show the possibility of much shorter pump pulse (about a half, see also comments in section 6.3.6). This can be caused by an error in the effective delay introduced by the phase shifter between the pump and signal pulses.

Spectral and temporal features of the amplified pulse

Ideally, the spectral and temporal characteristics of the amplified pulse should be similar to those of the input signal FEL pulse. This is necessary for maintaining a high power in the output pulse. In a previous section, 8.3.1, the influence of the stretcher–compressor system alone on the input pulse characteristics has been investigated. It was shown that a signal pulse of a few picosecond pulse duration traversing the stretcher-compressor system preserves its spectral and temporal characteristic. But the stretcher – compressor is just one of the factors with possible influence on the spectral and temporal characteristics of the amplified pulse. Because the output pulse duration can be minimized with a correct configuration of the compressor, the temporal characteristics are considered for the minimum pulse

duration that can be obtained out of the compressor. This situation corresponds to a near transform limited pulse at the exit of the compressor. If the output pulse were chirped, the pulse duration would be naturally longer and autocorrelation traces broadened. One can then consider that the main changes in the spectral and temporal characteristics of the stretched-amplified and compressed pulses are caused by the parametric amplification and the factors related to it.

These factors which can affect the spectral/temporal characteristics of the amplified pulse are: the pump pulse duration, the synchronisation of the pump with the signal, the jitter, the absorption in water vapours and other molecules present in the atmosphseric environment, and the amplification process itself. It can be noticed that, in comparison with the situation of OPA, there are some specific issues related to the pulse-chirping and the relation between the stretched pulse length and the pump pulse. The pump/stretched signal pulse durations, the jitter between them and the actual delay of the two interacting pulses can be considered together, because they are all related to the temporal overlap.

The first factor to be mentioned is the pump pulse duration. The pump pulse has to be long compared with the stretched signal length (ideally top hat). In a stretched pulse, there exists a temporal distribution of wavelengths. Consequently, if the pump pulse were too short compared with the signal pulse, the initial spectrum could be altered (only part of the spectrum will get enough gain and will be amplified).

In an analogous way the influence of the pump temporal instabilities can be explained. Even if the pump pulse were long enough compared with the stretched signal pulse, if the jitter between them is comparable with the pump pulse length, the amplified spectrum and energy become extremely unstable. The situation of the high jitter can appear for example when the regenerative amplifier of the pump pulse is not properly seeded, or can be caused by the noise in the electronics ruling the synchronization between the two interacting pulses.

Another factor influencing the spectral and temporal characteristics is the delay between the pump and the signal pulses. Due to the fact that the pump pulse length is several tens of picoseconds long and the stretched pulse duration is of the same order of magnitude, if the pump pulse is not centred on the stretched signal pulse, the maximum intensity of the pump will favour amplification of wavelengths different than the central one, while other wavelengths can be even not overlapped

with the pump pulse. This shifts the central wavelength and possibly modifies the bandwidth of the amplified pulse.

There are also some common features to OPA and OPCPA, as the influence of the pump power and the saturation effects, but, because of the wavelength distribution they act in a different way on the spectral and temporal characteristics, as it will be shown by experimental results in the next sub-section and in Chapter 6 by simulations. However, the influence of saturation is reduced by the loss in the input signal energy due to the stretcher efficiency, and by the decrease in intensity due to the pulse-chirp.

The experimental results presented in this section show that the amplification process, in proper conditions of pulse duration (input signal bandwidth), does not significantly influence the spectrum of the amplified pulse. The compressed pulse duration is very close to the input one.

Spectral measurements

Figure 8-36 presents the input stretched pulse, without being amplified, at 6.3 μm and 57 cm displacement, while Figure 8-37 (a) and (b) presents the measured spectra of the stretched measurements performed with the 17 mm long crystal. The measurements showed a change from approximately 16 nm bandwidth of the stretched pulse to 20 nm bandwidth of the stretched amplified pulse at the pump energy of 73.5 mJ. These results confirm the spectral broadening due to the saturation effect, with increasing pump energy.

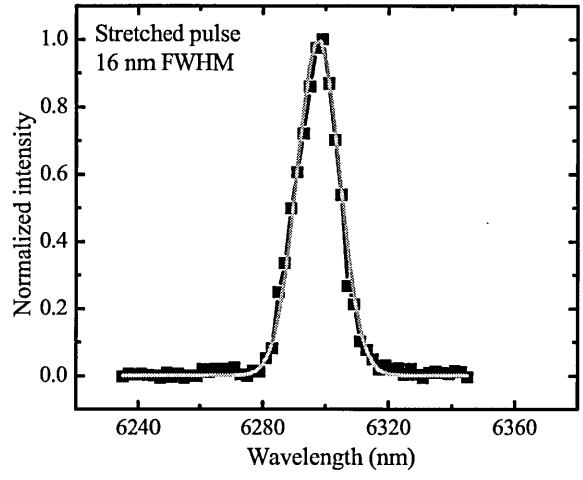

Figure 8-36 The spectrum of the stretched pulse at 6.3 μm and 57 cm displacement

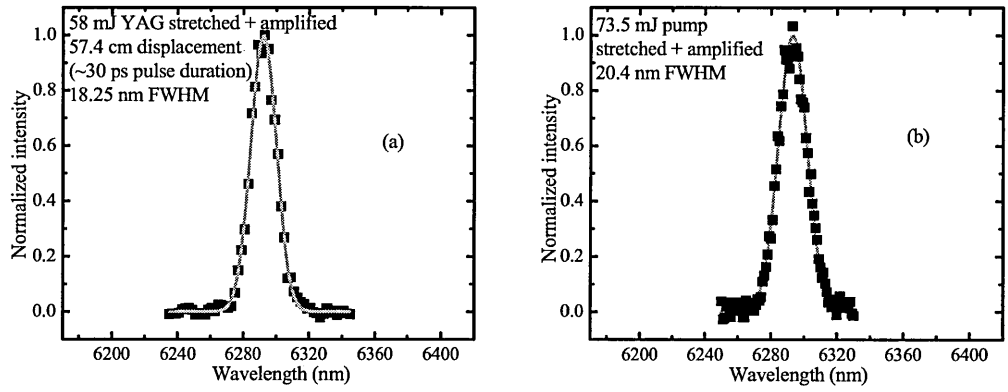

Figure 8-37 The spectrum of the stretched-amplified pulse at 6.3 μm, at 57 cm displacement of the stretcher and approximately 30 ps pulse length. (a) for 58 mJ pump energy and (b) for 73.5 mJ pump energy. The not-amplified stretched-pulse spectrum is given in the previous figure

Figure 8-38 presents the effect of the stretching on the amplified pulse spectra. The measurements have been performed at a central wavelength close to 10 μm (9.95), and for different stretched pulse durations.

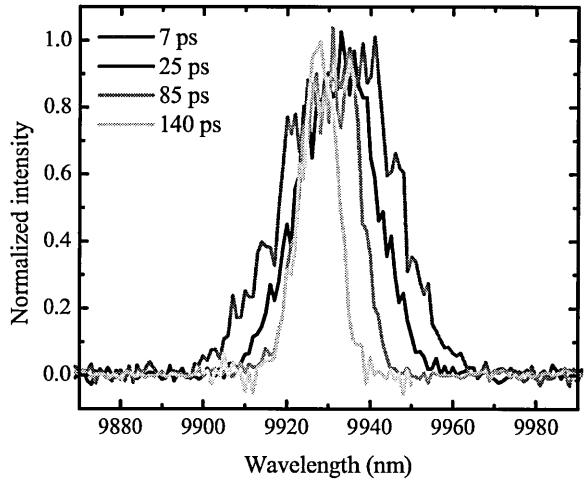

Figure 8-38 The influence of the stretched pulse duration on spectra at a central signal wavelength of approximately 9.94 μm. The increasing stretched pulse duration causes a spectral narrowing due to the limited overlap with the pump pulse and to the wavelength distribution in the stretched signal pulse

It can be noticed that, for short pulse durations, the spectra of the amplified pulse is broader than the ones corresponding to longer pulse durations. For a pulse length of approximately 140 ps, the spectral bandwidth becomes at least two times narrower than for pulse durations of 7-25 ps. The shift of the central wavelength is due to the saturation effect and to the delay between the maximum intensities of the two interacting pulses.

The shift of the central wavelength and the spectral narrowing due to the poor temporal overlap between the pump and stretched-signal pulses is shown also in Figure 8-39.

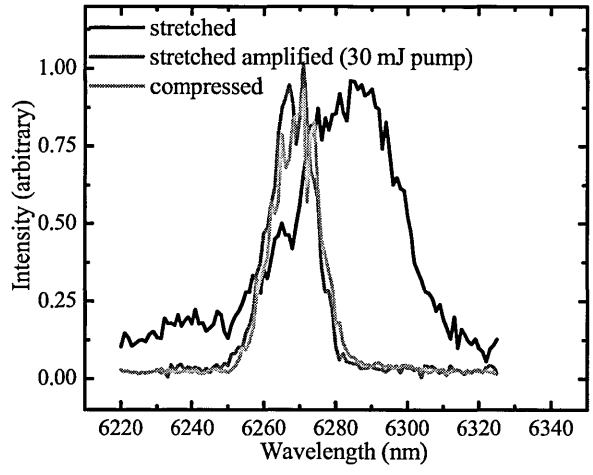

Figure 8-39 Comparison of the stretched (solid line) stretched-amplified (dotted line) and compressed pulses spectra around 62.9 μm central wavelength of the stretched pulse and for 30 mJ pump energy. The central wavelength of the stretched-amplified and compressed pulses shifts to shorter wavelengths with ~20 nm. The wavelength shift is attributed to the incorrect temporal overlap of pump and stretched signal pulses

In Figure 8-39, the spectra of the stretched pulse before amplification, of the stretched amplified pulse, and the compressed pulse are plotted together. The spectra of the stretched-amplified and compressed pulses are almost the same, but the not amplified stretched pulse has a different central wavelength and is broader. This effect typically appears when one optimises the value of the amplified energy while adjusting the delay between the pump and signal pulses. This type of measurements could be an easy way to determine, on a scale of picoseconds-tens of picoseconds, of the long and short-time stability of the electronics governing the delay between FELIX pulses and any other laser synchronized to it. If, for any reason, the actual delay between the pump pulse and FELIX shifts in time, this is visible by simultaneous grabbing the spectra of stretched and stretched-amplified pulses.

Another example of the influence of the delay on the spectral characteristics of the stretched-amplified pulse is shown in Figure 8-40 (a)-(c). Measurements are performed at low pump energy, so the wavelength shift cannot be due to saturation effects. The displacement in the stretcher is 48 cm and corresponds to a-calculated stretched-pulse duration of 49 ps, more than one half of the pump pulse length.

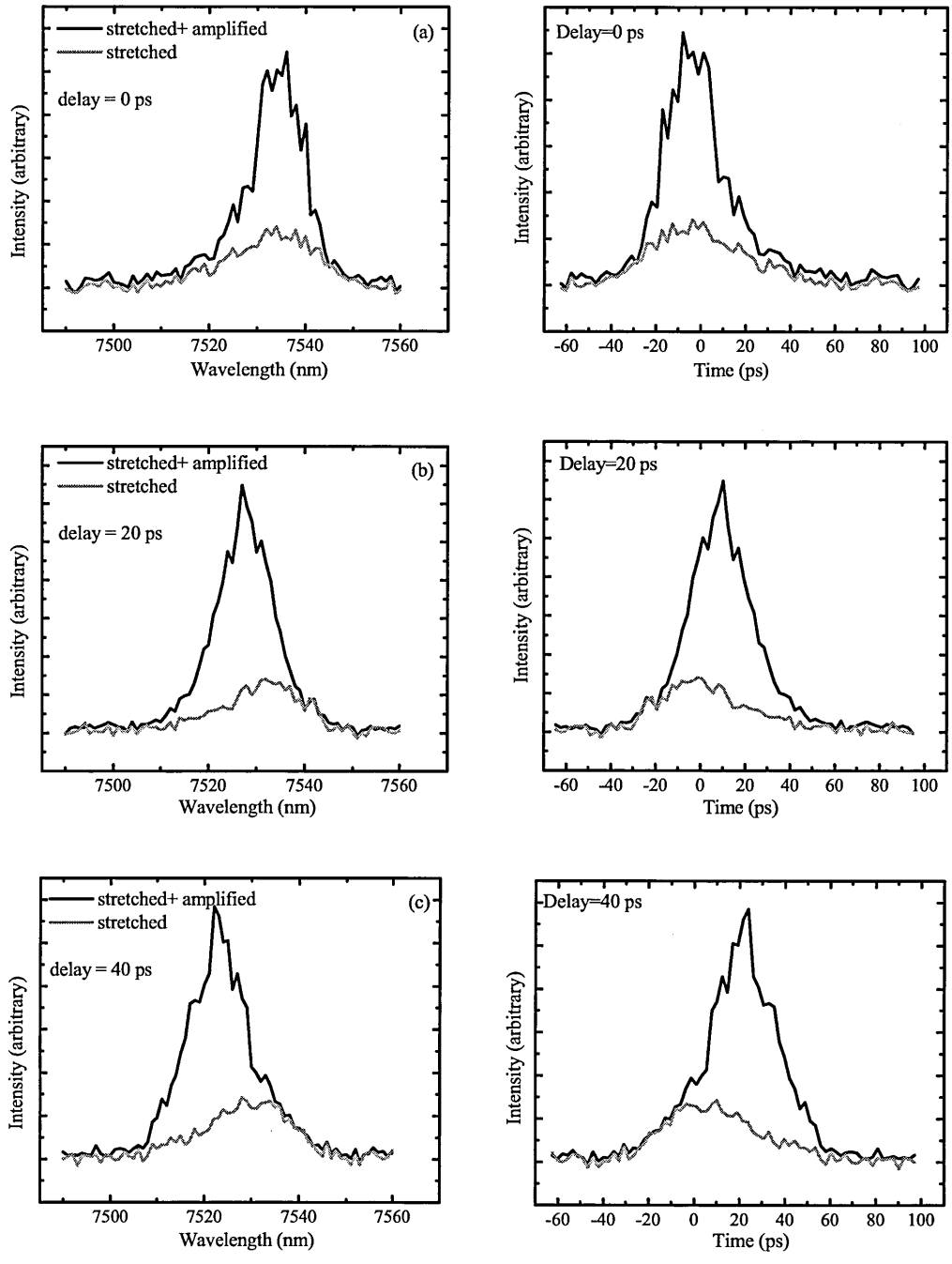

Figure 8-40 Spectra of the stretched and stretched amplified pulses with different delays: (a) 0 ps; (b) 20 ps; (c) 40 ps. The central wavelength of the stretched amplified pulses is shifted to lower values with increasing delay. Measurements are performed at low pump energy, so the wavelength shift cannot be due to saturation effects. The displacement in the stretcher is 48 cm and corresponds to a-calculated stretched-pulse duration of 49 ps, more than one half of the pump pulse length. The plots on the left side of the figure are recorded plots and the ones on the right side are converted to the time domain using the chirp value of 3.637×10^{-3} THz/ps.

The spectra of the stretched and stretched amplified pulses are recorded for three different values of the delay. The pump energy is low (around 8 mJ). As previously mentioned, the central wavelength shift effect is due to the wavelength

distribution in the stretched pulse and the preferential amplification of the wavelengths with the maximum intensity of the pump pulse. The wavelength shift of the stretched amplified pulse can be noticed while the delay is increased. Because the pulses are chirped, it is possible to convert the plots on the left side of Figure 8-40 (panels (a)) in time (panels (b)), by using Eq.(8-2) .The frequency chirp *b*, calculated using Eq.(8-10), corresponding to a displacement of 48 cm in the stretcher and to the central wavelength of 7.53 μm, is 3.637×10^{-3} THz/ps.

The "0 delay" is considered when no wavelength shift takes piace, i.e. in Figure 8-40 (a). One can notice that the temporal-wavelength shift does not coincide with the delay between pump and signal, but is lower. Figure 8-41 shows the measured spectrum of the input stretched pulse and the corresponding Gaussian shape.

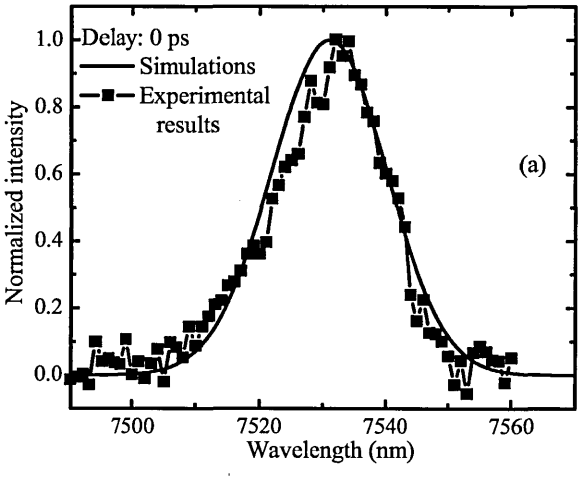

Figure 8-41 The spectrum of the input stretched pulse. Comparison between simulations (Gaussian shape) and measured spectrum, at a central wavelength of 7.53 μm

The parameters of the Gaussian shape were used for simulations presented in Figure 8-42-Figure 8-44. They present a comparison between the normalized measured spectra at 7.53 μm central wavelength, 10 mJ pump energy and 10 μJ input signal energy and the simulated ones, for three different delays between the pump and the signal is shown in. In the simulations all values of the input parameters were evaluated experimentally. The experimental data are the same presented in Figure 8-40 for the amplified pulse. The simulations show a similar shift of the central wavelength as the experimental data. Contrary to simulations, the experimental data show a spectral narrowing of the amplified pulse. This effect can be caused by the non-Gaussian shape of the stretched-signal or pump pulses.

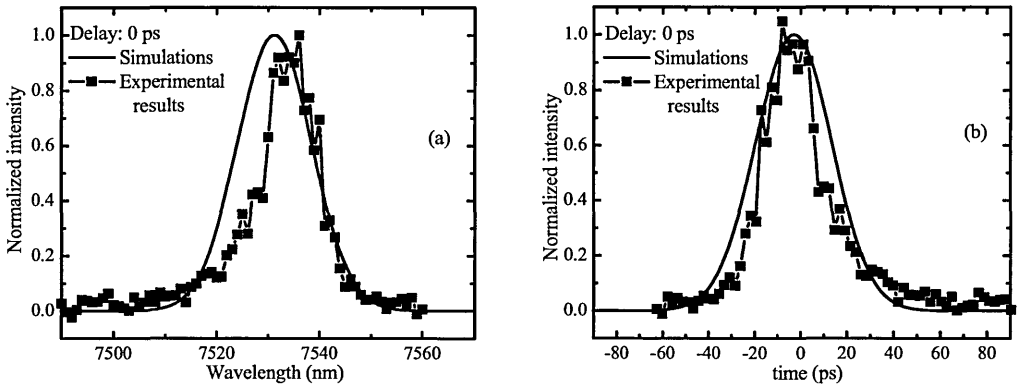

Figure 8-42 Simulated (continuous lines) and normalized experimental spectra (lines and symbols) of the signal pulse at 7.53 μm central wavelength, for 0 ps delay, 10 mJ pump energy and 10 μJ input signal energy. (a) are spectra as a function of wavelength and (b) are spectra as a function of time. The simulations show a similar wavelength shift, but experimental spectra are accompanied by a spectral narrowing, which is not revealed by simulations.

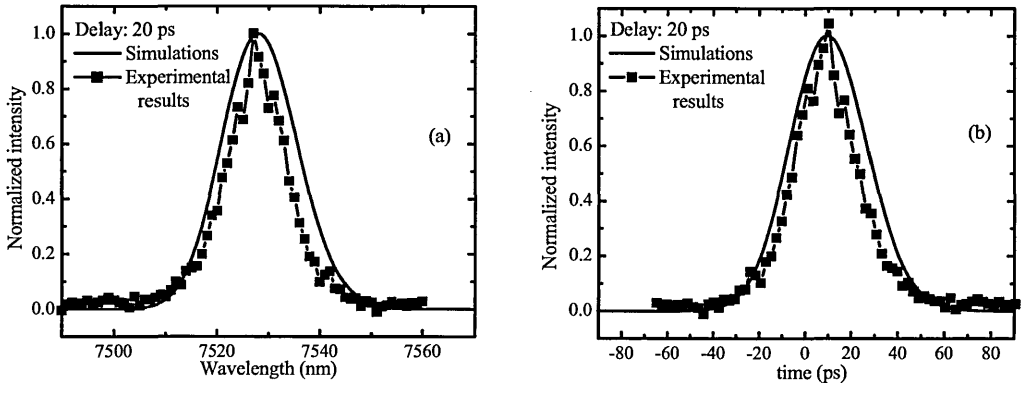

Figure 8-43 The same as Figure 8-42 for 20 ps delay between the pump and stretched-signal pulses

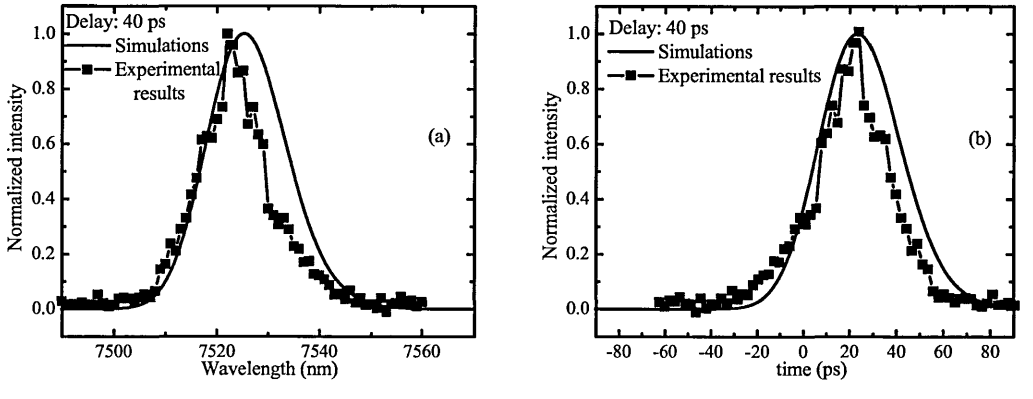

Figure 8-44 The same as Figure 8-42 for 40 ps delay between the pump and stretched-signal pulses

The effect of saturation (or, the influence of the pump intensity on the central wavelength of the stretched-amplified pulse) can manifest also in a central wavelength shift. This effect is shown in Figure 8-45. The measurements were performed at a signal wavelength of 7.54 μm. A wavelength shift of ~10 nm for a pump energy of 70 mJ is noticeable. The stretched pulse duration is comparable to the pump, estimated from the initial bandwidth and displacement to be 72 ps.

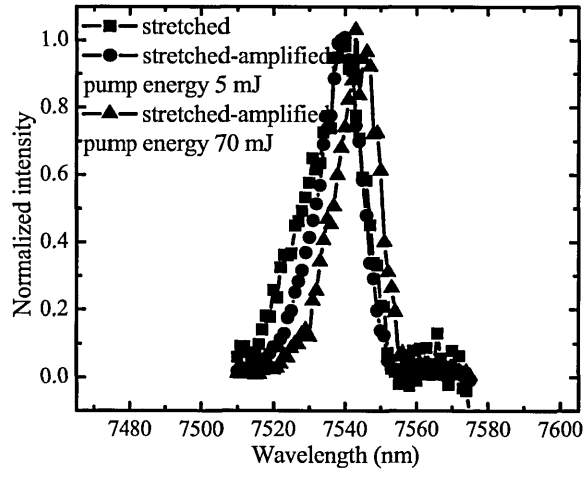

Figure 8-45 The spectra of stretched and stretched-amplified pulses at 7.54 μm signal central wavelength. A wavelength shift occurs for the high-pump energy of 68 mJ. The displacement in the stretcher is 70 cm and corresponds to a calculated stretched pulse duration of 72 ps, which is comparable to the pump pulse length

Autocorrelation traces

In this section some autocorrelation traces for the stretched-amplified pulse and for the compressed pulse are presented. It is of great importance that the compressed pulse preserves a high power. Two main requirements are to minimize the energy loss in the compressor and maintain short pulse duration, close to the one of the input pulse in the stretcher. The most important factors in preserving the short pulse duration are optimisation of the position of the horizontal retroreflector in the compressor resulting in the minimum possible duration of the output pulse and avoiding any loss of spectrum at the optical components. A possible source of spectral/temporal modification is the amplification process itself.

In principle, the factors modifying the stretched-amplified pulse duration are similar to those modifying the spectra. The excessive stretching, or incorrect temporal overlap between the pump and the stretched signal modify the amplified spectra (by narrowing the bandwidth). The stretched amplified pulse becomes

shorter than the stretched pulse and in turn the compressed pulse longer than the initial unstretched pulse, and in these conditions the output power can drop significantly. Additionally, the output wavelength might be shifted, as shown in the previous section.

Figure 8-46 presents the autocorrelation traces for the input and compressed pulses, for two different input energies, 20 and 40 mJ, at a signal wavelength of 6.3 μm. The measurements were performed using the same procedure as described in section 6.1. The autocorrelation traces of the amplified pulse after compression show no significant change compared to the input pulse.

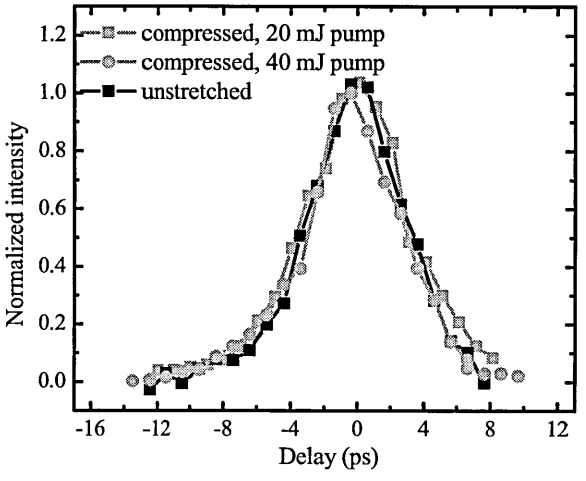

Figure 8-46 Autocorrelation traces for the unstreched and compressed pulse at 6.3 μm and pump energies of 20 mJ and 40 mJ.

Figure 8-47 shows the aurocorrelation for the input, stretched-amplified and compressed pulses at a signal wavelength of 6.3 μm. The noise in the autocorrelation traces of the stretched-amplified and compressed pulses is most probably due to the absorption in the water vapours and the long path in the air for the stretched and compressed pulses. From the same reason, in this case, the compressed pulse is slightly enlarged.

If the initial pulse is chirped, even if the pulse is narrowed by the amplification process, the same pulse duration can be obtained if the compressor is adjusted for the position corresponding to the minimum pulse duration.

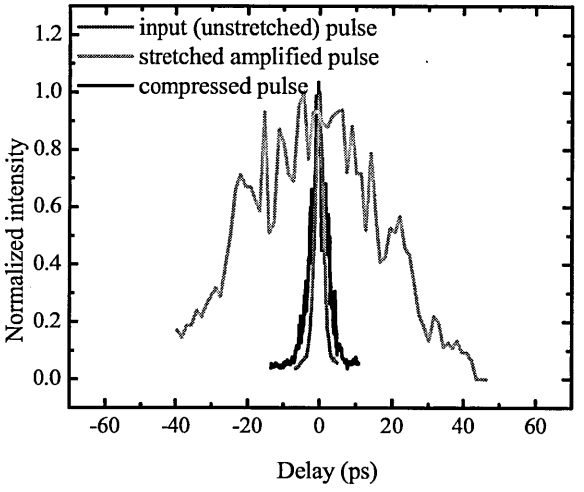

Figure 8-47 Autocorrelation traces for the input (unstretched), stretched-amplified, and compressed pulses at lambda= 6.3 μm, at 49.5 cm displacement.

The noise is not present in the autocorrelation traces taken at a wavelength where the absorption in water vapours is not present and with stable operation of the pump pulse. Thus, Figure 8-48 presents the autocorrelation traces for the un-stretched and compressed pulses for a high pump energy (68 mJ), at 7.5 μm.

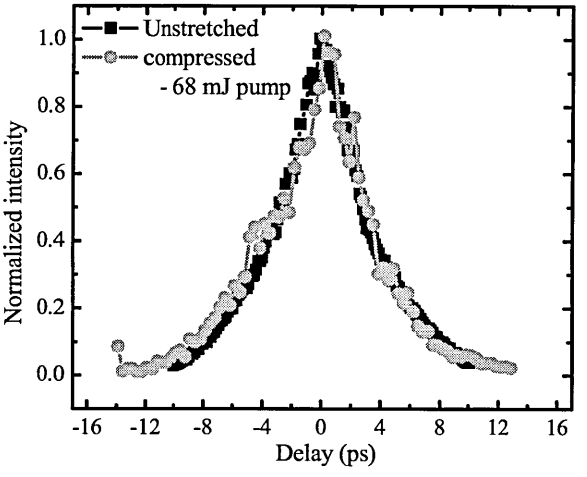

Figure 8-48 Autocorrelation traces for unstretched and chirped-amplified- compressed pulse at 7.5 μm and pump energy 68 mJ, and 48 cm displacement in the stretcher and the compressor

Figure 8-48 shows that the autocorrelation trace of the stretched-amplified and compressed pulse is not modified when compared with the input un-stretched pulse. The pulse duration resulting from the autocorrelation traces in the Gaussian shape pulse hypothesis are 3.9 ps for the input stretched pulse and 3.7 ps for the compressed pulse. Autocorrelation traces represented in Figure 8-48 correspond to the same pulses which spectra are plotted in Figure 8-45. When calculating the time

bandwidth product $\Delta\omega\Delta t$ for the two pulses in the hypothesis of Gaussian shapes, it results a value of 2.4 for the input (unstretched) pulse and a value of 2.5 for the compressed pulse. The time bandwidth product for a Gaussian pulse is 2.773.

8.4 Conclusion

In this chapter, the OPCPA method and the associated experimental results for the amplified signal pulse, which is provided by the FEL at FELIX, at a rate of 10 Hz, have been presented. It has been shown that, using OPCPA method, it is possible to amplify the energy of the signal pulse to values of milijoules (2.2-2.4 mJ at 6.3 μm), while maintaining the initial short pulse duration (~ 2 ps). Most of the energy data are measured for the stretched-amplified pulse (section **Energy measurements**), before compression. The method is applicable for the whole wavelength range considered (5-10 μm). The efficiency of the method depends on the crystal properties, especially on the damage threshold and available length, and on the grating properties (diffraction efficiency). Due to the comparable length of the pump and signal pulses, the stability in energy and central wavelength are highly influenced by the correct synchronization between the interacted pulses and by its long and short term accuracy. The correct seeding of the regenerative amplifier providing the pump pulse is also a crucial factor for a high output energy, good stability of the amplified pulses and the stability of the wavelength of the amplified pulse.

The results could be improved by using a crystal with higher nonlinear constant and gratings with improved efficiency on the whole wavelength range.

8.5 Bibliography

1. D. Strickland and G. Mourou, "*Compression of amplified chirped optical pulse*" Opt. Commun., Vol. 56, pp. 219-222, 1985

2. A. Dubietis, G. Jonusauskas, and A. Piskarskas "*Powerful femtosecond pulse generation by chirped and stretched pulse parametric amplification in BBO crystal*", Opt. Commun., Vol. 88, pp. 437–440, 1992

3. I. N. Ross, P. Matousek, M. Towrie, A.J. Lanley, J.L. Collier, "*The prospect for ultrashort pulse duration and ultrahigh intensity using optical parametric chirped pulse amplifiers*", Opt. Commun., Vol. 144, pp. 125–133, 1997

4. P. Matousek, B. Rus, I.N. Ross. "*Design of a multi-petawatt optical parametric chirped pulse amplifier for the iodine laser ASTERIX IV*", IEEE J Quantum Electron", Vol. 36, pp.158–63, 2000

5. X. Yang, Z. Xu, Y. Leng, H. Lu, L. Lin, Z. Zhang, R. Li, W. Zhang, D. Yin, and B. Tang "*Multiterawatt laser system based on optical parametric chirped pulse amplification*", Opt. Lett., Vol. 27, pp. 1135-1137, 2002

6. I. N. Ross, J. L. Collier, P. Matousek, C. N. Danson, D. Neely, R. M. Allott, D. A. Pepler, C. Hernandez-Gomez, and K. Osvay, "*Generation of terawatt pulses by use of optical parametric chirped pulse amplification*", Appl. Opt., Vol. 39, pp. 2422-2427, 2000

7. I. Jovanovic, C.A. Ebbers, C. P. J. Barty "*Hybrid chirped-pulse amplification*", Opt. Lett., vol. 27, pp. 1622-1624, 2002

8. I. Jovanovic, B. J. Comaskey, C. A. Ebbers, R. A. Bonner, D. M. Pennington, E.C. Morse "*Optical parametric chirped-pulse amplifier as an alternative to Ti:Sapphire regenerative amplifiers*", Appl. Opt., Vol. 41, pp. 2923-2929, 2002

9. J. Collier, C. Hernandez-Gomez, I. N. Ross, P. Matousek, C. N. Danson, J. Walczak, "*Evaluation of an ultrabroadband high-gain amplification technique for chirped pulse amplification facilities*", Appl. Opt., Vol. 38, pp. 7486-7493, 1999

10. I. N. Ross, P. Matousek, G. H. C. New, K. Osvay "*Analysis and optimization of optical parametric chirped pulse amplification*", J. Opt. Soc. Am. B, Vol. 19, pp. 2945-2956, 2002

11. A. Galvanauskas, A. Hariharan, and D. Harter, M. A. Arbore and M. M. Fejer "*High-energy femtosecond pulse amplification in a quasi-phase-matched parametric amplifier*", Opt. Lett., Vol. 23, pp.1-3, 1998

12. T. Harimoto, K.Yamakawa "*Numerical analysis of optical parametric chirped pulse amplification with time delay*", Optics Express, Vol.11, pp. 939-943, 2003

13. M. J. Guardalben, J. Keegan, L. J. Waxer, V. Bagnoud, I. A. Begishev, J. Puth, and J. D. Zuegel, "*Design of a highly stable, high-conversion-efficiency, optical parametric chirped-pulse amplification system with good beam quality*", Optics Express, Vol. 11, pp. 2511-2524, 2003

14. L. J. Waxer, V. Bagnoud, I. A. Begishev, M. J. Guardalben, J. Puth, and J. D. Zuegel "*High-conversion-efficiency optical parametric chirped-pulse amplification system using spatiotemporally shaped pump pulses*", Opt. Lett., Vol. 28, pp. 1245-1247, 2003

15. I. Jovanovic, J. R. Schmidt, and C. A. Ebbers, "*Optical parametric chirped-pulse amplification in periodically poled $KTiOPO_4$ at 1053 nm*", Appl. Phys. Lett. Vol. 83, pp. 4125-4127, 2003

16. P. Zhu, L. Qian, S. Xue, Z. Lin, "*Numerical studies of optical parametric chirped pulse amplification*", Optics & Laser Technology, Vol. 35, pp. 13– 19, 2003

17. A. Siegman, *Lasers*, University Science Books, Mill Valley, California, Chapter 9, pp. 334-335, 1986

18. E. B. Treacy, "Optical *Pulse compression with diffraction gratings*", IEEE J. Quantum Electron., Vol. 5, pp. 454-458, 1969

19. www.spectra-physics.com

20. E.G. Loewen, and E. Popov,. *Diffraction gratings and applications*, Marcel Dekker (New York, New York) ISBN: 0-8247-9923-2, 1997

21. E. G. Loewen , M. Neviere and D. Maystre, "*Grating efficiency theory as it applies to blazed and holographic gratings*," Appl. Opt., Vol. 16, pp. 2711-2721, 1977

22. R., Petit, editor, *Electromagnetic theory of gratings*, Springer-Verlag (New York); Vol. 22, in "Topics in Current Physics" series, Chapter 4, 1980

23. J. Xu, G.M.H. Knippels, D. Oepts, A.F.G. van der Meer, "*A far-infrared broadband (8.5-37 μm) autocorrelator with sub-picosecond time resolution based on cadmium telluride*", Opt. Commun. Vol. 197 pp. 379-383, 2001

Chapter 9 Conclusions and further work

This thesis describes the work performed for obtaining an intense source of a tuneable picosecond mid-infrared radiation in the wavelength range of 4-11 μm.

The first three chapters aim to introduce the reader to the main subject and goal of the thesis: the parametric amplification of picosecond mid-infrared radiation.

Chapter 1 gives an overview of the work undertaken. The main theoretical ideas required to understand the second order nonlinear processes -with an emphasis on parametric amplification, a fundamental physical process used in the experimental work- are reviewed in Chapters 2 and 3. They introduce also the most important parameters that influence the efficiency of the parametric amplification, which are used in Chapters 6, 7 and 8 for interpreting the experimental results and simulations.

Chapters 4 and 5 described the laser sources and the nonlinear crystal used for carrying out the parametric amplification of the mid infrared radiation. Chapter 4 presented the signal and pump laser sources: the FEL at FELIX and the Nd:YAG regenerative amplifier, emphasizing the properties that make them appropriate for parametric amplification experiments. Chapter 5 is a detailed overview of the nonlinear crystal, $AgGaS_2$. Besides the general description of the crystal properties, it contains also transmission measurements performed on the crystal used in experiments, the history of its damage and some conclusions related to the absorption coefficient and the nature of the damage. The main results show that, for a wavelength range of 4-8.8 μm, the losses introduced by coating are smaller than the losses caused by multiple reflections at the faces of the uncoated crystal. For longer wavelengths the coating seems to introduce additional losses, probably caused by absorption in the thin layer between the crystal surface and coating. This absorption can be the cause of the crystal damage, which takes place at pump energies of ~80 mJ, and a beam diameter of 11 mm, after few minutes of operation.

The simulations, grouped in Chapter 6 point out the importance of several parameters related to the crystal (nonlinear constant, crystal length), and to the laser sources (signal and pump intensities, delay, signal chirp, phase mismatch) for an efficient extraction of the amplified energy in the parametric amplification process, while maintaining short pulse durations. The impact of saturation on the energy of

the amplified pulse for the both cases of OPA and OPCPA is also presented. Regarding the energy of the amplified pulse, the comparison with experimental results gives a better fit for the OPCPA results than for OPA. The simulations were also useful for highlighting the influence of the jitter between pump and signal pulses in OPCPA. The central wavelength fluctuates with tens of nanometres for ~ 20 ps jitter. Its stability is dictated by the relation between the pump and stretched pulse durations, level of saturation, and jitter.

Chapter 7 and Chapter 8 present the most important experimental results. Chapter 7 describes the experimental set-up and results obtained with the OPA method. The results show an amplified energy of the order of hundreds of microjoules to 1.4 milijoules depending on wavelength, but with a strong saturation manifested by the dependence of the amplified pulse energy on the input signal energy and by the spectral/temporal modifications. Figure 9-1 shows the energy of the amplified pulse for the OPA case, crystal length of 16 mm, as a function of wavelength and 66 mJ pump energy.

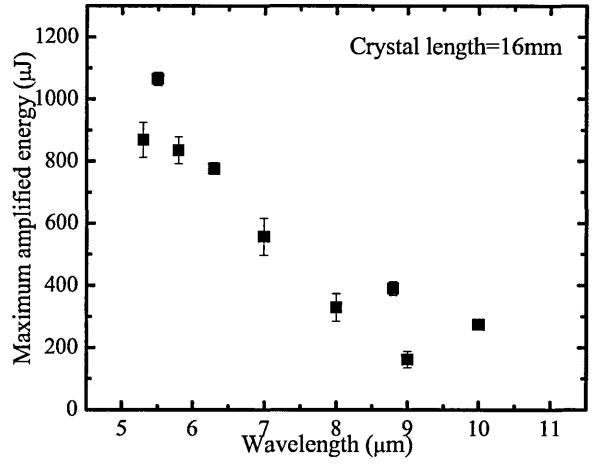

Figure 9-1 Energy of the amplified pulse as a function of the signal wavelength, at a pump power of 66 mJ. Beam diameters and input signal energies are different for each wavelength, but spectral width is 2%-3% from the central wavelength (respectively). The results are taken by scanning the FELIX wavelength and rotating the crystal for phase matching

Figure 9-2 presents the energy gain for the data in Figure 9-1, together with the crystal transmission, input signal energy and beam diameters as functions of wavelength.

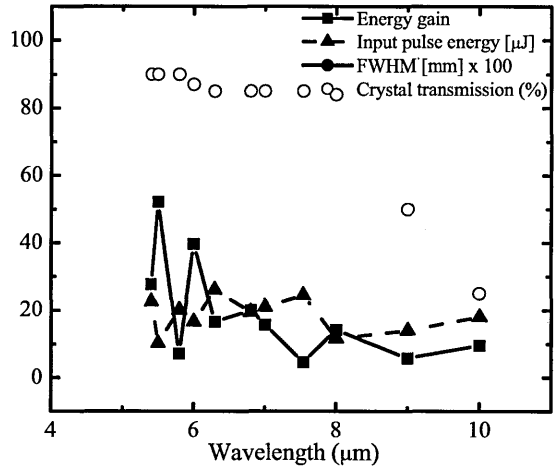

Figure 9-2 The energy gain, FEL beam diameter, input FEL energy and crystal transmission as a function of wavelength for the OPA, for data in Figure 9-1

The high values of the amplified energy obtained with the OPA scheme for short wavelengths could not be explained by simulations, which are presented in Chapter 6, section 6.2. The simulations predict a stronger saturation of the pulse energy, which predicted values of approximately half of the ones determined by experiments.

Chapter 8 reveals the advantages of using the OPCPA method and the corresponding experimental results. OPCPA overcomes the saturation effects. The OPCPA setup is based on the OPA setup. A stretcher placed before the nonlinear crystal modifies the signal pulse length, while the compressor after the amplification stage restores the short initial signal pulse duration. A detailed description of the structure of the stretcher and compressor used for OPCPA and the way they work for different input signal wavelengths is included. The experimental results obtained with the OPCPA scheme show an improvement of the amplified pulse energy, (till 2-2.5 mJ at 6 μm after amplification and ~ 1 mJ after compression), with only slight or no modifications of the spectral and temporal characteristics. Figure 9-3 shows an example of the improved values of the amplified pulse in the OPCPA case, at 6.3 μm, for an input stretched pulse duration of 35 ps.

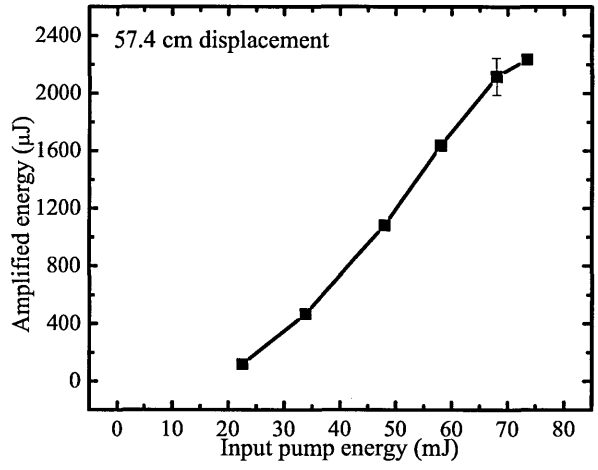

Figure 9-3 (a) Energy of the stretched-amplified pulse against the pump pulse energy for an input stretched-pulse duration of 35 ps. The input energy of the micropulse, at the crystal, was 10 μJ. The input signal wavelength was 6.3 μm and the crystal length 17 mm.

The energy of the amplified pulse depends on wavelength, input signal energy, beam diameters, pulse duration and spectrum, at the same pump energy. At 10 μm wavelength, values as high as 800 μJ before the compressor could be obtained. The results presented by Figure 7-30 show the dependence of the stretched-amplified pulse energy on the wavelength in two cases, characterized by different FEL settings.

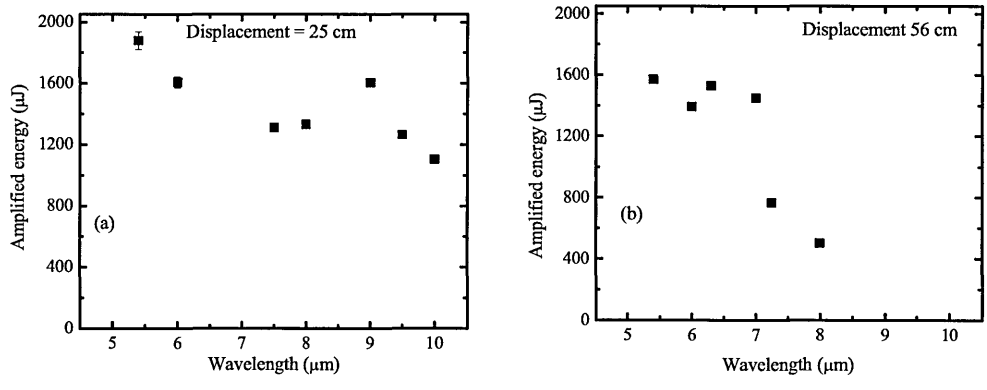

Figure 9-4 Stretched-amplified pulse energy as a function of wavelength for FEL settings optimized for 8-10 μm and displacement of the stretcher of 25 cm (a) and 56 cm (b), input bandwidth 0.2% and pump energy ~ 64 mJ

Figure 9-5 presents the energy gain for the data in Figure 9-4, together with the crystal transmission, input signal energy and beam diameters as functions of wavelength.

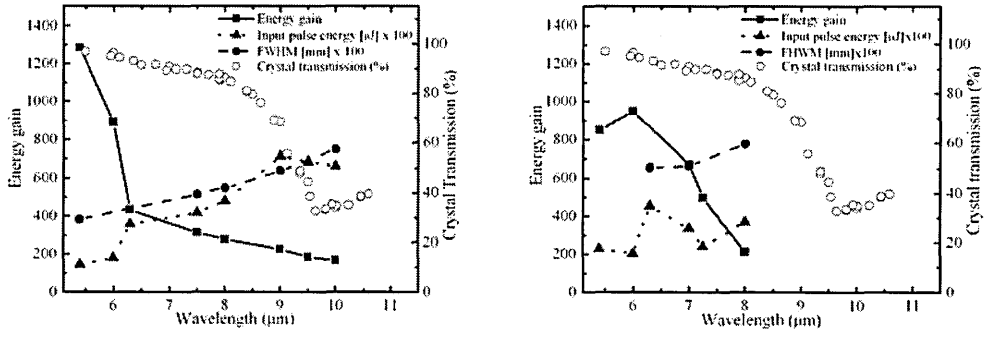

Figure 9-5 The energy gain, FEL beam diameter, input FEL energy and crystal transmission as a function of wavelength for OPCPA. The plots are calculated with the data shown in Figure 9-4

The amplified energy at the output of the compressor at 6.3 μm signal wavelength is shown in Figure 9-6, and is plotted against the pump energy. A value as high as 800 μJ amplified energy was determined, at 65 mJ pump energy.

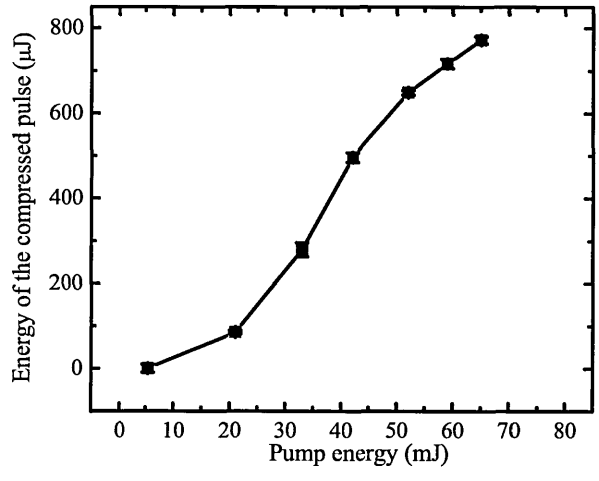

Figure 9-6 Energy of the compressed pulse against the pump energy at 6.3 μm wavelength and 10 μJ input energy of the FEL pulse

The spectrum and pulse durations of the amplified pulse can be modified by several factors, like saturation, stretched pulse duration and delay between the pump and signal pulses. Because of the comparable lengths of the pump and signal pulses, the spectral characteristic (shape and central wavelength) are sensitive to the jitter between the signal pulses. As shown by Figure 9-7, with a proper choice of the stretched-pulse duration, at high pump energies the autocorrelation trace does not show modification and a short pulse duration is preserved after compression.

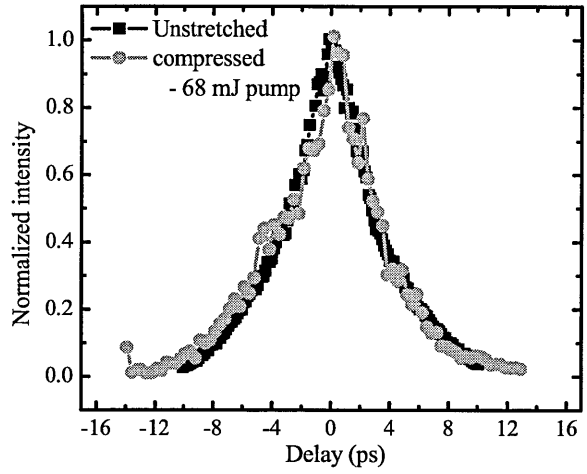

Figure 9-7 Autocorrelation traces for unstretched and chirped-amplified- compressed pulse at 7.5 μm and pump energy 68 mJ, and 48 cm displacement in the stretcher and the compressor

The amplified pulse energy is limited by the diffraction grating efficiency used by the stretcher and compressor with lower efficiency for short wavelengths in the range 4-5.5 μm and 7-9 μm) and by the pump pulse duration, which does not allow efficient amplification for stretched signal pulses longer than ~ 80 ps. An improvement of the output power results could be realised by using a crystal with higher nonlinearity and higher damage threshold, gratings with high damage threshold for the stretcher/compressor system in order to maintain efficiency and higher diffraction efficiency over the whole signal wavelength range and pump pulses with longer pulse duration to make advantage of the OPCPA method. The wavelength range could be extended by the use of other crystals like GaSe, with a proper choice of the pump laser, because this crystal has higher absorption coefficient for the pump wavelength used in this work (1.064 μm).

As outlined in the Introduction, the high energy (~ 1 mJ) in picosecond pulses with a repetition rate of 10 Hz is useful in nonlinear spectroscopy experiments and dynamics studies on picosecond scale of samples with long relaxation times.

The advantages of using an FEL as the signal source are the rapid tuneability, the possibility of adjusting the pulse length and spectral properties, and the quite high initial pulse energy. In principle, the FEL can be replaced with an OPO pumped by a Ti: sapphire-pumped OPG/OPA system. For the wavelength range of 4-11 μm the main advantage of the FEL as signal source in parametric amplification is the higher pulse energy.

The method can be also applied for amplifying signal pulses in other wavelength ranges, either using the FEL as a signal source, or replacing it with virtually any other tuneable picosecond signal source. However, the particular pump source and nonlinear crystal have to fulfil the conditions mentioned in Chapter 4, sections 4.1 and 4.2 and to take into account also the requirements imposed by applications to the amplified pulses (energy, spectrum, repetition rate and pulse duration). An excellent overview of the possible solid-state signal sources is given in [1], but other lasers sources can be used as well. The choices of the nonlinear crystal and pump sources are related tightly through the phase matching condition and the transparency of the crystal at the useful wavelengths, but also by issues like damage threshold and commercial availability. Regarding the stretcher compressor system, this should work with high efficiency for the signal wavelength range considered for amplifying and preserve/control the spectral characteristics, without introducing aberrations and beam fluctuations. For reliable stretched-amplification, the central wavelength of the signal source has to be stable on short and long-term operation.

9.1 Bibliography

1. T. Sorokina and K.L. Vodopyanov, *Solid Stated Mid-Infrared Laser Sources*, Topics in Applied Physics, vol. 89, Springer Verlag, Berlin, 2003